An experimental study of plastic deformation of materials

Knudsen, Tine

Publication date:
2008

Document Version
Publisher's PDF, also known as Version of record

Risø DTU
National Laboratory
for Sustainable Energy

Risø-PhD-thesis

An experimental study of plastic deformation of materials

Tine A. Knudsen

Risø-PhD-41(EN)

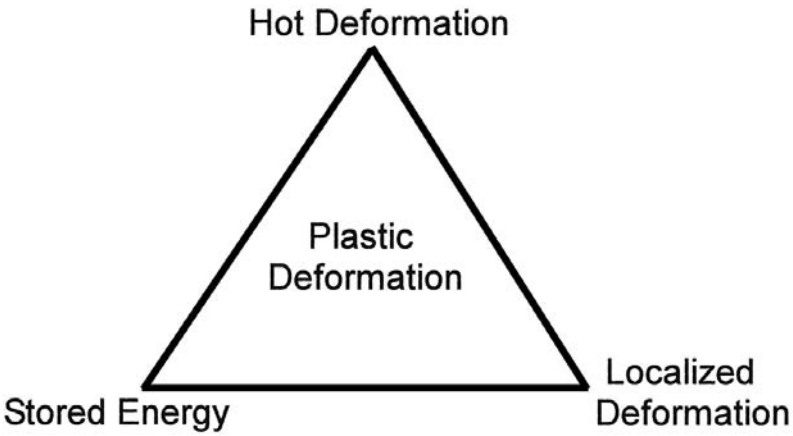

Risø National Laboratory for Sustainable Energy
Technical University of Denmark
Roskilde, Denmark
March 2008

Author: Knudsen, Tine A.
Title: An experimental study of plastic deformation of materials
Department: Metallurgy Research Department, Center for Fundamental Research: Metal Structures in Four dimensions

This thesis is submitted in partial fulfilment of the requirements for the Ph.D. degree at Roskilde University, Department of Science, Systems and Models

Supervised by: Senior scientist Grethe Winther, Risø,
Dr. Techn. Niels Hansen, Risø and Prof. Jeppe Dyre, RUC

Abstract (max. 2000 char.):

The thesis falls in three parts, focusing on different aspects of plastic deformation of metals. Part I investigates the dislocation structures induced by hot deformation and compares these with the structures after cold deformation.
In particular, it is shown that the dislocation structures in the investigated hot deformed samples (lnZ= 27.5 to 32) in general are cell block structures, and that the alignment of the cell block boundaries at low strain depends on the grain orientation, often in the same manner as in cold deformation.
Part II investigates the energy stored in the dislocation structure after cold deformation by calorimetry and by analysis of the dislocation structure. The stored energy measured by calorimetry is found to be larger than that determined from the dislocation structure by a factor between 1.9 and 2.7, and this factor decreases with the plastic strain. Part III aimed at investigation of localized deformation in the form of Lüders bands by in-situ measurements using three-dimensional X-ray diffraction. This part concluded that modifications to the experimental setup is needed to obtain reliable data.

Resumé
Afhandlingen falder i tre dele, der fokuserer på forskellige aspekter af plastisk deformation af metaller. Del I undersøger dislokationsstrukturer induceret under varmdeformation og sammenligner disse med kolddeformation.
Specifikt findes at dislokationsstrukturerne i de undersøgte varmdeformerede prøver (lnZ = 27.5 til 32) i reglen er celleblokstrukturer, og at retningen af celleblokvæggene ved lave tøjninger afhænger af kornorienteringen, ofte på samme måde som efter kolddeformation. Del II undersøger den energi, der er lagret i dislokationsstrukturen efter kolddeformation vha. kalorimetri og analyse af dislokationsstrukturen. Den lagrede energi målt med kalorimetri er en faktor 1,9 til 2,7 højere end bestemt ud fra dislokationsstrukturen, og denne faktor falder med den plastiske tøjning. Del III stilede mod undersøgelse af lokaliseret deformation i form af Lüders bånd vha. in-situ målinger med tre-dimensionel Røntgen spredning. Denne del konkluderede, at ændringer i den eksperimentelle opstilling er nødvendige for at kunne få troværdige data.

Risø-PhD-41(EN)
March 2008

ISBN 978-87-550-3695-6

Contract no.:

Group's own reg. no.:

Sponsorship:

Cover :

Pages: 298
Tables:
References:

Information Service Department
Risø National Laboratory for Sustainable Energy
Technical University of Denmark
P.O.Box 49
DK-4000 Roskilde
Denmark
Telephone +45 46774004
bibl@risoe.dk
Fax +45 46774013
www.risoe.dtu.dk

Preface

This thesis is submitted in partial fulfillment of the requirements for obtaining the Ph.D. degree from the Department of Science, Systems and Models, at Roskilde University (RUC).

The research presented in this thesis, has been carried out within the Center for Fundamental Research: Metal Structures in Four Dimensions, at Risø National Laboratory for Sustainable Energy, Technical University of Denmark.

The thesis has been conducted under the supervision of Senior Scientist Grethe Winther (Risø), Dr. Techn. Niels Hansen (Risø) and Prof. Jeppe Dyre (RUC). I would like to take the opportunity to thank my Risø supervisors Niels Hansen and Grethe Winther for introducing the metallic world to me and for dedicated supervision and Jeppe Dyre for help in general.

The thesis included a four month stay during the spring/summer 2005 at the European Synchrotron Radiation Facility (ESRF) in Grenoble. I would like to thank the beam line staff at ID11 - ESRF especially Jonathan Wright for indispensable help during my beam time.

I would also like to thank the metal 4D group, particular Preben Olesen for help in general, Gitte Christansen for very skillful preparation of TEM foils, Senior Scientist Xiauxu Huang for teaching me TEM, and Palle Nielsen and Lars Lorentzen for sample preparation. I would also like to thank Jake Bowen for always being willing to answer questions regarding EBSD, Kristófer Hanneson for some of the initial SEM characterizations, and Professor Brian Ralph (Brunel University) for proof reading this thesis.

Dr. E. J. Palmiere and Mr. A. J. Lacey, The Department of Engineering Materials at The University of Sheffield are thanked for plane strain compression of the samples.

Special thanks to the *Coffee - Office Club* Rasmus Godiksen, Bo Jakobsen and Kristoffer Haldrup, for many enjoyable times

I would like to thank my husband Peter Ahrendt for beam time participation and support through the time as a Ph.D. student.

To Peter and Matilde
Thank you for the empathy and patience during the long nights of working.

Tine A. Knudsen
Tranbjerg Marts 2008

The authors gratefully acknowledge the Danish National Research Foundation for supporting the Center for Fundamental Research: Metal Structures in Four Dimensions, within which this work was performed.

Papers

Paper A Microstructural evolution in aluminium (AA1050) plane strain compressed at 0.7 T_M
T. Knudsen, G. Winther and N. Hansen, Proceedings of the 25th Risø International Symposium on Materials Science: Evolution of Deformation Microstructures in 3D: C. Gundlach, K. Haldrup, N. Hansen, X. Huang, D. Juul Jensen, T. Leffers, Z.J. Li, S.F. Nielsen, W. Pantleon, J.A. Wert, G. Winther Risø National Laboratory, Roskilde, Denmark 2004, pp. 383-385

Paper B Image analysis for X-ray studies of the dynamics of individual embedded subgrains during recovery
C. Gundlach, S. Schmidt, L. Margulies, T. Knudsen, W. Pantleon and H. F. Poulsen. Materials Science and Technology vol. 21 (2005) no.12, pp. 1476-1479

Paper C Stored energy in nickel cold-rolled to large strains
-measured by calorimetry and evaluated from the microstructure
T. Knudsen, W.Q. Cao, A. Godfrey, Q. Liu, and N. Hansen
Metallurgical and Materials Transactions A - vol. 39A, (2008) pp. 430-440

Reports

Report A AA1050 Basic material

List of commonly used notation

AA 1050 :	Aluminium 99.5% pure
3D-XRD :	3 dimensional x-ray diffraction
EBSD :	Electron backscattered diffraction
HAB :	High angle boundaries
IDBs :	Incidental dislocation boundaries
GNBs :	Geometrically necessary boundaries
MAD :	Mean angular deviation
PSC :	Plane strain compression
RT :	Room temperature
SEM :	Scanning electron microscopy
TEM :	Transmission electron microscopy
Z :	Zener Hollomon parameter
θ :	Bragg angle

Contents

Chapter 1

Introduction

Processing of metals has been a skill known to man since the early civilization and metallurgy may be considered as one of the oldest applied sciences. The importance of metals is nicely illustrated by the fact, that historic time periods are named after which metal or alloy were the dominating one used. Gold was one of the first metals used mainly as jewelery as early as 6000BC. Later copper was discovered, and processing of this lead to the first metal tools and weapons (Lund, 1998). The real difference for civilization in terms of metallurgy, came with the discovery of iron (steel) and the ability to process it. In a sense iron/steel can be considered one of the key factors for the evolution of modern civilization, as with the discovery of iron/steel it became possible to make advanced tools and weapons, due to the heavy and hard metal alloy (Thomsen, 1975). In 1825 another lighter metal was isolated for the first time by the Dane Hans Christian Ørsted, when he isolated a small amount of aluminium. Approximately 60 years later the Hall-Héroult process, which is production refining of aluminium, was invented (Bastue Christensen, 1949). The electrochemical extraction process, enabled aluminium production at a much lower price, making it favorable for industrial use. The Hall-Héroult process is still used in the aluminium industry today.

Even though the processing of metals was conducted on a trial and error basis, the knowledge of processing was quite advanced. The theoretical fundament for understanding the processing of metals (work hardening, recrystallization, etc.) was however lacking, and it was not until the existence of dislocations was proposed by Taylor, Orowan and Polyani in 1934 (Weertman and Weertman, 1992), theories describing the deformation of metals were formulated. These theories are still used today.

So metals and metal processing has played and continues to play and

important role for the developing of materials for a variety of applications. The increase in technology furthermore leads to a demand of more designed products and thereby a further demand of knowledge to produce yet more advanced products. Hence understanding of the fundamental mechanisms for metal working, is important not only from a scientific point-of-view but also from an industrial perspective (Ricks, 1999). The demand for knowledge of the fundamental science behind metal working applicable to industry is the overall driving force for the current thesis. The more specific scientific objective of the study will in the following be described in more detail.

Metal working, is in the following denoted by the more general term deformation, and is divided into regimes of cold, warm and hot deformation. Cold deformation is defined by processing below $0.4\,T_M$, where T_M is the absolute melting point of the metal. Hot deformation is processing above the recrystallization temperature ($>0.6\,T_M$) and warm deformation is the range in between cold and hot (McQueen and Blum, 2000).

Cold and hot deformation have different industrial applications, due to the different properties induced by the deformation. Cold deformation is characterized by increasing strength due to work hardening, while hot deformation leads to a softer product, due to less work hardening and in some cases recrystallization during or after the deformation.

A method to understand how the properties of a metal relate to the processing of it, has been to characterize the microstructure of the metal after deformation. Through such a characterization of cold deformed aluminium[1], it has recently been established that cold deformation to medium strains of aluminium induces a dislocation structure, which is dependent on the orientation of the individual grains in the polycrystal and not primarily on the macroscopically most stressed planes.

The orientation dependence of a deformation-induced dislocation structure has been known to apply for deformed single crystals, and has been related to the active slip systems in the metal. The findings that the same applies to cold deformed polycrystals, established that the deformation microstructure developed, is due to slip of specific active slip systems, where the active slip systems relates to the orientation of the grain and the imposed deformation.

[1]Or more general fcc metals with a medium-to-high stacking fault energy

The scientific objective of the current thesis is to explore different aspects of plastic deformation with special focus on the possible orientation dependency of the deformation structures. Part one of the current thesis explores whether or not there is a similar grain orientation effect in aluminium when it is hot deformed as observed in cold deformation. Hence, the aim is to determine if the microstructure evolved after hot deformation depends on the orientation of the grain, as observed during cold deformation.

To further the characterization of the microstructure both cold and hot deformed differential scanning calorimetry was conducted (described in part II). This was chosen due to the anticipation, that the energy stored in the microstructure shows the same orientation dependence. To evaluate this, stored energy measurements were conducted on initially cold deformed polycrystalline metals to further the characterization of the cold deformation structure with the aim of characterizing the corresponding hot deformed structure.

Part III of this thesis concerns studies conducted in part at the European Synchrotron Radiation Facility (ESRF), Grenoble France. The tensile deformation of Armo Iron was investigated. The aim of the project was to explore the localized deformation associated with the formation of Lüders band during tensile testing, to elucidate, if deformation of bcc metals also display an orientation dependency and to further the understanding of localized deformation. This is described in part III of the thesis.

A short introduction to metals

Metals are crystalline structures either single or polycrystalline. In polycrystalline metals the individual crystallites are commonly referred to as grains.

Crystals are structures of high symmetry and thereby the reverse of amorphous solids. Crystals are described with a unit cell, which is the smallest unit containing all symmetry elements of the entire crystal. The metals described in the current study have either face centered cubic (fcc) or body centered cubic (bcc) crystal structures. In the description of crystals it is assumed, that the crystal is perfect through out the entire space. This however is not the case in metals, as defects are practically always present. In pure metals the common defects are vacancies, dislocations and twins. Vacancies are missing atoms in the crystal lattice, dislocations are an extra half plane of atoms[2] and twins is a fault in the stacking sequence of the crystal planes.

During plastic deformation of metals the concentration of defects increases significantly. In metals especially the multiplication of dislocations which leads to work hardening has been investigated. The dislocations created assemble in dislocation walls creating areas of perfect crystal lattice surrounded by dislocation walls or boundaries. It is the evolution of these dislocation walls or boundaries after deformation, that is analyzed in the current thesis.

Plastic deformation structures in crystals are thereby the macroscopic evidence of dislocation movements, multiplication and storage in the crystal lattice. When a dislocation moves in the lattice the movement is called slip. Slip occurs on the closed packed planes in the most closed packed directions, which in fcc metals are one of the planes {111} in the <110> directions giving a total of 12 possible slip systems. In bcc the most common slip planes are the {110} planes in the <111> directions, hence also 12 slip systems are the most common ones in bcc. Other slip systems in bcc are slip on the {112} and {123} planes in the <111> direction. In bcc also pencil glide can occur, which is slip in the <111> direction on multiple planes, that all contains the slip direction. Cold deformation usually takes place by slip whereas at elevated temperatures (hot deformation) dislocation climb may also occur.

In order to plastically deform a crystal one or more slip systems has to be

[2]for simplicity only edges dislocations are described

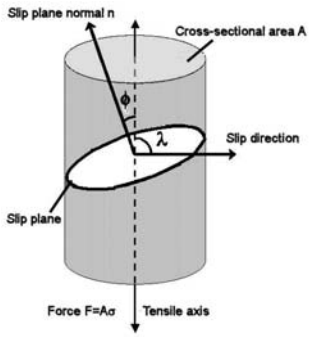

Figure 1.1: Illustration of the connection between slip direction and slip plane and the deformation axis in tensile testing

activated i.e. a minimum shear stress has to be applied to the respective slip system. This shear stress is denoted the *critical resolved shear stress* τ_c. So to activate a slip system the shear stress τ_{nd} on a slip plane has to be equal to the critical resolved shear stress. Hence:

$$\tau_{nd} = \tau_c \tag{1.1}$$

In this the slip plane normal is denoted n, and the slip direction is denoted d.

The shear stress on the slip plane can be related to the applied stress through coordinate transformations from the crystal lattice to the macroscopic system defined by the deformation geometry. This is illustrated in figure 1.1 for a single crystal tensile deformed. In this set up, λ is the angle between the tensile axis and the slip direction, ϕ the angle between the slip plane normal, and the tensile axis, while F is the force and A the cross-sectional area. Hence from the geometry of the setup the resolved shear stress is:

$$\tau_c = \frac{F}{A} \cdot \cos\lambda \cdot \cos\phi \tag{1.2}$$

where $\cos\lambda\cos\phi$ is termed the Schmid factor. The slip system with the highest Schmid factor is the one activated (Hosford, 1993).

The slip systems activated during deformation of polycrystals have also been described by (Taylor, 1938). In Taylor's model, the deformation of a fcc polycrystal required the activation of 5 independent slip systems, to accommodate any shape change of the individual crystallites. According to Taylor the slip systems activated out of the possible 24 combinations, were

the combinations, which require the least work (minimum shear stress) to produce the given deformation.

The individual crystallites of poly-crystalline metals are often aligned in a preferred direction. This non-random orientation of the crystallites is termed *texture* in metallurgy. The texture arises in materials due to the processing of the metals. The deformation textures which evolve as a result of glide on the active slip systems, gives rise to a displacement gradient in the grain. The displacement gradient can be decomposed in a symmetric strain component and an antisymmetric rotation component. These rotations are the basic for the texture evolution.

Part I

Grain orientation dependence in hot deformed aluminium

Chapter 2

Literature review

In the following chapter a literature review of cold and hot deformation of aluminium alloys are presented in order to specify the aim of the study in chapter 3.

2.1 Cold deformation

Deformation of aluminium and aluminium alloys at room temperature are often referred to as cold deformation, however, as the melting temperature of aluminium is quite low, room temperature deformation ($0.33T_M$) approaches the warm deformation regime (0.4 T_M-0.6 T_M).

During cold deformation of fcc metals the dominating process is dislocation multiplication which leads to work-hardening. As the original grains deform, the dislocations created arrange in dislocation boundaries i.e. low-energy dislocation structures (Kuhlmann-Wilsdorf, 1989), (Bay et al., 1992) and the grains divide into cell blocks consisting of nearly equiaxed cells separated by incidental dislocation boundaries (IDBs). It is suggested that IDBs are created due to statistical trapping of dislocations. The cell blocks are enclosed or traversed by extended planar dislocation boundaries also termed geometrical necessarily boundaries (GNBs). GNBs are assumed to be boundaries formed, when the individual cell blocks rotate. The rotation is related to either activity of different slip systems in the regions of the grain created by the neighbouring grains (Kuhlmann-Wilsdorf and Hansen, 1991), (Bay et al., 1992), unequal partition of the shear amplitude on the same slip systems within a grain (Wert, 1998) or local strain differences (Hughes, 2003).

An example of a cell block structure delineated by GNBs is displayed in

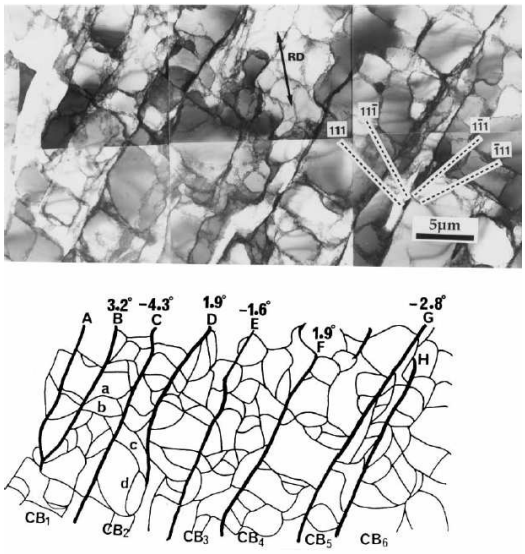

Figure 2.1: TEM micrograph with tracing of aluminium 99.996% pure cold rolled 10% from (Liu et al., 1998)

figure 2.1, which is a micrograph obtained from a 99.996% pure aluminium cold rolled to a thickness reduction of 10% from (Liu et al., 1998).

As the grains are strained dislocations accumulate in the dislocation boundaries, creating an increasing misorientation across the boundary, making the individual cell blocks rotate apart. Upon further straining, the cell block becomes thinner, i.e. more GNBs are created and the 1st and 2nd generation of microbands and S bands evolve. At large strains the cell block structure is reduced to narrow spaced GNBs one IDB wide aligned with the rolling direction. This structure is also termed as a lamellar structure and the IDBs between the GNBs or lamellae are denoted a bamboo structure (Hughes and Hansen), (Hughes and Hansen, 1993), (Hughes and Hansen, 2000).

The difference in formation of GNBs and IDBs results in different behaviour of the boundaries with strain, as initial seen in 99.996% pure polycrystaline aluminium cold rolled 5% 10% and 30%. In this the misorientation was found to be larger across the GNBs and to increase more with strain compared to the IDBs. Likewise the average spacing between GNBs were larger than for the IDBs and decreases more rapidly with strain (Liu and Hansen, 1995). This was later found also to apply in 98% pure aluminium cold rolled to true thickness strain of 5 (Liu et al., 2002) and in 99.99% purity nickel

cold rolled up to 98% (Hughes and Hansen, 2000).

Also the distribution of misorientation angles and spacings differs between the two boundary types. They both however *scale*, i.e. when the misorientation angle distributions are normalized by the averaged values and given as the corresponding probability function, IDBs and GNBs plotted separately have been found to follow the same distribution irrespective of material and strain. This phenomena, has been referred to as scaling, and the scaling indicates that the creation of boundaries are of universal character (Hughes and Hansen, 2000), (Hughes et al., 1998). In (Pantleon and Hansen, 2001) the scaling of IDBs and GNBs was found to be best described by a Rayleigh function. The scaling has also shown to apply to the spacing of the GNBs (Godfrey and Hughes, 2000).

The boundaries generally cluster around the macroscopically most stressed planes, which has lead to the suggestion, that the deformation structure evolved depends solely on the deformation mode (Hurley et al., 2003) (Humphreys and Bate, 2005).

However TEM analysis of 84 grains in a polycrystaline 99.996% pure aluminium (Huang and Hansen, 1997) deformed in tension up to true strain of 0.34, found the developed dislocation structure could be classified into 3 different characteristic structures, type 1 2 and 3, with different orientations and morphologies, which indicated an orientation dependent dislocation structure. Type 1 were characterized by a cell block structure delineated by straight GNBs parallel or nearly parallel with the trace of a {111} slip plane. The tensile axis of the grain was oriented between [100] and [111] in the inverse pole figure. Type 2 were characterized by more curved GNBs delineating a cell block structure. These GNBs were not parallel to the trace of a slip plane, and the tensile axis of the grains were oriented towards [111]. The third structure were equiaxed cells with the tensile axis oriented along [100].

This was followed by a similar study in polycrystaline copper (Huang, 1998), where the 3 classes of dislocation structures where compared to deformation structures of single crystals of identical orientations. 3 types of structures (A^I, A^{II}, and B) where also identified in polycrystalline 99.996% pure aluminium cold rolled up to 50 % by (Liu et al., 1998). In this, B structures were characterized by having no GNBs aligned with the trace of a {111} plane and were oriented around the cube orientation. A^I and A^{II} were characterized by having GNBs aligned with the trace of {111} planes.

The difference between the two groups were, that A^I had very straight GNBs and were oriented around the Goss and S orientations, while the boundaries in A^{II} were less straight, and no clear orientation relationship was found in this group. This lead to the conclusion, that the grain orientations was the main factor determining the dislocation structure developed. Recently this orientation relationship was expanded to apply generally to copper and aluminium deformed in rolling and tension strained to medium strain, irrespectively of purity and grain size (Huang and Winther, 2007).

More evidence of grain orientation-dependent dislocation structures were seen through analysis of the GNB alignment in individual grains in polycrystals. In this the boundaries were found also to align with respect to the macroscopically most stressed planes, but the most dominating factor for boundary plane alignment was the crystallographic orientation of the lattice, where the connection between the two observations were the active slip systems (Winther et al., 2000) (Winther, 2003). This was recently further extended to establish that the dislocation structure developed in fcc metals of medium-to-high stacking fault energy strain up to medium strain, depend solely on the active slip systems (Winther and Huang, 2007).

The textures evolved during cold deformation are the texture components brass, S and copper while Goss and any initial cube texture decreases. The strength of the individual texture components, for a given strain and deformation mode, depend on the material i.e. grain size, particle content, degree of deformation and initial orientation (Hansen and Juul Jensen, 1986), (Rollet and Wright) and (Hirsch and Lücke, 1988).

Stress-strain curves obtained during cold deformation display stages of different work-hardening behaviour, and the stress-strain curves are therefore divided into the stages I, II, III and IV, according to their characteristics. In polycrystals only stages II, III and IV are observed. Stage II is characterized by constant work-hardening, stage III by constant decreasing work-hardening rate (parabolic stress-strain relationship) while stage IV displays nearly linear work-hardening (Mughrabi, 1993).

The yield stress has also been found to be dependent on the grain size of the samples given by the Hall-Petch relationship:

$$\sigma = \sigma_0 + \frac{K}{\sqrt{D}} \tag{2.1}$$

where σ_0 and K are constants, and D the diameter of the grain (Hall, 1951), (Armstrong et al., 1962).

2.2 Hot deformation

During hot deformation of aluminium and aluminium alloys the mobility of the dislocations are increased, which enables edges dislocations to climb (vacancy diffusion) and cross clip occurs more readily. This increase in dislocation mobility makes it possible for dislocations to entirely or partly annihilate (McQueen and McGregor Tegart, 1975) (McQueen and Hockett, 1970) a mechanism termed dynamic recovery. The microstructure developed during hot deformation is traditionally characterized by the development of equaixed subgrains within the deformed original grains. As the subgrains develop in the grains the grain boundary becomes serrated (McQueen et al., 1995b).

The microstructure developed is related to the process conditions as recovery is temperature-dependent and work hardening at elevated temperatures is strain rate depended. The process conditions are combined into one parameter: the Zener-Hollomon parameter Z (Zener and Hollomon, 1944), defined as:

$$Z = \dot{\varepsilon} \exp\left(\frac{Q}{TR}\right) \tag{2.2}$$

where $\dot{\varepsilon}$ is the strain rate, Q the activation energy for dislocation climb equal to the activation energy for vacancy diffusion in the metal, T the absolute temperature and R the gas constant.

One may say, that the process parameters define the ratio between recovery and work hardening, and thereby the microstructure developed. This is also reflected in the relationship between the the subgrain diameter d_s and the process parameters:

$$d_s^{-1} = a + b \cdot logZ \tag{2.3}$$

where a and b are constants and Z the Zener-Hollomon parameter (McQueen, 1977), (McQueen et al., 1967), (Jonas et al., 1969). A similar relationship is found between the microstructure and the subgrains developed during deformation and the steady state stress σ, as given by:

$$\sigma_s = c + e \cdot d_s^{-1} \tag{2.4}$$

where c and e are constants (McQueen et al., 1967), (McQueen, 1977), (Jonas et al., 1969). The relations do not depend on the deformation mode (Furu et al., 1996).

Stress-strain curves obtained during hot plane strain compression and rolling exhibit initially parabolic work-hardening followed by constant stress i.e. a steady-state at the highest temperatures and constant work-hardening at lower temperatures (McQueen et al., 1967), (Shi et al., 1997a), (Diak and Verlinden, 2002), (Sircar and Humphreys, 1996). This does not however apply to torsion, where work softening is observed after an initial steady state and a second steady state is obtained at large strains. The work softening has been attributed to an effect of the texture by (Kassner et al., 2002) (McQueen et al., 1989) and the texture and microstructure by (Pettersen and Nes, 2003).

The texture evolved during hot deformation has been reported by (Juul Jensen and Vandermeer, 2003) and (Samajdar et al., 2001) to be very similar to the texture evolved during cold deformation, i.e. Goss, S, copper and brass textures, while (Vante et al., 1996) and (Humphreys and Bate, 2005) suggest a difference in strength of the texture components evolved during cold deformation compared to hot deformation.

These differences may be related to different initial textures of the materials, impurity content etc. or they may be due to activation of non-octahedral slip (Barcroix and Jonas, 1988), as investigated by (Maurice and Driver, 1997a) and (Maurice and Driver, 1997b) in a Al-1%Mn-1%Mg polycrystal. In this a stronger rolling texture was seen to evolve during hot deformation at 400°C compared to the deformation at 200°C , and the strength of the individual texture components shifted with temperature. At 200°C the strongest rolling texture component was copper, while at 400°C it was brass and the cube texture appeared. This shift in texture strength was attributed to activation of $\{110\}< 011 >$ and $\{112\}< 011 >$ slip systems.

The microstructure developed during hot deformation (Doherty et al., 1997) in extrusion (McQueen and Hockett, 1970), rolling (Hollinshead and Sheppard, 1987), torsion (Pettersen and Nes, 2003), (Kassner and McMahon, 1987), (Kassner et al., 1989), (Solberg et al., 1989) and compression (Huang and Humphreys, 1997), (Verrnon-Parry et al., 1996) all describe the evolution of a microstructure consisting of equiaxed subgrains within the original grains. The average subgrain size obeyed the relationships given in eq. 2.3 and eq. 2.4, that is the subgrain size increased with decreased stress and

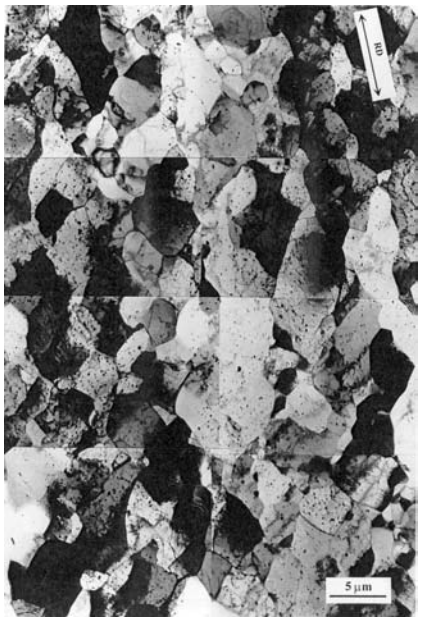

Figure 2.2: TEM micrographs of a hot deformed equiaxed structure from polycrystalline aluminium (96.8%) deformed at 510°C at $5s^{-1}$ from (Liu, 1998)

increased temperature. In the characterizations conducted at lower temperature and low strains dislocation cell structures where found to evolve, which at higher temperatures evolved into a subgrain structure. The subgrain sizes were found to be constant in the steady state regime i.e. independent of strain and the same applied to the misorientation angles across the boundaries and in some experiments also the dislocation density. The distribution of the misorientation angles where furthermore determined to be binominal by (Kassner and McMahon, 1987). A hot deformed microstructure is displayed in figure 2.2.

The constant subgrain size, misorientation and dislocation density during the steady state stage, indicates that as the original grains are strained i.e. becomes flatter, the subgrain boundaries rearrange in order to continue being equiaxed.

During hot deformation aluminum does not dynamically recrystalize due to a large amount of recovery (McQueen et al., 1995a) (McQueen and Hockett, 1970), instead the formation of high angle boundaries surrounding equiaxed grains has been described as being formed by geometric dynamic recry-

stallization. According to geometric dynamic recrystallization, high angle boundaries are formed in torsion when the elongated original grains become around 2-3 subgrains wide, at this stage further straining results in pinching of subgrains by annihilation of high angle boundaries from each side of the grain (Solberg et al., 1989), (McQueen et al., 1989), (McQueen, 2004). This was partly confirmed by experiments with the deformation of single crystals preformed by (Kassner, 1989), where the fraction of high angle boundaries were roughly 3 times higher in an aluminium polycrystal deformed to high strain in torsion, compared to a similar deformation of an aluminium single crystal. High angle boundaries were however also observed in the deformed single crystal.

Another possible origin of high angle boundaries in aluminium and aluminium alloys, is the creation of high angle boundaries by evolution of low angle boundaries, which during straining accumulate dislocations and thereby increase there misorientations. This has been known as continuous dynamic recrystallization (Gourdet et al., 1996) (Gourdet and Montheillet, 2000). According to (Gourdet and Montheillet, 2000) both recrystallization mechanisms operate during deformation of aluminium, where it is the deformation mode that determines which mechanism is the dominating one.

In the above studies no distinction has been made between grains of different orientations. In the study by (Bardal et al., 1995) a hot deformed Al-1Mg-1Mn aluminium alloy hot deformed showed a difference between grains of different orientations in that the average subgrain diameter of cube grains were found to be larger compared to subgrains of rolling textures and Goss oriented grains.

An orientation-dependent microstructure is also described in (Liu, 1998). In this study a Al-1%Mn-1%Mg polycrystal was plane strain compressed at 510°C at a strain rate of $5s^{-1}$. The microstructure was found to be characterized as a cell block structure delineated by GNBs at low strains, at higher strains equiaxed subgrains evolved. The low strain structure was classified in to 3 different classes, according to the morphology of the deformation structure. The classification indicated that at low strain a deformation structure evolved dependent on the orientation of the grains.

Experiments conducted on the border between the hot and warm deformation regimes have been conducted by (He et al., 2005), where 99.5% pure aluminium samples tensile deformed at 300°C and 400°C at a strain rate of $0.1s^{-1}$ were characterized. In this study a deformation structure charac-

teristic of cold deformation was seen to evolve at 300°C , i.e. a structure characterized by the 3 types as found by (Huang and Hansen, 1997). At 400°C the structure displayed no clear orientation dependence.

Similar cold-like dislocation structures were seen to evolve in a 98.5% pure aluminium polycrystal deformed in plane strain compression at a temperature of 305°C and a strain rate of $25s^{-1}$ to strains of 2.5 by (Duly et al., 1996). In this study no correlation with orientation of the grains was conducted however, but at low strains, cell block structures delineated by dense dislocation walls and, at higher strains the microstructure evolved into a lamellar structure, enclosing well-defined, dislocation-free cells, as is characteristic of cold deformation.

From the literature review it is seen, that only a few studies has been conducted, focusing on any possible orientation dependency of the dislocation structures developed in polycrystals during straining.

Single crystals experiments have however been conducted. In the studies by (Driver et al., 1996) (Glez and Driver, 2003), (Theyssier et al., 1995) and (Maurice and Driver, 1993) the general conclusions were, that the microstructure developed after hot plane strain (channel die) deformation displayed a significant orientation dependency, in that brass oriented crystals were found to have boundaries aligned with the trace of {112} planes in one direction, and the misorientations were lower compared to S and copper oriented crystals. S oriented crystals had boundaries aligned with the trace of {111} planes in one direction and copper orientations had boundaries parallel to {100} and{110} traces of the {100} and {110} planes. All crystals developed two sets of boundaries. The cube orientation was furthermore found to be stable, which was attributed activation of the {110}<110> slip systems.

Chapter 3

Aim

Based on the literature review following can be summarized with respect to deformation of aluminium and aluminium alloys.

Deformation at room temperature leads to a dislocation structure consisting of cells or cell blocks delineated by GNBs inclined to the deformation axis. The dislocation structure developed displays a morphology dependent on the grain orientation up to medium strains. At larger strains S bands are observed and finally a lamellar structure appears, where the lamellae in rolling are roughly parallel to the rolling direction.

Hot deformation of aluminium alloys in the steady state regime leads to a deformation structure consisting of more-or-less equiaxed subgrains, with sizes related to the deformation conditions. The work-hardening regime of hot deformation structures display some resemblance to cold deformation structures, that is a cell block structure delineated by GNBs.

Hence it appears as if the structural evolution observed during cold deformation applies to the hot deformed regime as-well, at least in the regime of work-hardening. If so, the dislocation structure evolved during hot deformation, will also show an orientation dependence, as a few studies conducted in warm and hot deformed poly-crystalline aluminium have indicated.

Based on this the aim in the following study is to clarify whether or not the dislocation structures developed during hot deformation are dependent on the orientation of the grains, as observed during cold deformation.

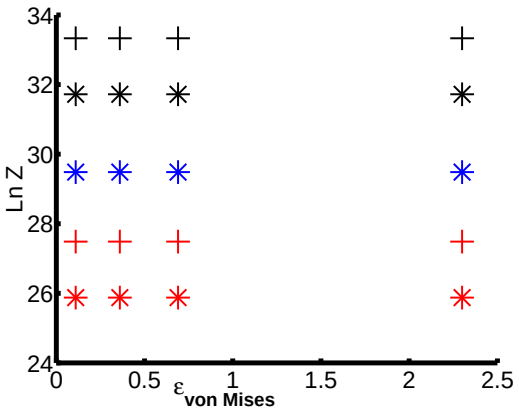

Figure 3.1: Deformation parameters used in the current study. Colour code. 350°C black, 400°C blue, 500°C red, $5s^{-1}$ star and $25s^{-1}$ plus

3.1 Choice of experimental conditions

To explore if the microstructure developed during hot deformation displays any grain-orientation dependency, material, deformation mode, deformation parameters and characterization techniques have to be chosen.

Aluminium has proven to be a good model material for describing the deformation of fcc-metals (Winther and Huang, 2007), (Huang and Winther, 2007), and has been studied extensively during cold and hot deformation, hence for comparison purposes, this metal was also chosen here. To be able to deform at relatively high temperatures without recrystallization a commercially pure aluminium (AA 1050) was chosen as a model material.

To obtain a range of deformations conditions (temperature, strain rate and strain) plane strain compression (PSC) was chosen as the deformation mode, because high strain, strain rates and temperatures are possible in PSC (McQueen, 1968).

The deformation parameters in terms of temperature, strain and strain rate were chosen in order to span the hot deformation regime and include both work-hardening and steady-state stress regions. The deformation temperatures were therefore 350°C (0.67 T_M), 400°C (0.72 T_M) and 500°C (0.83 T_M) with strain rates of $5s^{-1}$ and $25s^{-1}$ (at 400°C only deformations at $5s^{-1}$ were conducted). By using the, for hot deformation, relative high strain rates, the region of work-hardening is enlarged, which is favorable with respect to a study of the initial structure. Thickness reductions of 10% (0.11

ε_{vM}), 30% (0.36 ε_{vM}), 50% (0.69 ε_{vM}) and 90% (2.3 ε_{vM}) were selected, in order to span both the work-hardening and steady-state stress region. The chosen deformation conditions are illustrated in figure 3.1 in terms of the Zener-Hollomon parameter.

The microstructures evolved after deformation are often characterized by electron microscopy, due to the possibility of obtaining high resolution micrographs and orientation measurements of the same regions. Electron microscopy was therefore the obvious choice of technique to characterize the deformed microstructures. Both transmission electron microscopy (TEM) and scanning-electron microscopy (SEM) were used.

Chapter 4

Experimental

The experimental details regarding material, deformation mode, characterization technique and sample preparation are given in the following chapter.

4.1 Material

Commercially pure aluminium (AA1050) was prepared by initially heat treating the as-cast aluminium to minimize the amount of Si and Fe in solid solution. This was followed by break-down cold rolling and recrystallization. The material is thoroughly described and characterized in appendix H. The specific batch used in the current study was cold rolled to a total reduction of 64%.

The material was 99.5% pure with the major impurities being Si (0.16%) and Fe (0.24%). In a similar material (Verrnon-Parry et al., 1996) determined the impurities as mainly $FeAl_3$ and FeAlSi particles with an average diameter of 1.7μm. The scale of the microstructure investigated in the current thesis is either on a scale of a grain or an individual boundary. As large particles induce local rotations during deformation in an area approximately one particle diameter from the particle (Clarke et al., 2003) and thereby not in any of the scales investigated, these distortions have not been characterized in the current thesis.

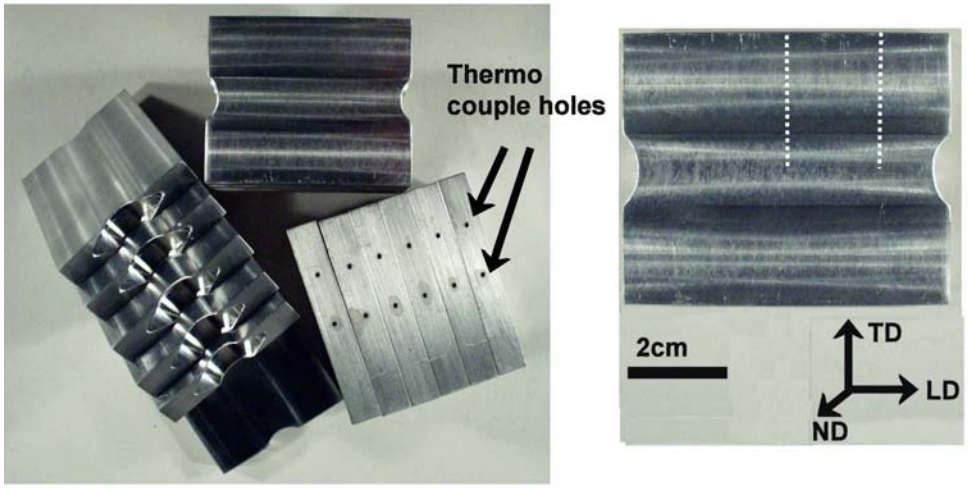

Figure 4.1: The machined undeformed samples. The position of the thermocouple holes are marked with punctured white lines in the sample on the right

4.2 Preparation of samples for plane strain compression

The plane strain samples were machined by the Risø workshop, from the material described in section 4.1. The samples were machined such that the TD direction in break drown rolling, were the LD direction in the samples. The sample dimensions were 60mm ×50mm × 9mm given as LD TD ND. The undeformed samples are displayed in figure 4.1. The samples were machined with thermocouple holes of 1.1mm in diameter in the middle and in the side of the samples, for temperature monitoring during the deformation. The thermocouple in the deformation zone is marked with a dotted line in the right image in figure 4.1.

In order to optimize the deformation conditions, the PSC samples were machined to fulfill the criteria $\frac{h_0}{W} \leq 0.67$, $\frac{b_0}{W} \geq 2$ and $\frac{l}{W} \geq 3$, where h is the hight, b the width and l the length of the sample, while w is the with of the tool (Loveday et al., 2000). The first condition is chosen in order to avoid extremely localized deformation, the second in order to minimize the spread during deformation and the last in order to impose lateral constrain during the deformation (Loveday et al., 2000) ,(Mira and Sellars, 2001a), (Beynon and Sellars, 1985). The ratios of the samples were $\frac{h_0}{W} = 0.6$, $\frac{b_0}{W} = 3.3$ and $\frac{l}{W} = 4$. The samples were heated at 500°C for 6h in order to remove defor-

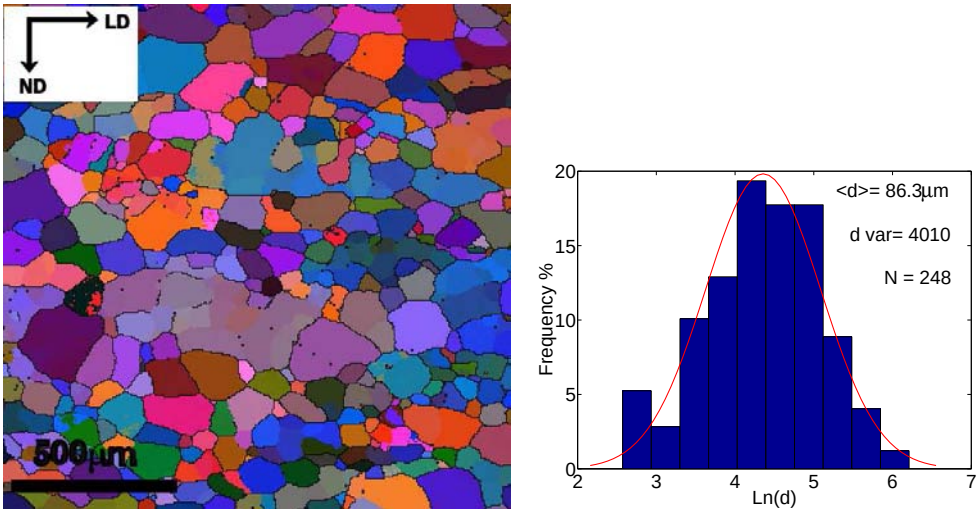

Figure 4.2: Left, EBSD-map of the undeformed material. Misorientations above 15^o are marked with black lines, and the grains have been coloured according to their Euler angles. See appendix B.2 for further details. Right grain size distribution

mation zones induced by the processing.

Undeformed PSC samples were characterized with respect to texture and grain size. An EBSD-map[1] of the initial material is displayed in figure 4.2, while the grain size in terms of mean cord length, determined in the channel 5 software, is displayed in table 4.1. From the table it can be seen, that the grains are slightly elongated in the longitudinal direction with an aspect ratio of 1.3 and an average grain size of 70μm.

Plane	LD (μm)	ND (μm)	Average(μm)	Aspect ratio (LD/ND)
Mean cord length	80	61	70.5	1.3

Table 4.1: Grain size (mean cord length) of the undeformed aluminium

The distribution of the grain sizes are displayed in figure 4.2, together with the average grain size. The data has been generated in CroPlot , which calculates the diameter of the equivalent sphere from the measured grain area (see appendix H for further details). The distribution is not log normal and the average grain size is 86μm. The ratio between the diameter of the equivalent sphere to the diameter measured with a linear intercept is expected

[1]Electron Backscattered diffraction (EBSD) is described in section 4.5.2

Texture component Vol(%)	Cube	Goss	Brass	S	Cu
Initial material	12.0	1.3	1.9	5.6	1.8
Random Vol (%)	2.2	2.2	4.4	8.8	4.4

Table 4.2: Texture composition of the undeformed aluminium

to be 1.224 (Cao et al., 2003), (Underwood, 1970), which also was found in the current study.

A textural analysis of the material[2] with respect to the texture components cube, Goss, brass, S, copper are displayed in table 4.2, together with the vol % of a randomly textured material. From the table it can be concluded that the initial material has a cube texture (5.5 × random).

4.3 Deformation mode - Plane strain compression

Plane strain compression (PSC) is a deformation mode, which enables large reductions at high temperatures and medium-to-high strain rates (up to 500°C and strain rates between $10^{-3}s^{-1}$ to $50s^{-1}$ in Al). PSC was introduced to simulate rolling, and it is sometimes referred to as ideal rolling, because the specimen during deformation ideally is restricted to elongate only in one direction and compress in another (Loveday et al., 2000).

PSC is illustrated in figure 4.3, where the longitudinal (LD), transverse (TD) and normal (ND) directions are defined, and the principal stresses given. During plane strain compression, the specimen is compressed in the ND and elongated in the LD, while spreading in the TD is reduced due to the geometry of the specimen (Loveday et al., 2000). In the current thesis LD is used to denote the direction in which the material elongates. In the literature LD is often replaced by RD.

The strain in PSC is calculated based on von Mises yield criteria and expressed in an invariant strain function equivalent strain[3] or von Mises strain, which is defined as:

$$\overline{\varepsilon} = \frac{\sqrt{2}}{3}[(\varepsilon_{11} - \varepsilon_{22})^2 + (\varepsilon_{22} - \varepsilon_{33})^2 + (\varepsilon_{33} - \varepsilon_{11})^2]^{\frac{1}{2}} \tag{4.1}$$

[2]Based on 3 EBSD measurements covering an area of 14.5mm^2

[3]also denotes effective strain

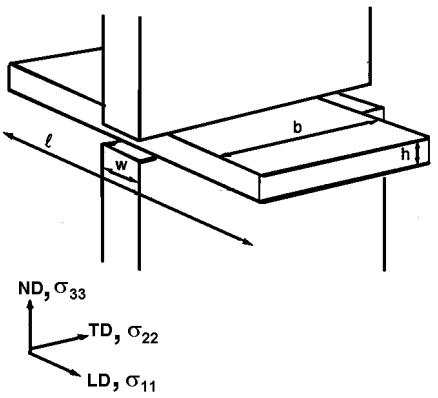

Figure 4.3: Sketch of plane strain compression

Under plane strain conditions $\varepsilon_{22} = 0$ and $\varepsilon_{11} = -\varepsilon_{33}$ therefore:

$$\overline{\varepsilon} = \frac{2}{\sqrt{3}} \ln \frac{h}{h_0} \tag{4.2}$$

where $\varepsilon_{33} = ln\frac{h}{h_0}$. In practice plane strain compression is not obtained, hence $\varepsilon_{22} \neq 0$, and the equivalent strain becomes ($\varepsilon_{11} = -\varepsilon_{33} - \varepsilon_{22}$)

$$\overline{\varepsilon} = \frac{\sqrt{2}}{3}[(-2\varepsilon_{22} - \varepsilon_{33})^2 + (\varepsilon_{22} - \varepsilon_{33})^2 + (\varepsilon_{22} + 2\varepsilon_{33})^2]^{\frac{1}{2}} \tag{4.3}$$

where $\varepsilon_{22} = ln(\frac{b}{b_0})$

Similarly for stress, in terms of the principal stresses this is:

$$\bar{\sigma} = \sqrt{\frac{1}{2}[(\sigma_{22} - \sigma_{33})^2 + (\sigma_{33} - \sigma_{11})^2 + (\sigma_{11} - \sigma_{22})^2]} \tag{4.4}$$

The von Mises stress is obtained during the testing in the following manner. The average pressure $\bar{p}$ applied from the tools is given by:

$$\bar{p} = F/wb \tag{4.5}$$

where F, w and b are the instantaneous force applied, width of the tool and instantaneous breath of the specimen. The instantaneous breadth is

estimated by:

$$b_{inst} = b_0\Big[1 + C - \Big(\frac{h_{inst}}{h_0}\Big)^n\Big] \tag{4.6}$$

where b_0 is the initial breath, h_0 the initial height, h_{inst} the instantaneous height, C a coefficient describing the spread and n a constant ~ 0.2 in aluminium. The average pressure is converted to the von Mises stress by correcting for friction. The friction conditions may be sticking, sliding or in between. The average pressure exerted by the tool under sliding conditions is given by:

$$\frac{\bar{p}}{2k} = \frac{h}{\mu w}\Big[\exp\Big(\frac{\mu w}{h}\Big) - 1\Big] \tag{4.7}$$

here k is the yield stress in pure shear, h the instantaneous height μ the friction coefficient, and w the tool width. If sticking friction conditions dominate, the mean pressure is given by:

$$\frac{\bar{p}}{2k} = 1 + \frac{w}{4h} \tag{4.8}$$

where k, h, μ and w are as described above. In the transition from sliding to sticking (Z(h)), the average pressure is:

$$\frac{\bar{p}}{2k} = \frac{h}{\mu w}\Big(\frac{1}{2\mu} - 1\Big) + \frac{(w/2 - Z)}{\mu w} + \frac{(w/2 - Z)^2}{hw} \tag{4.9}$$

The von Mises stress is finally obtained from the yield stress in pure shear through:

$$\bar{\sigma} = \sqrt{3}k \tag{4.10}$$

which follows from equation 4.4. For more elaborate descriptions see (Ricks, 1999), (Silk and van der Winden, 1999), (Loveday et al., 2000) and (Argon et al., 1966) and the references there in.

The flow curves obtained by hot PSC of aluminium has been shown by (Shi et al., 1997a) and (Davenport et al., 2000) to be well described by a modified Voce equation (Voce, 1948) displayed in equation 4.11:

$$\sigma = \sigma_0 + (\sigma_s - \sigma_0)\Big[1 - \exp\Big(-\frac{\varepsilon}{\varepsilon_r}\Big)\Big]^m \tag{4.11}$$

where σ_0 is the initial flow stress, σ_s is the steady-state stress, m is a constant and ε_r is a transient strain constant, which determines the curvature of the

curve between σ_0 and σ_{ss}.

The plane strain compressions presented here, where conducted at the Institute for Microstructural and Mechanical Process Engineering: The University of Sheffield (IMMPETUS) by the technical staff. The samples were lubricated with a graphite lubricant, which was allowed to dry. A thermocouple was inserted in the centre of the samples compressed to strains of 0.11, 0.36, 0.69, while samples compressed to strain 2.3 had the thermocouple in the side, in order to avoid interference during deformation. The samples were heated to the test temperature in 120s in an induction coil and held at the temperature for 1 minute. The samples were thereafter transferred to the preheated test furnace and deformed under the given conditions, and afterwards quenched with a water spray. Temperatures below 100°C were reached within 1s-2.5s and room temperature within 2s-6s.

The flow curves were obtained by recording the applied load and the displacement of the tool during deformation. The displacement of the tool translate to thickness strain (ε_{33}) by correcting the measured displacement for zero off-set and the von Mises strain and stress are calculated as outlined above [4] (Loveday et al., 2000), (Shi et al., 1997b), (Silk and van der Winden, 1999). The correction of the raw data to obtained the stress and strain values was conducted after the compression test by the technical staff at IMMPETUS in Sheffield.

4.4 Preparation of samples for microscopical characterization

4.4.1 Sample selection from the PSC samples

The microstructure developed during cold rolling is characterized by cell blocks delineated by GNBs as described in section 2.1. The GNBs cluster around the macroscopically most stressed planes i.e. around 45° to RD in the RD/ND plane, while they are parallel to TD. The optimum choice of plane for characterizing the microstructure in PSC is therefore the LD/ND plane (RD/ND) where the boundaries are highly inclined, and thereby makes it possible to obtain a sharp trace in TEM, which is needed for the characteri-

[4] In the actual set up the initial calibration reduces the effects of the machine compliance and the graphite lubricant is thin. Corrections for these effects are therefore not needed

zation (Huang, 2007), (Winther et al., 2004a). This plane is therefore chosen in the current study, for microstructural characterization.

In order to characterize the microstructure developed after PSC, the inhomogeneity of the deformation mode has to be taken into consideration. Several studies have been conducted to explore this (Mira and Sellars, 2001a), (Mira and Sellars, 2001b), (Colãs and Sellars, 1987), (Colãs and Sellars, 1985) and (Beynon and Sellars, 1985), where the general findings are, that the strain is distributed in the LD/ND plane of the PSC specimen, were special areas around tool edges and in regions corresponding to slip field lines, are very highly strained. The distribution depends on the initial geometry of the sample (the tool width to sample height ratio) and the friction but not the strain rate.

To explore the strain distribution in current samples, an EBSD-map was recorded of a 1/6 of the LD/ND plane of the specimen strained to ε_{vM}=0.69 PSC at 350° with a strain rate of $5s^{-1}$. The map is displayed in figure 4.4 together with a sketch of where in the LD/ND plane the EBSD-map was recorded. In the figure the EBSD-map shows the original grains, which are elongated parallel to the longitudinal direction in the centre, but towards

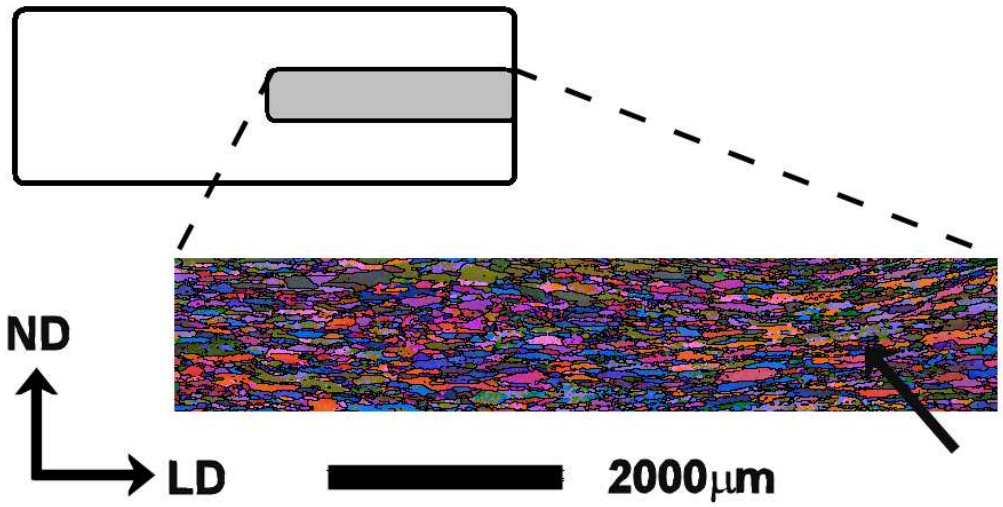

Figure 4.4: EBSD-map of the region illustrated in the sketch. The EBSD-map has been noise reduced by replacing zero-solution and grains are coloured after their euler angle

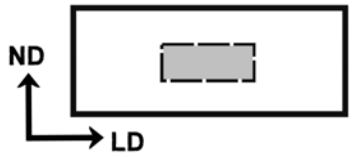

Figure 4.5: Sketch of the sample, the area marked in gray is selected for microstructural investigations

the edges it seems like an area is more compressed, in that the grains bowed towards the centre. The area is marked with an arrow in figure 4.4. Hence the sample does not appear homogenously strained, as also referred to in the literature.

The consequence of the strain being distributed in the LD/ND plane is, that the areas examined in the microstructural characterizations might be strained or most likely are strained to a strain different from the macroscopically measured strain. Therefore in order to correct for the uncertainly in the microstructural characterization all samples for TEM and SEM are prepared from the same centre region of the LD/ND plane. The centre region is taken as the region seated in the middle of the sample, when this is partition equally in 3 parts in the normal and longitudinale directions, as illustrated in figure 4.5. In this way all the specimens examined at a given macroscopical strain, have the same local strain, even though it might deviate form the macroscopical stain. By choosing the centre of the LD/ND plane for microstructural investigations, any effect of friction is avoided, because the friction conditions effect especially the surface region (Mira and Sellars, 2001a), (Mira and Sellars, 2001b). Using the centre of the LD/ND plane is similar to the studies by (Furu et al., 1996), (Verrnon-Parry et al., 1996).

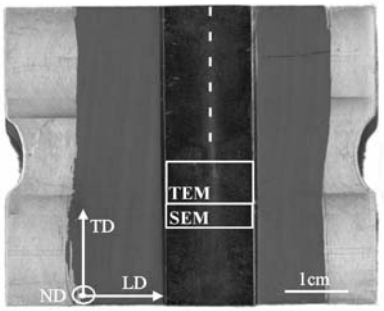

Figure 4.6: Sample deformed to von Mises strain 0.11. The sample parts used for microscopical investigations are illustrated. The broken white line marks the thermocouple.

In the TD/LD plane the most ideal plane strain compression conditions are at the centre of the deformation zone, while the deformation conditions at the end of the deformation zone in the TD direction are more axially symmetric, as the material can spread in TD (Loveday et al., 2000). The material used for microstructural characterization was therefore taken from the centre of the specimen, as illustrated in figure 4.6. More precisely the material for TEM foils was the material 3mm to 1.3cm from the centre along TD. The 3mm distance to the centre was chosen, in order to avoid any effect of the hole made for the thermocouple. The samples for SEM were the material from 1.3cm to 1.8cm from the specimen centre. TEM foils was fabricated from the material closest to the centre and the SEM analysis was also conducted on the surface closest to the centre of the specimen.

4.4.2 Sample preparation

The samples for microscopical investigation were prepared by initially removing the undeformed and partly-deformed region of the samples by cutting along the edge of the deformation zone in TD with a Mesotron using wheel 05TREE from Struers under water cooling. The sample materials for SEM and TEM were thereafter prepared by cutting along LD in the deformation zone at the above given distance from the centre using an Accutom-5 from Struers with wheel 459CA using a speed of 0.01mm s^{-1} and water cooling.

TEM samples

Sample material for TEM foils was prepared form the centre of the LD/ND plane of the PSC samples as described above and illustrated in figure 4.6 and figure 4.5. Slices 0.5mm in thickness were cut by a diamond string and polished with silicon carbide paper grit 1000. The first slices cut off were not used, in order to ensure, any possible deformation induced by the accutom were not included. Foils 3mm in diameter were thereafter punched out from the centre of the LD/ND plane and electrolytically polished (Christiansen et al., 2003). All foils were prepared by Gitte Christiansen.

SEM samples

Samples for SEM characterization were cut from the PSC samples as described above and illustrated in figure 4.6 and figure 4.5. The entire LD/ND plane was polished with silicon carbide paper at increasingly finer grits until grit 4000. Samples were then prepared manually or by the use of the electropolishing mashine Polectrol from Struers. Manually-prepared samples were polished with diamond paste (1μm) and thereafter in a suspension of silica and electropolished (Landolt, 1987),(Landolt, 2003). The electropolishing was conducted in an electrolyte of 13% water, 67% ethanol, 11% 2-butoxy ethanol and 9% percloric acid. The electropolishing was conducted with an aluminium plate as the cathode at 0°C and 12V until the surface of the sample was mirror like. The automatic electro polishing was preformed by cooling the same electrolyte to 0°C and electropolishing at 12V for 30 s.

The author prepared all the specimens herself, except for those deformed at 500°C at a strain rate of $25s^{-1}$, which were prepared by Kristófer Hanneson.

Microstructural characterizations in SEM were only conducted on the centre part of the SEM sample, as discussed above. The textural measurements however were conducted on the entire LD/ND plane in order to be able to compare the textural evolution with the mechanical properties.

4.5 Electron microscopy

The deformed microstructures were in the current study characterized by electron microscopy. Electron microscopy has the advantage that it is possible to obtain high resolution micrographs (images) together with the orientation of the region of interest by the use of diffraction. In the current study both transmission and scanning electron microscopy have been used to characterize the deformed microstructure. In the following a short general introduction to electron microscopy will be given, followed by a more detailed description of specific methods.

In electron microscopy electrons are used to create the signal. The principle behind electron microscopy is the same irrespective of it being a transmission or a scanning electron microscope. The signal is created by electrons being extracted from a source, accelerated, focused and directed to the specimen, where some of the electrons, due to their wave character, are diffracted.

Diffraction from crystals are most often described by Braggs law (eq. 4.12), which describes the conditions for constructive interference when waves are scattered by a crystal lattice. This is given in terms of the wave length λ, of the electrons, distance between lattice planes d, the scattering angle (or Bragg angle) θ, between the elastic scattered waves on the lattice planes in the crystal, and the order of the diffraction n:

$$n\lambda = 2d_{hkl}sin\theta \tag{4.12}$$

In this formulism the intensity of the diffracted waves are not considered. The diffraction conditions for fcc metals are listed in appendix A.

In transmission electron microscopy (TEM) the electrons are transmitted and/or diffracted/scattered in the specimen, and afterwards directed to a fluorescent screen. In scanning electron microscopy (SEM) the electrons impinge on the sample surface and a signal is obtained from the electrons

diffracted/scattered from the surface and the sample volume just below the surface (Williams and Carter, 1996), (Goodhew and Humphreys, 1992).

4.5.1 Transmission electron microscopy

The TEM studies were conducted on a Jeol 2000FX electron microscope using an acceleration voltage of 200kV. The TEM is equipped with a double tilt sample holder and connected to a computer containing a semi-automatic program for orientation measurements.

The fundamental phenomenon behind TEM imaging and the orientation measuring techniques used in the present study is the creation of Kikuchi-diffraction patterns and analysis of these. The principle of Kikuchi-diffraction is therefore briefly described here.

Kikuchi-diffraction patterns

The formation of Kikuchi-diffraction patterns in a TEM arises from diffraction of inelastically scattered electrons as illustrated in figure 4.7 A. When an electron beam enters the sample, a fraction of the electrons are inelastically scattered in all directions, most electrons are however scattered in the forward direction, as illustrated in figure 4.7 A. After the scattering some of the inelastic scattered electrons travel at the Bragg angle (eq. 4.12) to the hkl plane, and are therefore diffracted on the plane[5], as illustrated in figure 4.7 B.

The diffracted electrons form two cones with angles θ and -θ to the hkl planes. The cones are known as Kossel cones and are illustrated in figure 4.7 C. The electrons diffracted with the angle θ have a higher intensity, than the electrons diffracted with the angle -θ, because they are closer to the incoming beam. The intensity of the Kossel-cone created by the Bragg angle θ have a higher intensity compared to the background, while the intensity of the Kossel cone created with the Bragg angle -θ has a lower intensity compared to the background. The Kossel-cones intercept the viewing screen in two parabolas on each side of the trace of the hkl plane. In practise only a small part of the parabolas are seen as the opening angle of the cones are large (the Bragg angle is of the order of 0.2°). The intercepts are therefore two straight lines - the Kikuchi-lines, one bright and one dark, and they are both parallel

[5]In this, it is assumed that the energy of the inelastically scattered electrons is approximately equal to the energy of the incoming electrons.

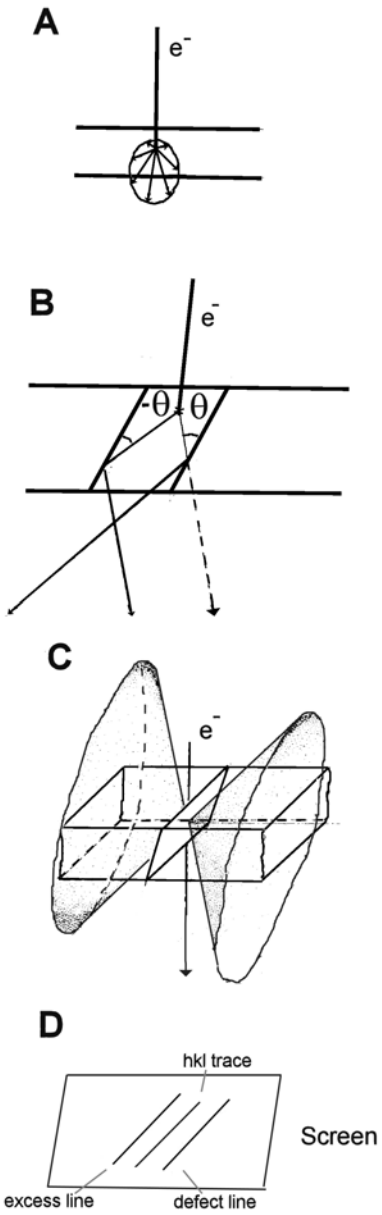

Figure 4.7: Illustration of Kikuchi pattern formation

to the trace of the hkl plane, from which they are diffracted as illustrated in figure 4.7 D. When the specimen/crystal is tilted the Kikuchi-line moves on the screen, and it is this characteristic, which makes it possible in TEM to determine the crystal orientation with a very high precision.

Every crystal plane can give rise to two Kikuchi-lines, hence diffraction from the entire crystal results in a range of Kikuchi-lines intersecting in a zone axis. The width and intensity of the Kikuchi-lines depends on the planes from where they were diffracted. Analysis of these Kikuchi-lines/Kikuchi-patterns makes it possible to determine the orientation of the specimen with a very high precision.

Imaging

In the current study, micrographs of the deformed structures were obtained as bright field images under strong diffraction conditions. This was chosen because the deformed microstructure developed in metals strained up to medium strains is a dislocation structure with relatively small orientation differences. To reveal such structures it is therefore necessary to use strong diffraction conditions. This is illustrated in figure 4.8, where micrographs obtained from the same region, but at different tilts are displayed. The left micrograph was obtained approximately 5° from the [011]-zone axis. From this it can be seen, that the microstructure under these conditions is only partly seen, as large areas without any internal structures occur.

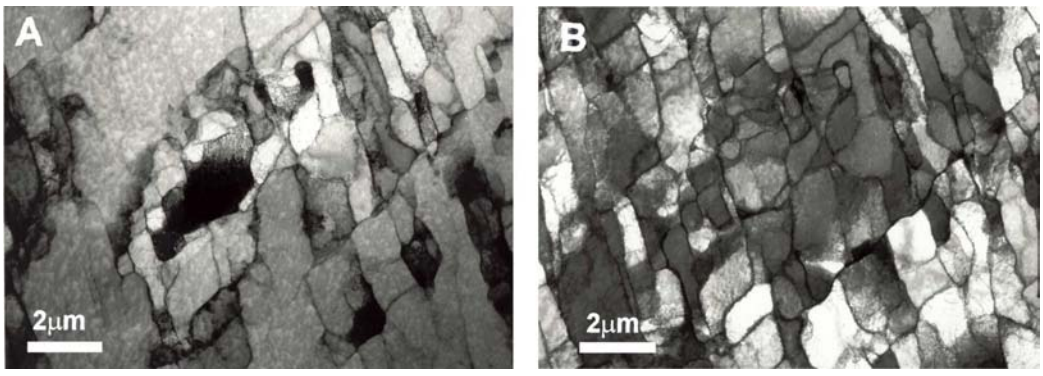

Figure 4.8: A bright field image obtained at zero tilt, $\sim 5°$ from [011] of many of the cells. B bright field image obtained with the beam very close to [011] of many of the cells. Courtesy of Xiaoxu Huang

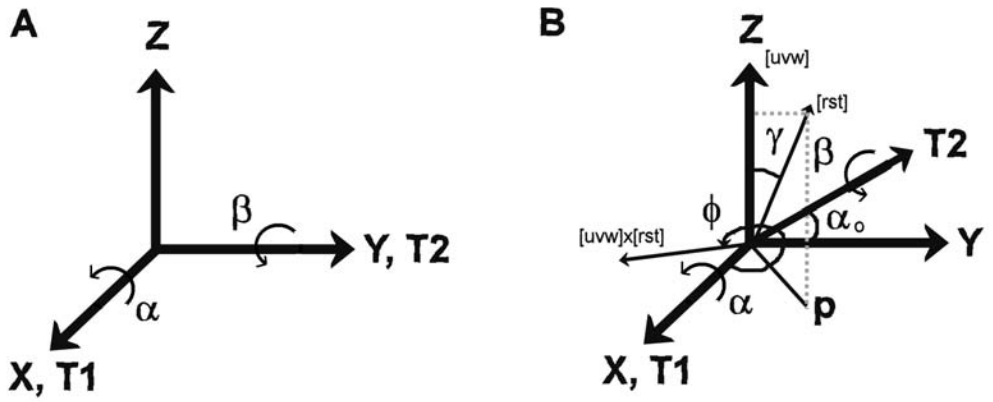

Figure 4.9: Sample holder geometry in TEM

The microstructure in the right micrograph was obtained with the beam very close to the [011]-zone axis. This position is an ideal position for diffraction from several planes, i.e. small misorientations are revealed in the contrast. The structures seen in the right micrograph of figure 4.8 exhibit typical deformation structure as all areas display cells and clear boundaries.

Bright field images under strong diffraction conditions are obtained in fcc metals with beam directions along the zone axes [100], [110], [112] or [114].

Orientation measurements

To determine the orientation of a grain (crystallite) and the misorientations between the grains (crystallites), an in-house developed, semi-automatic technique was used (Liu et al., 1989),(Liu, 1994a), (Liu, 1994b) and (Liu, 1995). In this, the orientation of a grain is measured by analyzing a Kikuchi-diffraction pattern from the grain.

The principle behind the orientation measurement of a grain is to determine the crystallographic directions in the crystal lattice of the grain with respect to the sample co-ordinate system. In figure 4.9 A the geometry of the un-tilted TEM sample holder is illustrated. In this, Z is parallel to the beam, X the T_1 tilt axis with the tilt angle α and Y the T_2 tilt axis and the corresponding tilt angle β. As the sample is tilted, an arbitrary vector $\vec{g}$ is rotated to $\vec{g'}$ given by:

$$\vec{g'} = T_1 T_2 \vec{g} \tag{4.13}$$

where T_1 and T_2 are rotation matrices describing the rotation around their respective axes. T_1 and T_2 are explicitly given in eqn. 1 and eqn. 2 in (Liu et al., 1998).

Assuming a zone axis of [uvw] is parallel to the beam at an initial tilt (α_0 and β_0), a new tilt position (α, β), where the sample is parallel to a new zone axis, can be calculated by equations 4.14 and 4.15.

$$\alpha = \sin^{-1}(\sin\gamma \cdot \cos\phi \cdot \cos\alpha_0 + \sin\alpha_0 \cdot \cos\gamma) \tag{4.14}$$

$$\beta = \tan^{-1}\Big(\frac{\tan\gamma \cdot \sin\phi}{\cos\alpha_0 - \sin\alpha_0 \cdot \tan\gamma \cdot \cos\phi}\Big) + \beta_o \tag{4.15}$$

where γ is the angle between [uvw] and [rst], ϕ is the angle between the tilt axis T_1 and the normal to the plane formed by [uvw] and [rst]. ϕ describes the rotation of the Kikuchi-pattern around Z, as illustrated in figure 4.9 B(Liu et al., 1989), (Liu, 1994a), (Liu, 1994b).

Hence, by aligning a known zone axis with the beam, determining the rotation angle ϕ around Z and reading the tilt angles (α, β) of the sample holder, it is possible to calculate the angles $(\alpha_1, \beta_1), (\alpha_2, \beta_2), (\alpha_3, \beta_3)$ by which the crystal directions [100], [010], [001] are aligned with the beam (se appendix B for orientation details). As the specimen is mounted with the LD along the T1-axis in the holder, the orientation of the crystal can therefore be found by:

$$\begin{pmatrix} H \\ K \\ L \end{pmatrix} = \begin{pmatrix} \cos\alpha_1 & \cos\beta_1 \\ \cos\alpha_2 & \cos\beta_2 \\ \cos\alpha_3 & \cos\beta_3 \end{pmatrix} \tag{4.16}$$

and

$$\begin{pmatrix} U \\ V \\ W \end{pmatrix} = \begin{pmatrix} -\cos\alpha_1 & \sin\beta_1 \\ -\cos\alpha_2 & \sin\beta_2 \\ -\cos\alpha_3 & \sin\beta_3 \end{pmatrix} \tag{4.17}$$

where [HKL] is the normal to the foil, and [UVW] is parallel with the longitudinal direction in the specimen. From the above, it is possible to calculate the misorientation angles and axes between measurements as given in (Liu, 1994a).

From the principle described above, the key parameters required to calculate $(\alpha_1, \beta_1), (\alpha_2, \beta_2), (\alpha_3, \beta_3)$ are the tilt angle (α_0, β_0) corresponding to

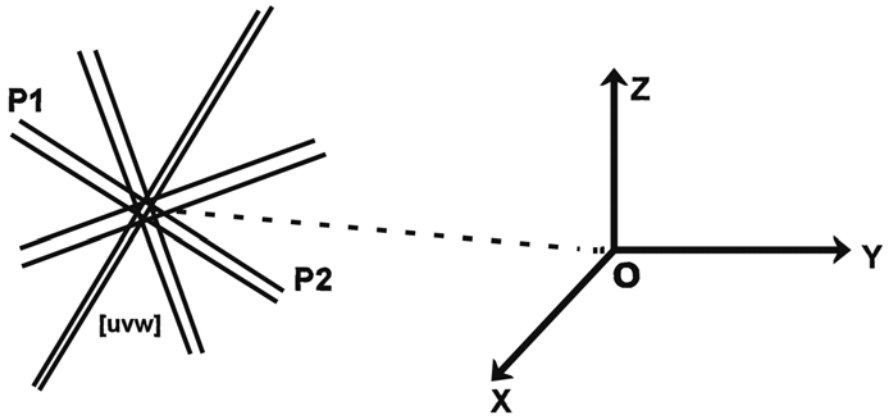

Figure 4.10: Sketch of a screen displaying a Kikuchi-diffraction pattern at the zone-axis [uvw] and the coordinate system of the setup, with the direct beam O.

a zone axis [uvw], which is parallel to the beam, and the rotation angle ϕ. In practice, it is not necessary to tilt the sample, so that [uvw] is perfectly parallel to the beam. This is illustrated in figure 4.10, where a sketch of the zone axis [uvw] is seen on the screen, but away from the center O of the direct beam, by a distance or angle θ. To move the centre of the Kikuchi-pattern [uvw] to the centre of the beam, requires tilting the specimen around the axis perpendicular to line, from [uvw] to O, by the angle θ. The tilt angles when [uvw] is aligned with the beam, can be calculated from equation 4.14 and 4.15 and thereby the orientation can be calculated.

The rotational position of the Kikuchi-pattern as well as the position of the zone axis is found by manually measuring on the screen using the projector lenses current, the position of the zone-axis and the direction of one of the Kikuchi-lines through the zone-axis, as also illustrated in figure 4.10. This is in practice done by measuring the initial position of the zone axis, followed by measuring at P1 and then at P2.

One of the main errors of the orientation determination is the error in the tilt angle due to the backlash of the sample holder. When large sample tilting is used, the accuracy is about 1° . If the measurements are conducted at zero tilt, the accuracy is better than 0.2° (Huang, 2008).

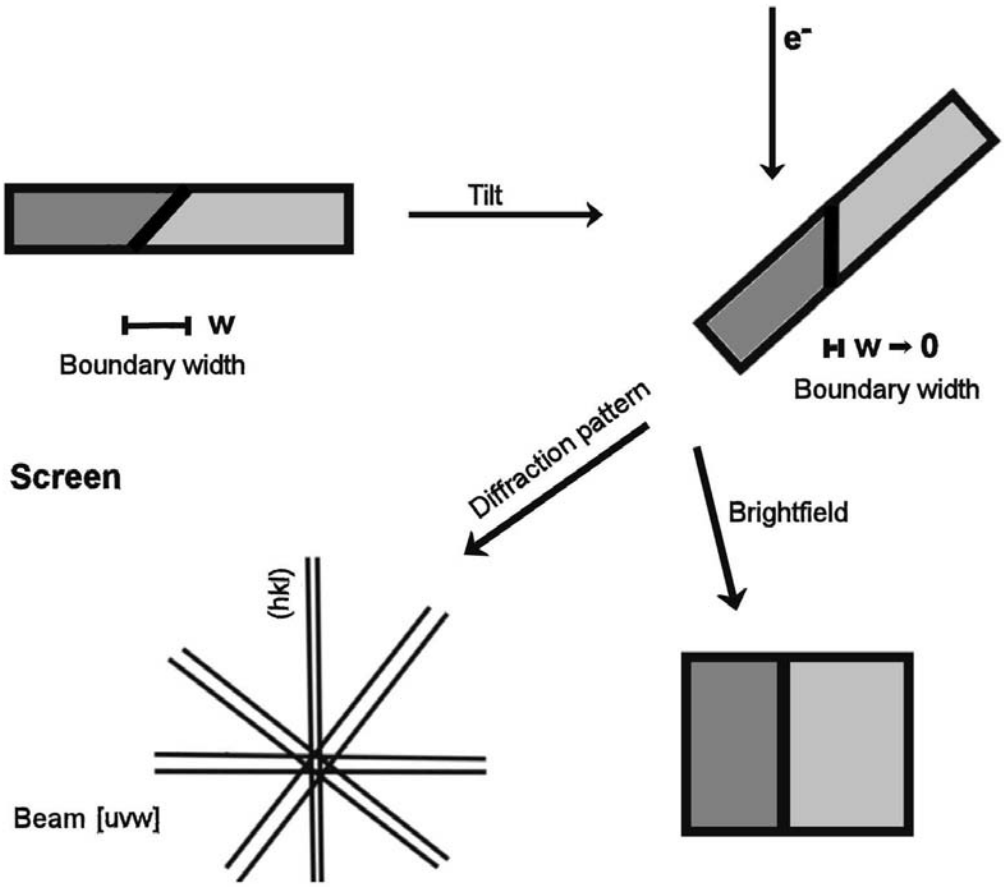

Figure 4.11: Boundary plane determination.

The other main error associated with the TEM measurements, is mounting of the sample in the TEM holder. In the current study, square shaped samples has been used which makes is easier to align the sample directions with the direction of the sample holder. All samples are mounted by an experienced technician and hence the accuracy has been found to be better than 2° . The spatial resolution is $\sim$ 0.2nm (Huang, 2008).

Boundary plane determination

The alignment of the dislocation boundaries with the crystallographic planes are determined by Kikuchi-diffraction and trace analysis under edge-on image conditions. The technique is a visual-based technique, as illustrated in the sketches in figure 4.11. In the top left part, the boundary is viewed from the side, which on the screen results in a boundary width w as indicated below

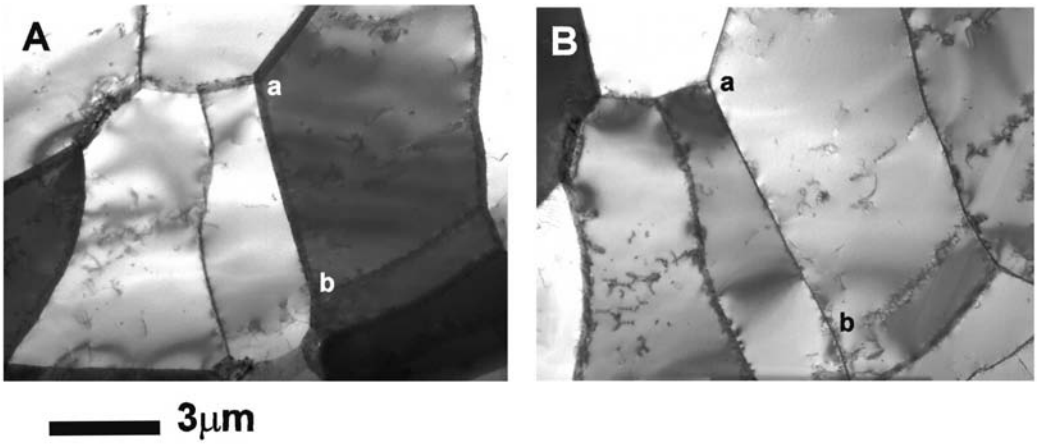

Figure 4.12: Boundary plane determination of Al PSC at 500°C at $25s^{-1}$ to a strain of 0.36. A beam = $[\bar{1}\bar{1}2]$ B beam = [112]

the sketch. After the specimen is tilted such that the boundary is parallel to the incident beam (edge-on) as illustrated in the top right part of figure 4.11, the width of the boundary is minimal. In the bottom right part of figure 4.11, the boundary trace is displayed, as it is viewed on the screen, when it is tilted to the edge on position. In the left bottom part of the figure, a Kikuchi-diffraction pattern of [uvw] zone axis is obtained from a region next to the boundary sketched. In this position the boundary is parallel with the beam. In the same position in diffraction mode, the Kikuchi-line from the (hkl) plane is found to be parallel to the boundary trace of the boundary (Huang and Liu, 1998), hence the (hkl) plane is determined to be the crystallographic plane of the boundary.

In the real process of boundary plane determination, the Kikuchi-pattern is not needed to be recorded but is calculated from the measured orientation. This is done by finding the Kikuchi-line (hkl), which is parallel to the boundary trace. An example of boundary plane determination is shown in figure 4.12. A boundary, marked ab, shows a wide projected image in figure 4.12 A, when the sample is tilted to a position where the [112] zone axis is parallel to the beam. This boundary is viewed edge-on (very sharp). By comparing the boundary trace and the calculated Kikuchi-lines, it was found that the boundary is parallel to the $(3\bar{5}1)$ planes, and thereby is the crystallographic plane of the boundary ab $(3\bar{5}1)$.

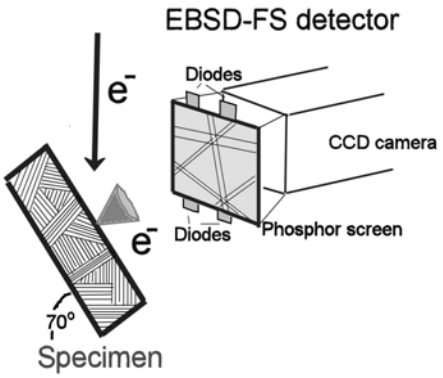

Figure 4.13: The setup in SEM for EBSD and CC

4.5.2 Scanning electron microscopy

Two SEMs were used in the study. All texture measurements were conducted on a Jeol JSM-840 with a LaB_6 filament and equipped with an EBSD detector from NORDIF. The microstructural characterizations were conducted on a Zeiss SUPRA-35 field emission gun equipped with a EBSD-forescatter Nordlys II detector.

Imaging - Channelling contrast images

Imaging in the SEM was conducted using channelling contrast (CC). CC images use the phenomena, that areas of different orientation diffracted/reflect electrons with different intensities. CC-images are obtained in the SEM with the same setup illustrated in figure 4.13. The image is obtained, by recording the intensity of the diffracted/reflected electrons with the diodes placed around the phosphor screen, as the electron beam is scanned across the surface. The intensity is orientation-dependent because the electron beam penetrates the specimen differently for different crystal planes (channelling in) and are diffracted at an angle, depending on which lattice plane is oriented for diffraction (channelling out) (Prior et al., 1999), (Day et al., 2004). The intensity depends on the diffraction/reflection conditions, all boundaries may therefore not be seen. The intensity of the diffracted/reflected electron furthermore depends on the element (Z-contrast), the dependency is however less than the orientation dependency, when the sample is tilted (Prior et al., 1999) and of no importance, when the sample only consists of one element.

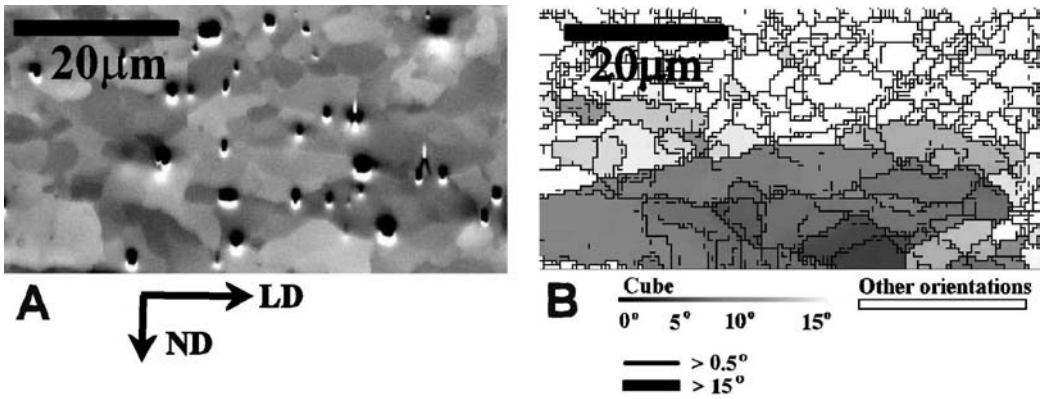

Figure 4.14: A CC image of Al PSC at 350°C and 5 s^{-1} to strain 0.69. In B an EBSD-map of the same region.

An CC image is displayed in figure 4.14 A together with and EBSD-map of the same region.

The angular resolution of the CC images may be as low as 0.1° , while the spatial resolution is around 0.25μm (Prior et al., 1999).

Orientation measurements - Electron backscattered diffraction

Electron backscattered diffraction (EBSD) is an automatic method to measure the orientation in a point on the sample surface in SEM. The principle is sketched in figure 4.13. The electron beam impinging on the sample surface, which is tilted 70° from horizontal and is scattered at and in the surface ($\sim$ 50nm depending on the acceleration voltage and material). The scattered electrons, which are inclined at a Bragg angle to one of the crystal planes, are channelled differently in the crystal compared to other scattered electrons. This leads to an intensity difference in backscattered electrons, which results in the formation of Kikuchi-patterns in front of the specimen (Prior et al., 1999). The Kikuchi-pattern is visualized on a phosphor screen and recorded by a camera connected to a computer. The Kikuchi-pattern is indexed automatically by the use of Hough transformations and the orientation of the measurement is afterwards found through the geometric relations between sample and detector (Lassen, 1994), (Wilkinson and Hirsch, 1997). By moving the beam or the sample stage to a new position where another Kikuchi-pattern is obtained, indexed and orientation calculated, an area (grid) of the

sample surface is characterized.

The data obtained is most often displayed as orientation images or EBSD-maps, where the orientation of each point measured in the grid, is displayed as a pixel with a colour defined by the equivalent Euler angle see appendix B, (Day et al., 2004). In the current study the commercial software Channel 5 ((Day et al., 2004)), has been used for data analysis.

The resolution of the EBSD measurements is determined by the interaction volume, which again is given by the acceleration voltage. A higher voltages leads to a higher signal (clearer Kikuchi-patterns), but also a higher interaction volume, which decreases the spatial resolution. Hence it is a trade off between reduced spacial resolution and an enhanced rate of correctly indexed Kikuchi-patterns (Humphreys, 2001). In the current study the measurements conducted by the author generally used an acceleration voltages of 15kV, however a few measurements were conducted with an acceleration voltages of 12kV. All measurements in the ZeissSupra were conducted with a step size of approximately d/4 or less, where d is the diameter of the minimum feature (cell or subgrain) in the microstructure (Humphreys, 2001), (Cao et al., 2003). The spatial resolution at 12kV in aluminium is evaluated to be 30nm and the angular resolution 1° in the ZeissSupra (Wu, 2006), hence the spacial resolution at 15kV is probably slightly lower and the angular resolution slightly better. EBSP-maps obtained from the same region, with acceleration voltages of 15kV compared to 12kV display an enhanced rate of indexed points at the higher acceleration voltage, but otherwise no other differences.

Some EBSD measurements of the 500°C strain rate 25 s^{-1} series, were conducted by Kristoffer Hannesón, where the microscopical settings were an acceleration voltage of 20kV and a step size of 1μm. In appendix C is a list of all measurements, their conditions and operators.

The use of EBSD for orientation measurements and microstructural characterizations has some limitations, due to orientation noise and wrongly or not indexed points (Godfrey et al., 2002), (Cao et al., 2003). In the Channel 5 software, data cleaning procedures are available to overcome these limitations. The orientation noise can be reduced by using a modified Kuwahara filter (Humphreys et al., 2001), while non-indexed points can be replaced with the most common orientation measured in the neighbouring measurements(Day et al., 2004).

Texture component	Cube	Goss	Copper	Brass	S
Colour	Pink	Dark blue	Green	Yellow	Light blue

Table 4.3: Colour used to display ideal orientations

Data representation

The EBSD-maps displayed in the current thesis are displayed by colouring all random orientations, according to their Euler angles, while grains of ideal orientations have been coloured with the colours given in table 4.3. Point not indexed are coloured white. The colouring is further described in appendix B.2. Lines marking misorientations between cells in the EBSD-maps use the following colour code:

$$gray : 1^\circ - 1.5^\circ \quad black : 1.5^\circ - 15^\circ \quad \textbf{black} : 15^\circ < \tag{4.18}$$

The data was initially noise-reduced by replacing all non-indexed points, which have a minimum of 6 indexed neighbour measurements, with the most common orientation. This was followed by an orientation noise reduction by using the modified Kuwahara filter included in the channel 5 software. The modified Kuwahara filter replaces the orientation of a measurement/pixel, with the average orientation of the sub-grid, which has the lowest variance

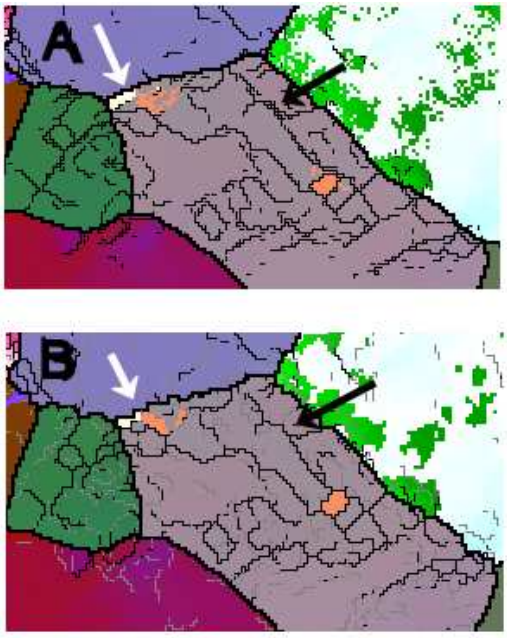

Figure 4.15: EBSD-map before and after noise reduction

and are misoriented to the measurement/pixel within a user-selected angle - the smoothing angle. The filter was applied twice using a 3×3 grid, a smoothing angle of 1.5° and an artifact angle of 1° (Humphreys et al., 2001), (Larsen, 2007), (Day et al., 2004).

In figure 4.15 two EBSD-maps are displayed. The EBSD-map marked A is a map noise reduced by replacing non-indexed points, while the EBSD-map B is map A after orientation noise filtering. In the EBSD-map A misorientations above 1° and below 1.5 ° are not added. By comparing the two maps the changes associated with the filter can be seen. In general the misorientation lines above 1.5° after filtering, are only one single lines contrary to the unfiltered lines, where often two lines one pixel apart are seen. An example is marked with a black arrow in the figure. The two lines in the unfiltered material is taken as an artefact of the measurements. An artifact created during orientation noise filtering is illustrated with withe arrows in figure 4.15. These show how the grain boundary has become very "squarish" after the filtering, which is a know artifact of the filter (Humphreys et al., 2001), (Day et al., 2004).

All EBSD-maps are displayed in as described above unless other is given.

Texture measurements

The texture measurements were conducted by measuring the orientation of the sample surface in a grid covering the entire LD/ND plane. The grid spacings were given by the average grain size expected after the given deformation of the initial grain size.

In practice the texture measurements of each specimen were conducted by measuring each half of the specimen separately and followed by an averaging of the measurements (Mishin et al., 2000).

The texture was calculated using Crystal, a free software program developed in house by Zhengjie Lie. In the program, an orientation was assigned to a texture component, if the orientation was within 15° of the ideal orientation of the texture component. In the case of overlap between the texture components, the orientation was assigned to the closest texture component.

The uncertainty of the texture measurements was calculated as the standard error (SE) of two measurements for each sample. The standard error is defined as:

$$SE = \frac{\sigma}{\sqrt{2}} \tag{4.19}$$

where σ is the sample standard deviation.

All measurements were conducted by the author herself apart from 4, which were conducted by Preben Olesen.

4.5.3 Comparison between electron microscopy techniques

The methods used to determine the deformed microstructure i.e. EBSD, CC and TEM each have their advantages and drawbacks. In the study by (Mishin et al., 2006) EBSD-maps, CCs image, TEM single tilt and TEM multiple tilt micrographs were obtained from the same region of an extruded aluminium alloy and the microstructures were compared. The conclusions of the study were that TEM single tilt micrographs were the method which reveal most boundaries in the microstructure determined by multi tilting in TEM. Kuhawara-filtered EBSD-maps were found to be better than CC images and the poorest resolution was found in EBSD-maps where no orientation noise reduction was preformed.

In the current thesis, bright field images were obtained under strong diffraction conditions, hence only one tilt position is necessary to determine the full microstructure. TEM images obtained in the current study are therefore regarded as the method with the highest resolution both spatial and angular. Another advantages of TEM is the possibility of obtaining 3D information through tilting, as in the cases of boundary plane determinations.

The drawback of TEM is that imaging and orientation measurements are only semi-automatic in that the operator needs to tilt to and identify the zone-axis, and the measurements requires manual reading of the tilts and movement of the beam, hence the measurement are more time consuming, and requires more knowledge of Kikuchi-diffraction patterns. Finally the sample preparation is more time consuming.

The advantages of EBSD are that the data acquisition is automatic, large areas can be covered and extensive knowledge of Kikuchi-diffraction patterns is not necessary. Besides this the sample preparation is easier. The drawbacks is the noise associated with the measurements, which limits both the

angular and spatial resolution, even though noise reduction procedures exist and EBSD is a 2D technique.

CC images were obtained under one diffraction condition, hence it can not be excluded, that some boundaries are not seen. A comparison between a CC image and a filtered EBSD-map are displayed in figure 4.14. In this it is seen, that generally there is a good agreement between the two images, when misorientations above 0.5° are marked.

Chapter 5

Evaluation of the experimental matrix

Initially a screening of the samples was performed to evaluate what microstructural and macrostructural properties have been obtained with the chosen experimental conditions. The PSC samples were therefore at first characterized with respect to the macrostructural properties i.e. the texture developed and the mechanical properties. The microstructures evolved in the deformation were thereafter characterized in EBSD and CC. From this, initial conclusions regarding the possible grain orientation-dependence of the microstructure is given and the effect of the process conditions discussed.

The texture measurements were only conducted on the samples deformed at 350°C and 500°C , as these samples mark the borders of the parameter study.

EBSD and CC were selected for evaluation of the experimental matrix, due to the possibility of quantifying large areas. Although the techniques have a poor angular resolution compared to TEM, leading to the entire deformation structure not being entirely displayed, the method still gives a way to observe relative differences between the structures developed. The 350°C and $25s^{-1}$ series were not characterized as initial studies showed the microstructure of the 350°C and $5s^{-1}$ series to be cold deformed like, hence the 350°C and $25s^{-1}$ series would just be more cold deformed like.

The microstructures were only characterized with respect to the morphology of the ideal oriented grains i.e. were extended dislocation boundaries observed, if so how many sets, were they straight or wavy and were they inclined to LD. If no extended boundaries were observed the microstructure

was classified as a rounded structure.

Spacings were not determined and neither were misorientation distributions calculated. Quantitative parameters were not included, as the micro structures were very complex, as will be seen, and it was therefore not trivial to measure reliable spacings. Furthermore a previous study conducted by (Verrnon-Parry et al., 1996) measured the average spacings and misorientation angles of plane strain deformed samples of the same alloy in the temperature range 300°C to 500°C at strain rates between $2.5s^{-1}$ and $25s^{-1}$ in the strain range ε= 0.5 to 2.

5.1 Texture measurements

The measured textures are displayed in figure 5.1, together with error bars in terms of the standard error, and the following trends are seen. The rolling texture components brass, S and copper increases with strain and the increase is larger at 350°C compared to 500°C . A slight decrease in copper texture is, however, observed at 500°C $25s^{-1}$.

The cube component decreases for strains up to 0.69, but more obviously at the lower temperature. Above strain 0.69 the cube texture increases significantly at 500°C , while it practically vanishes at 350°C . The Goss component increases up to 0.69 and then drops somewhat in all samples.

The samples strained to 2.3 at 500°C were partly recrystallized, as judged from the cube texture, and EBSP-maps in figure 5.18 and figure 5.23 and they are therefore not discussed any further.

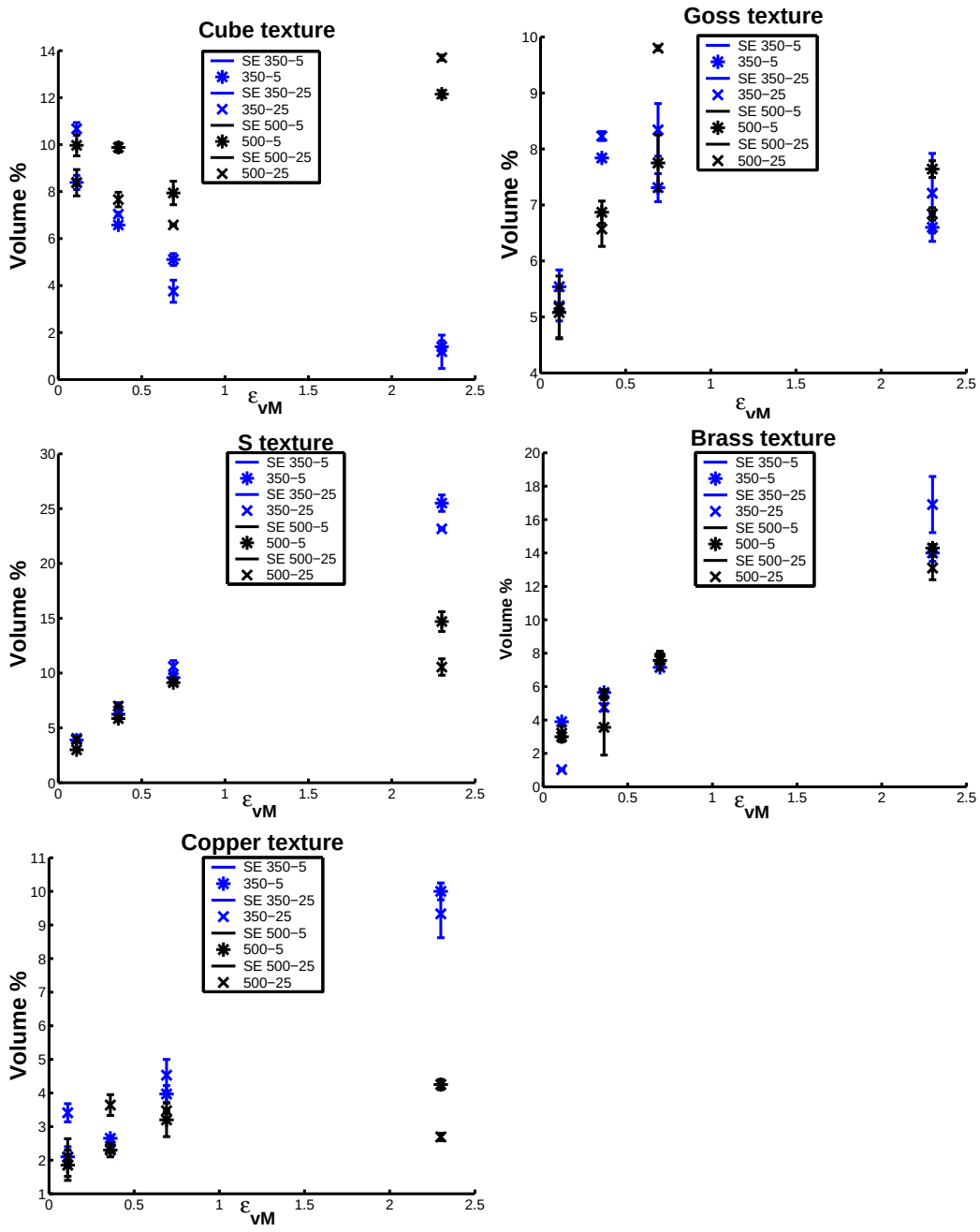

Figure 5.1: Texture components as a function of strain

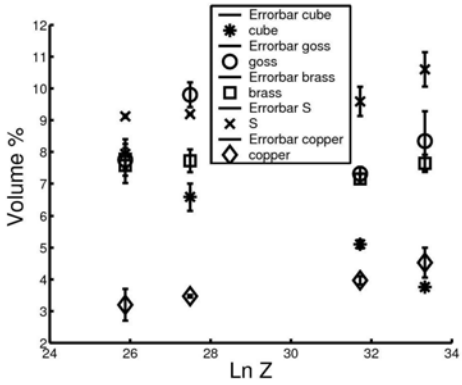

Figure 5.2: Texture components as a function of ln Z at $\varepsilon_{vM} = 0.69$

If the texture variation is analyzed as a function of Z at constant strain ($\varepsilon_{vM} = 0.69$), as displayed in figure 5.2 the overall tendency is an increase in copper and S texture components and a decrease in the cube components with increasing Z. The brass texture is practically constant, while the Goss texture is more irregular. The sum of the rolling texture components (brass, S, copper) increases with Z. The strength of the rolling texture components increases 2-2.5 times at strain 0.7, which is lower than the observation of a 4-5 times increase during cold deformation in a similar material (Hansen and Juul Jensen, 1986).

The observed textural evolution with strain and temperature is similar to observations by (Samajdar et al., 2001) and (Verrnon-Parry et al., 1996) and (Humphreys and Bate, 2005). The relative increase in strength of the texture components are slightly higher when compared to hot deformation of a similar material (Verrnon-Parry et al., 1996). The evolution of a stronger brass texture as observed by (Maurice and Driver, 1997a) and (Maurice and Driver, 1997b) was not observed.

5.2 Mechanical properties

5.2.1 Mechanical data

The flow-curves obtained during plane strain compression in the current study are displayed in figure 5.3 together with a curve displaying the work-hardening rate of the flow-curves. Each curve is marked with the deforma-

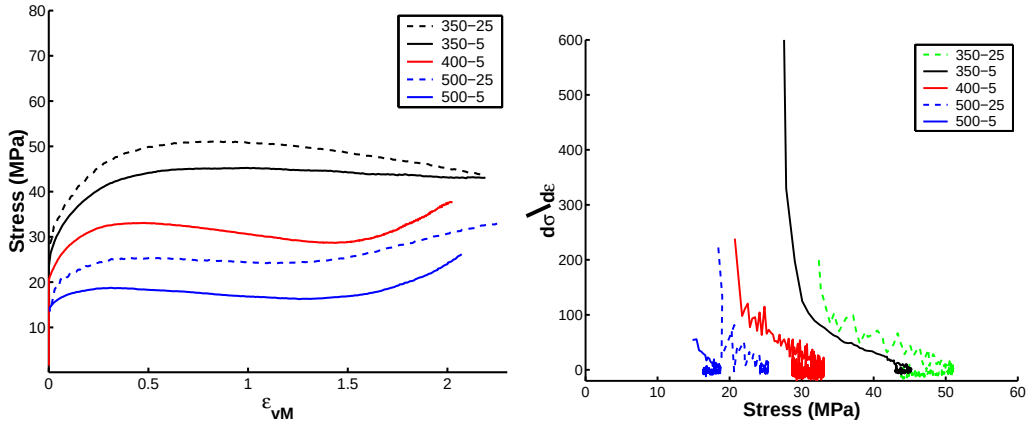

Figure 5.3: Left: flow-curves obtained during PSC. Right: work-hardening rate

tion temperature and strain rate. The flow-curves display an initial parabolic work-hardening followed by steady state or softening. The flow-curves obtained at 400°C and above display an increase in stress at the largest strains. This increase is due to degradation of the lubricant and these parts of the curves will therefore be neglected in the remaining parts of the thesis.

The work-hardening curves can be divided into three regimes. Initially, the work-hardening rate is high in a short stress range, in this elastic deformation occur. This is followed by a linear work-hardening curve, which continues until the work-hardening is approximately zero. The linear work-hardening region is larger in the curves obtained at lower temperatures and at higher strain rates i.e. at higher Zener-Hollomon parameters. The last regime is a region of softening which all the curves display more or less.

5.2.2 Observed softening - discussion

The softening observed to a different extent, is a well-know phenomena in torsion, where it is related to the evolved texture (Kassner, 1989), (Kassner et al., 2002) and texture and microstructure (Pettersen and Nes, 2003). In the current study, the softening is explored further in the 350°C - $5s^{-1}$ flow curve, where the effects of friction are at a minimum[1]. During PSC the temperatures may rise due to adiabatic heating. This effect will be most pronounced in the curve deformed at $25s^{-1}$, where the deformation-produced

[1]As will be shown this was also the most interesting deformation series at 350°C

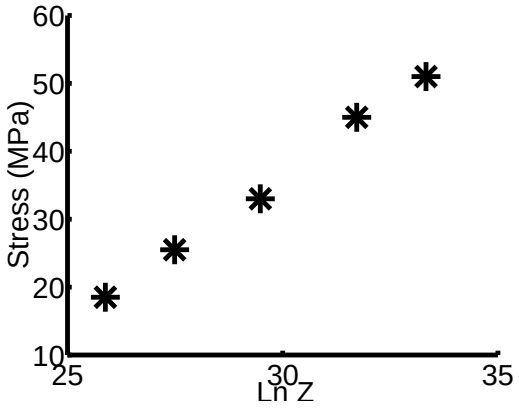

Figure 5.4: Logarithm of Zener-Hollomon parameter as a function of maximum stress

heat will have a shorter time to diffuse away. In the current study, the temperature was not monitored in the deformation zone during deformation to the highest strain, in order to avoid any affects on the microstructure from the thermocouple. It is therefore not possible directly to evaluate any effect on the process parameters on the flow curves.

In (Shi et al., 1997b) the temperature increase during PSC of an Al-1% Mn alloy deformed to $\varepsilon_{vM} = 1.8$ at 400°C and at a strain rate of 2.5s^{-1} was 4°C . Such a temperature increase will naturally decrease the flow stress. If it is assumed, that the total temperature increase during PSC at 350°C at the strain rate of 5s^{-1} , was 4°C the effect on the flow stress can be estimated through the Zener-Hollomon relationship (eq. 2.2) as follows. A temperature increase of 4°C corresponds to a deformation temperature of 354°C . In the work softening regime, the strain rate fluctuates between 4 and 6s^{-1} , so to illustrate the highest possible effect on the flow curve, the strain rate is taken as 4s^{-1} , hence Z changes from initially $5.96 \cdot 10^{13}$ to $3.93 \cdot 10^{13}$. Such a decrease in Z can be correlated to a decrease in flow stress, through the parameters in table 5.1, plotted in figure 5.4. In this, a decrease in Z of $2 \cdot 10^{13}$ corresponds to a decrease in stress of 1.5MPa. The observed stress decrease is 2.5MPa in the strain range ε_{Vm}=1 to ε_{Vm}=2.3.

Another possible origin of the decrease in the flow stress is the textural evolution. From the texture measurements Taylor factors were calculated for the specimen deformed to strains 0.69 and 2.3 [2]. In this strain range, the

[2]all calculations of Taylor factors were conducted by Grethe Winther

Temp-strain rate	ε_{vM}	Stress(MPa)	Z
350-25	0.85	51	$3.0{\cdot}10^{14}$
350-5	1	45	$6.0{\cdot}10^{13}$
400-5	0.50	33	$6.4{\cdot}10^{12}$
500-25	0.45	25.5	$8.7{\cdot}10^{11}$
500-5	0.35	18.5	$1.7{\cdot}10^{11}$

Table 5.1: Transition stresses and strains for the individual flow-curves

Taylor factor increases from 3.1 to 3.19 in the same strain regimen, which corresponds to a 2.9% increase in the flow-stress corresponding to 1.3MPa. Hence, the textural evolution is expected to increase the flow-stress by 2.9%, and therefore cannot contribute to the observed softening.

The estimated temperature-based softening of 1.5MPa is very near the observed 2.5MPa, and even more so, as the estimated temperature is based on an experiment conducted at a lower strain rate, which leads to lower adiabatic heating.

The softening is therefore concluded to be due to adiabatic heating during PSC at 350°C at $5s^{-1}$, and the textural evolution increases the flow stress.

The flow-curves have been fitted to a modified Voce-equation (equation 4.11) displayed in figure 5.5. The modified Voce-equation describes a flow-curve with an initially decreasing work-hardening followed by a saturation stress, that is a steady state between work-hardening and dynamic recovery. As can be seen from the fit in figure 5.5 all curves are initially described well by the modified Voce-equation, in that the initial flow curves display decreasing work-hardening rates. At the higher stresses, neither of the flow-curves display steady-state. Instead, softening occurs and, hence, the modified Voce equation does not describe the flow curves well.

The stresses and strains, at which the flow curves shift from being dominated by work-hardening to a steady state are given in table 5.1. If the 350-25 flow-curve is neglected, the transition stresses and strains decrease with increasing temperature, as would be expected since recovery is enhanced by a higher temperature and a lower strain rate.

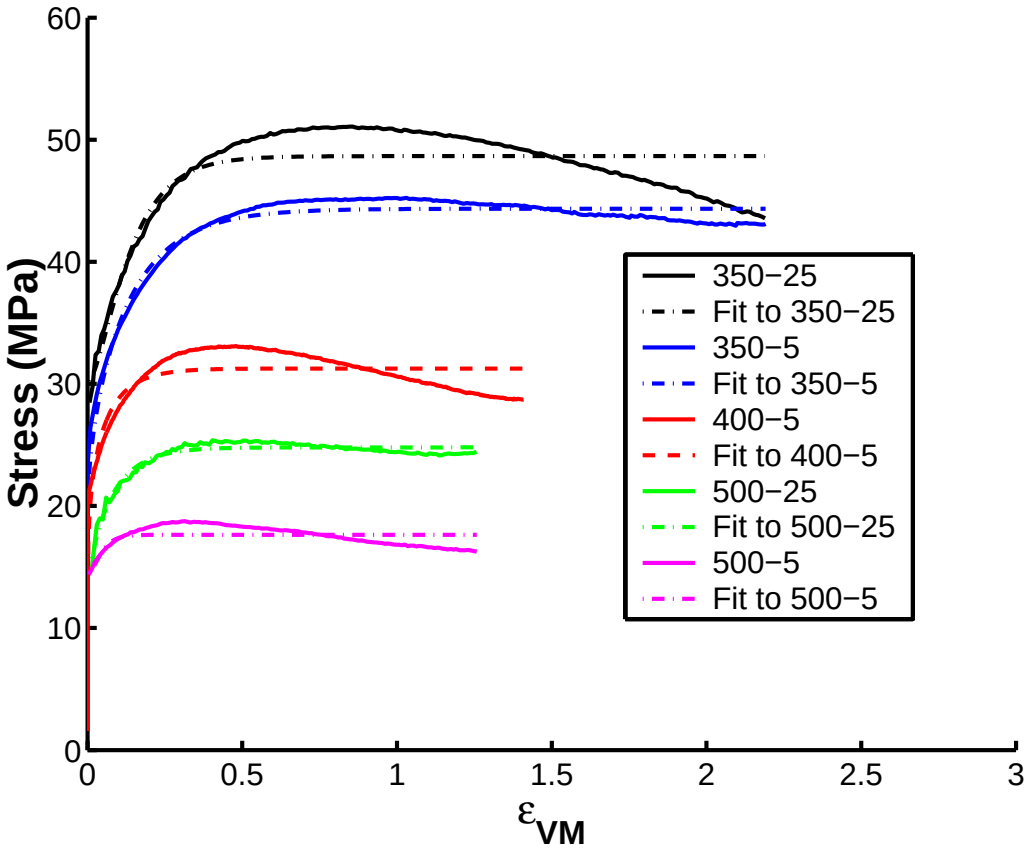

Figure 5.5: Flowcurves obtained during PSC

5.3 Overview of EBSD/CC measurements

The microstructure evolution within the chosen experimental conditions are reviewed in the following.

5.3.1 Microstructures characterized in the SEM

350°C strain rate 5 s^{-1}

The microstructure evolved during PSC at 350° and at a strain rate of 5 s^{-1} is displayed in figure 5.6 to figure 5.9.

350° C strain rate 5 s^{-1} strained 0.11

The microstructure evolved at strain 0.11 is illustrated by the CC image in figure 5.6. The CC image clearly shows the original grains, within which

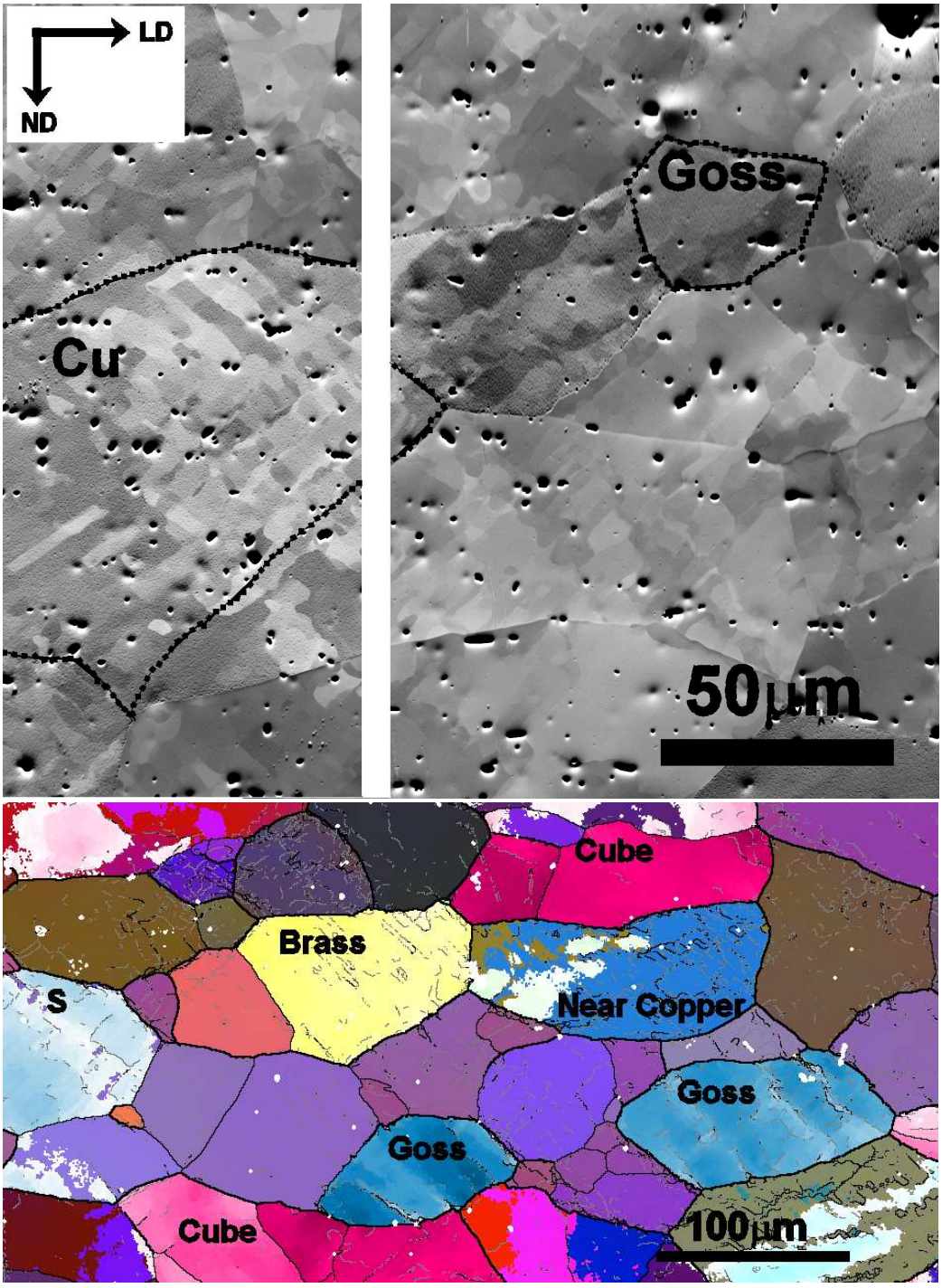

Figure 5.6: CC and EBSD-map of sample 350°C $5s^{-1}$ strained 0.11

the microstructure can be seen. The holes in the surface are due to the electro-polishing, and are presumably where iron-rich particles have been. The microstructure consists of either bands inclined to LD (one or two) or more rounded structures with a not-so-clear directionality. In the CC image two grains, one within 15° of the ideal copper orientation and one within the ideal Goss orientation, are seen and marked. The copper grain displays two bands inclined $\sim 35°$, and $\sim 45°$ to the LD direction, while the Goss grain displays a structure with more rounded shapes, and no clear directionality to LD. The other ideal orientations cube, brass and S are displayed in the EBSD-map in figure 5.6, together with another Goss orientation. The EBSD-map displays the original grains in which no clear microstructure is resolved, hence the microstructure evolved, has low misorientations. There is, however, a difference between cube and the other ideal orientations, in that the other ideal orientations, display an orientation gradient illustrated by a colour difference in bands inclined with the LD direction around $\pm 45°$, while the cube grain shows no clear directionality and clear structure. These two types of behaviour are also found in grains of orientations outside the ideal components considered here (so-called random orientations).

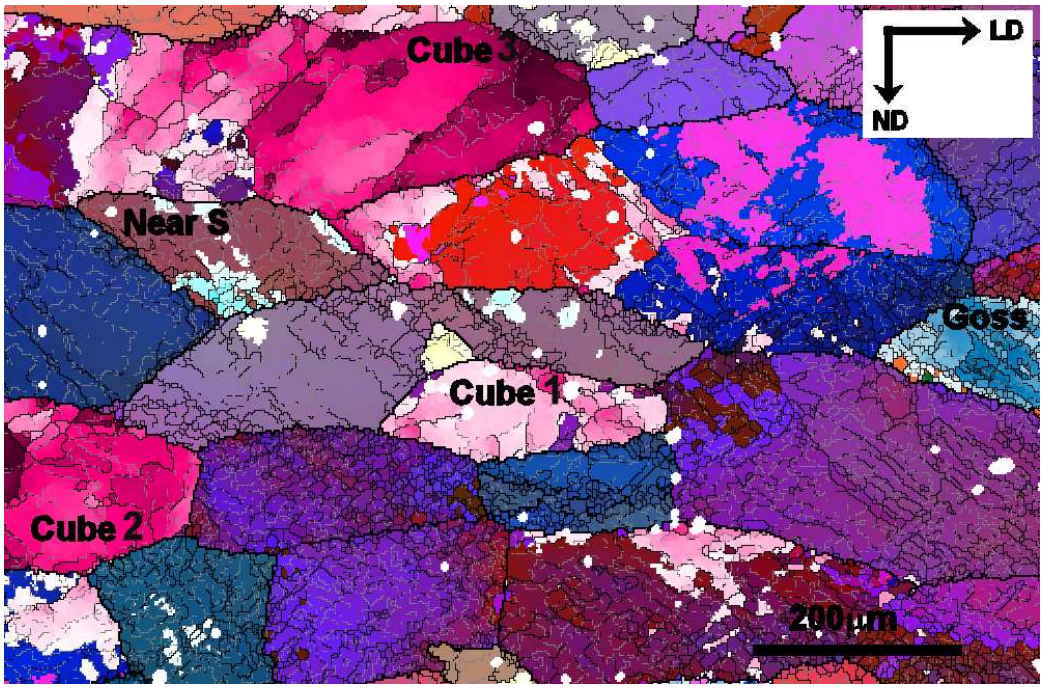

Figure 5.7: EBSD-map of sample 350°C $5s^{-1}$ strained 0.36

350°C strain rate 5 s^{-1} strained 0.36

The microstructure evolved after straining to 0.36 is displayed in the EBSD-map of figure 5.7. From this, the original grains are clearly seen, and a visible microstructure has evolved in large areas. The cube orientation displays no band-like structures in some areas (cube1 and cube2), while a few bands inclined 45° with very large spacings are observed in other parts of the map (cube3). The Goss orientation displays one clear set of bands and a less clear set inclined at 45° - 50° to the LD direction. The other ideal rolling textures is not observed in large enough areas, to make any conclusions. The microstructures of random orientation regions are a mixture of the observed structures, that is, in some areas 2 sets of bands inclined $\sim$ 35° - 40° to LD are observed, while in some areas only one set of bands inclined $\sim$ 40° - 45° to LD. Yet in other areas are microstructures, with no clear directionality and structure observed.

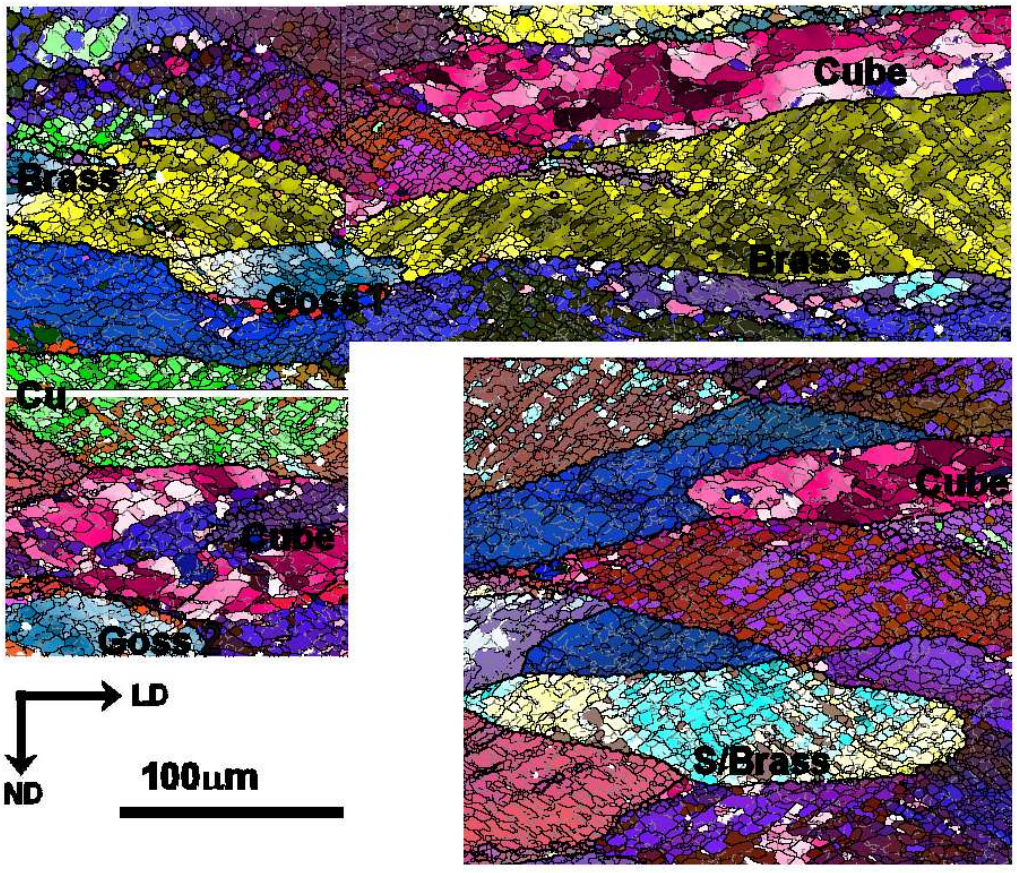

Figure 5.8: EBSD-maps of sample 350°C 5s^{-1} strain 0.69

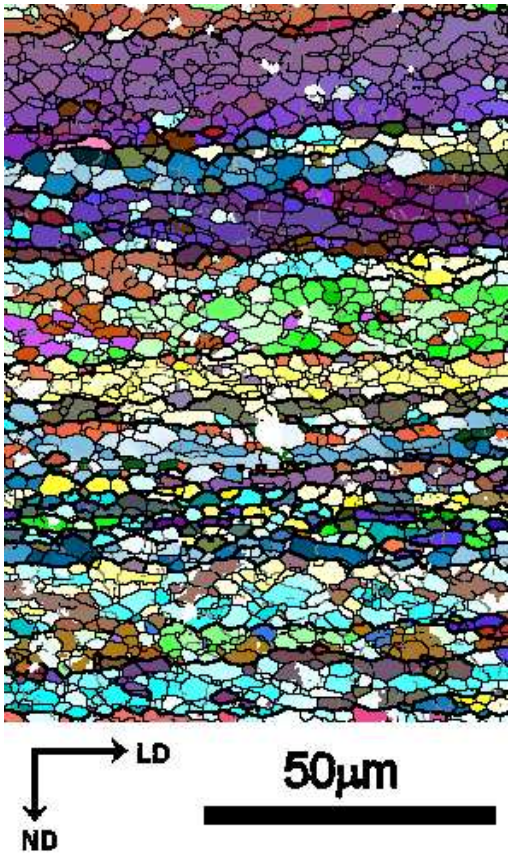

Figure 5.9: EBSD-map of sample 350°C 5s^{-1} strained 2.3

350° C strain rate 5 s^{-1} strained 0.69

The microstructure observed after PSC to strain a 0.69 is illustrated in the EBSD-maps displayed in figure 5.8. In general, the microstructure appears well-revealed, which is ascribed to the higher misorientation angles expected with increasing strain. From this the microstructure of the cube orientation is seen to be rounded structures without any clear directionality, and the scale of the structures is larger than the microstructures observed in the rolling texture components. Grains with copper orientations display two sets of bands inclined to $\sim$ 35° to 40° LD. Grains of either S or brass orientation display one or two bands. In brass grains the bands are inclined 30° -35° or 40-45° to LD. In the S/Brass grain the boundaries are inclined 30° -35° or 40° -50° . Goss oriented grains display either a more rounded structure (Goss 2) with directionality or a set of bands inclined $\sim$ 50° to LD (Goss 1). The bands are straight in some regions, and more wavy in others. The mi-

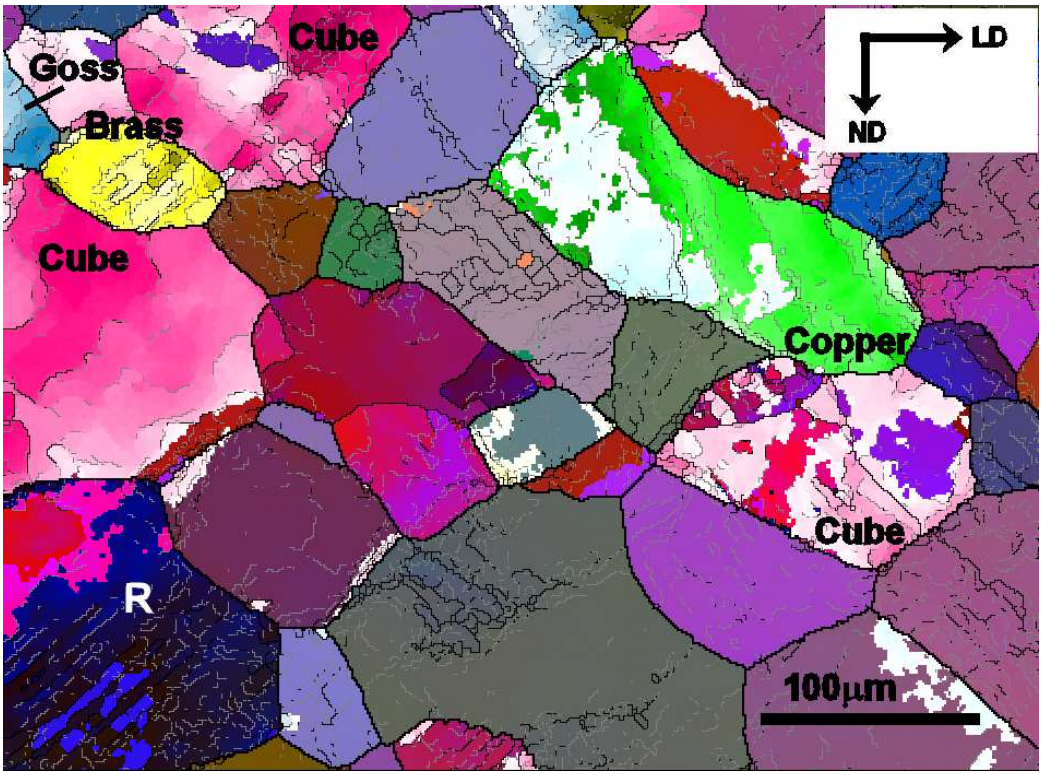

Figure 5.10: EBSD-map of sample 400°C 5s^{-1} strained 0.11

crostructure of random oriented grains are best described as being a mixture of the cube and rolling texture structures.

350°C strain rate 5 s^{-1} strained 2.3
An EBSD-map of the highest strained sample is shown in figure 5.9. In this, it is seen that the microstructure consists of bands of different orientations and widths parallel with LD. The microstructure of the individual bands consists of cells elongated along LD and it is not possible to define a microstructure which is unique for a given ideal orientation.

400°C strain rate 5 s^{-1}

The microstructure evolved after PSC at 400°C is displayed in figure 5.10 to figure 5.13 and described in detail in the following.

400°C strain rate 5 s^{-1} strained 0.11
The microstructure evolved after PSC at 400°C to a strain of 0.11 is displayed

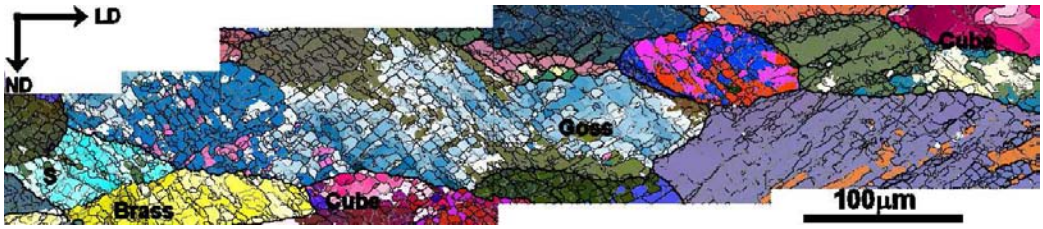

Figure 5.11: EBSD-map of sample 400°C 5s^{-1} strained 0.36

in the EBSD-map in figure 5.10. In the figure, the original grains are clearly seen, and only a few of them have evolved a detectable microstructure. This includes a brass grain, where bands inclined $\sim$ 45 ° to LD are weakly seen. Copper and Goss oriented grains displays no clear microstructure, and the same applies to cube oriented grains. In the random oriented grain marked R a clear set of boundaries inclined 40° to LD is seen

400°C strain rate 5 s^{-1} strained 0.36

At a strain of 0.36 the microstructure of the original grains (figure 5.11) consist of one or two sets of bands inclined 35° - 55° to LD or of a microstructure of more rounded shapes, with no clear directionality. The last structure is of the cube orientation. The structure of the Goss orientation is found to consist of two bands inclined 35° - 45 ° to LD, while one set of bands has evolved around 40° - 55 ° in a brass grain. S oriented grains displayed boundaries inclined 30-45° to LD.

400°C strain rate 5 s^{-1} strained 0.69

The microstructure evolved after PSC to strain of 0.69 is illustrated in the EBSD-map in figure 5.12, where rounded structures and wavy bands (one or two sets) are seen. The microstructure of the Goss orientation is 2 sets of bands inclined 35-´50° to LD. Grains oriented partly in the cube orientation have rounded structures in the area of cube orientation, while an area

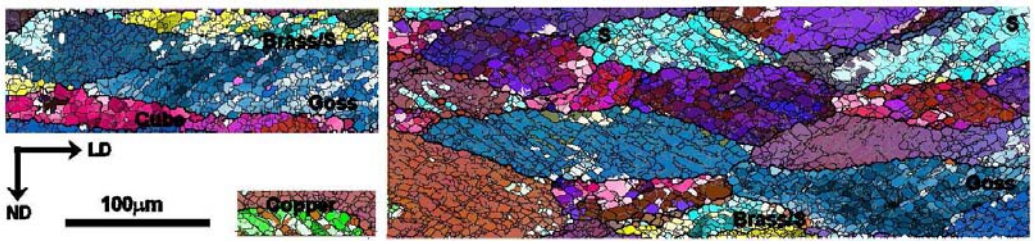

Figure 5.12: EBSD-maps of sample 400°C 5s^{-1} strained 0.69

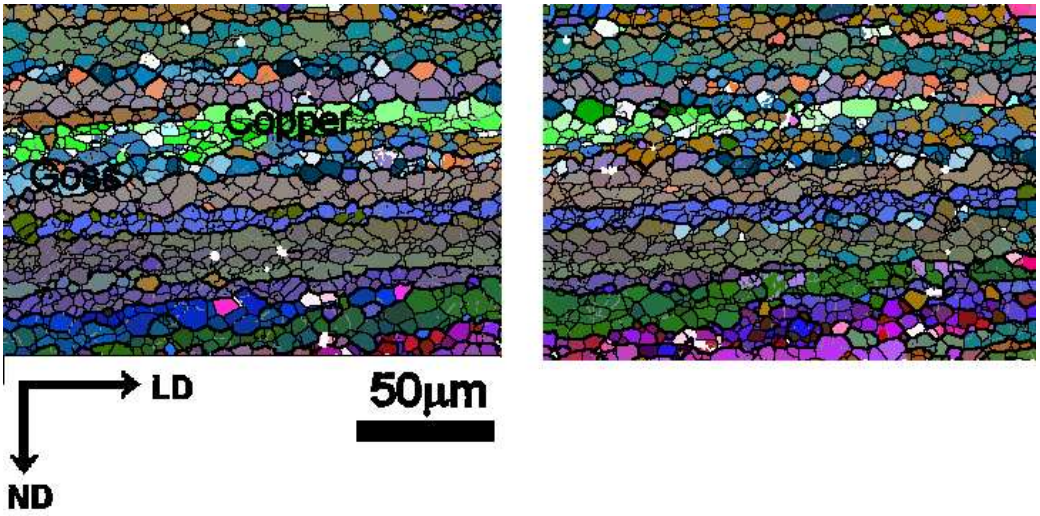

Figure 5.13: EBSD-maps of sample 400°C 5s^{-1} strained 2.3

of copper orientation has one set of bands inclined around 45° to LD. The microstructure of S oriented grains consists of one sets of bands inclined 30° -40° to LD or two sets of bands one clear set inclined 50-55° to LD, and a less clear set of bands inclined 35° to LD. The microstructure of a brass/S oriented grain, displays one set of bands inclined 35-45° to LD.

400°C strain rate 5 s^{-1} strained 2.3

At the highest strain, a microstructure consisting of bands parallel with LD surrounding more-or-less equiaxed cells has evolved (figure 5.13), and the grain boundaries have become clearly serrated.

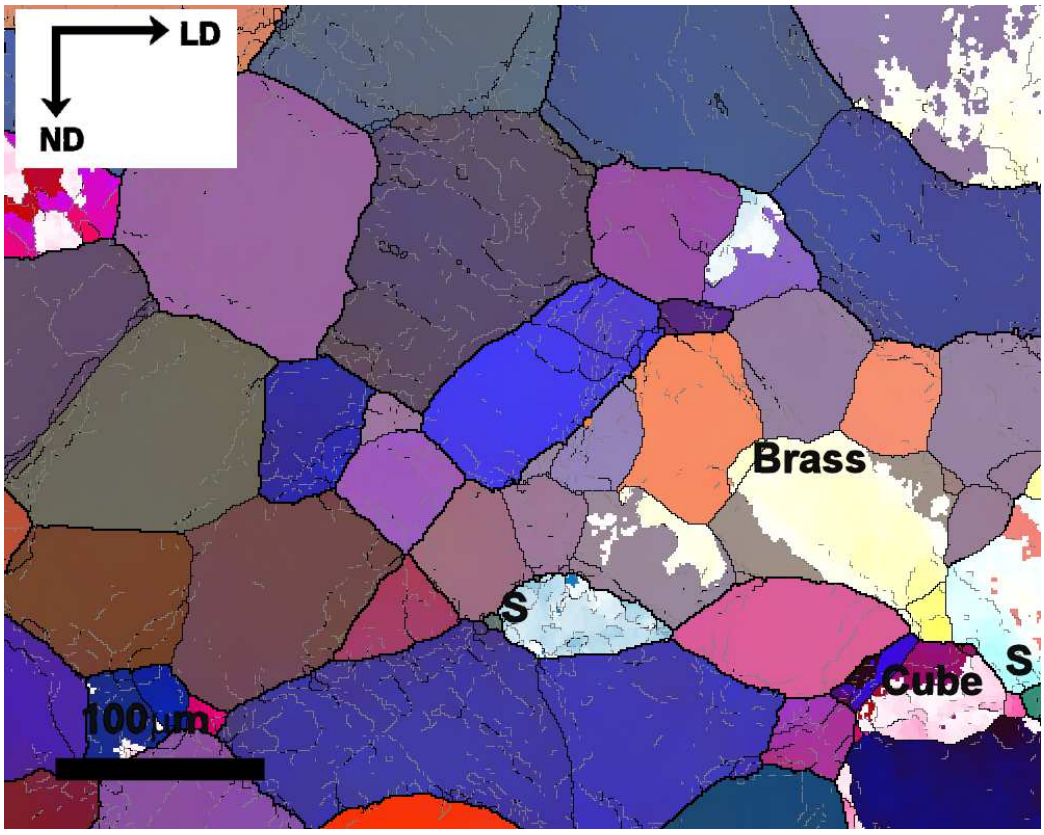

Figure 5.14: EBSD-map of sample 500°C 25s^{-1} strained 0.11

500°C strain rate 25 s^{-1}

The microstructure evolved after PSC at 500°C and a strain rate of 25s^{-1} is displayed in figure 5.14 to figure 5.18 and described in detail in the following.

500° C strain rate 25 s^{-1} strained 0.11

Figure 5.14 is an EBSD-map of a sample strained to 0.11 displayed. In this, a microstructure consisting of original grains is seen, and if a deformation structure has been formed, the misorientation within each grain is rather low, as only fraction of the boundaries are seen in the major parts of the grains.

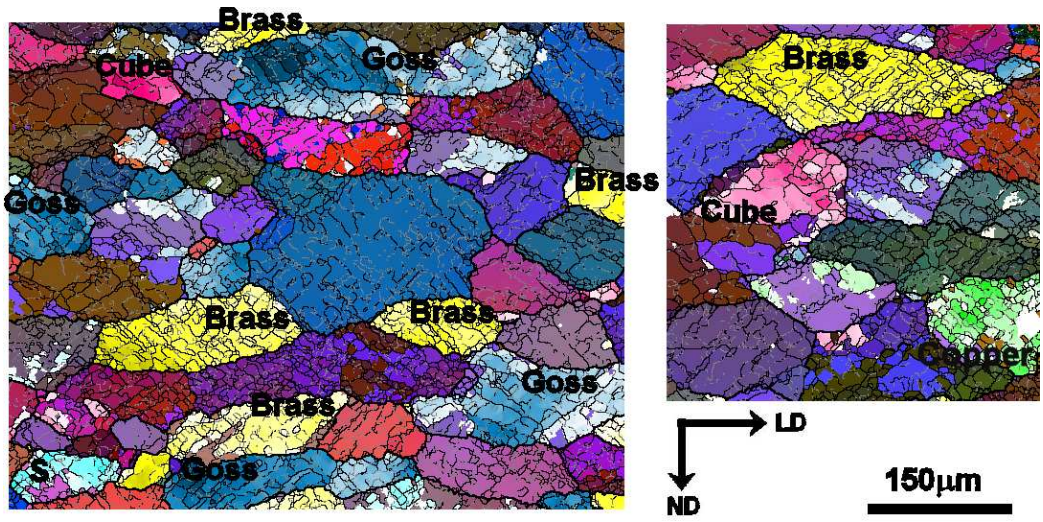

Figure 5.15: EBSD-maps of sample 500°C 25s^{-1} strained 0.36

500° C strain rate 25 s^{-1} strained 0.36
At a strain of 0.36 the microstructure in the original grains is more-or-less clear. The microstructure in each grain is either rounded structures or structures of elongated cells with a directionality inclined to LD. Cube oriented grains have a microstructure which is round, while Goss grains consist of widely-spaced bands inclined at 35° to 45° to LD. The microstructure of brass grains consist of either one or two wavy bands inclined between 35° and 50° to LD. A copper and a partly S oriented grain, display one set of bands inclined 40° -45° to LD. Random oriented grains have structures as observed in all other orientations.

500° C strain rate 25 s^{-1} strained 0.69
The microstructure developed after straining to 0.69 is illustrated in the EBSD-map in figure 5.16 and in the CC image in figure 5.17. The microstructure consists of rounded structures of cube orientation and structures of one or two more-or-less wavy bands inclined to LD. Brass oriented grains have evolved a microstructure consisting of one or two sets of bands inclined 30° to 40° to LD were observed. A copper/S grain have one clear set of boundaries inclined 35° - 45° to LD, while S oriented grains display one or two sets of boundaries inclined 40° to 50° . Grains of the Goss orientation display more rounded structures, but still with a directionality to LD.

In the CC in figure 5.17 a serrated boundary, most likely a grain boundary is displayed. The images have been shown to illustrate the changes in

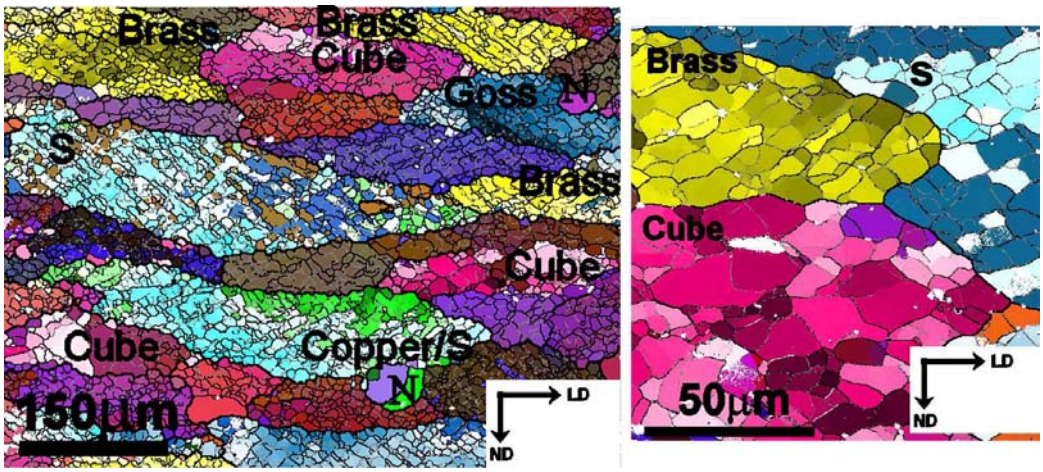

Figure 5.16: EBSD-maps of sample 500°C 25s^{-1} strained 0.69

boundary character under these deformation conditions.

In the deformed microstructure several nuclei are formed, some of them are marked with N in the EBSD-map in figure 5.16. The nuclei have no detectable internal microstructure, hence it is possible that they are formed just prior to quenching of the sample and not during deformation.

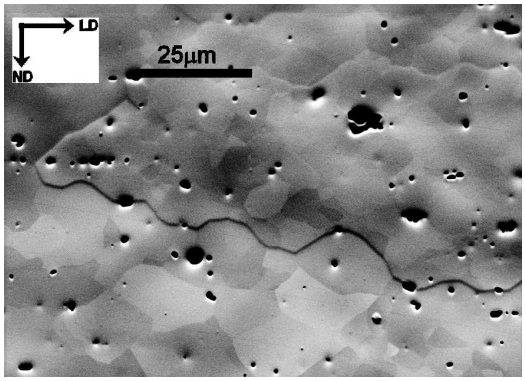

Figure 5.17: CC image of sample 500°C 25s^{-1} strained 0.69

500° C strain rate 25 s^{-1} strained 2.3

The sample strained to 2.3 has partly recrystallized as seen in the EBSD map of figure 5.18, where large non-deformed grains are seen. The other part of the sample consists of bands parallel with LD, with a microstructure between the bands consisting of rounded cells or subgrains mainly oriented along one

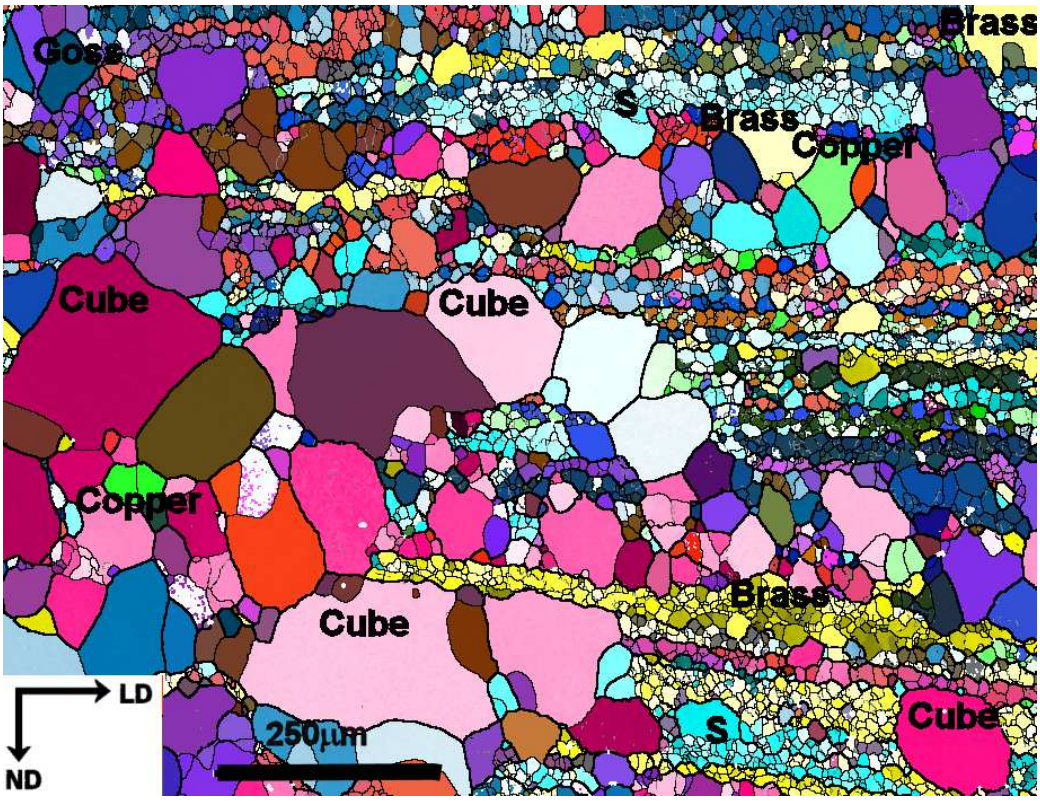

Figure 5.18: EBSD-map of sample 500°C 25s^{-1} strained 2.3

of the rolling texture components.

500°C strain rate 5 s^{-1}

The microstructure evolved after PSC at 500°C and a strain rate of 5s^{-1} is displayed in figure 5.19 to 5.22 and described in detail in the following.

500° C strain rate 5 s^{-1} strained 0.11
The microstructure evolved after PSC at 500°C at a strain rate 5s^{-1} to a strain of 0.11 is illustrated in figure 5.19. The microstructure developed within the original grains are of too low a misorientation in order to be classified. No variation in microstructure between the individual grains was seen.

500° C strain rate 5 s^{-1} strained 0.36
The microstructure evolved after a strain to 0.36 is displayed in figure 5.20, in this a not entirely developed weak microstructure is seen in most grains.

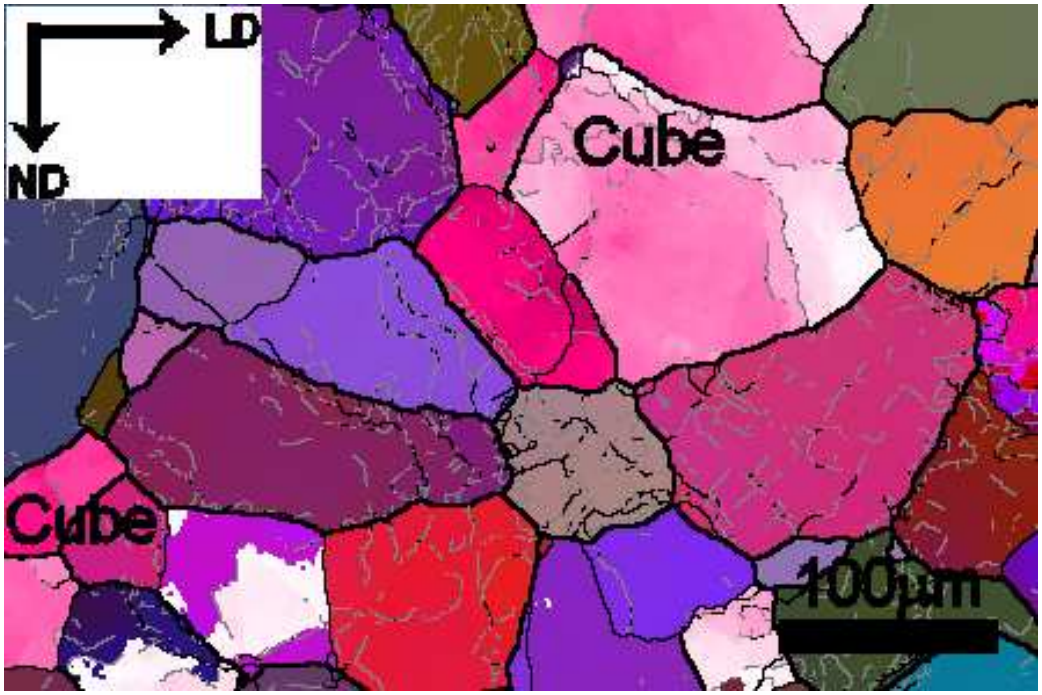

Figure 5.19: EBSD-map of sample 500°C $5s^{-1}$ strained 0.11

The tendency is for an evolution of band structures in the grain Goss 2 and in the copper oriented grain. The bands are inclined 30° to 35° in the copper grain and in the Goss grain around 40° to LD. Brass oriented grains are more irregular in structure. The Goss 1 oriented grain displays a structure consisting of more rounded structures and the cube grains are only seen partly, where more rounded structures are observed.

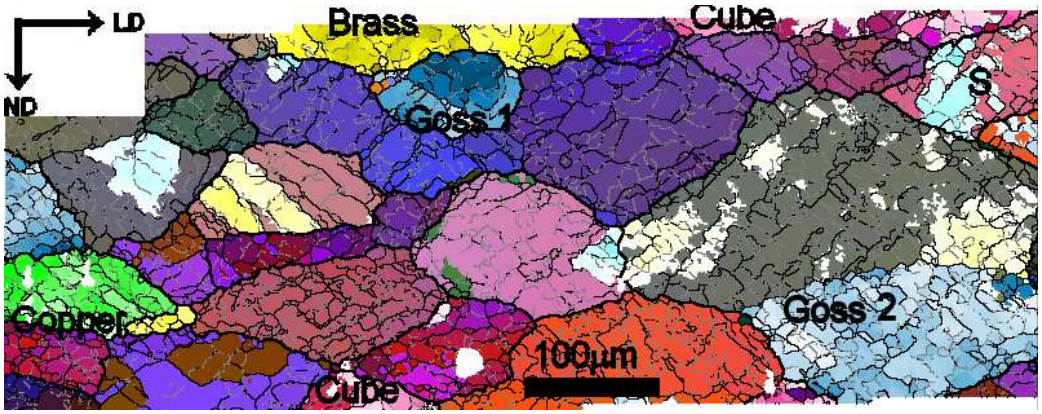

Figure 5.20: EBSD-map of sample 500°C $5s^{-1}$ strained 0.36

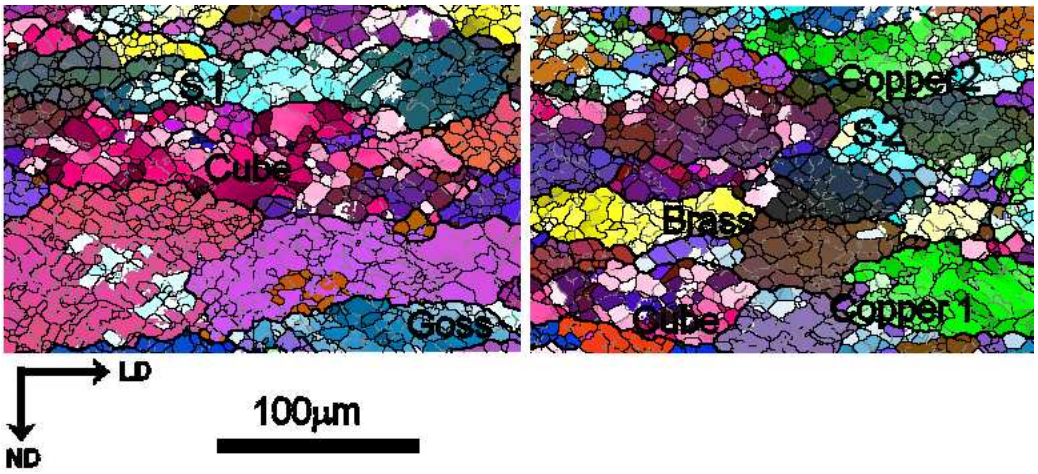

Figure 5.21: EBSD-map of sample 500°C 5s^{-1} strained 0.69

500° C strain rate 5 s^{-1} strained 0.69
The microstructure evolved after a strain of 0.69 is displayed in the EBSD-map in figure 5.21. In this, a microstructure of rounded cells is seen in most of the original grains including cube, Goss, S two, brass and the copper two grain. A few other grains display a microstructure which shows elongated cells, with a weak directionality, this includes the copper one and S one grains.

500° C strain rate 5 s^{-1} strained 2.3
The microstructure evolved at the largest strain is shown in the EBSD-map in figure 5.22. The microstructure consists of bands of different orientations parallel with LD. The microstructure within the bands consists of rounded cells with a high misorientation. The size of the cube oriented subgrains are generally larger than the other cells or subgrains. A high resolution EBSD-map is furthermore displayed in figure 5.23, in which there is no microstructure observed within the subgrains, hence the structure is recovered or recrystallized.

5.3.2 Evaluation of the SEM results

After the plane strain compression, a deformation microstructure consisting of either rounded structures or one or two bands was seen to evolve within the original grains during straining. The misorientation of the dislocation boundaries increases as they were observed to become clearer (or better de-

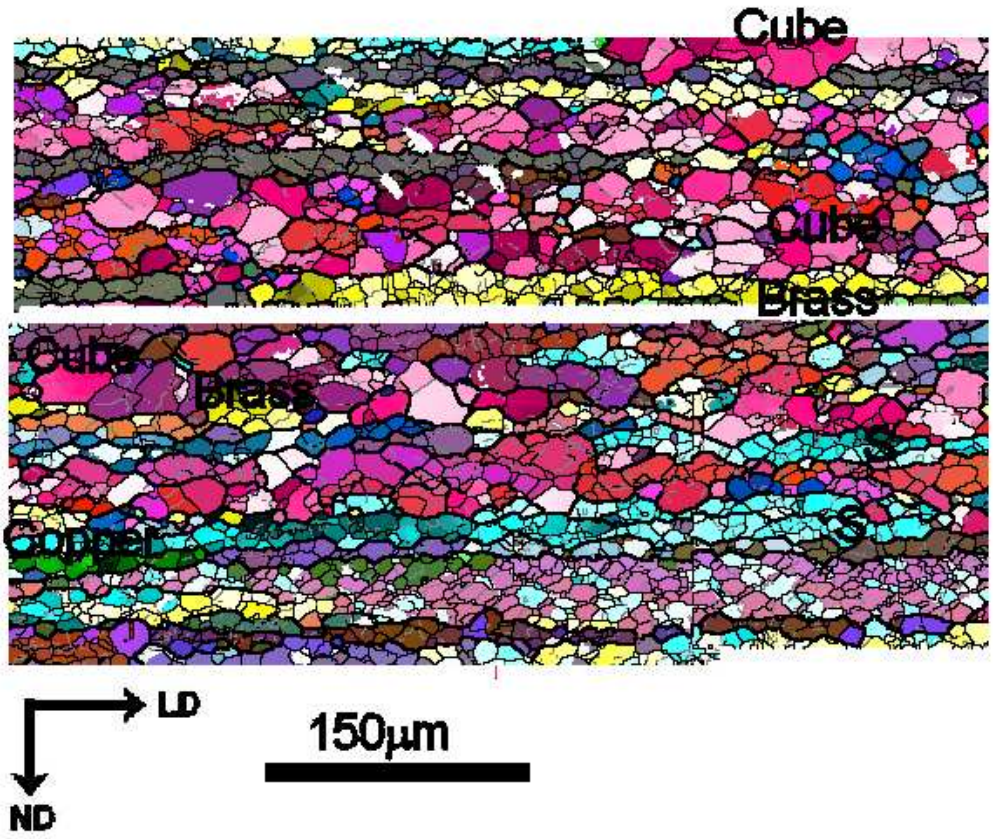

Figure 5.22: EBSD-maps of sample 500°C $5s^{-1}$ strained 2.3

Figure 5.23: Another EBSD-map of sample 500°C $5s^{-1}$ strained 2.3. This map has not been noise reduced

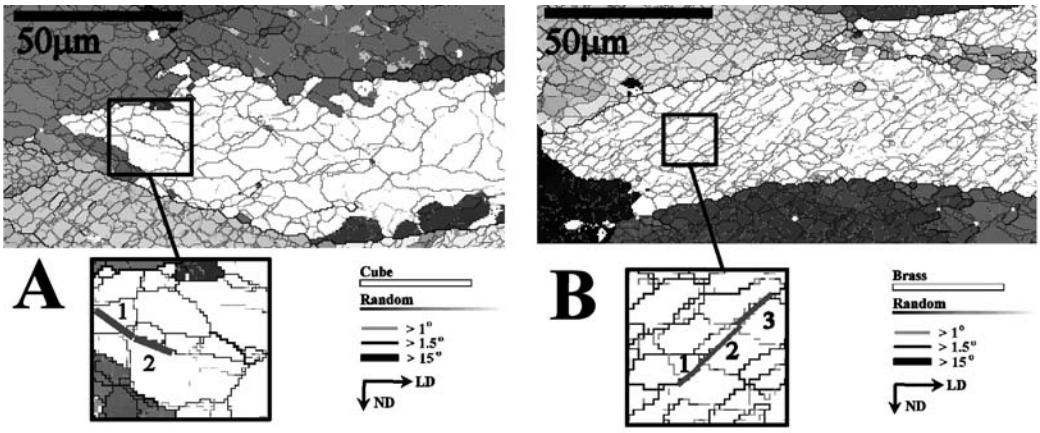

Figure 5.24: A cube oriented grain, B brass oriented grain from sample 350°C $5s^{-1}$ strained 0.69

tectable) at higher strains. At the highest strain, the original grains were transformed into bands of variable width parallel with LD. At temperatures above 350°C , the structure of the grain boundaries, follows the internal microstructure. This is clearly seen at 500°C , where serrated grain boundaries are clearly developed.

The observed microstructural characteristics found in the samples strained to strains from 0.36 to 0.69 are summarized in table 5.2, where the clearest microscopical structures are given. The structure in cube oriented grains are, in general, somewhat different from the other ideal grain orientations, in that the structure consisted most often of rounded structures, with no clear directionality to LD. In the ideal orientations, brass, S, and copper is either one or two sets of bands inclined to LD observed. The inclination angle varied between 30° and 55° to LD, and there is no observed difference in inclination angle between the ideal orientations. The Goss orientations, however, displayed a microstructure somewhat different in that sets of bands were observed in some regions, while more rounded structures were observed in other regions. Randomly oriented grains displayed a microstructure characterized as a mixture of the structures observed.

The inclination of one or two sets of boundaries 30° to 55° to LD is commonly observed in EBSD studies of cold deformed aluminium (Hurley et al., 2003), (Bay et al., 1989), (Juul Jensen and Hansen, 1990), (Hughes and Hansen, 1991) as well as in hot deformed aluminium single crystals (Theyssier et al., 1995).

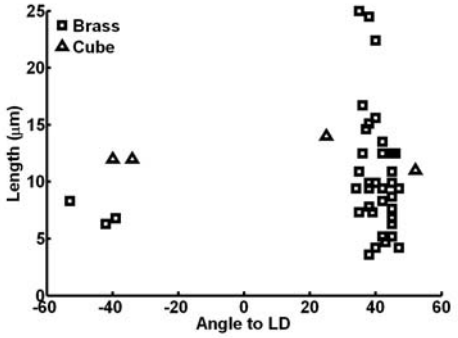

Figure 5.25: Inclination to LD of the segments identified in cube and brass grains

The general difference in structure of cube oriented grains compared to other ideal oriented grains indicates an orientation dependency of the evolved microstructure. These apparent differences in structure is therefore further explored by comparing the alignment of the boundaries in a cube oriented grain, with a brass oriented grain of similar size (about $5000\mu m^2$).

In the comparison, the alignment of boundaries more than one cell/IDB long, were determined by joining straight boundary segments within 10° of each other and measuring the angle of the joint segments to LD. The method is illustrated in figure 5.24. The analysis was conducted manually on EBSD-maps noise reduced by replacing zero solutions, with a minimum of 6 indexed neighbours. No reduction of the angular noise was performed. The result is displayed in figure 5.25, from which it can be seen, that in the cube oriented grain only 4 boundaries fulfilled the criteria, while about 40 boundaries in the brass grain were identified, hence the visual impression of the difference in structure of the two differently oriented grains are also found by a more systematic investigation .

The difference in microstructure between the ideal orientations are, however, not clearly observed during deformation at 500°C at a strain rate of $5s^{-1}$ strained to 0.69. Under these deformation conditions nearly all original grains display a deformation structure consisting of nearly equiaxed cells.

The microstructures developed at the highest strains, were below 500°C characterized by grain boundaries parallel with LD enclosing cells. From the EBSD-maps it was not possible to determine any differences between the

$350°C\ 5s^{-1}$	0.36 ε_{vM}	0.69 ε_{vM}
Cube	rounded or widely spaced bands 45°	rounded
Goss	two bands 40° -50°	rounded with direc. or one band 50° .
Copper	no data	two bands 35° -40°
Brass	no data	one or two bands 30° -50°
S	no data	one or two bands 30° -50°
$400°C\ 5s^{-1}$	$0.36\varepsilon_{vM}$	0.69 ε_{vM}
Cube	rounded	rounded
Goss	two bands 35° - 45°	two bands 35° -50°
Copper	no data	one band 45°
Brass	one band 40° -55°	one band 35° -45°
S	one band 30° -45°	on or two bands 30° -40° or. 50° -55°
$500°C\ 25s^{-1}$	$0.36\varepsilon_{vM}$	$0.69\varepsilon_{vM}$
Cube	rounded	rounded
Goss	widely spaced bands 35° -45°	rounded with directionality
Copper	one band 40° - 45°	one band 35° -45°
Brass	one or two bands 35° -50°	one or two bands 30° -40°
S	one band 40° - 45°	one or two bands 35° -50°
$500°C\ 5s^{-1}$	$0.36\varepsilon_{vM}$	0.69 ε_{vM}
Cube	rounded	rounded
Goss	rounded or one band 40°	rounded
Copper	one band 30° -35°	cells with directionality
Brass	irregular	rounded
S	no data	cells with directionality

Table 5.2: Microscopical characteristics of the samples examined

structures of the individual ideal orientations. The microstructure developed at a strain of 2.3 at 500°C and strain rate of $5s^{-1}$ displayed a microstructure which either was recovered or recrystallized. Quenching to RT of this particular sample was performed in 3 seconds.

The structures evolved during straining at 500°C at strain rates of $25s^{-1}$ all except the lowest strains, displayed undeformed nuclei, hence recrystallization has occurred. Quenching to RT of these samples were "rather slow" in that it was performed in 6 seconds. Unless quenching is performed within 2 seconds, static recrystallization is observed to occur under current deformation conditions (Verrnon-Parry et al., 1996). The reason for the large quenching time is unknown.

5.4 Discussion of the experimental matrix

Plane strain compressions of 99.5% pure aluminium at 350°C , 400°C and 500°C at a strain rate of $5s^{-1}$ and at 350°C and 500°C with a strain rate of $25s^{-1}$ were conducted. The textural evolution was characterized by an increase with strain in the strength of the rolling texture components, S, copper and brass, while the strength of Goss oriented grains was less clear. The strength of the individual rolling texture components changes with temperature, as S/copper texture decreased with increasing temperature, the brass texture was practically constant, while the Goss was irregular. The cube texture decreased with strain and increased with temperature.

The flow curves obtained during deformation displayed initial work-hardening followed by either a saturation stress or softening. At the lowest temperature work-hardening was the dominating process up to a strain of 1 or 0.85, while at the highest temperature it was only up to a strain of 0.35 or strain 0.45.

The microstructural evolutions were characterized as a cold-like deformation structure at low temperature consisting of one or two sets of bands inclined to LD or rounded structures in the original grains up to medium strains. At high strains, bands of subgrains/cells elongated in and parallel with LD evolved and the original grains were no longer visible. At the highest temperature and strain rate i. e. 500°C and a strain rate of $25s^{-1}$, the evolved microstructure up to medium strains still displayed, bands inclined to LD in the rolling texture components and the cube oriented grains had a more rounded microstructure. The scales of the microstructure were, how-

ever, larger compared to the low temperature deformed microstructure, and the boundary character different in that the grain boundaries had become clearly serrated and the bands within the individual grains were more wavy. The high strain structures were recrystallized.

The structure evolved after PSC at 500°C and $5s^{-1}$ at medium strain were nearly equiaxed in all grains, as commonly observed in hot deformation. Hence, it appears that the chosen experimental conditions span the entire range form cold deformation like structures to typical hot deformed microstructure.

The evolution of cube texture at the highest strain at 500°C , together with the EBSD-maps, leads to the conclusion, that the samples obtained at the highest strain at 500°C , are recrystallized. The deformation of these samples was also irregular in that the lubricant degraded, therefore no further conclusions seem to be reliable.

The evolution of microstructure does not seem to be directly connected to the flow stress in the sense, that the microstructure continues to evolve even though the flow curve has saturated. This is, for instance, seen at 500°C and $5s^{-1}$, where the work-hardening dominated regime terminates at a strain of 0.36, but the microstructure and texture continue to evolve.

A possible interpretation of flow curves obtained from polycrystalline metals, is that the flow stress is the result of all contributions from the individual grains deforming. If it is assumed that hot deformation is grain orientation dependent, the flow curve can be viewed upon as a sum of flow curves from the individual grains. In (Glez and Driver, 2003) single crystals of an Al-1wt%Mn alloy were plane strain compressed at conditions very similar to the ones used in the current study. In this article a significant difference is observed between flowcurves obtained of different orientations. The flow curves may reflect different contributions from the individual grains. Hence the interpretation of the flow curve might only reflect the average properties of the individual grains. The consequence of this is that even though the flow stress has saturated an equilibrium microstructure i.e. an equiaxed microstructure need not have been obtained in all orientations.

Similarly from the flow curves it is seen, that an increase in temperature leads to a lower transition stress and strain, where work-hardening is no longer the dominating process. Hence, the temperature effects in terms of recovery become more pronounced.

The change in microstructure with temperature and strain to a more equiaxed structure is followed by a textural evolutions, where deformation at 500°C leads to a stronger cube texture compared to the formation at 350°C and a decrease in the copper/S texture. In this comparison it has to be remembered however, that the microstructural characterization was only conducted at the center of the LD/ND plane, while the textural measurement was conducted on the entire plane.

From the EBSD measurements it is, however, not possible to determine any variation within the rolling components, as the bands observed are only the traces of the boundaries, and the technique has limited angular resolution (Winther et al., 2004a).

5.5 Conclusions of experimental matrix evaluation

From the evaluation of the experimental matrix the following can be concluded:

- The chosen deformation conditions ranging from lnZ=33 to lnZ=26 leads to structures which in terms of texture, flow stress and microstructural evolution as investigated by EBSD covers the region from the characteristics typically reported for cold to characteristics of hot deformation, respectively.

- The textures exhibit a gradual change in the investigated range with increasing Cube texture and decreasing Cu/S texture components with decreasing Z. The texture evolution with strain is smooth at each Z value, when excluding samples with recrystallization.

- The flow stress curves initially display work-hardening followed by either a saturation stress or softening. The work-hardening regime extends over a fairly large strain range (up to $\varepsilon_{vM} \sim 0.85$) for the highest Z value, while the lowest Z value only exhibits work-hardening up to $\varepsilon_{vM} \sim 0.35$.

- The dislocation structures as revealed by EBSD are typical cell block structures dominated by straight and parallel dislocation boundaries

up to $\varepsilon_{vM} \sim 0.7$ for all conditions, except the lowest Z value (lnZ=26, 500°C , $5s^{-1}$) where cell blocks are only clear at$\varepsilon_{vM} \sim 0.36$. At $\varepsilon_{vM} \sim 0.7$ for this low Z condition a more rounded structure is seen. The alignment of the cell block boundaries resembles that of cold deformation in the sense that they are inclined 30-55°C to LD. Indications of grain orientation dependent structures are seen, with the Cube orientation being more rounded than the other orientations already from the highest Z value and $\varepsilon_{vM} \sim 0.36$.

Based on this evaluation the following samples are selected for a more detailed investigation of the dislocation structure morphology and in particular the alignment of the dislocation boundaries by TEM:

350°C , $5s^{-1}$ (lnZ=31.7). The structures in this sample should resemble the typical cold deformation structures most and it was also observed to display differences for the Cube orientation. The investigation is concentrated on the low strain (ε_{vM}=0.11). The reason for this is partly to investigate a strain where the EBSD technique was insufficient to reveal the structures and partly to facilitate the analysis as dislocation boundaries in cold deformation are known to be straighter and easier to analyze than at higher strains. In addition a brief investigation is made at ε_{vM}=2.3.

500°C , $25s^{-1}$ (lnZ=27.5). This is the lowest Z value, which still exhibit clear structures with a directionality to LD. Comparison of the dislocation structure alignment at this value with that observed at 350°C , $5s^{-1}$ should therefore best reveal potential changes originating from the changing conditions. Investigations are conducted at ε_{vM}=0.11 for the reasons described above and also at ε_{vM}=0.36 as the dislocation structure at this Z value is expected to have lower misorientations and a higher strain therefore may be needed to observed a well-defined structure.

Note that these samples (with the exception of the brief investigation at ε_{vM}=2.3) are all within the work-hardening regime.

Chapter 6

TEM investigation

In this section, TEM characterizations of the 350°C - 5s^{-1} ε_{vM} = 0.11 and 500°C - 25s^{-1} ε_{vM}= 0.11 and 0.36 samples are presented. The aim was to characterize grains of ideal cube, Goss and brass, S or copper orientations and a few randomly oriented grains. The samples were characterized with respect to their structure/morphology, i.e. is it a cellblock structure, are there GNBs and are they inclined to LD and are the boundaries aligned with specific crystallographic planes.

Initially, however, a short discussion regarding the boundary plane determination is given, as this is important for interpretation of the findings in the TEM data analysis. This is followed by data representation, and the findings are thereafter correlated with the corresponding characteristics of cold deformation in an initial discussion regarding the possible orientation dependency of the microstructure. Finally, a discussion regarding the effect of strain and temperature is given.

In the micrographs, traces of relevant crystal planes are given, where the sign of the trace is as defined in figure 6.1. If orientation gradients were

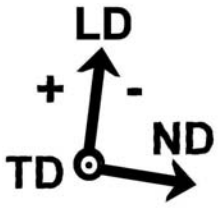

Figure 6.1: Definition of sign in the TEM micrographs

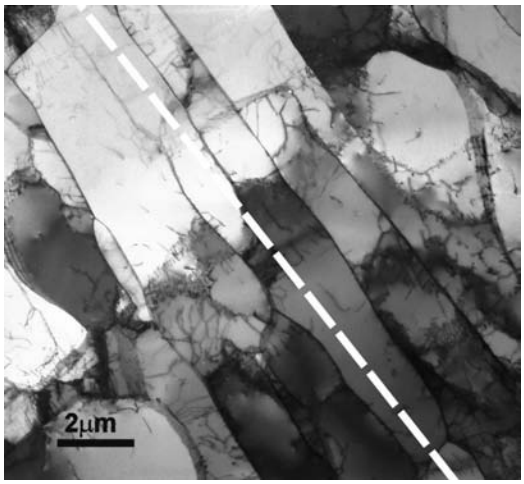

Figure 6.2: Characteristic structure of a boundary formed at 350°C $5s^{-1}$ at strain 0.11 in a grain oriented 26° from Goss. The beam direction is parallel to [112] and traces of a {111} plane is marked

observed in a grain, the orientations measured in the middle of the grain, are given as the grain orientation.

6.1 Crystallographic alignment of hot deformed boundaries

The boundary plane determinations presented in the following section were obtained with the same technique used to determine the crystallographic alignment of dislocation boundaries formed in cold deformed metals. Application of the technique to the current boundaries after hot deformation was not straightforward as described here.

The measurements were conducted by initially selecting boundaries, which displayed the general characteristics of the observed microstructure. They were thereafter tilted to determine the crystallographic plane, they were parallel with.

In the measurements conducted at 350°C , the morphology of the boundaries, varied somewhat. In some orientations extended probably highly misoriented almost parallel boundaries, where observed. An example is given in figure 6.2. In this nearly edge-on boundaries are general alignment with the

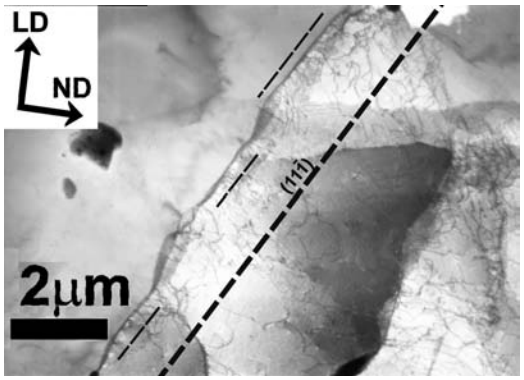

Figure 6.3: Characteristic structure of a boundary formed at 350°C $5s^{-1}$ at strain 0.11 in a brass oriented grain. The beam direction is parallel to [112]

trace of the {111} plane and the alignment with the crystallographic plane on this scale is therefore clear. On a smaller scale the precise boundary plane determination in some orientation found, that the crystallographic plane to which the boundary was aligned deviated from the plane determined in the trace analysis. An illustration of a boundary of were the plane was determined is given in figure 6.3.

The boundary follows the trace of the $(11\bar{1})$ plane, but the individual boundary segments deviates slightly from the trace. In this boundary, the nearly edge-on straight segment of the boundary at the top is aligned with the trace of the $(11\bar{1})$ plane, and the same applies to the middle and bottom part of the boundary, while segments between, are aligned with other planes. A boundary observed in the same alloy cold rolled 10% is displayed in figure 6.4 A, while a scaled version of figure 6.3 is displayed in figure 6.4 B. In both micrographs are arrows, which marks the connections between two segments. From the figure, it appears as if the boundaries formed during cold rolling are straighter, and have shorter intersections compared to the hot formed boundary, but otherwise they are very similar.

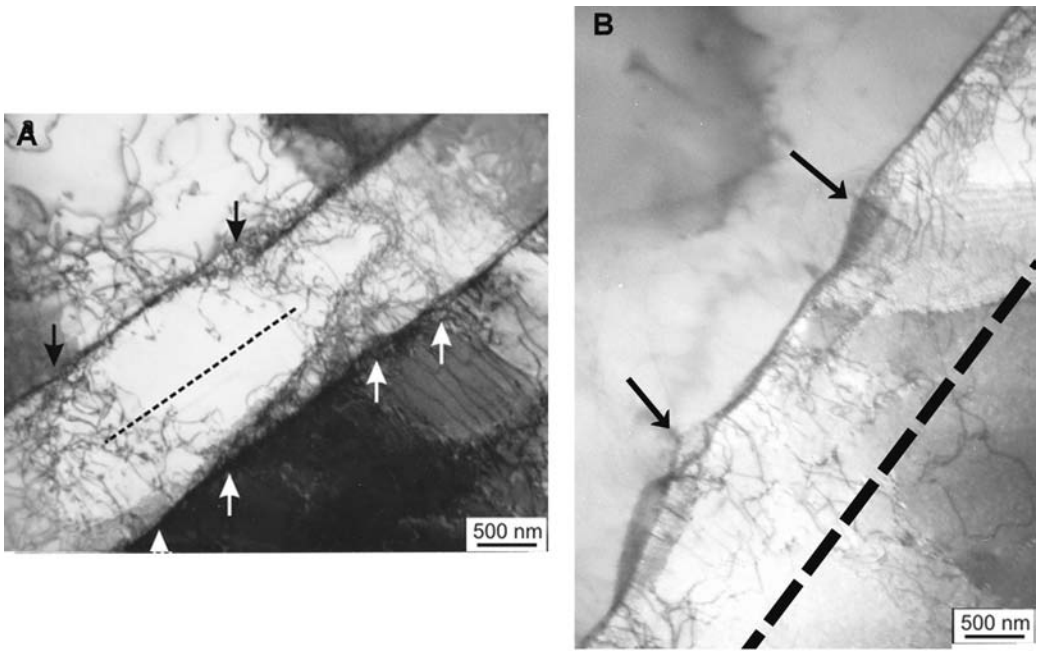

Figure 6.4: 99.5% pure al cold rolled 10% in A. B 99.5% pure al PSC 10% at 350°C . The punched lines mark the trace of a {111} plane. A is from (Huang and Winther, 2007)

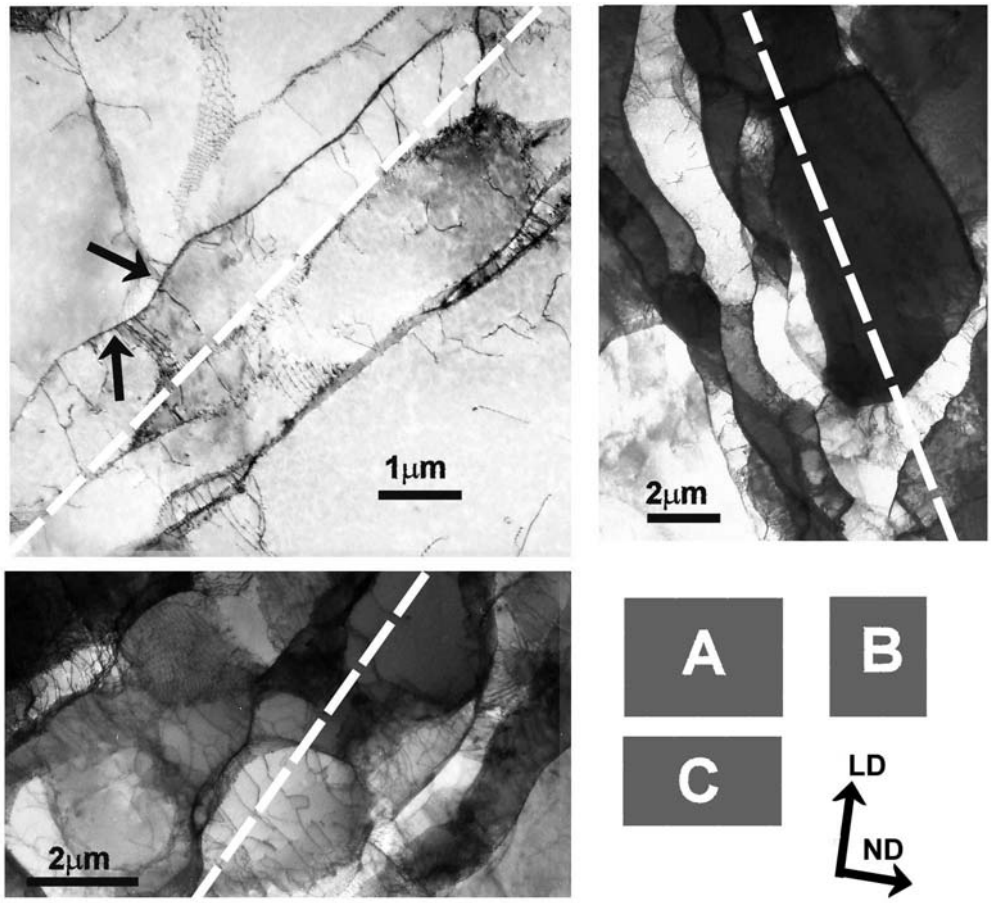

Figure 6.5: Wavy boundaries formed after PSC at 350°C $5s^{-1}$ strained 0.11. A and B are from a Goss oriented grain, C from a brass oriented grain. Traces of {111} planes are marked on the micrographs. The beam direction is parallel to [112] in A and C and parallel to [011] in B.

In other parts, boundaries of more "wavy "character was seen to evolve as illustrated in figure 6.5. In the micrograph A, a boundary nearly edge-on is seen. The boundary follows the trace of {111} over all, but some of the individual segments - marked with arrows, deviates from the trace. On a larger scale in figure 6.5 B and C are the "wavy" boundaries displayed. In this also the general alignment with the marked {111} traces are seen, but appearance of the boundaries being "wavy" boundaries are very clear.

This "wavy" boundary character, leads to findings of boundaries or segments of boundaries being aligned with different crystallographic plane, whit in one orientation and in some regions, whit in one boundary. In such cases, the most common plane observed in the characterization is given followed by the less frequent ones found.

The boundary plane determinations conducted at 500°C , determine the plane of the boundaries which displayed a alignment to LD. As some of the structure were more or less equiaxed, the boundaries characterized, where only those associated with the alignment to LD. Hence, boundaries aligned with other planes might also be present, but were not measured. Therefore, the planes given in the measurements conducted at 500°C , is representative for the overall developed structure.

6.2 350°C $5s^{-1}$ strained 0.11

In the following, the TEM characterizations of cube, near cube, near S, Goss, brass and three grains of other orientations are presented from a specimen strained to 0.11 at 350°C at a strain rate of $5s^{-1}$. The structure developed after straining at these process conditions, can in most cases be described as a cell block structure delineated by GNBs. The details for the specific orientations are given in the following.

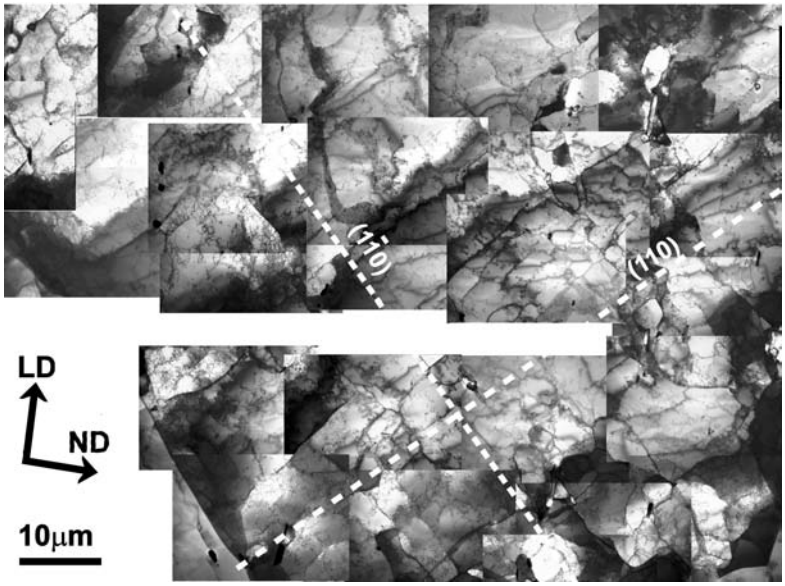

Figure 6.6: Grain oriented 8° from ideal cube orientation (-1.0 -0.03 -0.03)[-0.03 0.99 0.15]. The beam direction is parallel to [001], and traces of $(1\bar{1}0)$ and (110) planes are marked. PSC, 350°C 5s^{-1} ε_{vM}=0.11.

Cube orientation

A grain oriented 8° form the ideal cube orientation is displayed in figure 6.6. The morphology of the grain consists of cells in most regions while a few GNBs are observed mainly in the middle of the grain. Two sets of GNBs are seen inclined $\sim$ 40° and $\sim$ -50° to LD. The set inclined -50° is the clearest. The traces of the $(1\bar{1}0)$ and (110) planes are also marked in figure 6.6. The traces are inclined 43° and -47° to LD, and thereby nearly parallel with the GNBs. Boundary plane alignments were determined by tilting of 12 boundaries, and it was found, that the boundaries were aligned with the 110 $(1\bar{1}0)$ planes, but also 230 $(2\bar{3}0)$ and 120 $(1\bar{2}0)$ planes were observed.

The area dominated by cells in the cube grain are displayed in the left micrograph of figure 6.7, while a region with the dominating sets of GNBs is displayed in the micrograph to the right. The GNBs are aligned with the trace of (110), where some of the GNBs are well developed, while others are less well developed.

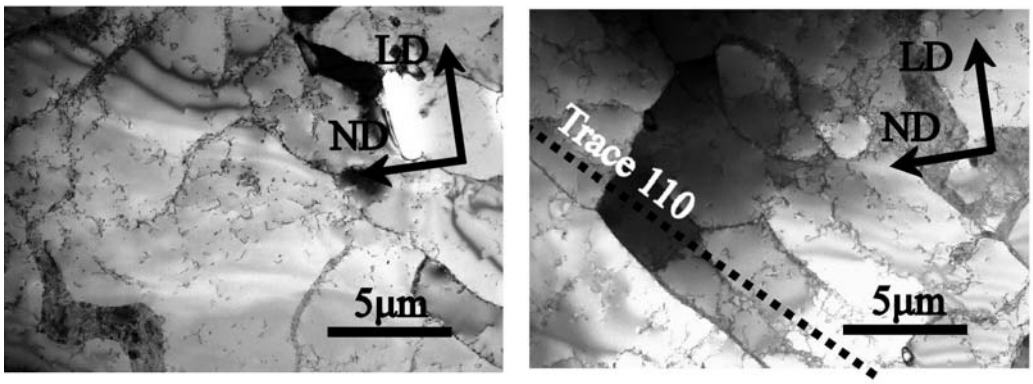

Figure 6.7: Morphology of cube grain. Left cells. Right more or less developed GNBs parallel to the trace of the (110) plane. Both micrographs were obtained with the beam direction parallel to [001] PSC, 350°C $5s^{-1}$ ε_{vM}=0.11.

Near cube orientations

In figure 6.8 is a grain oriented 15° from the ideal cube orientation. The morphology of the grain consists of a cell block structure delineated by curved GNBs inclined 40° to 45° to LD. The GNBs are roughly one cell wide, and viewed practically edge-on. The misorientation of a few random segments were found to be up to 7° and the density of dislocations in many of the cells appears to be very low. Three boundaries were characterized with respect to their crystal plane alignments. In general the boundaries were parallel with the $(1\bar{2}0)$ plane, while segments were found also to be aligned with $(1\bar{3}0)$ and $(1\bar{1}0)$ planes. The trace of the $(1\bar{1}0)$ plane is marked on the micrographs and from this it can be seen, that the GNBs are curved and not well aligned with the trace. This might be an effect of the boundary seen in the top of the micrographs.

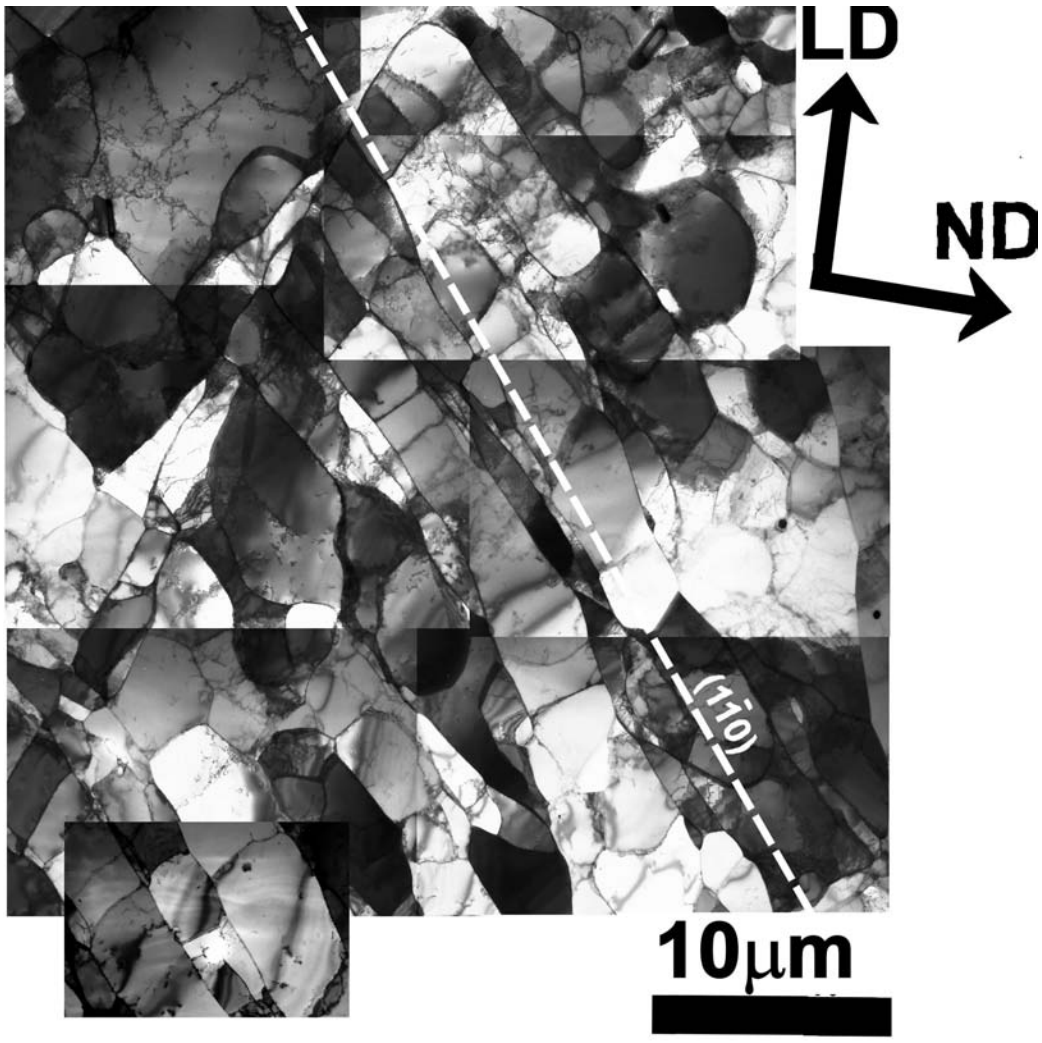

Figure 6.8: Grain oriented 15° form the ideal cube orientation (-0.25 -0.97 0.002)[-0.96 0.25 -0.01]. The beam direction is parallel to [001], PSC, 350°C $5s^{-1}$ ε_{vM}=0.11.

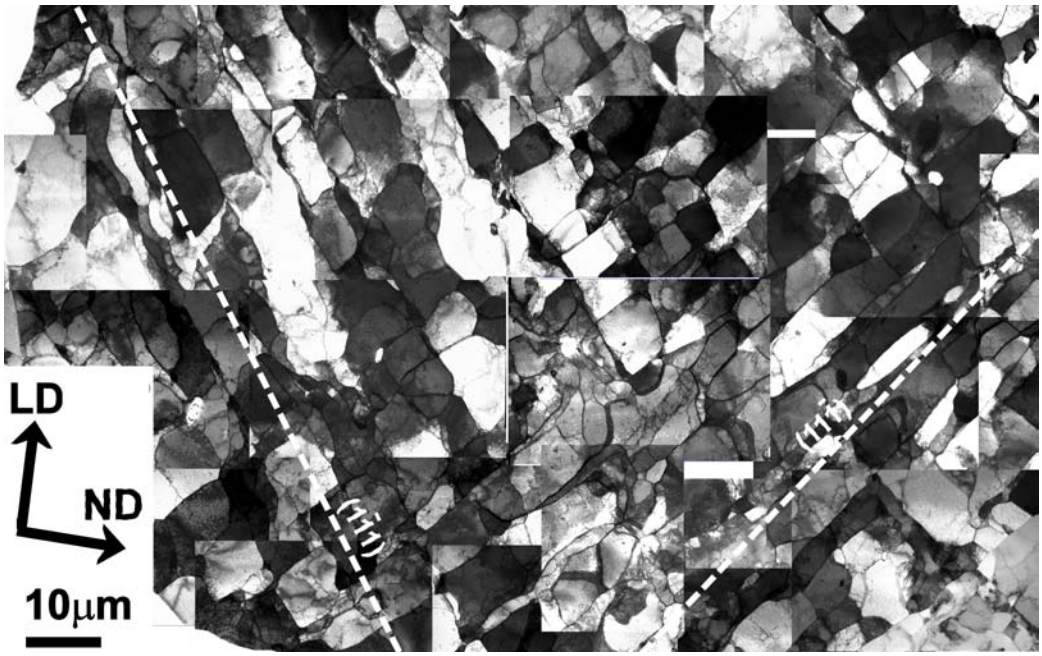

Figure 6.9: Grain oriented 12° from ideal Goss (0.98 -0.14 -0.16)[0.007 -0.73 0.68]. The Beam direction is parallel to [011]. PSC, 350°C 5s^{-1} ε_{vM}=0.11.

Goss orientation

In the micrographs of figure 6.9, a grain oriented 12° from the ideal Goss orientation is displayed. The grain morphology consists of two sets of GNBs inclined 35° - 45° and -30° to -40° to LD, one in each side of the grain. The GNBs intersect in the middle of the grain, creating a morphology consisting of two sets of GNBs. The GNBs in the right part of the grain are straight and closer to the ideal Goss orientation, compared to the GNBs in the left part which are more wavy. The GNBs were overall aligned with the trace of the $(1\bar{1}1)$ and $(11\bar{1})$ inclined 35° and -35° to LD. The orientation spread is 4° across the grain

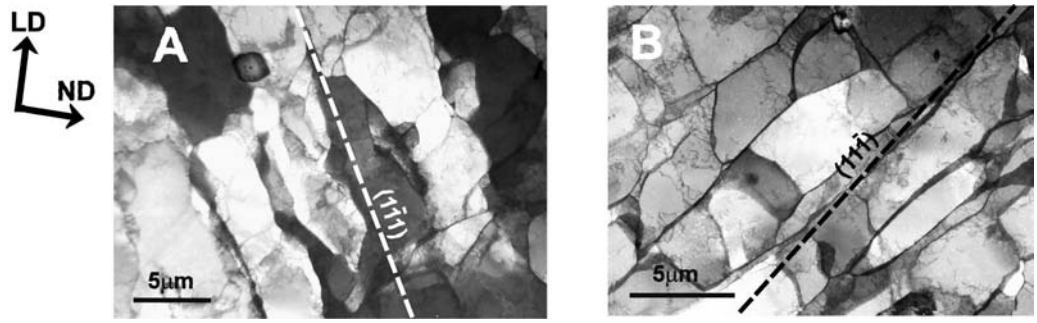

Figure 6.10: Grain oriented 12° from the ideal Goss orientation. A, area of wavy bands, B area of straight bands. The beam direction is parallel to [011]. PSC, 350°C 5s^{-1} ε_{vM}=0.11.

The three morphologies observed in the grain is illustrated in the micrographs in figure 6.10 and figure 6.11. Trace analysis of the wavy boundaries showed that they were overall aligned with the (1$\bar{1}$1) plane as also marked in the figures 6.9 and 6.10 A. The precise boundary plane alignment determined by tilting, showed boundaries to be aligned with the (1$\bar{1}$1) plane. Few segments were found to be aligned with the planes (01$\bar{1}$) and (1$\bar{3}$3). Due to the wavyness of the boundaries, it was very difficult to determine the boundary planes.

The other part of the Goss grain with the more straight boundary as illustrated in figure 6.10 B, are aligned with the (11$\bar{1}$) planes in the trace analysis. This is confirmed by the boundary plane analysis, where the boundaries are found in general to be parallel with the (11$\bar{1}$).

In the middle region where the two sets of GNBs meet, the boundaries are generally aligned with the traces of (11$\bar{1}$) and (1$\bar{1}$1) as illustrated in figure 6.10 B. The exact alignment of the boundaries were generally (1$\bar{1}$1) in one direction, where two boundary segments were parallel with the (3$\bar{3}$1) plane. The other set of boundaries were aligned with (11$\bar{1}$).

A total of 22 boundary plane measurements were conducted in this grain.

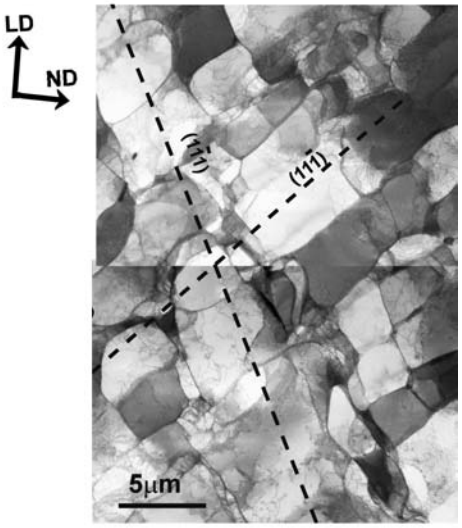

Figure 6.11: Grain oriented 12° from the ideal Goss orientation. The centre of the grain, where the two sets of GNBs intersect. Notice with this beam direction only the $(1\bar{1}1)$ boundaries are edge on. The beam direction is parallel to [121]. PSC, 350°C $5s^{-1}$ ε_{vM}=0.11.

Brass orientation

Two grains within the ideal brass orientation were characterized.

The first grain oriented 14° from ideal brass is displayed in figure 6.12, where a large montage of the grain is displayed and in figure 6.13 where the characteristic structures of the brass grain are displayed in detail. The orientation spread within the grain is 4° . From the montage of the grain it can be seen, that the microstructure can be divided into regions. In the right part, a microstructure consisting of a cell block divided by two set of GNBs are observed. In the left part, one dominating sets of GNBs only one cell wide is aligned with the trace of $(1\bar{1}1)$. The trace is inclined 31° to LD. In the region with one dominating set of GNBs widely spaced row of cells or microbands are observed.

The structure of the region with two sets of GNBs are displayed in detail in figure 6.13 A. In this, the alignment of the GNBs with the trace of $(1\bar{1}1)$ is clear, and the GNBs alignment is overall aligned with the trace of the $(11\bar{1})$ plane. The structure of the boundaries are rather wavy, which makes the alignment determination less clear. The structure of the region, with one

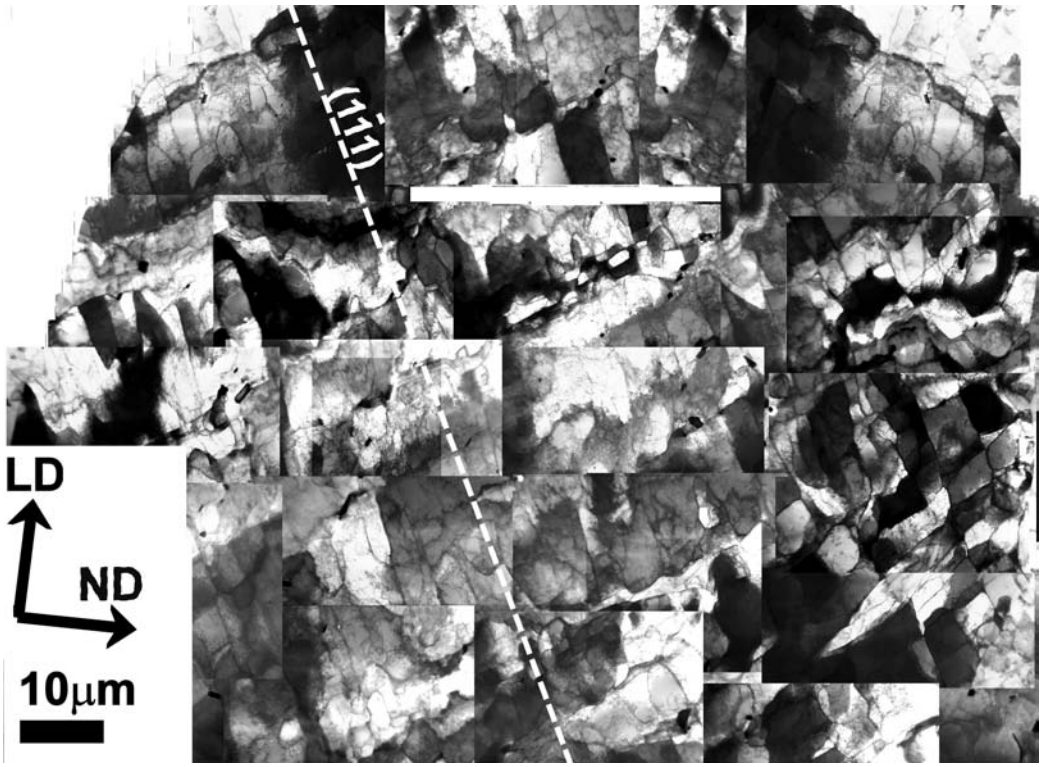

Figure 6.12: Montage of brass grain oriented 14° from ideal brass (0.93 -0.22 -0.29)[0.04 -0.74 0.68]. The beam direction is parallel to [121]. PSC, 350°C $5s^{-1}$ ε_{vM}=0.11.

dominating sets of GNBs is displayed in figure 6.13 B. In this micrograph, GNBs are very well aligned with the trace of (1$\bar{1}$1). Some of the GNBs are not well developed, and there appear to be a high dislocation density in the structure. No quantitative determination of the dislocation density was, however, performed. Boundary plane alignment were only conducted on the clearest set of boundaries. Two measurements determined the boundaries to be aligned with (1$\bar{1}$1).

The part of the structure, displaying microbands or cells is displayed in figure 6.13 C, which show cells which overall are aligned with the (10$\bar{1}$) plane.

The boundaries in the brass grain are inclined 25° - 35° and -30° - -35° to LD.

The morphology of the second brass grain, displayed a significant effect of the neighbouring grains, therefore only the centre of the grain displayed

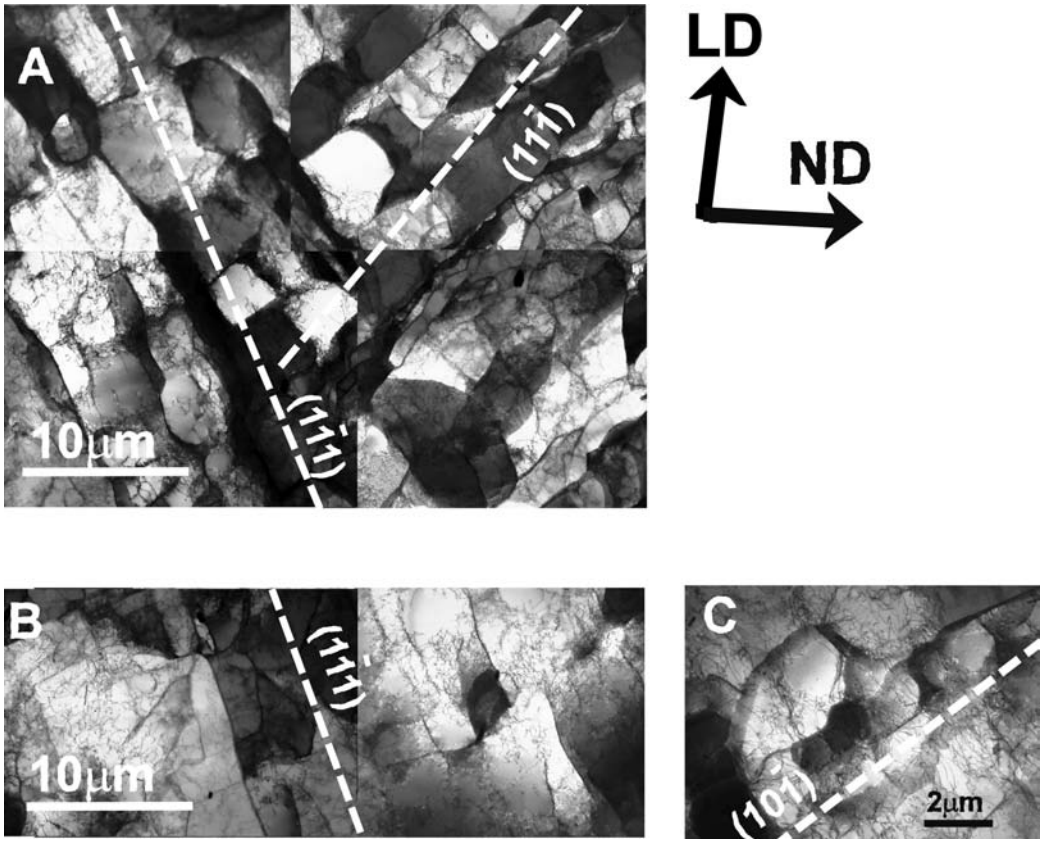

Figure 6.13: Micrographs of the three different morphologies observed in a grain oriented 14° from ideal brass. PSC, 350°C 5s^{-1} ε_{vM}=0.11. A 2 sets of GNBs, in this the beam direction is parallel to [011]. B one set of GNBs, in this the beam direction is parallel to [121]. C row of cells, in this the beam direction is parallel to [121].

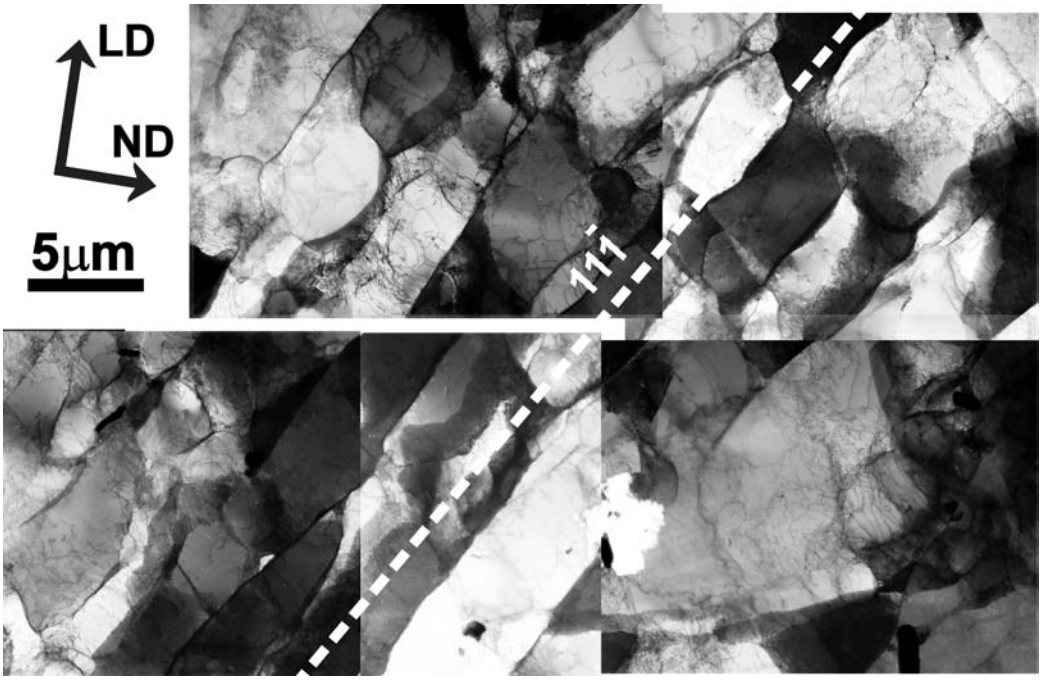

Figure 6.14: Grain oriented 11° from ideal brass (-0.89 0.37 0.27)[0.11 0.75 -0.65]. The beam direction is parallel to [112]. PSC, 350°C 5s^{-1} ε_{vM}=0.11.

a regular structure. The morphology consists of a cell block structure delineated by wavy GNBs one cell wide as seen in figure 6.14. The grain is oriented 11° from the ideal brass orientation and the GNBs are inclined -25° to -35° to LD. The orientation spread within the grain is 3° . Trace analysis finds an alignment of the boundaries with the trace of the $(11\bar{1})$ plane. The same alignment is also found in three boundary plane determinations of the edge-on parts of the boundary segments. Due to the wavyness of the boundaries, it is however, difficult to obtain large edge on boundaries segments and thereby accurate determinations of the boundary planes.

Near S orientation

A grain 18° from the ideal S orientation is displayed in figure 6.15. The morphology of the grain consists mainly of GNBs inclined -35° to -40° to LD, apart from in the centre part of the grain, where randomly oriented cells are seen (marked with an arrow). The cells might be a part of a second band traversing the GNBs. If the cells are characterized as a band, the band is less than 10° from the trace of the $(1\bar{1}0)$ plane. Many of GNBs are nearly

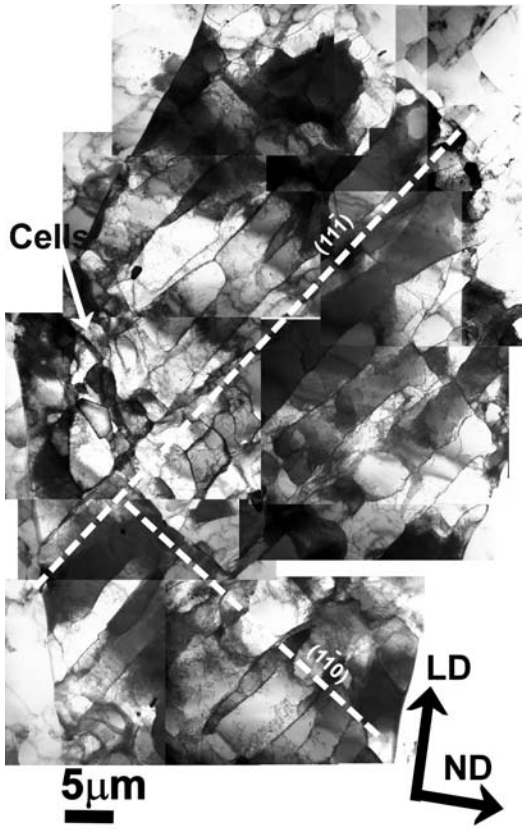

Figure 6.15: Grain oriented 18° from ideal S (-0.93 0.21 0.30)[0.05 0.88 -0.48]. The beam direction is parallel to [112]. PSC, 350°C 5s^{-1} ε_{vM}=0.11.

edge-on and parallel with the trace of the $(11\bar{1})$ plane. The trace of $(11\bar{1})$ is inclined -36° to LD as also shown in figure 6.15.

Other orientation

A grain oriented 22° from the ideal brass orientation is displayed in figure 6.16. In the montage of micrographs the entire grain is seen. The morphology consists of well developed GNBs in the lower part of the grain, and GNBs just starting to form in the upper part. The GNBs is inclined -40° to -45° to LD and are traversed by a microband in the centre of the grain which is inclined 45° - 50° to LD. In the region of less developed GNBs a fairly high density of dislocations is seen. The morphology of the grain appears not to be affected by the grain boundary on the top left and right sides, while in the lower left there is an area, consisting of randomly oriented cells.

Figure 6.16: Grain oriented 22° from ideal brass (-0.91 0.11 0.40)[-0.01 0.89 -0.44]. The beam direction is parallel to $[11\bar{2}]$. PSC, 350°C 5s^{-1} ε_{vM}=0.11.

The GNBs are viewed edge on, as the boundaries are very narrow and sharp. The trace of the (111) is marked on the micrographs. The trace is inclined -47° to LD and are parallel to the GNBs. An alignment of the GNBs with the (111) planes is also observed in 2 boundary plane determinations.

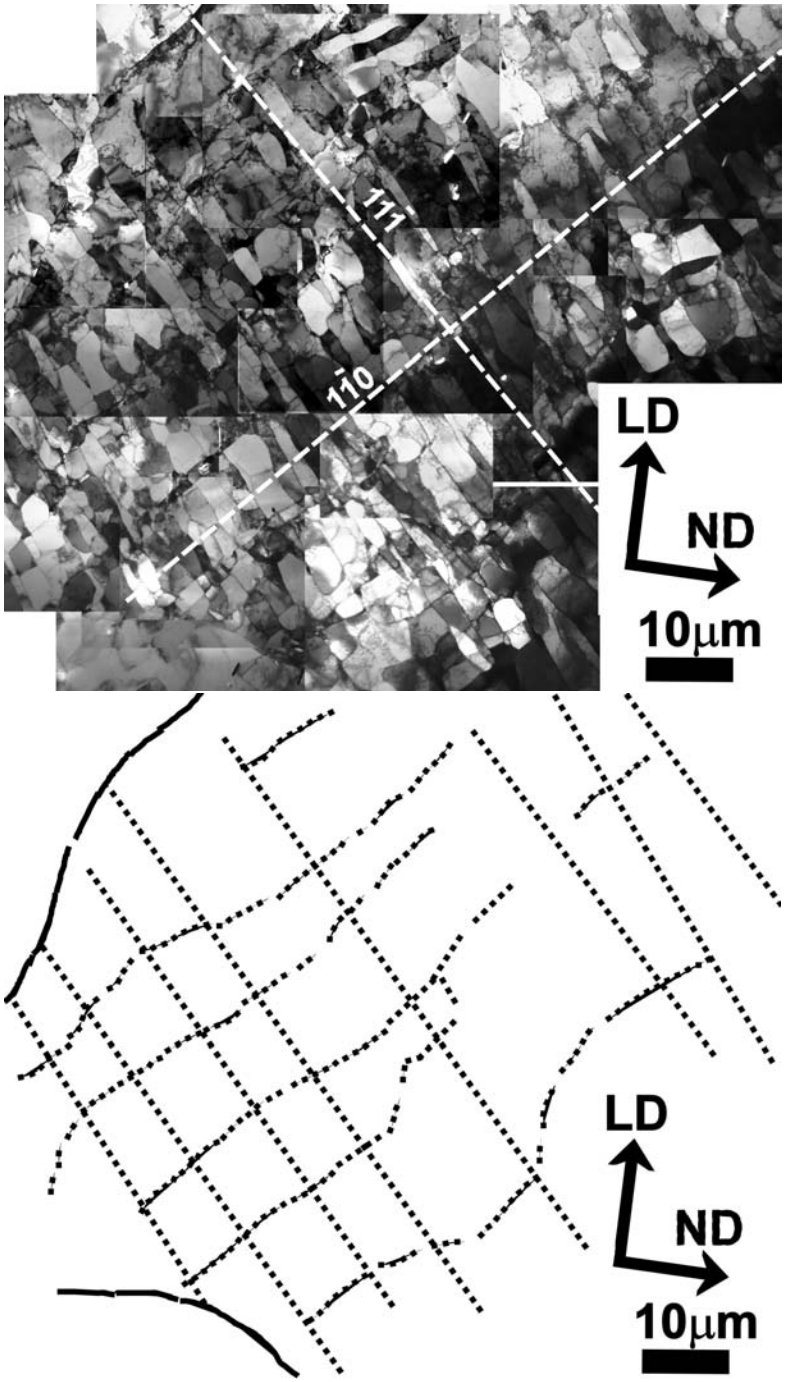

Figure 6.17: Orientation (0.003 0.92 -0.39)[0.88 -0.19 0.44]. The beam direction is parallel to [112], and traces of the $(11\bar{1})$ and $(1\bar{1}0)$ planes are marked. PSC, 350°C $5s^{-1}$ ε_{vM}=0.11.

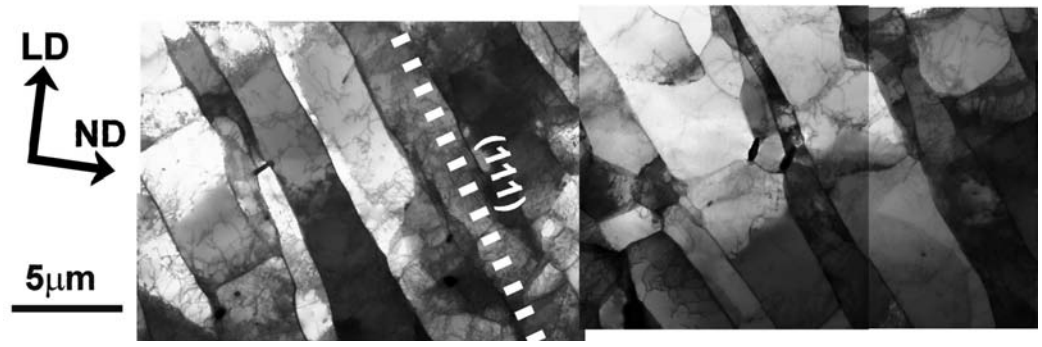

Figure 6.18: Grain oriented 27° from ideal S (-0.07 0.89 0.45)[0.96 -0.07 -0.27]. The beam direction is parallel to $[112\bar{1}]$. PSC, 350°C 5s^{-1} ε_{vM}=0.11.

Grain with microband - other orientation

In figure 6.17 the upper part of a grain oriented 26° between Goss and brass is displayed. The structure of the grain is homogenous, in that there is no observed effect of the grain boundaries. The morphology of the grain consists of cell blocks delineated by 2 sets of GNBs. One set is straight GNBs 1 cell wide and inclined 40° to 45° to LD. The other set is a widely spaced pair of boundaries or a microband, which are perpendicular to the other set of GNBs. The pair of boundaries are about 1 to 2 cells wide, and they are illustrated in the sketch of the micrographs, displayed below figure 6.17.

The boundary pair are more irregular, in that they bend through the grain. Boundary plane determination of the boundary pairs found a general alignment between the $(1\bar{1}0)$ and $(1\bar{3}1)$ planes possible the $(3\bar{5}1)$. The other set of GNBs were parallel to the traces of the$(11\bar{1})$ planes in the trace analysis, while boundary plane determination of five boundaries determined the boundaries to be aligned with the $(11\bar{1})$ plane.

Other orientation

A second grain is oriented 27° from the ideal S orientation. Micrographs of it are displayed in figure 6.18. The morphology consists of parallel GNBs nearly edge-on inclined 35° to 40° to LD. The GNBs are thereby roughly aligned with the trace of the (111) plane, which is inclined 32° to LD. Between the GNBs dislocations are clearly is seen.

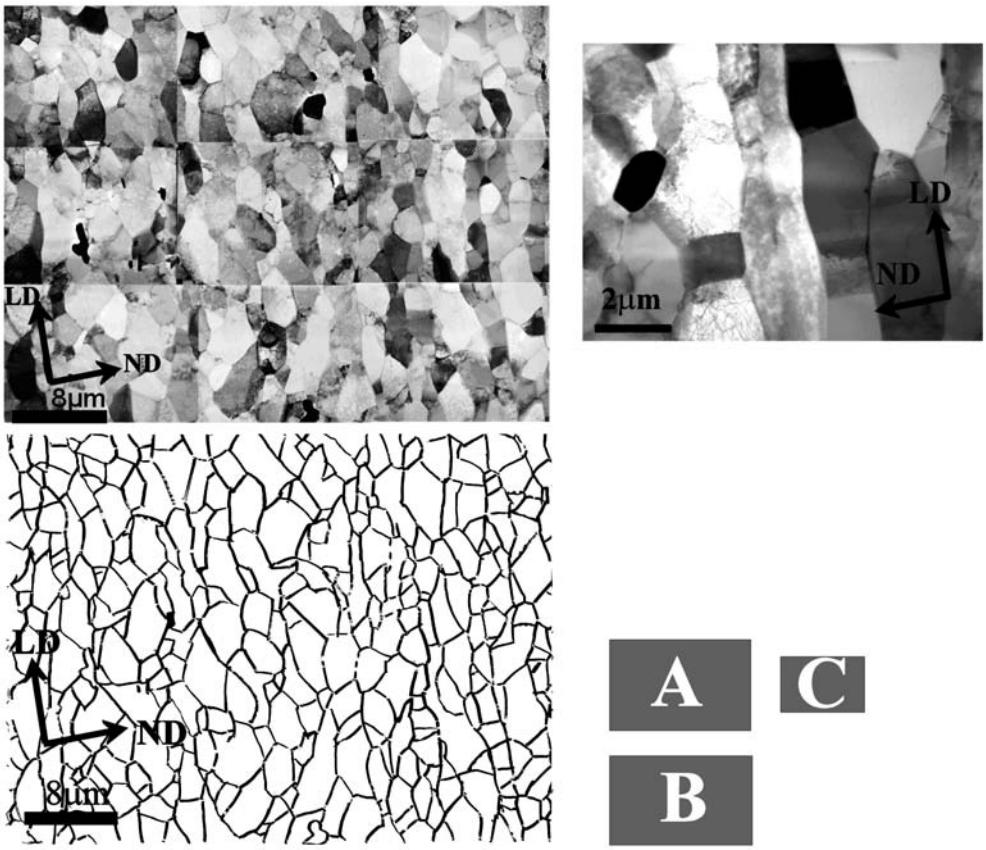

Figure 6.19: Sample PSC at 350°C $5s^{-1}$ strained 2.3 Bright field no tilt. A montage of the sample. B high magnification micrograph of A. C Tracing of montage in A.

6.3 350°C $5s^{-1}$ strained 2.3

A montage of the high strain structure was also obtained in the TEM, and it is displayed in figure 6.19 together with a sketch and a high magnification micrograph. In the montage bands of cells/subgrains are seen to be aligned with LD with an aspect ratio of 1.5 i.e. the cells/subgrains are elongated along LD. The elongated cells are very rectangular in some parts, and more equiaxed in other areas as illustrated in figure 6.19.

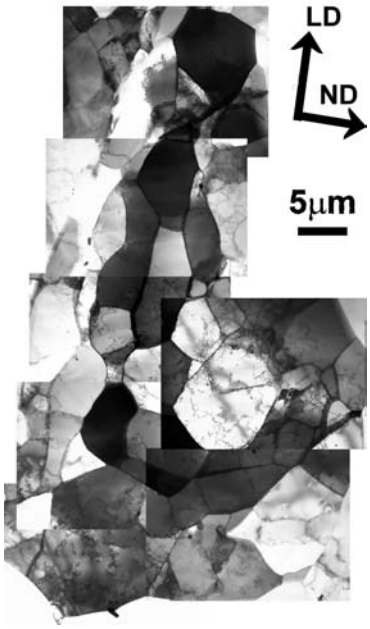

Figure 6.20: Grain oriented 9° from the ideal cube (-0.99 0.12 -0.10)[0.12 0.99 0.04]. The beam direction is parallel to [100]. PSC, 500°C 25s^{-1} ε_{vM}=0.11.

6.4 500°C 25s^{-1} strained 0.11 or 0.36

In the following the TEM characterizations of cube, brass, near S and two grains of other orientations are presented from a specimen strained to 0.11 or 0.36 at 500°C at a strain rate of 25s^{-1} . The structure developed after straining at these process conditions, can in most cases be described as a cell block structure delineated by GNBs or as an equiaxed structure. The details for the specific orientations are given in the following.

Cube strained 0.11

A grain oriented 9° from cube is displayed in figure 6.20. In this orientation, an equiaxed cell structure has evolved, where some of the cells are slightly aligned with LD. In some of the cells an internal dislocation structure is observed, as if small equiaxed cells are starting to form. In other cells the dislocation content is nearly zero. No boundary plane determination was performed in this grain.

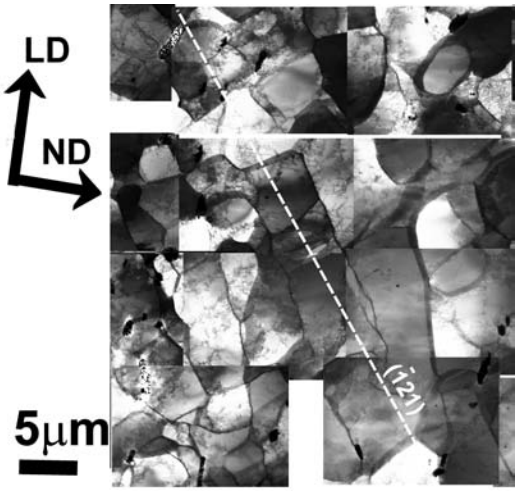

Figure 6.21: Grain oriented 12° from the ideal brass (0.89 -0.37 -0.25)[-0.02 -0.59 0.81]. The beam direction is parallel to [101]. PSC, 500°C 25s^{-1} ε_{vM}=0.11.

Brass strained 0.11

A grain oriented 12° from brass is displayed in figure 6.21 together with the trace of the $(\bar{1}21)$ plane. In this, a structure of cells and GNBs inclined roughly 30° to LD are seen. The edge-on boundaries are roughly aligned with the trace of the $(\bar{1}21)$ plane. Boundary plane analysis of the structure, also determined 3 boundary segments to be aligned with either the $(\bar{1}21)$ or the $(\bar{1}22)$ planes.

Other orientation strained 0.11

The structure of a grain oriented 23° from the ideal cube, is displayed in figure 6.22. The microstructure consists of GNBs enclosing elongated cells inclined $\sim$ 20° to LD. Boundary planes positively inclined to LD were found to be aligned with the $(3\bar{5}1)$ or $(\bar{3}51)$ planes, while boundaries inclined negatively to LD were parallel with the (530) or $(\bar{7}\bar{3}5)$ planes.

Other orientation strain 0.11

In figure 6.23, a grain oriented 25° from the ideal Goss orientation is displayed. In this, a cellblock structure is seen, which in some regions is delineated by GNBs and in others more random cells are seen. The GNBs are inclined -50° and 45° to LD. Trace analysis found no alignment with {111} planes.

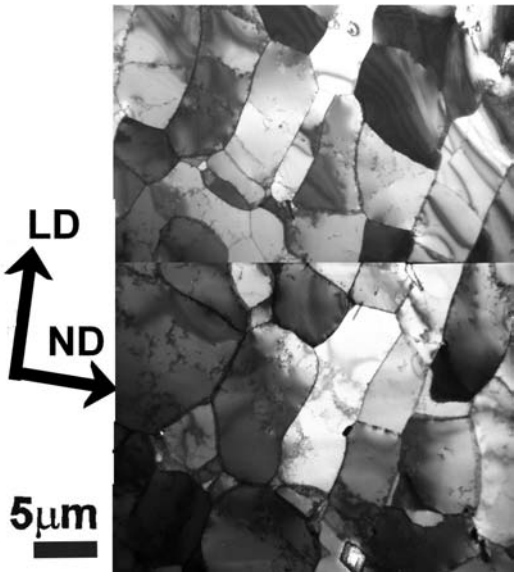

Figure 6.22: Grain oriented 23° from the ideal cube (0.92 -0.32 -0.24)[-0.31 -0.95 0.09]. The beam direction is parallel to [112]. PSC, 500°C $25s^{-1}$ ε_{vM}=0.11.

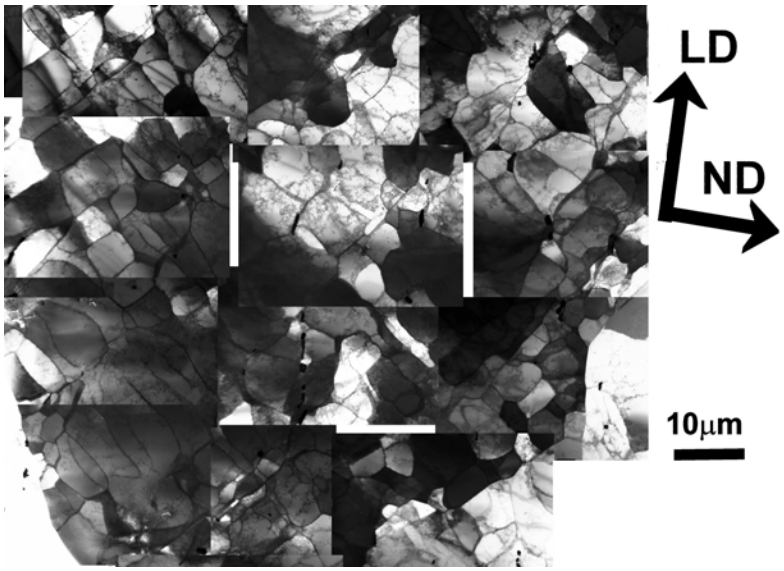

Figure 6.23: Grain oriented 27° from the ideal Goss (0.89 0.46 -0.08)[0.37 0.59-0.72]. The beam direction is parallel to [101]. PSC, 500°C $25s^{-1}$ ε_{vM}=0.11.

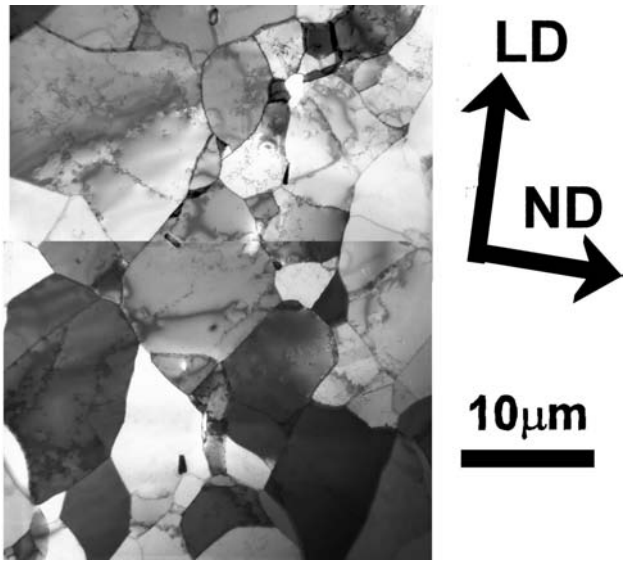

Figure 6.24: Grain oriented 10° from the ideal cube (-1.0 0.02 -0.02)[0.02 0.98 -0.18]. The beam direction is parallel to [001]. PSC, 500°C 25s^{-1} ε_{vM}=0.36.

Cube strained 0.36

The morphology of a grain oriented 10 ° from cube is displayed in figure 6.24, in which a recovered nearly equiaxed structure is seen. Tilting experiments determined some of the segments in the equiaxed structure to be parallel with the (531) crystal plane.

Near S strained 0.36

In figure 6.25, a grain oriented 17° from S is displayed. The structure consists of a cell block structure with a clear set of GNBs inclined 35° to LD traversing the structure. Trace analysis finds a general alignment of the boundaries with the (111) planes, which was also confirmed in tilting experiments.

6.5 Discussion: Grain orientation dependence

Initial discussion regarding grain orientation dependency is based on the data obtained at 350°C , as this is the data set explored most thoroughly. The data set obtained at 500°C is discussed in the following section regarding temperature effects.

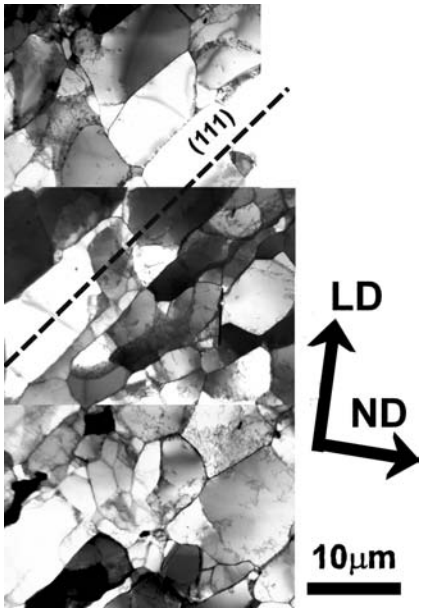

Figure 6.25: Grain oriented 17° from the ideal S (-0.92 0.30 0.25)[0.14 0.86 -0.48]. The beam direction is parallel to $[11\bar{2}]$. PSC, 500°C 25s^{-1} ε_{vM}=0.36.

6.5.1 Morphology - general

In the TEM results presented above, it is seen that the deformation structure developed during deformation at 350°C at 5s^{-1} to a strain of 0.11 in general can be characterized as a cell block structure delineated by one or two sets of GNBs. The morphology of the structures developed varies significantly between the characterized grains. In figure 6.6, cells were mainly observed and a few GNBs partly formed while the grain displayed in figure 6.8 showed clear curved GNBs in areas with high misorientations enclosing nearly bamboo like IDBs. Similarly the grain in figure 6.16 showed a morphology of a not well developed structure with GNBs of low misorientations, while the structure in figure 6.17, displayed more contrast, and thereby higher misorientations. The different morphologies were all found in grains of different orientation.

In general, the grains can be divided into three groups, one group of grains with a clear morphology with a high enough misorientation for clear boundaries to have been formed. This group contains the Goss, near S, near cube and a grain of other orientations, displayed in figures 6.8, 6.9, 6.17 and 6.15. The other group consists of the brass grains and a grain of other orientation shown in figures 6.12 and 6.16. This group displays a morphology character-

ized by well developed GNBs in some areas, and GNBs less developed. The last group is the cube grain (figure 6.6), which displayed a different morphology compared to any of the others in that the cell block structure only in some areas was delineated by GNBs, while only cells were observed in other regions.

The findings are summarized in table 6.1 together with the findings of the EBSD/CC study.

Validity of the TEM measurements

In many of the investigated grains, for instance in figure 6.17, whole montages of the grains were obtained, hence the morphology characterized and the structures observed could be selected such that they were representative of the entire grain, and not just a local phenomena. From the mapping of the entire grains, it was furthermore observed, that the microstructure observed in many of the grains, displayed nearly no effect of the grain boundaries, as the morphology of the individual grains ranged from grain boundary to grain boundary. Grain boundary effects were, however, also observed, as mentioned in the description of figure 6.14 and figure 6.8. The observations are similar to observations by (Randle et al., 1996), where nearly no effect on the microstructures from the grain boundaries were found in 5% cold rolled aluminium only around triple junctions. At higher strains the effects of the grain boundaries on the microstructure of the grains were found to be higher.

Even though the statistics in the TEM study is poor, the findings are in good agreement with the EBSD/CC study as seen in table 6.1. Hence, it is still possible to draw some conclusions regarding the orientation dependency of the microstructure.

350°C $5s^{-1}$	TEM 0.11 ε_{vM}	EBSD/CC 0.11 or. 0.36 ε_{vM}
Cube	mainly cells	rounded (EBSD) or widely spaced bands (EBSD)
Goss	two bands	rounded (CC) or two bands (EBSD)
Copper, brass, S	one or two bands	two bands (CC)

Table 6.1: Overview of the morphological findings in the microscopical characterization of the samples PSC at 350°C and $5s^{-1}$

6.5.2 Morphology - cube orientation

The most significant difference in structure between the grains examined, were the cell structure observed in the cube oriented grain. This was also observed in the EBSD/CC measurements, clearest seen at the higher strains - see table 6.1 and table 5.2.

Cell formation has also been observed in single crystal experiments of cold rolled cube oriented aluminium crystals (Liu and Hansen, 1998). In this study, the cell structures were seen to evolve in part of the crystal and maintain the original orientation during deformation.

The evolution of a cell structure in cube oriented grains, is also observed in cold rolled copper (Huang and Winther, 2007), where it has been shown to be due to the grain orientation dependency of the dislocation structure (Huang and Winther, 2007) (Winther and Huang, 2007). Hence, the different morphology of the cube oriented grain compared to the grains oriented along one of the rolling texture components indicates, that a similar orientation dependency applies at 350°C .

Cube grains with cell structures have, however, not been observed in aluminium cold rolled. This can be due to the cube orientation being metastable, i.e. unless the grain is oriented ideally, the grain will break-up and rotate away during deformation (Driver et al., 1996). Furthermore, hot deformation experiments of single crystal of Al-1% Mn have shown, that the cube orientation is stable at temperatures above 300°C (Maurice and Driver, 1993), this may therefore be the reason for the lack of observation of cube-grains at room temperature compared to the current study.

The cube orientation has also received special attention in recrystallization studies, due to the fact, that recrystallization textures of deformed aluminium are dominated by the cube orientation. It has also been shown, that recovery occurs rapidly in the cube orientation compared to other orientations (Bolingbroke et al., 1996).

The enhanced rate of recovery in cube oriented grains, compared to other orientations, might be the reason for the general observation, that the microstructure of the cube oriented hot deformed grains, are coarser than grains of other orientations (Bardal et al., 1995), (Humphreys and Bate, 2007) as also visual observed in the EBSD/CC study in the current thesis. This might, however, be due to the processing. Even though great care is taken

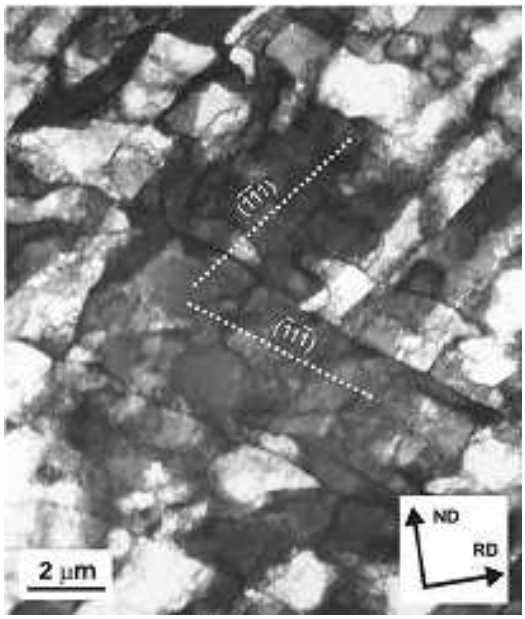

Figure 6.26: Polycrystalline 99.5% aluminium cold rolled 25%. The presented grain is oriented 7° from the ideal brass orientation. The beam direction is parallel to [011] and the traces of $(\bar{1}\bar{1}1)$ and $(\bar{1}1\bar{1})$ planes are marked from (Winther et al., 2004a)

to quench samples after deformation, recovery will always occur and possibly with a larger effect in cube oriented grains. Recovery is, however, not expected to change the morphology significantly, so even though grains of cube orientations might be more recovered, the observed difference in morphology is not expected to be affected.

6.5.3 Morphology - rolling texture components

The morphology of grains oriented along the α or β fibre, were all characterized by more or less developed GNBs, delineating the cell block structure. This is similar to the finding in the EBSD/CC study also at the slightly higher strains as seen from table 6.1. A minor discrepancy exists between the EBSD, TEM and CC study in that the Goss orientation displayed rounded structures in CC, but bands in EBSD and TEM. This is taken as being due to limited resolution in the CC image.

For comparison, characteristic cell block structures obtained after 25%

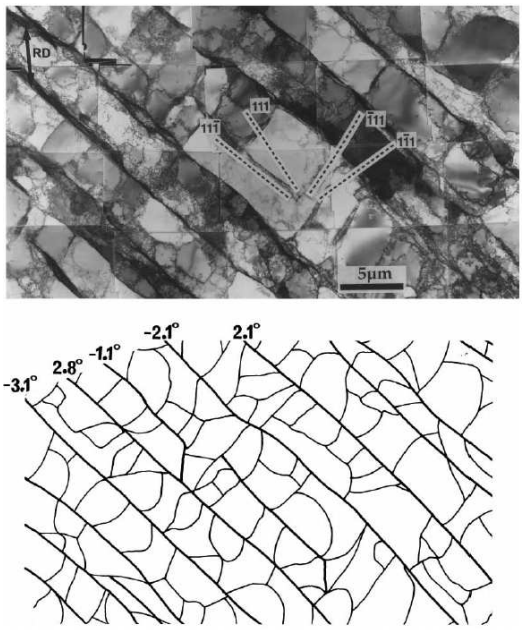

Figure 6.27: Polycrystalline 99.996% aluminium cold rolled 10%. The boundaries are straight and aligned with a (11$\bar{1}$) plane from (Liu et al., 1998)

cold rolling of a 99.5% pure polycrystalline aluminium are displayed in figure 6.26. The grain is oriented 7° from the ideal brass orientation and the morphology consists of two sets of GNBs inclined to LD. The boundaries are aligned with the ($\bar{1}\bar{1}$1) and ($\bar{1}$1$\bar{1}$) planes, and the traces of the planes are marked on the micrographs. The dislocation structure of the cold rolled brass grain, is very similar to the structure observed in figure 6.13 and figure 6.14, of the hot deformed brass grains in current study. The only difference is the scale of the structures.

Figure 6.27 shows the morphology of a grain from a 10% cold rolled 99.996% pure polycrystalline aluminium sample displayed, together with a tracing of the micrographs. The cell block structure in figure 6.26 display one set of GNBs aligned with the (11$\bar{1}$) plane, enclosing one to three IDBs. This structure is also very similar to, for instance, the hot deformed structure in figure 6.18, where a set of GNBs aligned with the (111) plane is displayed. The hot deformed structure appears to be slightly clearer i.e. some recovery might have occurred.

The morphology of the grains oriented within one of the rolling texture components were characterized by the presence of GNBs, hence the discus-

Orientation	Trace, angle to LD	Boundary plane
22° from brass	(111) 47°	(111)
11° from brass	(11$\bar{1}$) 27°	(11$\bar{1}$)
14° from brass	(1$\bar{1}$1) 31° (11$\bar{1}$) -36°	(1$\bar{1}$1), no data
8° from cube I	(110) -47 °	(110) but also (230) and (120)
8° from cube II	(1$\bar{1}$0), 43°	(1$\bar{1}$0) but also (2$\bar{3}$0) and (1$\bar{2}$0)
15° from cube	No fit	**($\bar{1}$20)**, but also ($\bar{1}$30),($\bar{1}$10)
12° from Goss I	(1$\bar{1}$1) 35°	**(1$\bar{1}$1)** but also (01$\bar{1}$),(1$\bar{3}$3), (3$\bar{3}$1)
12° from Goss II	(11$\bar{1}$) -35°	(11$\bar{1}$)
18° from S	(11$\bar{1}$) -36°	No data
27° from S	(111) 32°	No data
26° from Goss	(11$\bar{1}$) 50°	(11$\bar{1}$)

Table 6.2: Overview of the boundary characterization conducted in the TEM, the planes marked in bold are the most common ones

sion of the possible grain orientation dependent structure is discussed from the boundary plane alignment.

6.5.4 Boundary plane alignment

The alignment of the GNBs was initially analyzed by trace analysis on edge-on micrographs followed by tilting experiments as summarized in table 6.2. The table does not include data regarding the observed microbands as they are discussed separately later.

In general, it is seen that grains with rolling texture have boundary traces aligned with {111} planes, while the cube oriented grain have boundaries aligned with the trace of {110} planes. The near cube oriented grain displayed no alignment.

The trace analysis was supplemented with boundary plane determinations of selected representative segments. These measurements overall found the same boundary plane, as the trace analysis. In some orientations, alignment with other planes were found as well, for instance in the Goss oriented grain, where it was due to the "wavy" boundary character. If more than one plane was determined in the boundary plane analysis, the plan marked with bold in table 6.2, was the most common plane observed. In the cube oriented grain, the crystallographic alignment of the boundary were equally partitioned. Hence, the hot deformed boundaries seemed to follow an over-

Grain orientation	Boundary plane	Angle to LD
$(011)[2\bar{1}1]$	(111), $(\bar{1}11)$	-30,30
$(123)[63\bar{4}]$	(111), (113)	-22, 40
$(112)[11\bar{1}]$	(111), (001)	-19,35
$(011)[100]$	(111), $(\bar{1}11)$	-35,35
$(001)[100]$	(101), $(\bar{1}01)$	45,-45

Table 6.3: The boundary planes of ideal orientated grains in cold rolled aluminium from (Winther and Huang, 2007) and (Huang and Winther, 2007)

all direction, but the boundary plane alignment of the individual boundary segments could vary.

In table 6.3, the general finding of boundary plane alignment and inclination to LD found in cold deformation is given. In this, it is seen that in cold deformed fcc metals cube oriented grains display a structure of boundary planes aligned with {110} planes as also observed in the current study, and consequently a similar macroscopical alignment around 45° to LD.

Likewise for brass, Goss and near S. In these texture components, the boundaries are found to align with the {111} planes, which also is the general finding in the trace analysis and in the boundary plane determinations.

The crystallographic/macroscopical alignment of the GNBs in the individual rolling texture components observed in cold deformation, are different as seen from table 6.3 and table 6.4. By converting the observed rolling texture components in the current study to the same reference orientations, the same specific boundaries are observed, hence the same variations between the individual rolling texture components also applies at 350°C .

The discrepancy between the number of boundaries observed in cold versus hot deformed grains, might be attributed to the orientation of the grains and probably also their orientation history, and not just a difference between hot and cold deformation. It is also observed in cold deformed metals, that one set of boundaries dominates in the structure, which depends on the precise orientation of the grains (Winther, 2008).

Overall there seems to be a good correspondence between the morphology and boundary plane alignment observed during cold deformation and the observation reported here at 350°C . Although differences exist as boundary

Orientation	GNB angle to LD
22° from brass	40° to 45°
11° from brass	-25° to -35°
14° from brass	25° - 35° , -30° to -35°
8° from cube	40° , -50°
15° from cube	40° to 45°
12° from goss	35° to 45° and -30° to -40°
18° from S	- 35° to - 40° to LD
27° from S	35° to 40°
26° from goss	-40° to -45°

Table 6.4: Overview of the findings of the TEM characterization conducted at 350°C

planes were also aligned with crystallographic boundaries not found in cold deformation.

Microbands

Microbands are considered as a class of GNBs and might therefore also display a crystallographic dependency. The microbands observed in, for instance, figure 6.17 and displayed in higher magnification in figure 6.28, consist of a set of closely spaced GNBs. The microband displayed in figure 6.28 is roughly aligned with the trace of the {110} planes. Boundary tilting in the same grain determined the exact alignment of a part of the microbands to be $(3\bar{5}1)$.

In the brass and near S oriented grains, resemblance of microbands were also seen. From trace analysis on the micrographs the microbands were aligned within 10° of the trace of {110} planes. As microbands are considered a type of GNBs the crystallographic alignment in cold deformed metals depend on the orientation of the grain (see table 6.3). The alignment with {110} is, however, not seen in other orientations beside cube, hence the observed crystallographic alignment here is different compared to cold deformation, at least in the brass oriented grain. As the other two grains are not oriented along one of the ideal texture components, any conclusions regarding orientation dependency can not be made.

The presumed crystallographic alignment of the microbands formed in hot deformed aluminium is in contrast to the findings of (Zhu and Sellars,

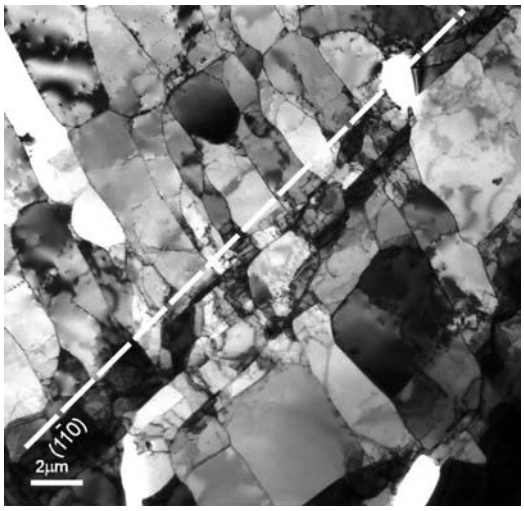

Figure 6.28: Micrograph of the microband observed. The beam direction is parallel to [112] and the trace $(1\bar{1}0)$ is marked. PSC, 350°C $5s^{-1}$ ε_{vM}=0.11.

2001). In their study, the conclusion was that the microbands formed during hot deformation of aluminium alloys, were not aligned with a preferred crystallographic plane. The alignment of GNBs is further discussed in the following section.

6.5.5 Boundary inclination to LD

The observed boundary inclinations observed in the current TEM study vary between grains of different orientations and in the individual grain. The variation ranges from 25° to 50° as seen in table 6.4, depending on the orientation. The similar inclination is seen in cold deformation (20° to 45°) given in table 6.3, where the boundaries are known to be grain orientation dependent (Winther, 2003), (Winther and Huang, 2007), (Huang and Winther, 2007).

In these studies, the inclination of the GNBs were attributed to the grain orientation and the associated slip systems activated during deformation. This is a somewhat different explanation compared to the studies by (Hurley et al., 2003), (Hurley and Humphreys, 2003) of cold deformed and by (Humphreys and Bate, 2007) of hot deformed aluminium alloys. In these studies the conclusions were, that the boundaries were inclined to LD, along the planes of maximum shear stress i.e. due to the deformation mode, and not due to the orientation of the individual grains. The differences might origi-

nate in the different techniques used to characterize the structures (Winther et al., 2004a).

6.6 Discussion: Effect of strain

From the above it appears that the dislocation structure developed at low strain at 350°C is orientation dependent. It is, therefore, interesting to examine if the corresponding high strain structure, also displays a structure characteristic of high strain cold deformation, that is, if the high strain structure develops into a lamellar structure characterized by a high amount of high angle boundaries (HABs) or a more equiaxed structure as typically formed in hot deformation.

In figures 5.6 to 5.9, EBSD-maps were presented of aluminium PSC at 350°C and $5s^{-1}$ to strains of 0.11, 0.36, 0.69 and 2.3. From the figures, the microstructural evolution up to strain 0.69 can be characterized, by either the formation of bands inclined to LD or rounded structures. The misorientation of the boundaries increased with strain, as the structure became more visible in the EBSD. At this strain, the original grain boundaries are clearly visible. The highest strained structure consists of bands of high angle boundaries enclosing cells or subgrains. The average spacing of the high angle boundaries were 4.3μm measured by a linear intercept in channel 5 software. The average spacing between HABs after 90% deformation of the original grains is 6.1μm, which indicates HABs are formed during deformation. If, however, the uncertainties of the measurements are taken as twice the standard deviation of the measurements, the difference between the two numbers are rather small (5.5μm versus 5.9μm), and it can therefore not be concluded whether or not high angle boundaries are formed. It can be concluded that the high amount of high angle boundaries created during cold deformation are not observed here (Hughes and Hansen, 1997).

A montage of micrographs obtained of the sample strained to ε_{vM}=2.3 is shown in figure 6.19. In the montage bands of elongated cells/subgrains aligned with LD, were seen in some regions while more equiaxed cells/subgrains were observed in other areas. The rectangular cells or IDBs were almost perpendicular to the high angle boundary and show strong resemblance with the lamellar structures, where GNBs enclose bamboo IDBs, as observed during high strain cold deformation.

Hence, the high strain structure developed at 350°C and $5s^{-1}$ displays

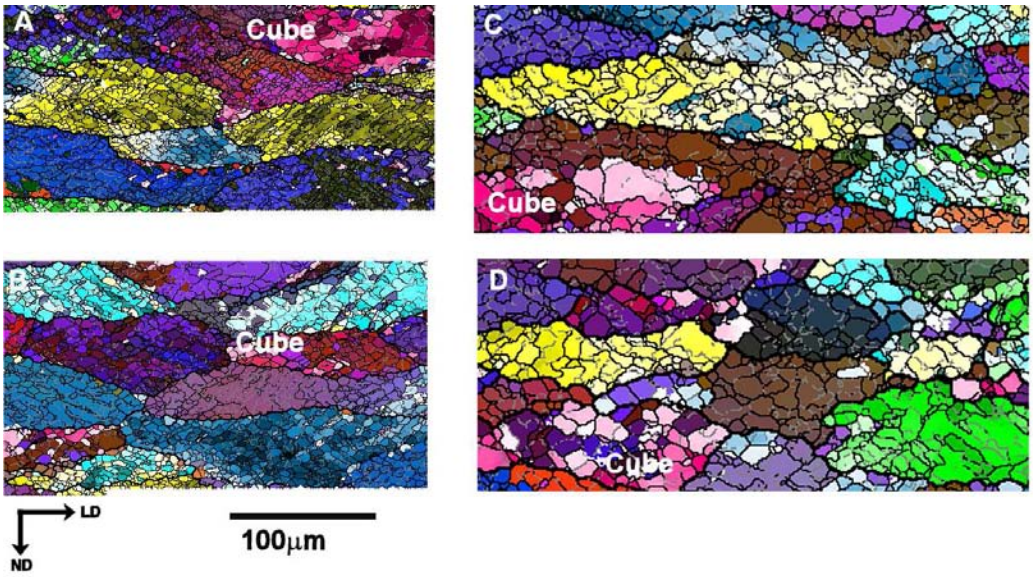

Figure 6.29: EBSD-maps at strain 0.69 A. 350°C $5s^{-1}$ B. 400°C $5s^{-1}$ C. 500°C $25s^{-1}$ D. 500°C $5s^{-1}$

some resemblance with a cold deformed high strain structure, one might term it a high temperature lamellar structure. The high strain structure is thereby different from the equaixed subgrain structure typically observed during hot deformation and displayed in figure 2.2 and similar to the banded structures observed at 305°C by (Duly et al., 1996).

It is interesting to notice, that a lamellar-like structure is observed at this high temperature high strain deformation, even though no intense bands of shear were observed. S-bands are observed during cold deformation as an intermediate state between the cell-block structure delineated by GNBs and the lamellar structure (Hughes and Hansen, 1993).

6.7 Discussion: Effect of temperature

In figure 6.29, EBSD-maps obtained at the 3 deformation temperatures are given. By comparing A, B, D in this figure it is seen, that at 350°C large parts of the grains irrespectively of orientation display structures with bands inclined to LD and cube oriented grains display rounded structures. As the temperature increases, the scale of the structures increases, the bands becomes "wavier", and the directionality observed in grains besides cube ori-

ε_{vM}	Orientation	Morphology	Incl. to LD	Planes
0.11	9° from cube	Equiaxed cells	∼ parallel	no data
0.11	23° from cube	One set of GNBs	20°	$(3\bar{5}1)$ or $(\bar{3}51)$
0.11	23° from cube	One set of GNBs	20°	(530) or $(\bar{7}\bar{3}5)$
0.11	25° from goss	One set of GNBs/Equiaxed	no	no data
0.11	11° from brass	One set of GNBs	30°	$(\bar{1}22)$ or $(\bar{1}21)$
0.36	10° from cube	Equiaxed	no	$\{351\}$
0.36	17° from S	one set of GNBs	35°	(111)

Table 6.5: TEM characterization of the samples PSC at 500°C at $25s^{-1}$ to strains of 0.11 and 0.36

entations, becomes less clear. At the highest temperature and lowest strain rate nearly all observed grains, display a more-or-less equiaxed cell structure, as commonly observed during hot deformation (Samajdar et al., 2001).

The effect of strain rate is also illustrated in figure 6.29, by comparing C and D, both deformed at 500° , but at strain rates of $25s^{-1}$ and $5s^{-1}$. The microstructure evolved in C display more directionality compared to the microstructure in D, which corresponds to a more cold deformed like structure, as also anticipated from the Zener-Hollomon relationship.

The microstructural evolution observed in figure 6.29 is coupled with a textural evolution, where the cube texture increases and S/copper decrease, the goss texture is irregular, while the brass texture was practically constant.

From the TEM characterization, it is seen that the dislocation structure evolved after PSC at 500° at $25s^{-1}$ may also be characterized as a cell block structure delineated by GNBs. The morphology of the structures also varies between the characterized grains in that some grains have nearly equiaxed cells structures, while others display GNBs inclined to LD. The findings are summarized in table 6.5 and compared to the EBSD data in table 6.6. Note that there is a difference in strain between the first four and the last two measurements presented. This is not attributed to have any other effect, than the developed boundaries is higher misoriented, and thereby easier to characterize. The discussion is therefore conducted without any special attention to the differences in strain.

The trend observed in EBSD and at 350°C , that the morphology of cube grains are different compared to grains of other orientations, is also found in the TEM study. At current process conditions the cube grains are equiaxed,

500°C 25s^{-1}	TEM 0.11 or 0.36ε_{vM}	EBSD 0.36ε_{vM}
Cube	Equiaxed	rounded
Goss	No data	widely spaced bands
Copper, brass, S	one band	one or two bands

Table 6.6: Microscopical characteristics of the samples PSC at 500°C at 25s^{-1}

while rolling texture components brass, and S display GNBs aligned with LD. The crystallographic alignment of the boundaries are different compared to lower temperature deformation in cube and brass oriented grains, while the near S oriented grains display the same alignment.

The boundary alignment with the {112} plane in the brass oriented grain is the plane expected if non-octahedral slip systems are activated during deformation. Slip systems are discussed further in chapter 7.2.2.

6.8 Conclusions

From the TEM characterization of cube, Goss, S, brass and three randomly oriented grains in the sample deformed at 350°C - 5s^{-1} to strain 0.11, the following can be concluded.

- The microstructure is a cell block structure.
- The structure of differently oriented grains displayed significant differences, the most pronounced is the difference in cube oriented grains.
- The GNBs of rolling texture oriented grains displayed overall alignment with {111} planes, while the GNBs in a cube oriented grains were aligned with {110}. Other planes were, however, also observed.
- The hot deformed boundaries were in some regions/orientations so irregular that the crystallographic alignment of the boundary plane was no possible.
- The high strain structures were characterized by elongated cells or more equiaxed subgrains aligned in bands parallel with LD.

From the few TEM studies of the samples deformed at 500°C to strain 0.11 and 0.36 at a strain rate $25s^{-1}$, the following can be concluded:

- The microstructure is a cell block structure delineated by GNBs
- Cube oriented grains are equiaxed or nearly equiaxed while other orientations display GNBs inclined to the LD
- The crystallographic plane alignment is different in cube and brass oriented grains and similar in near S orientations compared to 350°C

The temperature effect was briefly discussed and it was found that changing the process conditions from ln Z=31.7 to lnZ=27.5 changes the crystallographic alignment of the boundaries in brass and cube oriented grains, while grains of near S orientation are aligned similarly. Furthermore, the morphology changes from banded/rounded structures to nearly equiaxed/rounded structures and the boundaries as seen by EBSD become "wavier". This is followed by an increase in cube texture and decrease in copper/S texture.

Chapter 7

Discussion: Orientation dependency

7.1 General findings

Plane strain compression of 99.5% pure aluminium has been conducted at 350°C , 400°C and 500°C at a strain rate of $5s^{-1}$ and $25s^{-1}$. The mechanical properties have been analyzed and the textural evolution from 350°C to 500°C measured. The dislocation structures evolved after deformation were characterized by EBSD/CC, bright field images in the TEM and boundary plane analysis. From this the main findings are the following:

The mechanical properties of aluminium hot deformed are characterized initially by work-hardening followed by either a constant stress or softening at higher strains. The flow stress is dependent on strain rate and temperature (Z), where deformation at higher temperatures leads to lower flow stresses while a higher strain rate leads to a higher flow stress.

Adiabatic heating during PSC leads to softening at high strains of the stress-strain curve. The effect is most pronounced at high strains.

The textural evolution with strain is characterized by the evolution of the rolling texture components, copper, S and brass, and a decrease in the cube texture. The Goss component also increases with strain, but not in a simple way. The textural evolution with decreasing Z at constant strain ($\varepsilon = 0.69$) is characterized by a decrease in the S/copper texture and an increase in cube texture. The brass texture is more or less constant and the Goss texture is irregular.

From the microstructural characterizations conducted by EBSD and CC up to medium strain, it was found, that the rolling texture components brass, S and copper generally could be characterized as having a deformed microstructure consisting of one or two bands inclined 30° -55 ° to LD. The cube oriented grains displayed rounded structures, while the Goss oriented grains mainly displayed a deformation structure with resemblance to the rolling texture components. Bands and rounded structures were also found in randomly oriented grains. At 500°C and $5s^{-1}$ the deformed dislocation structures consisted of nearly rounded structures irrespectively of the orientations of the grains. Only a few copper and S oriented grains displayed a weak alignment with the longitudinal direction.

The high strain structures at 350°C displayed bands of high angle boundaries parallel with the longitudinal direction. The bands enclosed cells or subgrains and were of variable width. The average spacings between the HABs were determined to be a little less than expected from a reduction of the initial grain size. Hence, whether or not HABs are formed is uncertain. The high strain samples were also investigated in the TEM, where the cell structure evolved between the bands, were seen to consist of either cells elongated along the LD or more equiaxed cells. No correlation between orientation and structure were done in these samples.

TEM characterization of the few selected samples determined, that the dislocation structure at 350°C - $5s^{-1}$ and 500°C - $25s^{-1}$ could be described as a cell block structure delineated by GNBs. The morphology of the individual grains varied, and most pronounced was the difference in morphology of cube oriented grains. A cube oriented grain at 350°C - $5s^{-1}$ displayed a morphology consisting of cells in which a few GNBs were formed observed in a cube oriented grain. At 500°C - $25s^{-1}$ 2 cube oriented grains displayed a morphology consisting of mainly equiaxed cells. The boundary plane determinations found the 350°C structure to be aligned with {110},{230} and {120} planes, while {351} were the most common planes at 500°C .

The morphology of rolling textured grains (brass, Goss and S) were at 350°C characterized by either one set of GNBs or two delineating a cell block structure. The cell block structures were very well developed in the Goss orientation, near S and in other orientations, while the brass oriented grains, displayed areas where GNBs were not well developed, and areas, where they were very well developed. The boundaries were generally aligned with the trace of {111}-planes. This was confirmed by boundary plane determina-

tions, where also the alignment of other planes was found.

At 500°C a difference in morphology between grains of different orientation was also observed. The cube oriented grains displayed equiaxed structures or elongated cells, but without extended planar dislocation boundaries, while Goss, brass and S oriented grains displayed a cell block structure delineated by GNBs inclined to the LD. Boundary plane alignment determined the S oriented grain, to have boundaries parallel to {111}, while brass grains displayed alignment with {112} or {122} planes.

The general inclination of the GNBs to the longitudinal direction also varied within the different grains. The inclination of the GNBs observed at 350°C varied within the individual rolling texture components as observed in cold deformation. The variation within the individual rolling texture components were not calculated at 500°C due to the pure statistics.

7.2 Orientation dependency

7.2.1 Cold versus hot

The mechanical properties determined were as commonly observed during hot deformation and different to cold deformation, in that, a constant or decreasing stress was observed at high strains. In cold deformation the stress continues to increase at high strains.

The textural evolution was similar to cold deformation studies in the evolution of rolling texture components, and a decrease in cube texture. It is, however, not possible to relate the absolute strength of the individual texture components to cold deformation, as the relative strength depended on the properties of the starting material, i.e. grain size, texture etc. It is, however, noted that the relative strength of cube texture increased with increasing temperature, while the strength of the copper/S texture components decreased.

Cold deformed dislocation structures deformed to medium strains are in the TEM often characterized by a cell block structure delineated by GNBs. This was in the current TEM study found also to apply to hot deformed structures at least up to 500°C at a strain rate of $25s^{-1}$. The general finding of a different morphology of the cube orientations also corresponds well

to the observation during cold deformation in copper (Huang and Winther, 2007) and in aluminium single crystals (Liu and Hansen, 1998).

The morphology of rolling texture oriented grains, also varied, seen as a difference in inclination of the GNBs to LD, which is reflected in the GNBs were often aligned with the {111} planes. Grains of rolling texture orientations have been observed to be aligned with specific planes during cold deformations as given in table 6.3. As described previously in section 6.5.4, the general findings are also found in cold deformation, which indicates that the dislocation structure is orientation dependent also at high temperature.

One may argue, however, that the observed boundaries are all inclined in the regions of maximum shear, consequently the observed dislocation structure is just GNBs aligning with the maximum sheared directions, and that the boundary planes are not determined by the grain orientation through the active slip systems. The critical test for this would be if characterization of an S oriented grain, which during cold deformation displayed boundaries aligned with {111} planes inclined 22° to the LD, and thereby well away from the plane of maximum shear. Likewise, if a copper grain was found, because this displays two sets of boundaries in cold deformation, aligned with the {111} and {100} planes and inclined 19° and 35° to LD.

Unfortunately, no such grains were found and characterized, but the morphological difference of the cube oriented grains observed not only in the TEM at 350°C , but also at 500°C and in EBSD/CC, strongly indicates that the dislocation structures developed are dependent on the orientation of the grain.

The many similarities between cold and hot deformed dislocation structures therefore strongly indicates, that the grain orientation determines the dislocation structure evolved during deformation at 500°C ($\ln Z = 27.5$) and thereby that the surrounding grains only to a minor extent influence the structure formed, and the deformation mode only affects the structure through the slip systems, which are activated by it.

Differences between cold and hot deformation were, however, also observed, i.e. less HABs are created at high strain, no localized shear was observed and the boundaries were found to align with additional planes than observed during cold deformation. All are effects of the temperature, and it is therefore not possible to conclude that the grain orientation dependency is the same as in cold deformation (same active slip classes (Winther and

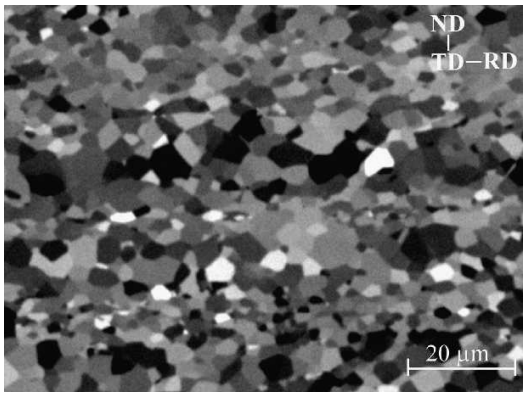

Figure 7.1: CC image of a single cube oriented crystal PSC at 350°C at a strain rate of 50 s^{-1} from (Huang and Ferry, 2000)

Huang, 2007)), but only that it exists .

7.2.2 Polycrystals versus single crystals

Comparison with single crystal experiments might also enlighten the possible orientation dependency of hot deformed microstructures.

Studies of cube oriented aluminium single crystals have been conducted by (Maurice and Driver, 1993), (Driver et al., 2000), and (Huang and Ferry, 2000) in which the general findings are, that the morphology developed after straining is an equiaxed cell/subgrain structure and the orientation is more stable at higher deformation temperatures. Both findings are in nice agreement with the findings of the current study. A CC image from (Huang and Ferry, 2000) is displayed in figure 7.1, where a morphology consisting of equiaxed cell/subgrains is seen. The structure is very similar to the cube morphology shown in, for instance, figure 5.16.

Single crystal studies of rolling texture orientations have been conducted by (Glez and Driver, 2003),(Driver et al., 2000), (Driver et al., 1996) and (Theyssier et al., 1995), where Al-1%Mn crystals were hot channel die PSC. The morphology of S copper and brass oriented grains were in general described as a checker board pattern, of which the average cell/subgrain sizes of each orientation were inversely proportional to Z. The brass orientation was less sensitive to Z, while S was the most sensitive. At medium strains, the misorientations within the S orientation, were furthermore found to be

higher compared to the brass orientation.

This is in overall agreement with the findings of the current study, as the structure of the brass grains appeared to be less developed compared to the S grains. Furthermore, the stability with respect to Z is as found in the current study, where the brass texture is constant in the region investigated, while the S texture decreases. A morphology of 2 sets of bands is in general also found in the current EBSD study, while the TEM study showed a structure consisting of only one dominating sets of bands. As the cited studies were conducted by EBSD it is, however, difficult to draw any direct comparisons between the more precise structural studies conducted in the TEM. Some surface studies regarding boundary plane alignment have, however, been conducted on single crystals, which are discussed in the following section.

Active slip systems

The activation of other slip systems besides the {111} <1$\bar{1}$0> slip systems during hot deformation in fcc metals, has been argued by slip trace analysis and from textural modelling.

Slip trace analysis concluded that during deformation above 300°C non-octahedral slip is initiated. So mixed slip has been observed between {111}<1$\bar{1}$0> and {112}<110> in brass grains, S might also slip on {100}<1$\bar{1}$0>, while the cube orientation is stabilized by slip on {110}<1$\bar{1}$0>(Driver et al., 1996), (Theyssier et al., 1995), (Maurice and Driver, 1993).

In another study, however, the possible activation of non-octahedral slip is only found indirectly, as the boundaries in brass oriented crystals formed at 400°C are found to align with {111}<1$\bar{1}$0>. The shape change imposed by the deformation corresponds, however, to slip on both {111}<1$\bar{1}$0> and {112}<1$\bar{1}$0> (Driver et al., 2000). Non-octahedral slip has also been included in textural models to predict a stronger brass texture observed in some hot textural studies (Driver et al., 2000) (Maurice and Driver, 1997a), (Maurice and Driver, 1997b), (Barcroix and Jonas, 1988).

(Samajdar et al., 2001), however, found unsatisfactory model results when using non-octahedral slip to model the textural findings of 99.5% pure polycrystaline aluminium, and therefore questions the activation of non-octahedral slip during hot deformation.

At 350°C the textural evolution observed may well be similar to a texture evolution of the same material at RT deformation. Likewise, the structures obtained display many similarities with dislocation structures characterized in cold deformed aluminium, especially the boundary plane alignment, which point to that only slip on octahedral slip systems occurs. As, however, other boundary planes were found as well, activation of non-octahedral slip system can not be excluded.

The non-octahedral slip system activated in brass crystals is believed to be $\{112\}<1\bar{1}0>$. The few boundary plane determinations conducted at 500°C - $25s^{-1}$ in the current study, where the brass oriented grain displayed GNBs aligned with the {112} or {122} planes, therefore strongly indicate activation of the non-octahedral $\{112\}<1\bar{1}0>$ slip systems at 500°C . This also corresponds to the textural evolution, where a higher strength of cube texture is observed at 500°C .

At 500°C - $5s^{-1}$ the developed microstructures were furthermore found to be more-or-less equiaxed cells or subgrains in nearly all orientations, which indicates that with these process conditions, the mobility of the dislocations were high, which might reflect the activation of other slip systems, or just be an effect of temperature.

The relatively more homogeneous deformation structure observed in hot deformed materials, which generally is attributed to dynamic recovery, might be attributed to the activation of other slip systems. Slip on several slip systems, would accommodate a given deformation more easily, than more restricted systems and thereby create a more homogeneous structure (Driver et al., 2000).

In conclusion, however, the similarity between the single crystal studies and the observation of the current thesis, point to that the deformation structures investigated up to medium strain are orientation dependent. Furthermore, indications of non-octahedral slip at 500°C are observed.

7.2.3 Other hot deformation studies

Not many studies have been conducted which relate the dislocation structure of a hot deformed metal with the orientation of the structure. A few, however, exist. Studies by (He et al., 2005) found an orientation dependent mi-

crostructure in 99.5% pure aluminium tensile deformed at 300°C (lnZ=30.5) at strain 0.11 , while (Liu, 1998) observed orientation dependent structures in a 96.8% aluminium alloy plane strain compressed at 510°C (lnZ=25.6) up to strain 0.5.

As the current findings are in good agreement with these studies as well, it is therefore concluded, that the dislocation structure observed during plane strain compression up to medium strain in the temperature interval 350°C (ln Z = 32) to 500°C (ln Z = 27.5) depends on the grain orientation. This regime, may well be extended to lnZ=33.3, as the sample PSC at 350°C at $25s^{-1}$ probably is the most cold deformed-like of all samples, due to the high strain rate.

Chapter 8

Conclusions

Commercial purity aluminium (99.5%) has been plane strain compressed at 350°C at $25s^{-1}$, 350°C at $5s^{-1}$, 400°C at $5s^{-1}$, 500°C at $25s^{-1}$ and at 500°C at $5s^{-1}$. In terms of Zener Hollomon parameter, this corresponds to the regime lnZ = 26 to lnZ = 33. The samples were characterized with respect to the mechanical properties, the textural evolution and morphology of the individual grains. The aim was to investigate whether or not the dislocation structures developed were orientation dependent as observed during cold deformation. The observed characteristics of the hot deformed samples were therefore compared with the findings of cold deformation. Below is listed the main findings of part one of the thesis:

- The mechanical properties display an initial work-hardening stage followed by either a saturation stress or softening. The softening is possibly due to adiabatic heating, and not due to the textural evolution.
- The textural evolution with strain is characterized by the evolution of the rolling texture components and a decrease in the cube texture component. The textural evolution with temperature at constant strain is characterized by an increasing strength of cube texture and a decreasing strength of copper/S texture. The strength of the Goss texture was irregular while the brass texture was constant.
- The morphology of cube oriented grains is different compared to grains of rolling texture orientations up to ε=0.69 and until deformation at 500°C (lnZ = 27.5).
- Deformation at 350°C to a strain of 2.3 leads to a structure characterized by high angle boundaries enclosing elongated IDBs parallel with the longitudinal direction

- Deformation at 500°C at a strain rate of $5s^{-1}$ and strain 0.69 leads to a nearly equiaxed microstructure in all orientations.
- The cell block structure formed during deformation at 350°C (lnZ=32) to ε_{vM}=0.11 was characterized by GNBs aligned with the crystallographic planes also observed in cold deformed dislocation structures. In some orientations, however, additional planes were found.
- During deformation at 500°C (lnZ=27.5), the low strain cell block structure indicated activation of non-octahedral slip systems.

Based on the findings, it is therefore concluded that the dislocation structures developed during plane strain compression of 99.5% pure aluminium in the temperature range 350°C to 500°C (ln Z= 32 to ln Z = 27.5) are grain orientation dependent up to $\varepsilon_{vM} = 0.7$.

Finally, indications were found that non-octahedral slip systems are activated during deformation at 500°C and $25s^{-1}$.

Part II

Stored energy

Chapter 9

Stored energy

9.1 Introduction

During the deformation/working of metals a small amount of the deformation energy is stored in the metal as dislocations, high angle boundaries, vacancies/interstitials and in some metals twins. The characterization of this stored energy facilitates the description of the structure developed during deformation and thereby furthers the understanding of the mechanism behind deformation.

Initially metals deforms elastically and later plastically. The elastic straining is reversible, while the plastic deformation structure is maintained after deformation. Hence the energy stored after deformation is stored due to the plastic deformation i.e. as defects and in current investigations more specifically dislocations. The introduction of defects/dislocations distorts the metal lattice i.e. stress fields are created. During deformation dislocations arrange into low energy dislocation structures (LEDS) which are maintained afterwards (Kuhlmann-Wilsdorf, 1989). The LEDS are characterized by the mutual screening of stress fields from individual dislocations, so long range stresses above the friction stress do not occur. According to the LEDS hypothesis the deformation-induced structures are the structures in equilibrium with the applied stress field, which minimizes the stored energy of the system (metal)(Kuhlmann-Wilsdorf, 1999).

The stored energy in metals have been extensively explored in the period up to the 1970s (from the review (Bever et al., 1973)). At this point, it was established that the energy stored during cold deformation in fcc metals, was stored as defects, where the amount of energy stored depended on the nature

of the metal i.e. metal type, purity and grain size and on the deformation, that is deformation mode, temperature and strain.

An understanding of the stored energy dependencies was also well developed, and is therefore summarized in the following together with newer findings.

The stacking fault energy of a metal determines the ability to cross slip, and thereby the ability to circumvent obstacles such as particles and also the potential creation of Koehler sources (dislocation sources) (Weertman and Weertman, 1992). The amount of stored energy is therefore different from metal to metal at a given strain. Impurities enhance the amount of stored energy, due to pinning of dislocations, where the nature of the impurity determines the distortion of the metal lattice, and thereby the degree of interaction with dislocations (Weertman and Weertman, 1992). The stored energy is higher in small grains compared to larger grains, due to difference in dislocation density at a given strain (Hall, 1951), (Armstrong et al., 1962).

The deformation mode only affects the stored energy in the measurements, where an increase in surface-to-volume ratio is observed (Bever et al., 1973). The deformation temperature however, is important because the mobility of defects decreases with temperature, which inhibits annihilation. Hence low temperature deformation leads to more energy stored.

The stored energy increases with the deformation (strain), as a metals continues to work harden (multiplication and trapping of dislocations), and a linear relationship between strain and stored energy was reported in pure copper (Clarebrough et al., 1955), (Baker and Martin, 1983) and in nickel (Clarebrough et al., 1955). This research of the relationship between strain and stored energy found the relationship to be characterized by 3 stages (Baker et al., 1995), (Mandal and Baker, 1995) in cold rolled pure copper and nickel. At low strain the stored energy increases linearly with strain, at a higher strain the relationship is still linear but with a lower slope while at the highest strain the stored energy nearly saturates. Hence the stored energy depends on the strain range considered i.e. to which work hardening stage the specimens were deformed.

9.2 Aim

The aim of the current study was to measure the stored energy in a deformed metal and correlate it with the stored energy evaluated from the microstructure, by using the current theoretical relationships between the microstructure and the energy it represents. This was done to further the understanding of a deformed microstructure.

A grain orientation-dependent microstructure implies a grain orientation-dependent stored energy. This cannot, however be measured by bulk measurements such as calorimetry but must be evaluated based on microstructural parameters. Before undertaking this it is, however essential to establish close agreement between calorimetric bulk measurements and calculations based on average microstructural parameters for the bulk sample. Two model systems were therefore selected to investigate this agreement and furthermore evaluate the feasibility of studies on hot deformed aluminium.

Initially the ability to measure stored energy of a cold deformed polycrystaline metal was investigated. For this nickel cold rolled to large strains was chosen as a model system for cold deformed fcc metals. This was chosen because the microstructure of the same nickel material, has been well characterized in a previous study (Hughes and Hansen, 1993) (Hughes and Hansen, 2000), and the stored energy in nickel is sufficiently high for measurements to be conduced on materials deformed at lower strains.

Next stored energy measurements of cold rolled aluminium was conducted, in order to evaluate the possibility of measuring the stored energy in hot deformed aluminium.

9.3 Stored energy

In the following section the theoretical fundamentals for the evaluation of the stored energy in metals are given. First the relation between stored energy and the deformed microstructure is presented, and in the following section the background is given for measuring stored energy in a differential scanning calorimeter (DSC).

9.3.1 Stored energy - microstructure

The energy stored in a metal after deformation is stored mainly as dislocations, hence the stored energy in a deformed microstructure can be described by the equation 9.1:

$$E_{stored} = \rho \cdot E \tag{9.1}$$

where ρ is the dislocation density and E is the energy per unit length of the dislocation line. The deformed microstructure characterized in the microscope is however not described by the total dislocation density, but by the structures evolved during the deformation, that is: boundary type, spacings between and misorientation angles across the boundaries. An evaluation of the stored energy through the dislocation density is therefore not possible. Given that the deformation-produced dislocations are arranged in low energy dislocation boundaries, it is however possible to correlate the stored energy with the microstructure, because the energy per unit area (γ) associated with such a boundary is related through the Read-Shockley equation (Read and Shockley, 1950) to the misorientation angle. The equation is presented here in equation 9.2 in the formalism used in (Godfrey et al., 2005):

$$\gamma = \gamma_m \cdot \left(\frac{\theta}{\theta_m}\right) \cdot \left(1 - \ln\left(\frac{\theta}{\theta_m}\right)\right) \qquad : \theta \leq \theta_m \tag{9.2}$$

$$\gamma = \gamma_m \qquad : \theta > \theta_m \tag{9.3}$$

In this γ_m is the energy per unit area of a high-angle boundary, θ is the boundary misorientation, and θ_m is the misorientation of a high angle boundary taken as 15° in the following.

The stored energy is then given by:

$$E_{stored} = \gamma \cdot S_V + E(\rho) \tag{9.4}$$

where E(ρ) is the energy associated with loose dislocations in the structure and S_V is the area per unit volume of the boundary. S_V relates to the spacial arrangement of the boundary, and is therefore different if 3D arrangements of the boundaries are different.

In the following the microstructure of cold rolled nickel is considered, and therefore the stored energy analysis is restricted to only contain parameters relevant for highly deformed fcc structures.

Calculation of stored energy from TEM data

The deformed microstructure in a highly strained fcc metal of medium-to-high stacking fault energy, is characterized by a cell block structure consisting of two boundary types GNBs and IDBs (see chapter 2.1). GNBs are parallel planar dislocation boundaries which enclose the nearly equaixed cell boundaries which are IDBs. The major part of the deformation-produced dislocations are stored in the boundaries, hence the contribution from loose dislocations is neglected.

TEM characterization of nickel cold rolled to high strains, has been conducted by (Hughes and Hansen, 1993) and (Hughes and Hansen, 2000), and these data are used for the present stored energy calculations. The calculation of the stored energy based on the microstructural characterization is conducted in two ways, the first method calculates the stored energy of the microstructure from the distribution of misorientation angles and the average boundary spacings, while the second method uses the average parameters of both the misorientation angle and the spacings:

$$S_V^{GNB} = \frac{1}{d_{GNB}} \tag{9.5}$$

$$S_V^{IDB} = \frac{\pi}{2d_{IDB}} \tag{9.6}$$

$$S_{V,total} = S_V^{GNB} + S_V^{IDB} \tag{9.7}$$

In the TEM study the average distances between the different boundaries were measured from large montages of the microstructures and from this the average values of S_V was calculated based on the stereological relationships given in equation 9.5 , together with a small correction relating to boundaries not being infinitely long (Godfrey and Hughes, 2000), (Godfrey and Hughes, 2002). For GNBs they were modeled by a rectangular parallelepiped, hence S_V is given by:

$$S_v = \frac{1}{d_{GNB}} + \frac{1}{d_{transverse}} + \frac{1}{d_{longitudinal}} \tag{9.8}$$

where $d_{transverse}$ and $d_{longitudinal}$ were estimated form the cell block aspect ratios. The boundary area fraction per unit volume of IDBs was corrected, so the boundary enclosing the cell block structure (a GNB) was not accounted for twice. This was done by correcting the S_V by a ratio, r_{IDB} which is the average number of IDB intercepts to the total number of intercepts encountered. Hence the boundary area fraction per unit volume for IDBs is given

by $S_V = r_{IDB}(\frac{\pi}{2d_{idb}})$

The misorientation angles of the given boundaries were measured by measuring all boundaries in a given area (not necessarily the same area as the area for spacing measurements). The measured angles were thereafter binned into histograms with bins of 2 degrees for GNBs, 0.5 degrees for IDBs and an average angle per boundary type was calculated.

The stored energy calculation based on the distribution of misorientation angles is calculated in the following way. At first the energy associated with each bin is calculated (γ_{bin}) by the use of equation 9.2, hence the energy per unit boundary area in a bin (γ_{bin}) is given by:

$$\gamma_{bin} = \gamma_m \times \left(\frac{\bar{\theta}_{bin}}{\theta_m}\right) \times \left(1 - \ln\left(\frac{\bar{\theta}_{bin}}{\theta_m}\right)\right) \tag{9.9}$$

where $\bar{\theta}_{bin} = \frac{q1-q2}{2}$, and q1, q2 are the limits in misorientation angles of the given bin.

The stored energy associated with the boundaries in the given bin is found from:

$$E_{stored-bin} = \gamma_{bin} \times S_{v-bin} \tag{9.10}$$

In this S_{v-bin} is the area per unit volume for the boundaries in the bin. The total amount of stored energy can now be calculated by summing over each bin for each boundary type (i.e. GNBs and IDBs):

$$E_{stored} = \sum_{bin}(\gamma_{bin}^{GNB} \cdot S_{v-bin}^{GNB}) + \sum_{bin}(\gamma_{bin}^{IDB} \cdot S_{v-bin}^{IDB}) \tag{9.11}$$

The area per unit volume for the given bin, is calculated by $S_{v-bin} = S_V \times \frac{n_{bin}}{N}$, where n is the number of boundaries in the given bin, N the total number of boundaries and S_V is the area per unit volume for all boundaries considered. It is important to emphasize, that in this calculation of S_{v-bin} it is assumed that the fraction $\frac{S_{v-bin}}{S_V}$ is equal to the number of boundary fractions ($\frac{n_{bin}}{N}$), which is the case, when measurements are conducted along random test lines in the TEM. In the current TEM dataset however, the misorientation measurements were conducted by measuring the misorientations in an entire region, so only if there is no correlation between the misorientation angle and the boundary length, is the assumption correct. In the following it is assumed to be the case, hence the above equation 9.11 can be generalized to:

$$E_{stored} = \sum_{bin}(\gamma_{bin}^{GNB} \cdot n_{bin}^{GNB}) \cdot \frac{S_V^{GNB}}{N^{GNB}} + \sum_{bin}(\gamma_{bin}^{IDB} \cdot n_{bin}^{IDB}) \cdot \frac{S_V^{IDB}}{N^{IDB}} \quad (9.12)$$

The second method calculates the stored energy of the given microstructure based on the average parameters as described in (Godfrey et al., 2005), and is given in equation 9.13:

$$E_S = \gamma(\theta_{av}^{GNB}) \cdot S_V^{GNB} \cdot C^{GNB} + \gamma(\theta_{av}^{IDB}) \cdot S_V^{IDB} \cdot C^{IDB} \quad (9.13)$$

In this the Cs are correction factors introduced to account for the over estimation of the stored energy due to use of average values (Godfrey et al., 2005).

9.3.2 Stored energy - DSC

Thermodynamic considerations

Calorimetry measures the energy change of a given system. Generally the change of internal energy of a system can be expressed by the first law of thermodynamics:

$$dU = dQ + dW + \Sigma dE_i \quad (9.14)$$

where Q is the heat change of the system, W the work and E other forms of energy. Assuming that W is equal to pressure volume work, which under current measurement conditions can be approximated to 0, and that no other energy form contributes, the heat change can be described by 9.15:

$$dU = dQ = dH = \left(\frac{\delta H}{\delta T}\right)_{p,\xi} dT + \left(\frac{\delta H}{\delta \xi}\right)_{T,P} d\xi \quad (9.15)$$

In 9.15 the first term is the heat capacity at constant pressure and composition, while the second term is the isobaric and isothermal enthalpy change, for example the melting enthalpy ΔH_{fusion}. From 9.15 it can be seen, that if the heat capacity of the system is known and corrected for (and w_{pV}=E_{other}=0) integration of 9.15 gives:

$$\Delta H = \Delta Q \quad (9.16)$$

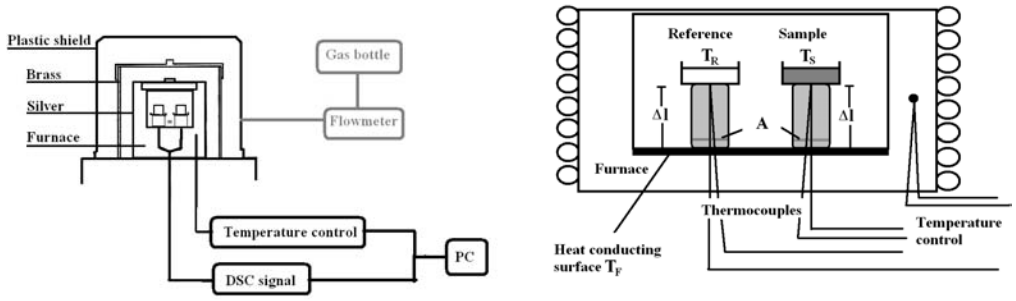

Figure 9.1: Setup of a DSC

which in the current study, is equal to the stored energy E_{stored} of the given metal.

In the DSC the quantity measured is the heat flow ϕ, which under ideal conditions (w_{pV}=E_{other}=0) is given by:

$$\phi = \frac{dQ}{dt} = C_{p,\xi}\frac{dT}{dt} + \left(\frac{\delta H}{\delta \xi}\right)_{T,P}\frac{d\xi}{dt} \tag{9.17}$$

where the first term $C_{p,\xi}$ is the heat capacity of the system (baseline), and the second term is the heat flow to/from the sample, which in the current study corresponds to the release of stored energy.

DSC theoretical measurements

In a current study a differential scanning calorimeter (DSC) from SEIKO - DSC120 has been used. The principle of the calorimeter is sketched in figure 9.1.

The calorimeter consists of a measuring module containing the specimen chamber, a PC and a flowmeter, which enables measurements conducted under different atmospheres. The specimen champer is a solid silver can, with a silver lid and the chamber is surrounded by a brass chamber, which again is surrounded by a high temperature resistant plastic shield. The silver chamber contains 2 sample holders/sensors consisting of Ag, Pt, inconel, stainless steel and C-A thermocouples. The thermocouples are connected to the PC. The gas inlet is located in the side of the chamber between the sensors. The temperature in the camber is controlled by the furnace, which is seated within the Ag block.

The DSC is a heat flux calorimeter, which determines the difference in heat flow[1] (ϕ) between the sample and reference by measuring the temperature difference of the two.

$$\phi = -K \cdot \Delta T \tag{9.18}$$

A sketch of the setup with a definition of the parameters used in the following, is displayed in figure 9.1.

Interpretation of the signal from the DSC, however requires a short introduction to heat conduction. Heat transfer by conduction is described by Fouriers law:

$$\vec{q} = -\lambda \cdot \nabla T \tag{9.19}$$

where $\vec{q}$ is the heat flux, λ is the thermal conductivity and T the temperature. Assuming that the temperature difference is linear and using definitions from figure 9.1 the heat flow from the heat-conducting surface (furnace) to the sample is given by:

$$\phi_{FS} = -\lambda \cdot A \cdot \frac{(T_S - T_F)}{\Delta l} \tag{9.20}$$

which relates to the heat capacity of the sample system by:

$$\phi_{FS} = C_S \cdot \frac{dT_S}{dt} \tag{9.21}$$

The same applies for the heat flow to the reference. If however a thermal event occurs in the sample, an extra heat flow term (ϕ_R) has to be added to the heat flow in 9.21, hence:

$$C_S \cdot \frac{dT_S}{dt} = \phi_{FS} - \phi_R(T,t) \tag{9.22}$$

Note in this ϕ_R <0 corresponds to an exothermic event. Since the reference does not undergo any internal thermal events, and remembering ΔT=T$_S$-T$_R$, the difference in heat flow between sample and reference is given by:

$$\phi_m(T,t) = \phi_{FS} - \phi_{FR} = C_S \cdot \frac{d\Delta T}{dt} + (C_s - C_R)\frac{dT_R}{dt} + \phi_R \tag{9.23}$$

As the temperature change with time in the reference is equal to the heating rate of the measurements β, the signal from the DSC can be described by the following 3 terms:

[1] In the following heat flow will be used to describe $\phi = \frac{dQ}{dt}$. The correct term for ϕ would be heat flow rate, but it is not so often used, and therefore not used here.

$$\phi_m = (C_s - C_R) \cdot \beta + \phi_R + C_S \cdot \frac{d\Delta T}{dt} \tag{9.24}$$

The first term describes the eventual difference in heat capacity between sample and reference setup, the second term is the contribution from thermal events in the sample, while the last term is related to an eventual time dependence of ΔT, denoting the thermal inertia of the system.

From equations 9.24 and 9.17, it is seen, that under ideal conditions the stored energy released during annealing of a metal can be found by correcting the signal for the difference in heat capacity and eventual thermal lag followed by integration of the signal. In this it is however assumed, that the heat capacity of the system, does not change with annealing. The heat capacity of deformed copper, is in (Gottstein et al., 1973) reported as being 0.2% higher compared to the annealed sample. Hence the approximation of a constant heat capacity during annealing, is a valid approximation in copper and is in the following also assumed to apply for aluminium and nickel.

A practical approach of integration and interpretation of the DSC signal is described further in section 9.5.1.

9.4 Experimental setup

In the following a description of the experiments will be given.

9.4.1 Sample preparation

Samples from copper, nickel and aluminium were prepared. Nickel and aluminium were chosen as described in section 9.2, while copper served as an internal and external laboratory standard, as it has previously been extensively characterized.

Copper samples were prepared by cold rolling to a thickness reduction of 90% as described in (Woldt and Jensen, 1995), which corresponds to a final sample thickness of 1.2mm. The initial grain size was 25μm and the maximum content of metallic impurities was 0.008%.

Aluminium samples were prepared from 99.5% pure aluminium, with an initial grain size of 70μm, (characterized in H). The material was cold rolled to thickness reductions of 90%, thereby reaching a final sample thickness of 1mm.

99.99% pure nickel samples, with a grain size of 80 to 100μm were prepared by cold rolling to thickness reductions of 70% 90% 95% and 98% as described in (Hughes and Hansen, 1993). The thickness of the samples varied from 3.1mm to 0.24mm.

DSC samples were prepared from the rolled sheets by punching out disks with a diameter of 6 mm, apart from the nickel samples cold rolled 70% and 90%, which were prepared by cutting square-shaped samples (approximately 5mm×5mm) on a ACCUTOM-5 from Struers using the lowest cutting rate and water cooling. In order to remove the deformation introduced by the punching and cutting, the samples were polished to disks with a final diameter of 4.5mm with SiC paper (grit 1000/4000). The bottom of the samples were also polished with Si-carbide paper (grit 4000) to obtain a good connection to the sample pans. After polishing the samples were cleaned in an ultrasonic bath with ethanol. The samples were prepared to meet the diameter constraint of the sample pan, hence the masses of the samples varied: aluminium (40mg-50mg), nickel (30mg-390mg) and copper (160mg-165mg). In D.2 is the validity of the sample preparation is discussed. Al and Cu samples were stored in the freezer prior to the experiments, while the nickel samples were stored at room temperature.

9.4.2 Experimental procedure

The experiments in the DSC were conducted with a constant heating rate of 5 K/minute in an atmosphere of argon (99.998% pure Alphagaz), with a flow rate of 100ml/minute. Aluminium pans heat treated at 500°C for one hour and afterwards cleaned in an ultrasonic ethanol bath were used for the specimens, and the reference material was a fully annealed material of a similar metal and mass as the sample. The experimental conditions were chosen to avoid oxidation of the metals and large thermal gradients.

The samples were heated above the recrystallization temperature, cooled, reheated and cooled again. The second run was conducted to obtain a baseline for the measurements, to be used in evaluation of the signal. The recrystallization temperatures were determined either by annealing exper-

Metal	Recryst. temperature	Method
Cu - 92% cold rolled	$\approx 170°C$	Annealing/hardness
Al - 97% cold rolled	$\approx 325°C$	(Davies et al., 1995)
Ni - 98% cold rolled	≈ 300	(Cao et al.)

Table 9.1: Recrystallization temperatures of copper, aluminium and nickel

iments followed by hardness measurements or from the literature - see table 9.1.

9.5 Data

9.5.1 Data/signal interpretation

In the DSC the heat flow difference between the sample and reference is measured as a function of time as well temperature[2].

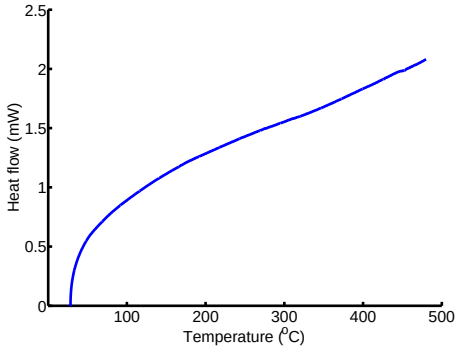

Figure 9.2: Heat flow of empty sample pans

In order to be able to interpret the signal associated with the stored energy, the signal for the DSC is characterized prior to the measurement, by measuring the signal from empty aluminium pans. This is shown in figure 9.2, the weight difference between the aluminium pans is 0.15mg. From this figure a constant increase in heat flow as a function of time and temperature above 100°C is seen, hence the DSC shows some asymmetry, which must be accounted for in the data analysis. A similar asymmetry is also observed during measurements with no sample pans, hence the asymmetry is attributed

[2]The measurements were conducted with a constant heating rate, so the temperature is proportional to time. The heat flow curves are therefore displayed as a function of temperature, to give the maximum of information

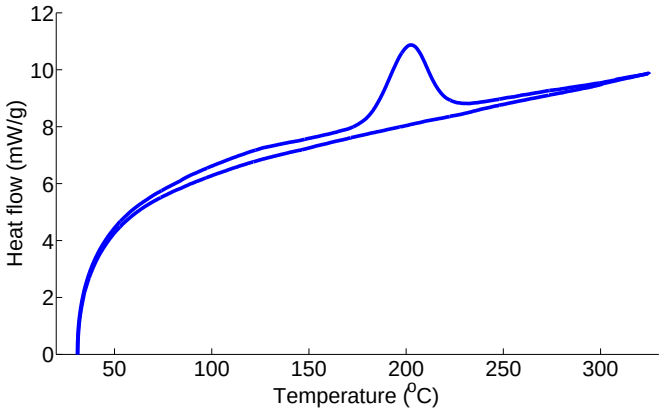

Figure 9.3: Heat flow curve of copper cold rolled 90%

to a difference in heat conduction between reference and sample sensor in the setup.

To obtain the signal associated only with the energy release from the metals, the first measured flow curve was compared with the flow curve obtained by consecutive measurements (the basis line). From this the peak corresponding to recrystallization was determined, and the stored energy was determined by integration of this peak.

Ideally 2 consecutive measurements of a sample would be identical apart from the recrystallization peak. In many experiments however, a difference between the baseline obtained, and the first heating experiment was observed, as seen most pronouncedly seen in copper (se figure 9.3). From this figure it is seen that the two copper curves deviate, where the deviation does not increase with temperature and this is also observed after recrystallization. The first assumption would be, that these differences are due to recovery, however if recovery was the main reason for the differences, it would be expected, that the difference between the two curves would increase with temperature until recrystallization, after which the two curves would be identical. The difference between the curves is therefore not attributed solely to recovery.

Another reason could be a change in surface conditions, leading to a difference in contact and thereby heat conduction conditions between the sensor and sample/reference pans after the cooling.

Regardless of the origin of the differences, the main energy release is ob-

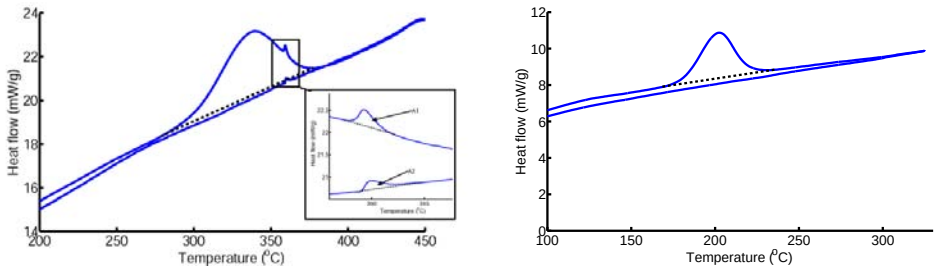

Figure 9.4: Peak definition; left method 1 (nickel), right method 2 (copper)

served in one peak, which is used to characterize the stored energy of the metal. The peak integration is conducted by defining the peak by comparing it with the base line. If the base line does not deviate from the first heat flow curve, apart from the recrystallization peak, the integration of the peak, is conducted between the points, where the base line deviates from the first curve, as illustrated by the dotted line in the left curve in figure 9.4.

If however, a larger deviation is seen between the two curves, the peak is defined as starting from the point, where the curve increases with temperature, is different from the curve evolution of the base line. This is a method similar to the one presented in (Rohatgi and Vecchio, 2002) and illustrated by the dotted line in the right curve of figure 9.4. Each peak is integrated 3 times, and the average of the 3 integrations is used to describe the stored energy of the given sample.

Nickel exhibited a Curie transition at 358°C in the current study, which is seen in the DSC measurements as a small peak on top of the recrystallization peak, if the signal is not counterbalanced by the reference (see insert of figure 9.4). If a peak is observed, the stored energy measurement is corrected by measuring the energy associated with the transition, found by integration of the peak on both curves, as illustrated in the insert of figure 9.4. The average of the two measurements are thereafter subtracted from the measured stored energy.

The temperature of recrystallization was taken as the onset temperature, as illustrated in figure D.1 in appendix D.1.

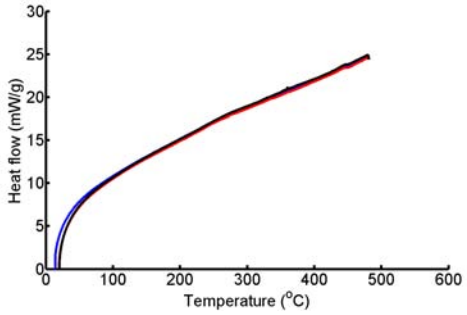

Figure 9.5: 3 consecutive baseline measurements of nickel cold rolled 95%

9.5.2 Data reproducibility

The reproducibility of the data was tested by measuring the baseline after an experiment 3 times. An example is given in figure 9.5, from which it is seen, that the baseline is reproduced satisfactory at temperatures above 100°C . The difference at lower temperature is probably due to a lower starting temperature, which is attributed to a difference in the environment (temperature of the room).

In order to verify the data further, copper and nickel samples were sent to NETZSCH Applications Laboratory, Selb, Germany, where calorimetric measurements were conducted under similar conditions as used in the current study. As described in G, the maximum difference between stored energy measurements conducted in house and stored energy measurements conducted at NETZSCH was 3.5%. Based on this it is concluded, that the experiments and data analyses give trustworthy results.

Parallel experiments on nickel of similar purity and cold rolled to similar strains, was conducted at Tsinghua University in Beijing (see G). These experiments were conducted on samples newly deformed and with nearly "constant" sample masses of 10mg to 30mg. Only one measurement was conducted per strain level. As will be presented, the stored energies determined in these experiments were similar to the data obtained in the current study, hence the variable sample mass used in the current study, does not contribute any effect to the data, and neither does the storing of the nickel samples.

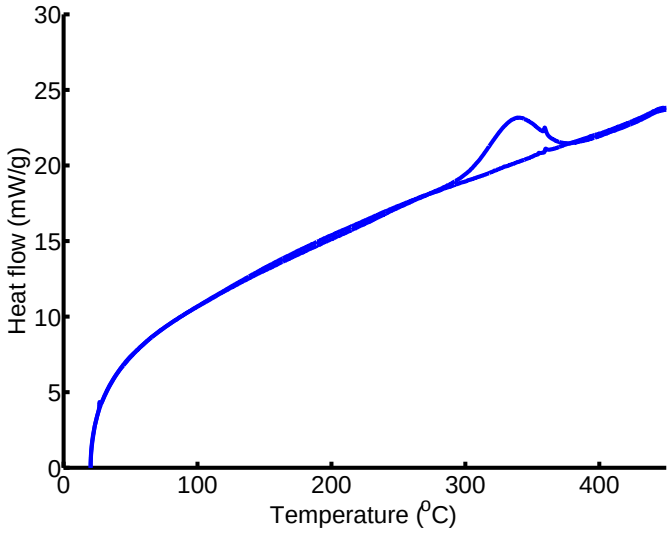

Figure 9.6: Heat flow of nickel cold rolled 95%

9.6 Results

9.6.1 Stored energy in cold rolled nickel

The results in the following section are described in more detail in G, hence the following will just summarize the main findings.

DSC measurements

The stored energy of nickel cold rolled to thickness reductions of 70%, 90%, 95% and 98% corresponding to von Mises strains of 1.4 to 4.5, was measured with the DSC. From the measurements it was found that the energy released during heating of the nickel samples displayed one peak associated with recrystallization and one minor peak associated with the Curie transition (see figure 9.6). Hence the energy released during heating of nickel was due to recrystallization (annihilation of dislocations) and no significant energy release from vacancy annihilation or solely recovery was observed.

This is somewhat different from earlier calorimetry measurements conducted on nickel, where peaks associated with vacancy annihilation, recovery and recrystallization (Clarebrough et al., 1955), (Michell and Lovegrove, 1960) were observed. The difference is attributed to annihilation of the vacancies during deformation in the current study.

Lab	Thickness reduction (%)	ε_{vM}	E_{stored}(MJ/m^3	σ	SE
Risø	70	1.4	9.3	1.1	0.64
Risø	90	2.7	12.5	1.3	0.78
Risø	95	3.5	14.2	1.89	1.09
Risø	98	4.5	15.2	1.5	0.86
Tsinghua	70	1.4	7.7	-	1.16
Tsinghua	90	2.7	10.9	-	1.64
Tsinghua	93	3.1	12.5	-	1.88
Tsinghua	96	3.7	13.6	-	2.04
Tsinghua	98	4.5	17.8	-	2.67

Table 9.2: Stored energy of nickel measured by DSC

The observation of only one peak associated with recrystallization furthermore justifies the assumption that only dislocations are considered, when the stored energy is calculated from the microstructure in section 9.3.1.

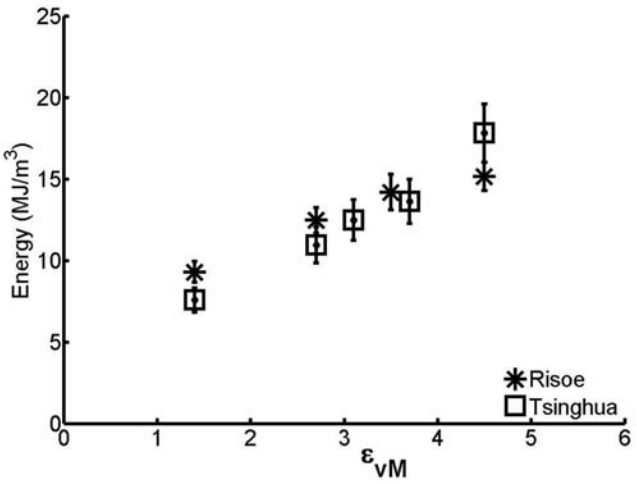

Figure 9.7: Stored energy of nickel as a function of strain, Risø plus Tsinghua data

The stored energy measurements of nickel at the different strain levels are given in table 9.2 together with the standard deviation (SE) of the measurements and the standard error. The data obtained at Tsinghua University are also displayed in table 9.2. The sample error observed in the Risø experiment were between 5% and 10%, based on this, the Tsinghua sample error was es-

timated to 10%. All stored energy measurements are plotted as a function of strain in figure 9.7 together with error bars of the respective measurements. From this figure, a good correspondence between the two sets of data are seen, especially when the experimental uncertainties are taken into consideration. A weighted average of all data measured more than once is therefore calculated and displayed in figure 9.8 together with a linear least square fit of the data.

The linear least square fit determines the relation between stored energy and strain to be well described by the linear relation:

$$E = 2.3 \cdot \varepsilon_{vM} + 5.9 \tag{9.25}$$

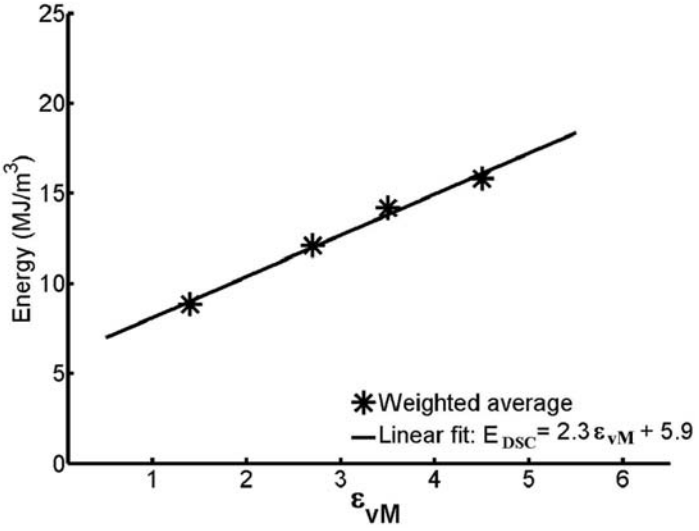

Figure 9.8: Weighted average of all stored energy measurements of nickel as a function of strain

TEM measurements

The microstructure of the specimens cold rolled 70%, 90% and 98% were characterized in the TEM in (Hughes and Hansen, 1993) and (Hughes and Hansen, 2000). Based on these measurements, the stored energy represented by the microstructure was calculated by two slightly different methods as described in 9.3.1. The average microstructural values determined in the TEM and the following stored energy calculations are given in table 9.3, and the

Reduction	70%	90%	98%
Strain	1.4	2.7	4.5
θ_{av}^{IDB} ($^\circ$)	2.2	2.7	3.0
θ_{av}^{GNB} ($^\circ$)	7.9	14.8	19.7
$D_{av}^{IDB}(\mu m)$	0.42	0.39	0.31
$D_{av}^{GNB}(\mu m)$	0.28	0.21	0.13
$S_v^{IDB}(\mu m^{-1})$	3.1	3.13	3.95
$S_v^{GNB}(\mu m^{-1})$	4.36	5.82	9.19
$E_{IDB}, average(MJ/m^3)$	1.09	1.26	1.70
$E_{GNB}, average(MJ/m^3)$	3.02	4.66	7.58
$E_{tot}, average(MJ/m^3)$	4.12	5.93	9.28
$E_{tot}, distribution(MJ/m^3)$	3.29	4.88	8.16

Table 9.3: Microstructural parameters and the stored energy values calculated based on these.

calculated stored energies are also displayed in figure 9.9.

From figure 9.9 a linear relationship between the calculated stored energies and strain is seen, as also observed in the DSC measurements. Furthermore the stored energies calculated based on the average parameters are higher than the stored energies calculated from the distribution of misorientation angles, while the slope is almost similar. In the following, the energies obtained from the distribution of misorientation angles are used for further analysis, as these are taken to be the most correct one.

Discussion

The stored energy in nickel was found to increase linearly with strain irrespective of the energy being calculated from microstructural parameters or measured by the DSC. The values of stored energy are given in table 9.4, from which the following is noted. The stored energy measured by the DSC is generally higher than the stored energy estimated from the microstructure and the ratio between the two decreases with increasing strain.

Previous work on stored energy has found a similar difference between stored energy evaluated form the microstructure (dislocation density) versus DSC measurements (Ungár et al., 1984), (Ungár et al., 2006), (Michell and Lovegrove, 1960). The difference between the two stored energy evaluations will be addressed in the following.

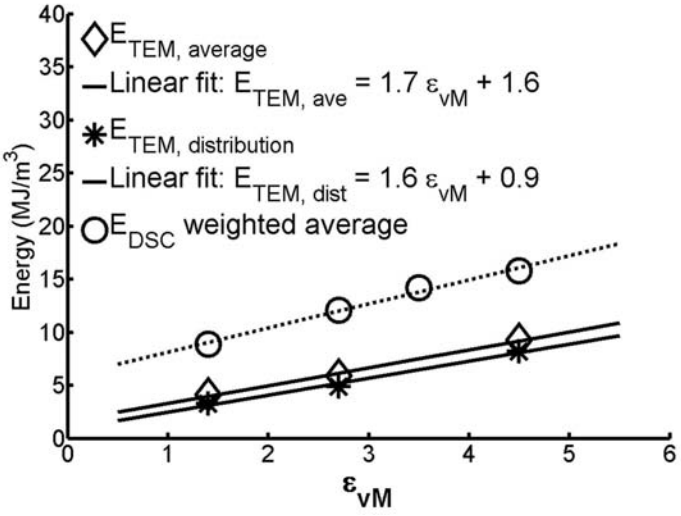

Figure 9.9: Stored energy calculated based on the microstructure as a function of strain

DSC measures all the energy released, contrary to the TEM measurements/calculations, which only evaluate the energy contribution from dislocations. Hence if vacancy annihilation occurred this would contribute to the energy measured by the DSC but not to the energy measured/calculated from the TEM observations. Since vacancy annihilation was not observed in the DSC measurements, this can not be the reason for the observed difference between the DSC and TEM data.

The stored energy calculations based on the microscopical measurements conducted in the TEM, assumed the microstructure to be a low energy dislocation structure, i.e. it is assumed that the structure does not contain any long range internal stresses and redundant dislocations. Furthermore any contribution from loose dislocations was taken to be negligible.

An estimate of the density of loose dislocations was given in (Hughes and

Energy/Reduction strain	70%	90%	98%
E_{DSC}(MJ/m^3)	8.9	12.1	15.8
E_{TEM}(MJ/m^3)	3.3	4.9	8.2
E_{DSC}/E_{TEM}	2.7	2.5	1.9

Table 9.4: Stored energy of nickel, measured and calculated

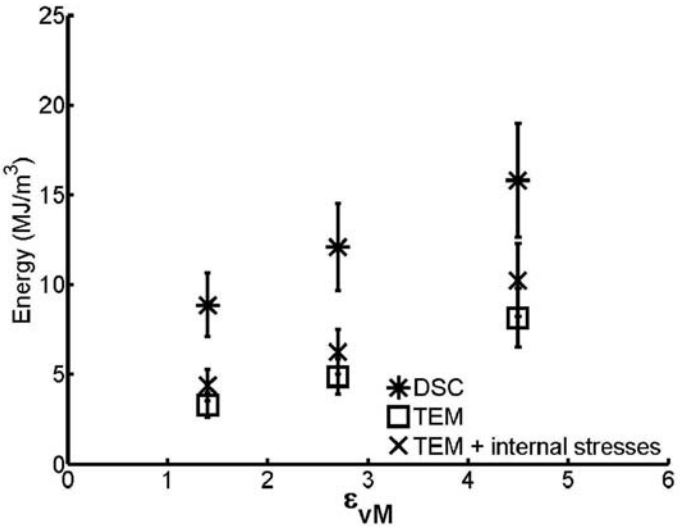

Figure 9.10: Stored energy as a function of strain

Hansen, 2000), to be less than one dislocation per cell volume at 98% strain. This corresponds an energy contribution of $0.24 MJ/m^3$, which is insignificant compared to energy difference observed (see appendix G). Hence the dislocation density of loose dislocations does not explain the discrepancy between the stored energies calculated from DSC and TEM data.

The observation, that the ratio E_{DSC}/E_{TEM} in stored energy decreases with strain, indicates, that the observed difference, might be related to the description of the low strain microstructure. The microstructure consists of IDBs and GNBs, in which the fraction of high angle GNBs increases with strain, i.e. there is a transition from low angle boundaries to high angle boundaries. The Read-Shockley formalism assumes all dislocations in the low angle boundary contribute to the misorientation angle, while high angle boundaries are considered as having a constant energy per unit area. If however dislocations exists, which mutually screen each other without contributing to the misorientation angle of the (low angle) boundary (redundant dislocations) (Kuhlmann-Wilsdorf, 1989)), these redundant dislocations, would not be accounted for in the TEM measurements, but would in the DSC measurements, and their relative contribution would be reduced with strain, and thereby this would be a possible explanation of the decreasing discrepancy in the E_{DSC}/E_{TEM} fraction with strain. Such boundaries have furthermore been observed in high resolution TEM of low angle boundaries in copper (Ikeda et al., 2004).

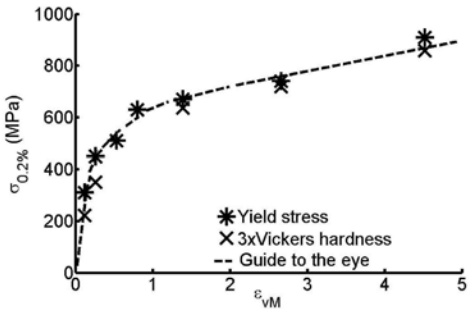

Figure 9.11: Flow stress of cold rolled nickel measured in tension and hardness measurements from (Hughes and Hansen, 1993)

Another possible contribution to the stored energy not considered in E_{TEM} is the energy associated with the junction between the GNBs and IDBs. The structure of low angle boundaries has been observed to be distorted in the vicinity and at the junction of high angle boundaries (Jones et al., 1979). This distortion might present more energy in the structure, than accounted for by the E_{TEM} calculations based on the Read-Shockley formalism.

A final possible contribution to E_{TEM} is the presence of internal long range stresses, which is evaluated in (Hansen and Kuhlmann-Wilsdorf, 1986) and here approximately by $0.5 \cdot \sigma^2/E$, based on flow stress data from Tsinghua (described below and illustrated in figure 9.11). By doing so the internal stresses corresponds to 25% - 35% of E_{TEM}, which increases the stored energy values significantly. In figure 9.10 E_{TEM}, E_{DSC} and $E_{TEM+internalstresses}$ are plotted as a function of strain, and error bars given by 20% of the value determined. From the figure it is seen, that at increasing strain, the DSC and TEM values approach each other, especially when internal stresses are also accounted for and the experimental uncertainties are taken into consideration.

The flow stress of the nickel deformed by cold rolling was measured in tension at Tsinghua University, and the data are given in figure 9.11 together with literature values from (Hughes and Hansen, 1993). The flow stress curve initially increases parabolically with strain, whereafter a linear relations ship between flow stress and strain is observed. This is characteristic for initially stage III followed by stage IV work hardening. The transition from stage III to stage IV work hardening is determined approximately from the figure to

be at a von Mises strain of 1-1.5.

By assuming linear work hardening in the region 1.4 ε_{vM} to 4.5 ε_{vM} the instantaneous energy stored compared to the energy expended can be evaluated by equation 9.26 described in detail in appendix G:

$$\beta = \frac{dE}{dW} \Rightarrow \frac{m}{\sigma} \tag{9.26}$$

where m is the slope of equation 9.25 and σ the flow stress. As m=2.3 and σ increases from 670MPa to 910MPa, the initial energy stored in stage III/IV is 0.3% of the expended energy, which drops to 0.2% further into the stage IV work hardening regime.

This decrease in energy storage may reflect the dominant storage mechanisms in the two strain hardening regimes. In stage III dislocations are stored in dislocation boundaries, where as in stage IV an increasing amount of high angle boundaries is formed. In these high angle boundaries dislocations may be absorbed and annihilated, which thereby leads to a lower energy storage rate.

Conclusions

The stored energy measured in nickel cold rolled 70% to 98% by DSC and evaluated from microstructural characterization in the TEM, leads to the following conclusions:

- The main energy released during deformation is released during recrystallization, hence vacancy annihilation and recovery does not contribute significantly to the stored energy
- The stored energy in nickel increases linearly with strain in the stage IV work hardening regime, irrespective of the method used to evaluate the stored energies
- The energy measured by DSC is higher by a factor of 1.9 to 2.7 than the energy calculated from TEM measurements, and the ratio between the two decreases with strain
- The deviations between the two methods may relate to the description of the low angle dislocation boundaries and indicates presence of long range stresses

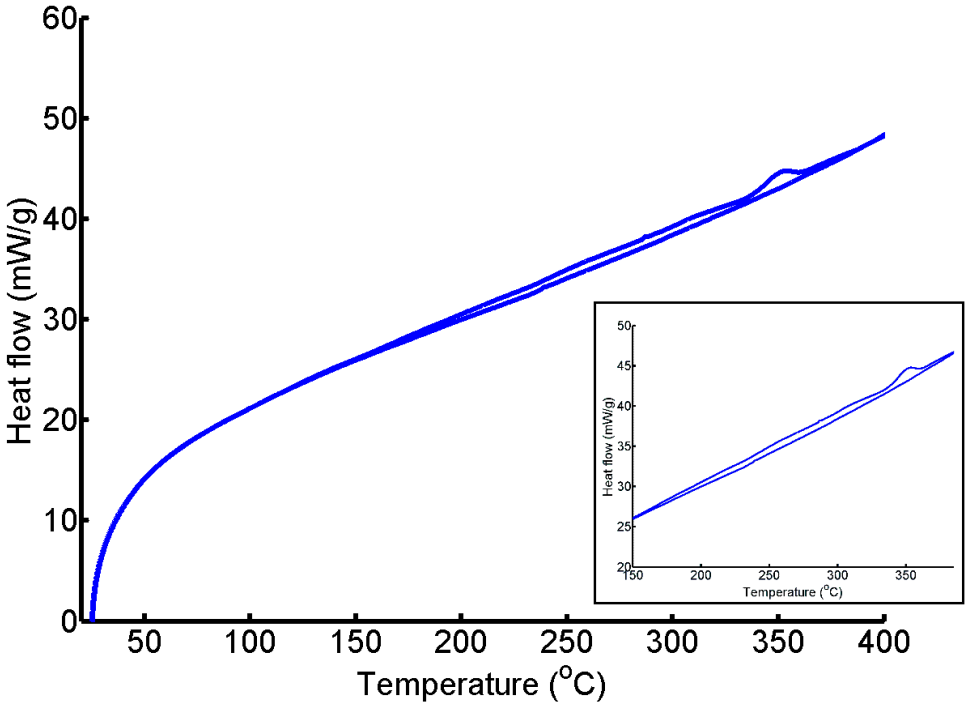

Figure 9.12: Heat flow during annealing of a 90% cold rolled aluminium

9.6.2 Aluminium cold rolled 90%

In the following section the feasibility of measuring stored energy with DSC in initially cold deformed aluminium and then hot deformed aluminium is described.

DSC measurements

A representative heat flow curve obtained during annealing of cold rolled aluminium is shown in figure 9.12. In this the recrystallization is initiated at 339°C and in the current curve an energy release of 0.44 J/g was measured. From the annealing curve, two observations are important. First the recrystallization peak is not pronounced compared to the basis line. Second the basis line, deviates from the first measured curve, as observed in copper, but here the deviations are comparable in area to the recrystallization peak. The average stored energy measured in cold rolled aluminium was 0.4MJ/m^3 (σ_{stdv}=0.03), based on 5 measurements.

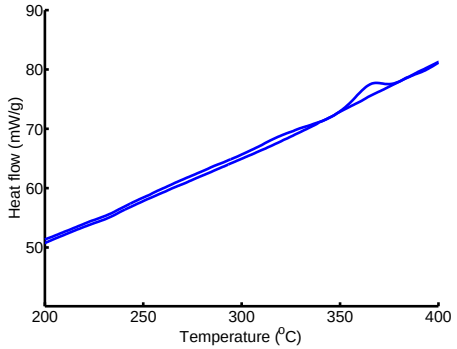

Figure 9.13: Heat flow during annealing (10K/minute) of cold rolled aluminium.

Discussion

The stored energy in AA1050 was determined to be 0.4MJ/m^3, and the heat flow curve showed one peak due to recrystallization. The peak area was however, not significantly different from the deviation between the base line and the measured signal observed from 150°C and until recrystallization.

The heat flow curve of calorimetric measurements of high pure aluminium (99.99% pure) compressed 75% in (Clarebrough et al., 1961) is similar to what is observed in the current study, in that above 100°C to approximately 250°C a constant signal was detected, while between 250°C and 350°C a recrystallization peak was observed. The energy released prior to recrystallization was estimated to be 35% of the total stored energy, and the total stored energy was 1.36MJ/m^3.

This indicates, that the deviation between first and second heating curves observed and illustrated in the insert of figure 9.12 is not only a consequence of uncertainties in experimental conditions, but might also be due to a significant amount of recovery during heating. If this is so, DSC measurements conducted with a higher heating rate, would lead to a larger amount of energy released during the recrystallization compared to measurements conducted at lower heating rates.

Experiments with a heating rate of 10K/minute were therefore conducted in order to explore the effect of heating rate and the heat flow curve is displayed in figure 9.13. Based on 3 such measurements an average stored energy of 0.59MJ/m^3, was determined. This is higher than the previous result, and

corresponds well to the observation of recovery during heating.

Taking the difference between the curves in figure 9.12 is due to recovery and recrystallization, integration of the area difference from 100°C and until 375°C would give an estimate of the total energy release. This corresponds to an average stored energy of 2.1MJ/m^3, which is more similar to the stored energy of 1.36MJ/m^3 determined by (Clarebrough et al., 1961), in aluminium deformed 75%.

The stored energy of AA1050 cold rolled 70% [3] has also been measured in a DSC by (Taheri et al., 2006) at an average heating rate of 50K/minute. In this study the energy was determined to be 0.293MJ/m^3, which is in the same region, as the energy found in current study, without considering recovery.

In (Godfrey et al., 2005) the energy stored after cold rolling of aluminium (99.99% pure) was calculated based on average microstructural data obtained in the TEM, as described in section 9.3.1. In this investigation the stored energy after 90% reduction was estimated to be 1.4MJ/m^3. This is a factor 3.5 larger than that observed in the current DSC measurements, and the tendency is opposite to what is observed in nickel, where the DSC stored energy measurements were larger than those estimated based on microstructural parameters. If however, the estimate of stored energy released during recovery and recrystallization is used, the stored energy values obtained from the microscopical characterization is 1.5 times lower, than the DSC measurement, which is in agreement with the observation from nickel.

From the above, it is concluded that the measured stored energies in aluminium are lower than anticipated, which could be due to recovery during heating. To improve the measurements, measurements would have to be conducted at yet higher heating rates or maybe under isothermal conditions. As the apparatus used did not allow for significant higher heating rates, and isothermal measurements were not an option, it was not possible to reduce the amount of energy released during recovery any further.

The initial intention of the experiments was to explore the possibility of measuring the stored energy in deformed aluminium and preferably hot deformed aluminium. This was investigated in aluminium cold rolled 90%,

[3]The reduction is not given in the article, the reduction given here is estimated form the stress given

Metal	Cu		Ni	
Heating rate (K/minute)	5	50	5	50
E_{stored}(J/g)	0.754	0.759	1.648	1.678
Difference	0.7%		1.8%	

Table 9.5: Stored energy measurements from NETSCH

which is the sample anticipated to contain the highest amount of stored energy, of aluminium deformed from 10% to 90% by cold rolling or in hot plane strain compression. The measurements however were on the edge of the capabilities of the apparatus, hence further measurements on lower strain specimens were not conducted, and measurements on hot deformed aluminium was not initiated.

Conclusions

The measured stored energy in commercial purity aluminium cold rolled 90% determined from the recrystallization peak, was lower than anticipated from microstructural investigations and other calorimetric measurements. This was attributed to energy release during recovery.

The signal obtained in the DSC was on the edge of the trustworthy detection limit of the apparatus, and as the stored energy of hot deformed aluminium is expected to be lower, than the cold deformed material, experiments were not conducted on the hot deformed material, nor on samples cold strained less.

9.7 Discussion

In the above, the heat flow curves of aluminium, copper and nickel were obtained in a heat flux DSC at a constant heating rate.

9.7.1 Method

These heat flow curves can be used to evaluate the dominant processes at a given temperature, i.e. vacancy annihilation, recovery and recrystallization. In the current study only recovery and recrystallization were observed, and

the main energy stored in nickel and copper was released during recrystallization. The energy released during recovery at lower temperatures in these metals can not however be excluded, but the effect was less significant compared to observations in aluminium. This is furthermore supported by stored energy DSC measurements conducted at NETSCH application laboratory given in table 9.5, in which different heating rates have been applied. From the table it is clearly seen, that a 10 fold increase in heating rate, does not alter the measured stored energy in copper and nickel.

In aluminium the area difference between the heat flow curve and the basis line, was comparable to the area of the recrystallization peak, and when the measured stored energies were compared to values obtained from microscopical analysis, the values were lower, opposite to the observation in nickel. A rough estimate of the total energy released during annealing and recrystallization of aluminium also did give a higher stored energy, which indicates, that a significant amount of the stored energy in aluminium is released during recovery. This makes it more difficult to measure the total stored energy by the chosen calorimetric method.

Another method of stored energy measurements has been shown by (Guiglionda et al., 2004). In this study stored energy measurements on hot deformed aluminium by the use of synchrotron radiation, has proven, not only to be able to measure the dislocation density (stored energy) of hot deformed aluminium, but also the stored energy of the individual texture components. A difference in stored energy of hot deformed aluminium grains with in the S texture compared to other texture components was found .

9.7.2 DSC versus microstructure (TEM)

Characterization of the stored energy in nickel measured by both TEM and DSC established a general difference, which decreased with increasing strain. This was rationalized as being due to the Read-Shockley description of the low angle dislocation boundaries being too simple (or idealized), possible junction energy between GNBs and IDBs and the presence of internal stresses. These findings illustrates the extra information, which becomes available, when bulk stored energy is measured and compared to the corresponding microstructure.

It is therefore suggested, that the characterization of deformation microstructures is supplemented with stored energy measurements, where possible.

9.8 Conclusions

Based on the stored energy measurements, it is concluded that the main energy release in copper and nickel is during recrystallization, while a non negligible amount of stored energy, is also released during recovery in aluminium.

The measurement of stored energy facilitates the characterization of the microstructure, as illustrated by the nickel measurements.

Reliable stored energy measurements from aluminium were difficult to obtain, due to recovery, hence stored energy measurements from aluminium, are not advisable using the current apparatus.

Part III

Localized deformation

Chapter 10

Localized deformation - Lüders bands in Armco Iron

10.1 Introduction

The development of the 3D-X-Ray Diffraction microscope (3D-XRD) at the Center for Fundamental Research: Metal Structures in 4D in cooperation with the European Synchrotron Radiation Facility (ESRF) has extended the knowledge of the bulk properties of polycrystals (Margulies et al., 2001), (Poulsen et al., 2003), (Winther et al., 2004b). In particular metals with a fcc crystal structure deformed at room temperature have been the object of extensive studies.

A study made abroad during the current investigation intended to use this newly developed microscope, to explore the rotation of the individual grains during hot tensile deformation of the aluminium alloy described in part I of the thesis. The aim was to see if other slip systems are activated during hot deformation. However due to delay with equipment from the supplier, the purpose of the experiments was shifted to investigate localized deformation - known as Lüders bands , which are observed during tensile testing of Armco Iron. Localized deformation is a general phenomenon observed during plastic deformation in metals and alloys, where zones of concentrated glide within the deformation structure are observed. The localized glide regions are important for understanding the evolution of plastic deformation structures.

The grain rotation in fcc metals at low strains, has been correlated with the initial orientation of the grains and thereby the active slip systems (Winther et al., 2004b). It is therefore anticipated that a similar correla-

tion would exist in bcc metals. In bcc metals the primary slip systems are slip along $<1\bar{1}1>$ directions on the $\{110\}$ planes, i.e. the opposite to fcc metals. The grain rotation is expected to be the same but opposite to the one observed in fcc metals.

Iron is a bcc metal which in its slightly impure state displays an inhomogeneous plastic deformation know as Lüders bands . Lüders bands can be viewed as a wave of plastic deformation, which travels through the unstrained material, leaving behind material strained to a characteristic strain - the Lüders strain (Häner, 1994). The Lüders bands can be observed as a macroscopical front inclined around 45° to the tensile axis, marking the transition between the deformed and un-deformed regions of the metal.

During tensile testing of iron, the metal deforms elastically followed by an upper yield point, which is relaxed during nucleation of Lüders bands and the stress drops to the lower yield point. The Lüders bands thereafter travel through the sample at a constant stress, i. e. no work-hardening is observed. When the Lüders bands have transversed the entire sample, the sample has been strained by the Lüders strain and further straining results in work-hardening.

Lüders bands have been described by (Cottrell and Bilby, 1949) as due to dislocations being pinned by impurities. Impurities are attracted to the dislocations, due to the strain imposed by the dislocations in the crystal lattice. During straining the dislocations pinned by the impurities, will be released when the stress is high enough, which in iron is at the upper yield point. The dislocations are thereafter free to move through the grain at a lower stress, the lower yield stress, thereby creating plastic deformation. The dislocations are blocked at grain boundaries, and the pile up of dislocations at boundaries eventually creates a large enough stress, for activation of dislocation movement in the neighbouring grain. This theory also explained the observation, that the lower yield stress is grain size dependent as given by the Hall-Petch relationship presented in equation 2.1 (Weertmann and Weertmann, 1968), (Hall, 1951), (Armstrong et al., 1962)

Another explanation by (Hahn, 1962), suggests that Lüders bands are a consequence of a rapid dislocation multiplication and the stress dependency of the velocity of dislocations. Lüders bands have been found to depend not only on the purity, but also the specimen geometry, deformation speed, grain size and material (Ananthan and Hall, 1991) (Moon, 1971), (Sylwestrowicz and Hall, 1951).

10.1.1 Aim

According to (Hutanu et al., 2005) the textural evolution in the Lüders region continues during the following work hardening region, which indicates, that the deformation process in the Lüders region is similar to the work-hardening region. The aim of this study was two fold. Initially to explore if grain rotations during straining of a bcc metal exhibit any dependency of the initial orientation of the grain and to determine if the localized deformation observed in the Lüders region is similar to the one in the region of work-hardening.

10.2 Experimental

10.2.1 Specimen preparation

High purity iron (99.9% pure) - Armco iron was chosen as the material. The material has been characterized by (Jargo and Hansen, 1986) and displays Lüders bands during deformation.

Armco iron samples was machined to a "dog bone" shape in the Risø work shop, the dimensions of the body of the sample were 1.5mm x 8mm 45mm. The initial grain size of the samples was 25μm. After machining the samples were heat treated at 600°C for 4 hours, to reach an average grain size of 50μm [1] and an almost random texture. This sample geometry and grain size was chosen to fulfil the criteria of a minimum thickness to ensure bulk conditions, a geometry to fit the possible experimental conditions in the 3D-XRD (Poulsen et al., 2003) and the right geometry for nucleating single Lüders bands (Ananthan and Hall, 1991).

10.2.2 Mechanical testing - Characterization of Lüders bands

The Lüders region was characterized by tensile testing of similar material prior to the 3D-XRD experiment, in order to determined the Lüders bands region and the deformation conditions, i.e. strain rate and amount of strain.

[1] measured with the linear intercept method

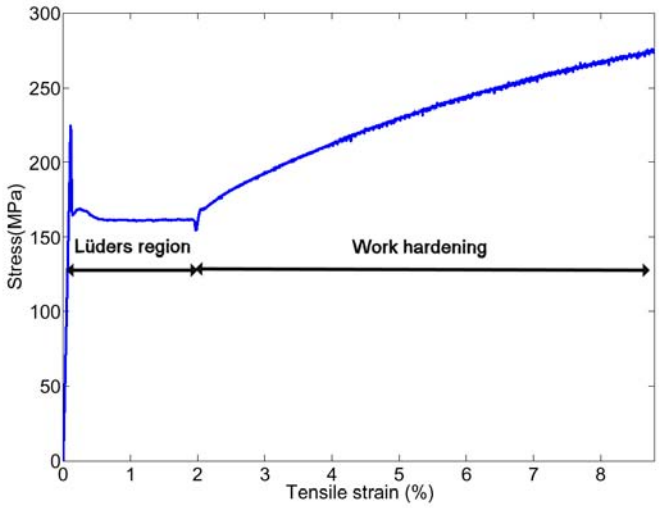

Figure 10.1: Stress strain curve of Armco Iron

After this tensile tests were conducted in the intended mode for data collection at ESRF.

Mechanical setup

Tensile testings in house were conducted on a stress rig from Instron (85R 8032) with a 5kN load cell. The deformation was conducted in strain control using a 25 mm gauge length extensometer connected to the Instron Software: Wave Maker and a strain rate of 1% strain per minute was used

Data

A representatively stress-strain curve is seen in figure 10.1. In this the deformation behaviour can be characterized by 3 different regions. Initially the iron deforms elastically and the elastic region is terminated at the upper yield stress at 225MPa followed by a lower yield stress of 160MPa, where the Lüders bands travel through the sample. The Lüders region is terminated at a strain of 2% were a small drop in the stress/strain curve is seen. After this the stress increases due to work-hardening, and as the stress reaches values close to the upper yield point, a serrated stress-strain curve appears.

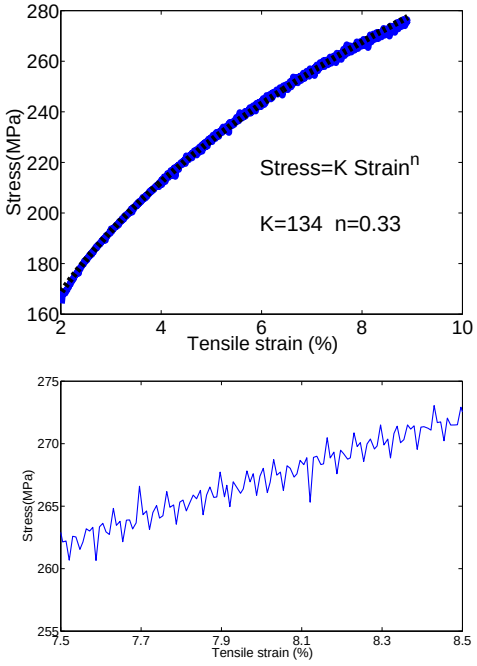

Figure 10.2: Top: The work-hardening region of the stress-strain curve fitted to a parabolic function. Bottom: Serrated flow of the stress strain curve

The work-hardening region was fitted to the empirical Holloman stress-strain relation: $\sigma = K \cdot \varepsilon^n$ The fit is displayed in the top curve in figure 10.2, from which it can be seen that Armco iron above 2% strain displays a parabolic stress-strain curve characteristic of stage III work-hardening. A serrated stress-strain curve, is furthermore displayed in figure 10.2. Serrated stress-strain curves are seen in metals showing ageing effects and yield points. A serrated stress-strain curve is a result of a continuous ageing and straining of the material (Cottrell and Bilby, 1949).

10.2.3 Macroscopical evolution of Lüders bands

From the stress-strain curve depicted in figure(10.1) the Lüders strain was found to be 2%, which also was confirmed in several deformation tests. During straining of the specimen pictures were taken, in order to record the macroscopical evolution of the Lüders bands. A snap shot of these images can be viewed in figure 10.3

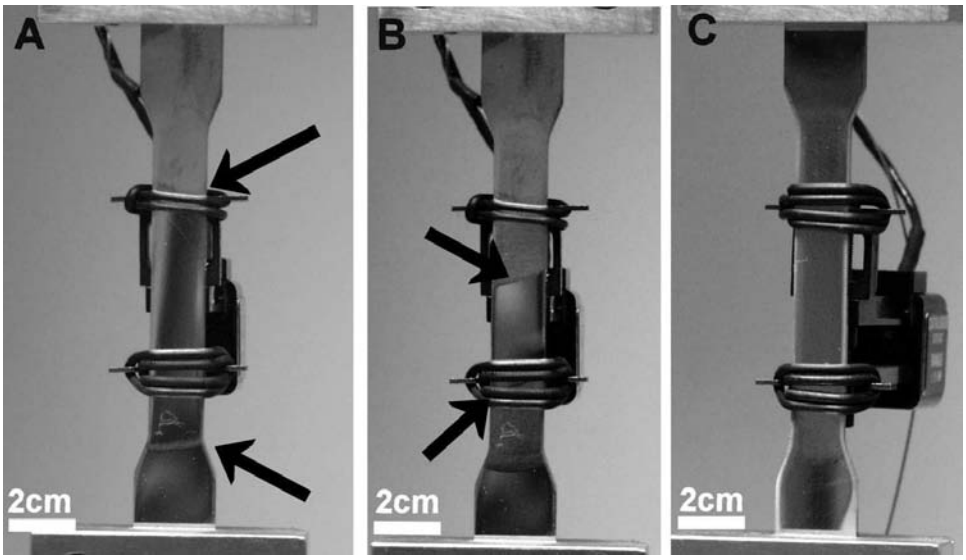

Figure 10.3: Stress-strain curves of Armco iron strain 2%

In image A the nucleation of the Lüders bands is illustrated. Two single parallel Lüders bands are formed, one from each shoulder of the specimen. The fronts of the Lüders bands formed are marked with arrows in the image. The Lüders bands nucleated in the lower shoulder has just formed, while the one from the upper shoulder, has travelled a short distance. In image B the Lüders bands are seen after further straining. The fronts of the Lüders bands are marked with arrows, and it is seen, that the fronts have angles of approximate 65° to the tensile axis. At a strain of 2% the Lüders bands from each side meet and annihilate and the entire gauge length of the sample has been strained 2%. A deformed sample is illustrated in figure 10.3 C. 9 samples where tested, all nucleated 2 Lüders bands one from each side. The Lüders bands were inclined to the tensile axis, with an angle changing with strain. As the strain approaches the Lüders strain however, the angle was between 50° and 55° . Parallel Lüders bands were nucleated in 8 out of the 9 tests.

10.2.4 Mechanical testing during data recording

From the above it was concluded, that the Lüders region is terminated at a strain of approximately 2%. This was therefore chosen as the strain step in between which data would be recorded, at the 3D-XRD in Grenoble. Data recording at the 3D-XRD microscope takes on average 6 hours per strain

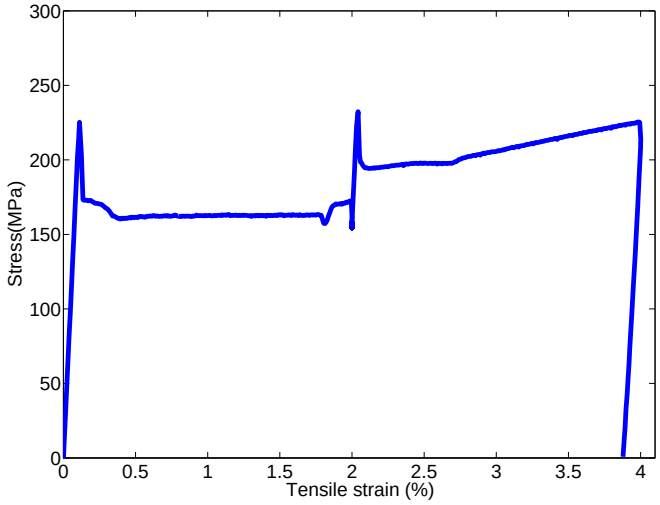

Figure 10.4: Stress-strain curves of Armco iron strain in steps of 2% to 4%

step. Therefore two tensile tests were conducted with a time scale mimicking the experimental conditions, that is straining to 2% maintaining the strain for 6 hours and then straining 2% more etc. This was done until a strain of 6%. 6% is the upper limit of what is possible in aluminium before the diffraction spots overlap, and data analysis is impossible and it was therefore expected that the same applied to Armco Iron during tensile testing. One of the curves is seen in figure 10.4.

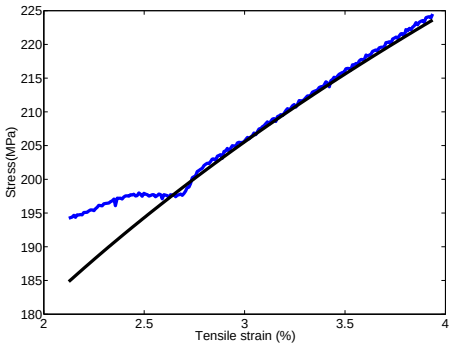

Figure 10.5: Stress-strain curve of Armco iron strained to 4%

In this figure the initial stress-strain curve is identical to the curve seen in figure 10.1, apart from the fact that the Lüders strain is at 1.8%. When the samples are strained further, a new slightly higher upper yield stress appears after which the stress-strain curve increases initially in a somewhat irregular manner. The stress-strain curve at strains above 2% is seen in figure 10.5, together with the Hollomon function determined in section 10.2.2, the function however is displayed 13 units higher in y in order to fit the stress-strain curve.

By comparing the two curves, it is seen that the stress-strain curve at strains above 2.8% are quite well described by the Hollomon function, hence this region might correspond to ordinary work-hardening.

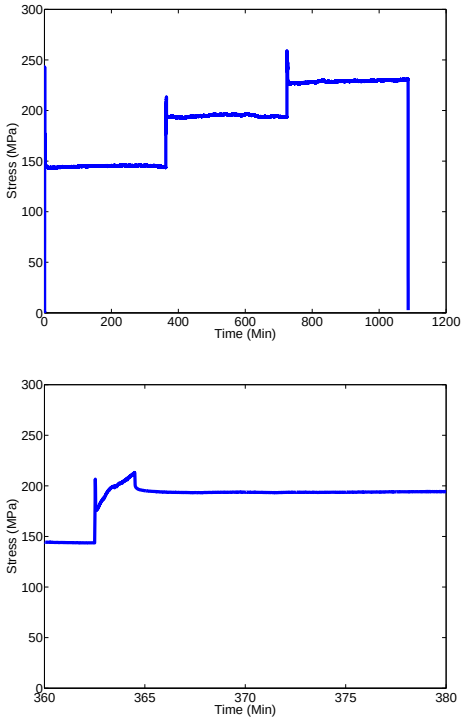

Figure 10.6: Stress-strain curves of Armco iron strained to 4%

The region below 2.8% displays a peculiar behaviour in that initially the stress-strain curve increases almost linearly followed by a plateau. Visually it was observed that new Lüders bands bands were formed, the stress-strain curve therefore probably reflects deformation by both work-hardening and a second Lüders band up to a strain 2.8% after which only work-hardening occurs. The return of yield points and Lüders bands are known to occur (Cottrell and Bilby, 1949).

Relaxation during data recording

When the specimen is fixed in the stress-rig at a constant strain, the force decreases due to relaxation in the iron structure. This relaxation was investigated to determine the time scale of the relaxation. In figure 10.6 stress/time curves from tensile tests of Armco iron are shown. From the curves, it is seen that yield points are observed every time deformation is preformed after the 6 hours of waiting. From the lower curve in figure 10.6, it is furthermore seen, that after the straining (2 minutes) the structure relaxes within 5 minutes Hence no changes in the iron sample occurs in the following 6 hours where data were recorded.

10.2.5 Lüders bands in Armco iron - settings for tensile tests

Based on the experiments described above following were concluded:

- The "dog bone" shaped Armco iron samples, with dimensions 1.5mm x 8mm x 45mm and a grain size of 50μ m displayed 2 single Lüders bands when tensile deformed at room temperature at a strain rate of 1% per minute.
- 2 Lüders bands were nucleated one on each side of the specimen
- The Lüders region corresponded to a strain of 2% under current conditions.
- The yield point and Lüders bands reappeared after 6 hours.
- Relaxation occurred after 5 minutes.
- The tensile tests in the 3D-XRD were to be deformed up to 6% in steps of 2% with a strain rate of 1% per minute.

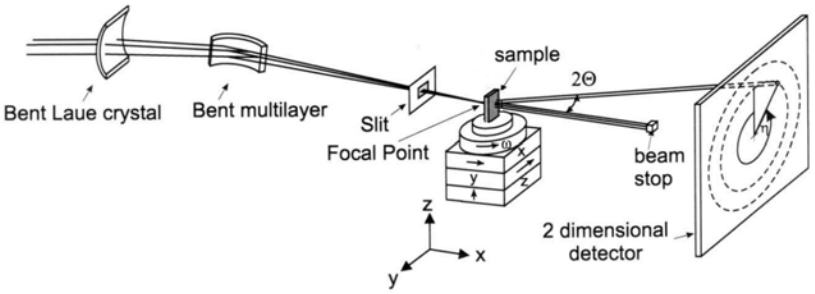

Figure 10.7: Setup in the 3D-XRD (from (Gundlach et al., 2004))

10.3 Grain rotation of Armco iron measured by synchrotron radiation

10.3.1 Principle of the 3D-XRD in deformation mode

The principle behind the 3D-XRD microscope, is the possibility of obtaining and analyzing diffraction spots on a 2D detector from the individual grains in a polycrystal. In this way single crystal diffraction is used to obtain information of the individual grains in a polycrystal. The principle is sketched in figure 10.7.

The white beam from the storage ring enters the optics, where it is monochromised to a wave length of 77.7 keV, focused on the sample and restricted to a size of 20μm x 20 μm.

As the beam enters the sample a fraction of it is diffracted on the crystal planes inclined at the Bragg angle (given by equation 4.12). This gives rise to diffraction spots, recorded on the 2D detector placed close to the sample. As the beam is small and focused on the sample, only a limited number of grains diffract. Indexing of the 2D diffraction image makes it possible to calculate the orientation of the individual grains in the polycrystal. The diffraction conditions for bcc metals are listed in appendix A.

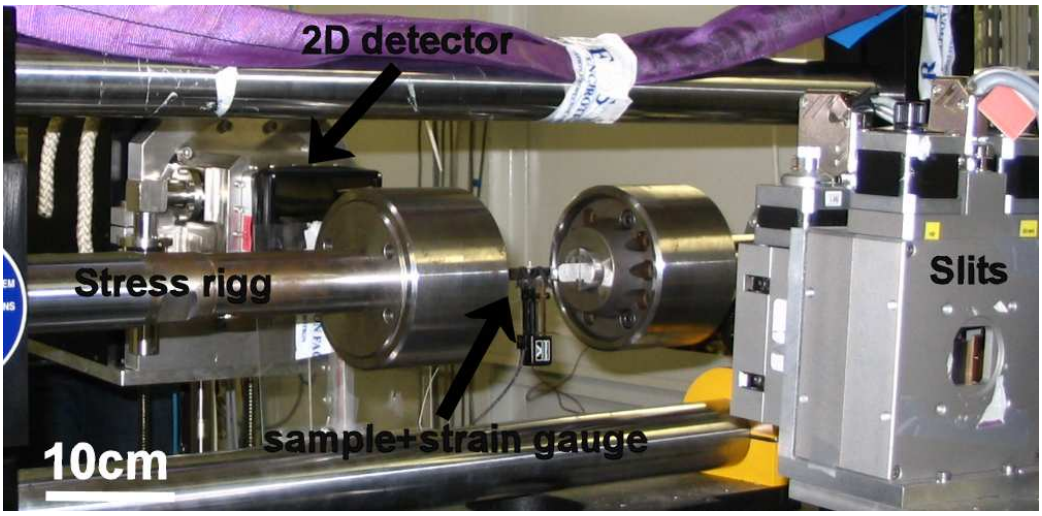

Figure 10.8: The setup for the deformation experiment

10.3.2 Deformation experiment

Setup

The specific setup used in the current study is displayed in figure 10.8. The stress rig (25kN from Instron) is placed on the translation and rotation tables sketched in figure 10.7 and the sample mounted in the grips with a strain gauge.

In front of the sample are slits used to define the size of the beam, and the 2D detector is seen behind.

Data acquisition

The sample was initially characterized by mapping 15 regions within the strain gauge prior to deformation, a method described in (Poulsen et al., 2003). Diffraction images were recorded from each region by rotating 55° around Z in steps of 0.25° . Diffraction images were recorded at each step. The sample was thereafter strained 2% with a strain rate of 1% per minute and the 15 regions were mapped again and so on until a strain of 6% were reached.

Data

The raw diffraction images obtained were after the experiment corrected for spherical distortion and background in fit2D (Hammersley, 2008) and indexed in GRAINDEX (Lauridsen et al., 2001).

In figure 10.9 diffraction images obtained from random regions from the initial material, after 2% strain, 4% strain and 6% strain are seen. From the diffraction patterns it can be seen, that the individual diffraction spots widen as the sample is strained.

Another thing, which can be seen, is the large number of diffraction spots. Unfortunately after data analysis, it became clear, that the noise associated with the experiments was too severe for any reliable data analysis to be conducted. This was mainly attributed to the large rotation angle used (the noise scales with the angle) and due to the fact that the sample volume probed was not restricted to the central volume as it was in (Poulsen et al., 2003). Therefore no results emerge regarding grain rotation in Armco iron during tensile deformation.

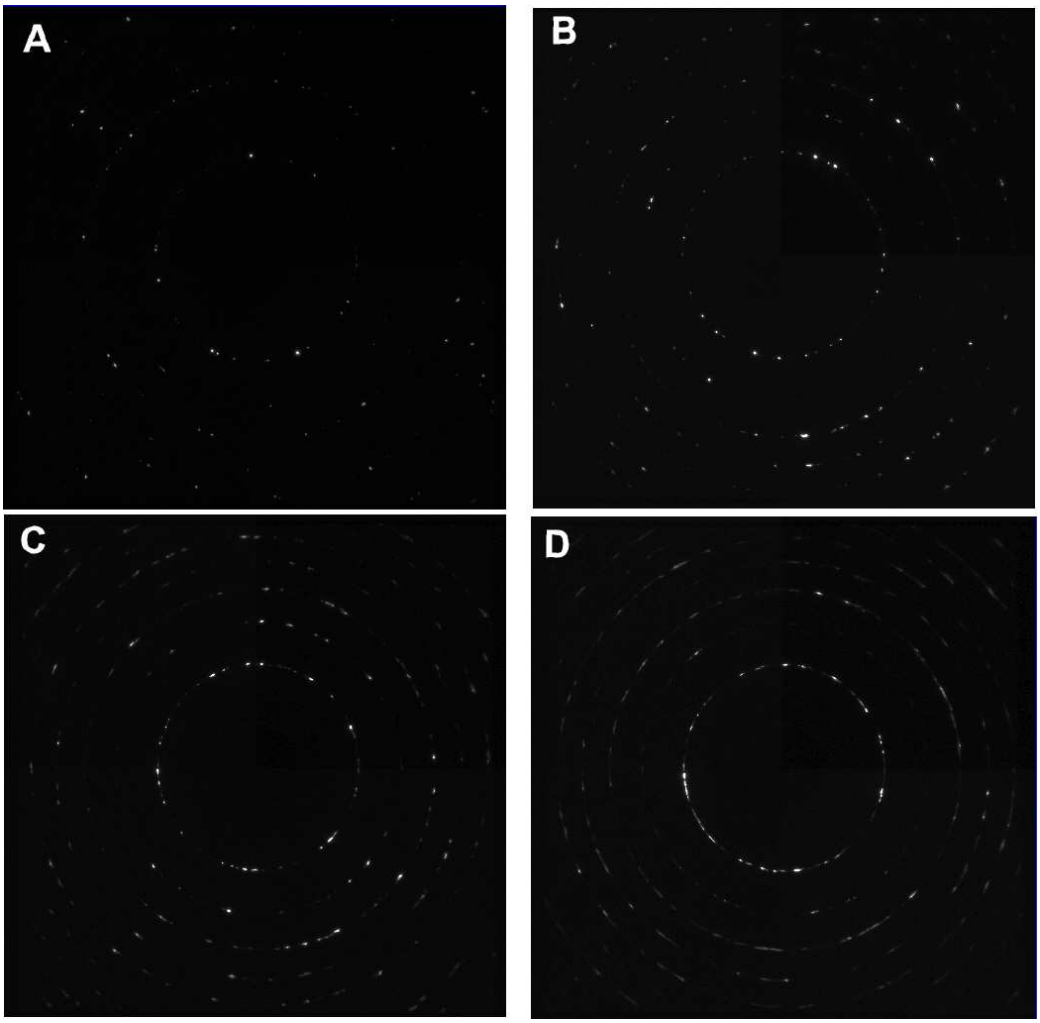

Figure 10.9: Diffraction image obtained from Armco iron sample A: undeformed B: 2% C:4% and D: 6%

Chapter 11

Outlook

The three parts of this thesis were designed to elucidate different aspects of plastic deformation. The findings of an orientation dependent hot deformed microstructure, the discrepancy between stored energy measured by calorimetry and evaluated based on microstructural characterization and the problem in data analysis of Lüders bands , all lead to conclusive findings, but also point to future investigations. Furthermore, the relationship between the three investigated subjects, i.e. hot deformation, stored energy and localized deformation is of interest.

The following is therefore suggested for future studies:

The possible activation of non-octahedral slip systems observed, may be finally concluded, by more studies of the dislocation boundaries crystallographic alignment at 500°C .

In the calculation of stored energy, based on the deformed microstructures, a better description might be obtained, if the grain orientation dependency of the individual grains is included, together with the bulk texture of the material. This would require quantitative studies of boundary spacings and misorientation angles of the individual grain orientations of the material studied in the current thesis.

Calorimetric stored energy measurements of single crystals or single grains compared to stored energy calculations, which takes the grain orientation dependency of the deformation microstructure into consideration, might also further the understanding of the difference observed between calculated and measured stored energies.

A more thorough description of the deformation structures evolved at high strain for both cold and hot deformation would be interesting. Recently, annealing of a cold deformed high strain structures have shown to enhance the structural differences observed in different texture components (Xing et al., 2006), indicating an orientation dependency of the high strain structures as well. Also here, stored energy measurements would be of interest.

Relations between texture, dislocation structures, flow stress and stored energy are of interest, since it was observed in the current study, that the evolution of both texture and dislocation structure morphology with strain did not lead to significant changes in the flow stress during hot deformation.

Reliable data of localized deformation might be obtained, in an experiment similar to the presented study by 3D-XRD, if the set-up used is modified by addition of a conical slit (see (Poulsen et al., 2003) for details). The localized deformation may be related to structural transitions and changes in flow stress, in cold as well as hot deformed materials.

Bibliography

www.crct.polymtl.ca/fact/xmltree/pdtree.php. *École Polytechnique de Montréal, Canada*, 2007.

V. S. Ananthan and E. O. Hall. Macroscopic aspects of lüders band deformation in mild steel. *Acta Metallurgical Materialia*, 39(12):2153–360, 1991.

S. S. Argon, S. Backer, F. A. McClintock, G. S. Reichenbach, E. Orowan, M. C. Shae, and E. Rabinowicz. *Mechanical behavior of materials*. Addison-wesley publishing company, INC. Reading, Massachusetts, USA, 1966.

R. Armstrong, I. Codd, R. M. Douthwaite, and N. J. Petch. The plastic deformation of polycrystaline aggregates. *Philosophical Magazine*, 7:45, 1962.

I. Baker and J. W. Martin. Effect of fine second phase particle on stored energy and recrystallization kinetics of cold rolled copper single crystals. *Metal Science*, 17:469–474, 1983.

I. Baker, L. Liu, and D. Mandal. The effect of grain size on the stored energy of cold work as a function of strain for polycrystalline nickel. *Scripta Metallurgica et Materialia*, 32:167–171, 1995.

B. Barcroix and J. J. Jonas. The influence of non-octahedral slip on texture development in fcc metals. *Textures and Microstrutures*, 8-9:267–311, 1988.

A. Bardal, I. Lindseth, H. E. Vatne, and Nes. E. Dislocation densities, subgrain sizes and subboundary misorientations within the different texture components of hot-deformed almgmn. In N. Hansen, D. Juul Jensen, Y. L. Liu, and B. Ralph, editors, *Proceedings of the 16th risoe international symposium on materials science: Microstructural and crystallographic aspects of recrystallization*, pages 261–266, 1995.

G. Bastue Christensen. *Let metaller - aluminium, magnium og deres legeringer*. Forlaget IVAR, 1949.

B. Bay, N. Hansen, and D. Kuhlmann-Wilsdorf. Deformation structures in lightly rolled pure aluminium. *Materials Science and Engineering A*, 113: 385–397, 1989.

B. Bay, N. Hansen, D. A. Hughes, and D. Kuhlmann-Wilsdorf. Evolution of f.c.c. deformation structures in polyslip. *Acta Metallurgical Materialia*, 40 (2):205–219, 1992.

M. B. Bever, D. L. Holt, and A. L. Titchener. *Progress in Materials Sciece*, volume 17. Pergamon Press Ltd., Headington Hill Hall, Oxford, first edition, 1973. ISBN 0 08 017011 0.

J. H. Beynon and C. M. Sellars. Strain distribution patterns during plane strain compression. *Journal of Testing and Evolution*, 13:28–38, 1985.

R. K. Bolingbroke, T. Furu, D. Juul Jensen, and K. Vernon-Parry. Annealing behaviour of dilute aluminium alloys following hot deformation. *Materials Science and Technology*, 12, 1996.

H. J. Bunge. *Texture analysis in materials science*. Butterworths., 1982.

W. Q. Cao, A. Godfrey, Q. Liu, and W. Liu. Deformation boundary characteris of high purity nickel revealed by dsc. Article draft from Thsinghua University, Beijing.

W. Q. Cao, A. Godfrey, and Q. Liu. Determining dislocation cell sizes for high-strain deformation microstructures using the ebsp technique. *Journal of Microscopy*, 211(219-229), 2003.

G. Christiansen, J. R. Bowen, and J. Lindbo. Electrolytic preparation of metallic thin foils with large electron-transparent regions. *Materials Characterization*, 49:331–335, 2003.

L. M. Clarebrough, M. E. Hargreaves, and G. W. West. The release of energy during annealing of deformed metals. *Proceedings of the Royal Society*, A 232:252, 1955.

L. M. Clarebrough, M. E. Hargreaves, and M. H. Loretto. Stored energy and electrical resistivity in deformed metals. *Philosophical Magazine*, 6: 807–810, 1961.

A. P. Clarke, F. J. Humphreys, and P. S. Bate. Lattice rotations at large second-phase particles in polycrystalline aluminium. *Materials Science Forum*, 426-432:399–404, 2003.

R. Colãs and C. M. Sellars. Effect of strain heterogeneity and adiabatic heating on the stress-strain behaviour of an austenitic stainless steel. *Proceedings of the 7th international conference on the strength of metals and alloys, Montreal, Canada*, 2:941–46, 1985.

R. Colãs and C. M. Sellars. Strain distribution and temperature increase during plane strain compression testing. *Journal of Testing and Evaluation*, 15:342–349, 1987.

A. H. Cottrell and B. A. Bilby. Dislocation theory of yielding and strain ageing of iron. *Proceedings of Physical Society Section A*, 62:49–62, 1949.

S. B. Davenport, N J. Silk, C. N. Sparks, and C. M Sellars. Development of constitutive equations for modelling of hot rolling. *Materials Science and Technology*, 16:539–546, 2000.

R. K. Davies, V. Randle, and G. J. Marshall. A study of discontinuous and continuous recrystallisation in commercial aluminium alloys. In N. Hansen, D. Juul Jensen, Y. L. Liu, and B. Ralph, editors, *Evolution of deformation microstructures in 3D*, volume 16 of *RisøInternational Symposium on Matierlas Science*, pages 315–320. Risø National Laboratory, 1995.

A. Day, P. Trimby, K. Mehnert, and B. Neumann. *Channel 5.* HKL Technology, March 2004.

B. J. Diak and B. Verlinden. A constitutive description of the hot working of aa1050 using the mean slip distance as a structure parameter. In T. Lewis, editor, *Light metals 2002 métaux légers*, pages 881–898, 2002.

R. D. Doherty, D. A. Hughes, F. J. Humphreys, J. J. Jonas, D. Juul Jensen, M. E. Kassner, W. E. King, Mcnelly, T. R., H. J. McQueen, and A. D. Rollett. Current issues in recrystallization: a review. *Materials Science and Engineering*, A238:219–274, 1997.

J. Driver, F. Perocheau, and C. Maurice. Modelling hot deformation and textures of aluminium alloys. *Materials Science Forum*, 331-337:43–56, 2000.

J. H. Driver, M. C. Theyssier, and Cl. Maurice. Electron backscattered diffraction microtecture studies on hot deformed aluminium crystals. *Materials Science and Technology*, 12:851–858, 1996.

D. Duly, G. J. Baxter, H. R. Shercliff, J. A. Whiteman, C. M. Sellars, and M. F. Ashby. Microstructure and local crystallographic evolution in an al-1 wt pct mg alloy deformed at intermediate temperature and high strain-rate. *Acter Materialia*, 44(7):2947–2961, 1996.

H. J. Flammersheim, W. F. Hemminger, and G. W. H Höhne. *Differential Scanning Calorimetry*. Springer-Verlag Berlin Heidelberg New York, 2nd edition, 2003. ISBN 3-540-00467-x.

T. Furu, R. Ø rund, and E. Nes. Substructure evolution during different hot deformation processes of commercial non-heat treatable aluminium alloys. *Materials Science and Engineering*, A214:122–132, 1996.

J. Ch. Glez and J. H. Driver. Substructure development in hot plane strain compressed al-1 pct. mn crystals. *Acta Materialia*, 51:2989–3003, 2003.

A. Godfrey and D. A. Hughes. Scaling of the spacing of deformation induced dislocation boundaries. *Acta Materials*, 48:1897–1905, 2000.

A. Godfrey and D. A. Hughes. Determination of boundary area and spacing in prismatic structures with applications to dislocation boundaries. *Materials Characterization*, 48:89–99, 2002.

A. Godfrey, G. L. Wu, and Q. Liu. Characterisation of orientation noise during ebsp investigation of deformed samples. *Materials Science Forum*, 408-412:221–226, 2002.

A. Godfrey, W. Q. Cao, N. Hansen, and Q. Liu. Stored energy, microstructure, and flow stress of deformed metals. *Metallurgical and Materials Transactions A*, 36A:2371, 2005.

P. J. Goodhew and F. J. Humphreys. *Electron Microscopy and Analysis*. Wykeham Publications Ltd., 1992. ISBN 0-85066-414-4.

G. Gottstein, G. Steffen, and H. Wollenberger. Discrepancy between specific heat and stored energy data for plastically deformed copper. *Scripta Metallurgica*, Vol. 7:451–456, 1973.

S. Gourdet and F. Montheillet. An experimental study of the recrystallization mechanism during hot deformation of aluminium. *Materials Science and Engineering*, A283:274–288, 2000.

S. Gourdet, E. V. Konopleva, H. J. McQueen, and F. Montheillet. Recrystallization during hot deformation of aluminium. *Materials Science Forum*, 217-222:441–446, 1996.

G. Guiglionda, A. Borbély, and J.H. Driver. Orientation-dependent stored energies in hot defomred al-2.5 their influence on recrystallization. *Acta Materialia*, 52(12):3413–3423, July 2004.

C. Gundlach, W. Pantleon, E. M. Lauridsen, L. Margulies, R. D. Doherty, and H. F. Poulsen. Direct observation of subgrain evolution during recovery of cold-rolled aluminium. *Scripta Materialis*, 50:477–481, 2004.

E. F. H. Arnold, Y. Bertaut, H. Billiet, M. J.and Buerger, J. D. H. Burzlaff, W. Donnay, D. S. Fisher, T. Fokkema, H. Hahn, E. Klapper, G. A. Koch, A. Langlet, P. M. Vos, H. de Wolff, H. Wondratschek, and Zimmermann. *International tables for crystallography*, volume Volume A Space-Group Symmetry. Kluwer Academic Publishers Dordrecht/Boston/London, third, revised edition edition, 1992. ISBN 0-7923-1678-9.

G. T. Hahn. A model for yielding with special reference to the yield-point phenomena in iron and related bcc metals. *Acta Metallurgical*, 10:727–738, 1962.

E. O. Hall. The deformation and agening of mild steel: Discussion of results. *Proceeding of the Physical Society London B*, 64:747–753, 1951.

A. Hammersley. http://www.esrf.eu/computing/scientific/fit2d/. *Homepage*, 2008.

P. Häner. Theroy of solitary plastic waves. *Applied Physics A*, 58:41–48, 1994.

N. Hansen and D. Juul Jensen. Deformation and recrystallization textures in commercially pure aluminium. *Metallurgical Transactions A*, 17A:253–259, 1986.

N. Hansen and D. Kuhlmann-Wilsdorf. Low energy dislocation structures due to unidirectional deformation at low temperatures. *Materials Science and Engineering*, 81:141–161, 1986.

Y. He, N. Hansen, and G. Winther. Effect of grain orientation on microstructures of aluminium in warm tension. *Materials Science and Technology*, 21(12):1471–1475, 2005.

J. Hirsch and K. Lücke. Mechanism of deformation and development of rolling textures in fcc metals 1 description of rolling texture formation in homogenous cu-zn alloys. *Acta Metallurgica*, 36(11):2863–2842, 1988.

P. A. Hollinshead and T. Sheppard. Substructure morphology in aluminium alloys aa 3003 and aa 3004. *Materials Science and Technology*, 3:1019–1024, 1987.

W. F. Hosford. *The mechanics of crystals and textured polycrystals*. Oxford University Press Inc, New York, 1993. ISBN 0-19-507744-X.

F. J. Huang, Y. Humphreys and M. Ferry. The annealing behaviour of deformed cube oriented aluminium single crystals. *Acta Materialia*, 48: 2543–2556, 2000.

X. Huang. Grain orientation effect on microstructure in tensile strained copper. *Scripta Materialia*, 38(11):1697–1703, 1998.

X. Huang. Characterization of nanostructured metals produced by plasic deformation. *Journal of Materials Science*, 42:1577–1583, 2007.

X. Huang. Privat communication. 2008.

X. Huang and N Hansen. Grain orientation dependence of microstructure in aluminium deformed in tension. *Scripta Materialia*, 37(1):1–7, 1997.

X. Huang and Q. Liu. Determination of crystallographic and macroscopic orientation of planar structures in tem. *Ultramicroscopy*, 74:123–130, 1998.

X. Huang and G. Winther. Dislocation structures part 1: grain orientation dependence. *Philosophical Magazine*, 87:5189–5214, 2007.

Y. Huang and F. J. Humphreys. Transient dynamic recrystallization in an aluminium alloy subjected to large reductions in strain rate. *Acter Materialia*, 45:4491–4503, 1997.

D. A. Hughes. Deformation structures developing on fine scales. *Philosophical Magazine*, 83(31-34):3871–3893, 2003.

D. A. Hughes and N. Hansen. Microstructural evolusion in nickel during rolling and torsion. *Materials Science and Technology*, 7:544–553, 1991.

D. A. Hughes and N. Hansen. Microstructural evolution in nickel during rolling from intermediate to large strains. *Metallurgical Transactions A*, Vol. 24A:2021–2037, 1993.

D. A. Hughes and N. Hansen. High angle boundaries formed by grain subdivision mechanisms. *Acta Materialia*, 45(9):3871–3886, 1997.

D. A. Hughes and N. Hansen. Microstructure and strength of nickel at large strains. *Acta Materialia*, 48:2985–3004, 2000.

D. A. Hughes and N. Hansen.

D. A. Hughes, D. C. Chrzan, Q. Liu, and N. Hansen. Scaling of misorientation angle distributions. *Physical Review Letters*, 81(21):4664–4667, 1998.

F. J. Humphreys. Grain and subgrain characterisation by electron backscatter diffraction. *Journal of Materials Science*, 36:3833–3854, 2001.

F. J. Humphreys and P. S. Bate. The alignment of low angle boundaries during deformation. In P. Van Houtte and L. Kestens, editors, *Proceedings of the 14th International Conference on Textures of Materials*. Trans Tech Publications, 2005.

F. J. Humphreys and P. S. Bate. The microstructures of polycrystalline al-0.1 w pct mg after hot plane strain compression. *Acta Materialia*, 55: 5630–5645, 2007.

F. J. Humphreys, P. S. Bate, and P. J. Hurley. Orientation averaging of electron backscattered diffraction data. *Journal of Microscopy*, 201:50–58, 2001.

P. J. Hurley and F. J. Humphreys. The application of ebsd to the study of substructural development in a cold rolled single-phase aluminium alloy. *Acta Materialia*, 51:1087–1102, 2003.

P. J. Hurley, P. S. Bate, and F. J. Humphreys. An objective study of substructural boundary alignment in aluminium. *Acta Materialia*, 51:4737–4750, 2003.

R. Hutanu, L. Clapham, and R. B. Rogge. Intergranular strain and texture in steel luders bands. *Acta Materialia*, 53:3517–3524, 2005.

K. Ikeda, K. Yamada, N. Takata, F. Yoshida, H. Nakashima, and N. Tsuji. Atomic structure of grain boundaries in arb processed copper. In C. Gundlach, K. Haldrup, N. Hansen, X. Huang, D. Juul Jensen, T. Leffers, Z.J. Li, S. F. Nielsen, W. Pantleon, J.A. Wert, , and G. Winther, editors, *Evolution of deformation microstructures in 3D*, volume 25 of *Risø International Symposium on Materials Science*, pages 357–362. Risø National Laboratory, 2004.

R. A. Jargo and N. Hansen. Grain size effects in the deformation of polycrystalline iron. *Acta Metallurgica*, 34(9):1711–1720, 1986.

J. J. Jonas, C. M. Sellars, and W. J. McG. Tegart. Strength and structure under hot-working conditions. *Metallurgical Reviews*, 14(130):1–24, 1969.

A. R. Jones, B. Ralph, and N. Hansen. Subgrain coalenscence and the nucleation of recrystallization at grain boundaries in aluminium. *Proceeding of Royal Society London A*, 368:345–357, 1979.

D. Juul Jensen and N. Hansen. Flowstress aniosotropy in aluminium. *Acta Metallurgica et Materialia*, 38:1369–1380, 1990.

D. Juul Jensen and R. A. Vandermeer. Recrystallisation growth rates in hot deformed aluminium. In Z. Jin, A. Beaudoin, T. A. Bielser, and B. Radhakrishnan, editors, *Hot Deformation of Aluminium Alloys III*, pages 13–25, San Diego, California, March 2003. Publication of TMS.

M. E. Kassner. Large strain deformation of aluminum single crystals at elevated temperture as a test of the geometric dynamic recrystallization concept. *Metallurgical Transactions A*, 20A:2182–2185, 1989.

M. E. Kassner and M. E. McMahon. The dislocation microstructure of aluminum deformed to very large steady-state creep strains. *Metallurgical Transactions A*, 18A:835–846, 1987.

M. E. Kassner, M. M. Myshlyaev, and H. J McQueen. Large-strain torsional deformation in aluminum at elevated temperatures. *Materials Science and Engineering*, A108:45–61, 1989.

M. E. Kassner, M. z. Wang, M.-T Perez-Prado, and S. Alhajeri. Large strain softening of aluminum in shear at elevated temperature. *Metallurgical and Materials Transactions*, 33A:3145–3153, 2002.

D. Kuhlmann-Wilsdorf. Theory of plastic deformation:-properties of low energy dislocation structures. *Materials Science and Engineering*, A113: 1–41, 1989.

D. Kuhlmann-Wilsdorf. Deformation bands, the leds theory, and their importance in texture development: Part ii. theoretical conclusions. *Metallurgical and Materials Transactions A*, 30A:2391–2401, 1999.

D. Kuhlmann-Wilsdorf and H. Hansen. Geometrically necessary, incidental and subgrain boundaries. *Scripta Metallurgica et Materialia*, 25:1557–1561, 1991.

D. Landolt. Fundamental aspects of electropolishing. *Electrochimica Acta*, 32(1):1–11, 1987.

D. Landolt. Electrochemical micromachining, polishing and surface structuring of metals: fundamental aspects and new developments. *Electrochimica Acta*, 48:3185–3201, 2003.

K. Larsen. Ebsd system specialist, oxford instruments hkl a/s, hobro. *Personal communication*, 2007.

N. C. K. Lassen. *Automated determination of crystal orientations from electron backscattering patterns*. PhD thesis, Technical University of Denmark, 1994.

E. M. Lauridsen, D. Schmidt, R. M. Suter, and H. F. Poulsen. Tracking: a method for structural characterization of grainsin powders or polycrystals. *Journal of Applied Crystallography*, 34:744–750, 2001.

Q. Liu. A simple method for determining orientation and misorientation of the cubic crystal specimen. *Journal of Applied Crystallography*, 27:755–761, 1994a.

Q. Liu. A new method for determining the normals to planar structures and their trace directions in transmission electron microscopy. *Journal of Applied Crystallography*, 27:762–766, 1994b.

Q. Liu. A simple and rapid method for determining orientations and misorientations of crystalline specimens in tem. *Ultramicroscopy*, 60:81–89, 1995.

Q. Liu and N. Hansen. Geometrically necessary boundaries and incidental dislocation boundaries formed during cold deformation. *Scripta Metallurgica et Materialia*, 32(8):1289–1295, 1995.

Q. Liu and N Hansen. Macroscopic and microscopic subdivision of a cold-rolled aluminium single crystal. *Proceedings of the Royal Society A*, 454: 2555–2591, 1998.

Q. Liu, M. Qing-Chang, and H. Bande. Calculation of tilt angles for crystal specimen orientation adjustment using double-tilt and tilt-rotate holders. *Micron and Microscopica Acta*, 20(3/4):255–259, 1989.

Q. Liu, D. Juul Jensen, and N. Hansen. Effect of grain orientation on deformation structure in cold-rolled polycrystalline aluminium. *Acta Materalia*, 46(16):5819–5838, 1998.

Q. Liu, X. Huang, D. J. Lloyd, and N. Hansen. Microstructure and strength of commercial purity aluminium (aa 1200) cold-rolled to large strains. *Acta Materalia*, 50:3789–3802, 2002.

W. Liu. Effect of grain orientation on microstructures in hot deformed aa 3104. Technical report, RisøNational Laboratory, Dk-4000 Roskilde, Denmark, 1998.

M. S. Loveday, G. J. Mahon, B. Roebuck, C. M. Sellars, and M. R. van der Winden. *Measuring flow stess in plane strain compression tests*. The National Physical Laboratory, Teddington, United Kingdom, 2000. ISBN 1368-6550.

J. Lund. *Den store Danske Encyklopaedi*. Gyldendalske Boghandel, Nordisk Forlag A/S, 1998.

D. Mandal and I. Baker. Measurement of the energy of grain boundary geometrically-necessary dislocations in copper. *Scripta Metallurgica et Materialia*, 33:831–836, 1995.

L. Margulies, G. Winther, and H.F. Poulsen. In situ measurement of grain rotation during deformation of polycrystals. *Science*, 291:2392–2394, 2001.

C.l. Maurice and J. H. Driver. High temperature plane strain compression of cube oriented aluminium crystals. *Acta Metallurgical Materialia*, 41: 1653–1664, 1993.

Cl. Maurice and J. H. Driver. Hot rolling textures of f.c.c. metals - part 1 experimental results on al single and polycrystals. *Acta Metallurgica*, 45 (11):4627–38, 1997a.

Cl. Maurice and J. H. Driver. Hot rolling textures of f.c.c. metals - part ii numerical simulations. *Acta Metallurgica*, 45(11):4639–4649, 1997b.

H. J. McQueen. Deformation mechanisms in hot working. *Journal of Metals*, pages 31–39, 1968.

H. J. McQueen. The production and utility of recovred dislocation substructures. *Metallurgical Transactions A*, 8A:807–824, 1977.

H. J. McQueen. Development of dynamic recrystallization theory. *Materials Science and Engineering A*, 387-389:203–208, 2004.

H. J. McQueen and W. Blum. Dynamic recovery: sufficient mechanism in the hot deformation of al (99.99 pct. purity). *Materials Science and Engineering*, A290:95–107, 2000.

H. J. McQueen and J. E. Hockett. Microstructures of aluminum compressed at various rates and temperatures. *Metallurgical Transactions*, 1:2997, 1970.

H. J. McQueen and W. J. McGregor Tegart. The deformation of metals at high temperatures. *Scientific American*, 232:116–125, 1975.

H. J. McQueen, W. A. Wong, and J. J. Jonas. Deformation of aluminium at high temperatures and strain rates. *Canadian Journal of Physics*, 45: 1225–1234, 1967.

H. J. McQueen, J. K. Solberg, N. Ryum, and E. Nes. Evolution of flow stress in sluminium during ultra-high straining at elevated temperatures. part ii. *Philosophical Magazine A*, 60:4473–485, 1989.

H. J. McQueen, E. Evangelista, N. Jin, and M.E. Massner. Energy dissipation efficiency in aluminum dependent on monotonic flow curves and dynamic recovery. *Metallurgical and materials transactions A*, 26A:1757–1766, 1995a.

H. J. McQueen, N. D. Ryan, E. V. Konopleva, and X. Xia. Formation and application of grain boundary serrations. *Canadian Metallurgical Quarterly*, 3:219–229, 1995b.

D. Michell and E. Lovegrove. Investigation of the annealing of nickel deformed by compression by x-ray and stored energy measurements. *Philosophical Magazine*, 5:499–518, 1960.

M. Z. Mira and C. M. Sellars. Modelling the hot plane strain compression test part 2 - effect of friction and specimen geometry on spread. *Materials Science and Technology*, 17:1142–1148, 2001a.

M. Z. Mira and C. M. Sellars. Modelling the hot plane strain compression test part 1 - effect of specimen geometry, strain rate, and friction on deformation. *Materials Science and Technology*, 17:1133–1141, 2001b.

O. V Mishin, B. Bay, and D. Juul Jensen. Through-thickness texture gradients in cold-rolled aluminum. *Metallurgical and Materials Transactions A*, 31A:1653–1662, 2000.

O. V. Mishin, A. Godfrey, and L. Östensson. Comparative microstructural characterization of a friction-stir-welded aluminum alloy using tem and sem-based techniques. *Metallurgical and Materials Transactions A*, 37A: 489–496, 2006.

D. W. Moon. Considerations on the present state of Lüders bands studies. *Materials Science and Engineering*, 8:220–234, 1971.

H. Mughrabi. *Materials Science and Technology, A Comprehensive Treatment*, volume 6. Weinheim, New York, 1993.

W. Pantleon and N. Hansen. Dislocation boundaries - the distribution function of disorientation angles. *Acta Materialia*, 49:1479–1493, 2001.

T. Pettersen and E. Nes. On the origin of strain softening during deformation of aluminum in torsion to large strains. *Metallurgical and Materials Transactions A*, 34A:2727–2736, 2003.

H.F. Poulsen, L. Margulies, S. Schmidt, and G. Winther. Lattice rotations of individual bulk grains. part i: 3d x-ray characterization. *Acta Materialia*, 51:3821–3830, 2003.

J. D. Prior, A. P. Bouyle, M. C. Cheadle, A. Day, G. Lopez, L. Peruzzo, J. G. Potts, S. Reddy, R. Spiess, N. E. Timms, P. Trimby, J. Wheeler, and L. Zetterström. The application of electron backscatter diffraction and orientation contrast imaging in the sem to textural problems in rocks. *American Mineralogist*, 84:1741–1759, 1999.

V. Randle, N. Hansen, and D. Juul Jensen. The deformation behaviour of grain boundary regions in polycrystalline aluminium. *Philosophical Magazine A*, 73, 1996.

W. T. Read and W. Shockley. Dislocation models of crystal grain boundaries. *Physical Review*, 78(3):275–289, May 1950.

R. A. Ricks. The deformation models needed by the aluminium industry. *The Royal Society*, 357:1513–1529, 1999.

A. Rohatgi and K.S. Vecchio. The variation of dislocation density as a function of the stacking fault energy in shock-deformed fcc materials. *Materials Science and Engineering A-Structural Materials Properties Microstructure and Processing*, 328(1-2):256–266, 2002. URL `ISI:000175494800034`.

A. D. Rollet and S. I. Wright.

I. Samajdar, P. Ratchev, B. Verlinden, and E. Aernoudt. Hot working of aa 1050 - relating the microstructural and textural developments. *Acta Materialia*, 49:1759–1769, 2001.

Seiko Instruments Division Seiko. *Manual, Differential Scanning Calorimeter Measurement Procedure Operation Manual DSC 120U*. Scientific Instruments Inc, 1995.

H. Shi, A. J. McLaren, C. M. Sellars, R. Shahani, and R. Bolingbroke. Constitutive equations for high temperature flow stress of aluminium alloys. *Materials Science and Technology*, 13:210–216, 1997a.

H. Shi, A. J. McLaren, C. M. Sellars, R. Shahani, and R. Bolingbroke. Hot plane strain compression testing of aluminium alloys. *Journal of Testing and Evaluation*, 25:61–73, 1997b.

N. J. Silk and M. R. van der Winden. Interpretation of hot plane strain compression testing of aluminium specimens. *Materials Science and Technology*, 15:295–300B, 1999.

S. Sircar and F. J. Humphreys. Moelling microstructural formation in two phase aluminium alloys after hot deformation. *Materials Science and Technology*, 12:158–162, 1996.

J. K. Solberg, H. J. McQueen, N. Ryum, and E. Nes. Influence of ultra-high strains at elevated temperatures on the microstructure of aluminium. part i. *Philosophical Magazine A*, 60:447–471, 1989.

W. Sylwestrowicz and E. O. Hall. The deformation and ageing of mild steel. *Proceedings of Physical Society Section A*, 64B:495–501, 1951.

M. Taheri, H. Weiland, and A. Rollett. A method of measuring stored energy macroscopically using statistically stored dislocations in commercial purity aluminum. *Metallurgical and Materials Transactions A-Physical Metallurgy and Materials Science*, 37A(1):19–25, 2006. URL `ISI:000234522800003`.

G. I. Taylor. Analysis of plastic strain in a cubic crystal. *Contributions to the mechanics of solids dedicated to Stephen P. Timoshenko on the occastion of his sixtieth birthday anniversary*, pages 218–224, 1938.

M. C. Theyssier, B. Chenal, J. H. Driver, and N. Hansen. Mosaic dislocation structures in aluminium crystals deformed in multiple slip at 0.5-0.8t_M. *Physica Status Solidi a*, 149:367–378, 1995.

R. Thomsen. *Et meget maerkeligt metal*. Varde staalvaerk, 1975.

E. E. Underwood. *Quantitative Stereology*. Addison-Wesley, 1970.

T. Ungár, H. Mughrabi, D. Rönnpagel, and M. Wilkens. X-ray line-broadening study of the dislocation cell structure in deformed [001]-orientated copper single crystals. *Acta Metallurgical et Materialia*, 32(3): 33–342, 1984.

T. Ungár, E. Schafler, P. Hanák, S. Bernstorff, and M. Zehetbauer. Vacancy production during plastic deformation in sopper determined by in situ x-ray diffraction. *Materials Science and Engineering A*, doi:10.1016/j.mesa.2006.03.156, 2006.

H. E Vante, R. Shahan, and E. Nes. Deformation fo cube-oriented grans and formation of recrystallized cube grains in a hot deformed commercial almgmn aluminium alloy. *Acta Materialia*, 44:4447–4462, 1996.

K. D. Verrnon-Parry, T. Furu, D. Juul Jensen, and F. J. Humphreys. Deformation microstructure and texture in hot worked aluminium alloys. *Materials Science and Technology*, 12:889–896, 1996.

E. Voce. The relationship between stress and strain for homogeneous deformation. *Journal of the Institute of Metals*, pages 537–562, 1948.

J. Weertman and J. R. Weertman. *Elementary Dislocation Theory*. Oxford University Press, New York, 1992. ISBN 0-19-506900-5.

J. Weertmann and J. R. Weertmann. *The plastic deformation of metals*. London Edward Arnold, 1968.

J. A. Wert. *Personal comumication*, 2004.

J. A. Wert. The influence of slip patterns on crystal subdivision at various length scales. In J. V. Carstensen, T. Leffers, T. Lorentzen, O. B. Pedersen, B. F. Soerensen, and G. Winther, editors, *Proceedings of the 19th Risoe international symposium on materials science: Modelling of structure and mechanics of materials from microscale to product*, pages 573–584, 1998.

A. J. Wilkinson and P. B. Hirsch. Electron diffraction based techniques in scanning electron microscopy of bulk materials. *Micron*, 28(4):279–308, 1997.

D. B. Williams and C. B. Carter. *Transmission electron microscopy: a textbook for materials science*. Plenum Press, 1996. ISBN 0-306-45247-2.

G. Winther. Slip patterns and preferred dislocation boudnary planes. *Acta Materialia*, 51:417–429, 2003.

G. Winther. *Personal communication*, 2008.

G. Winther and X. Huang. Dislocation structures part ii: slip system dependence. *Philosophical Magazine*, 87:5215–5236, 2007.

G. Winther, X. Huang, and N. Hansen. Crystallographic and macroscopic orientation of planar dislocation boundaries - correlation with grain orientation. *Acta Materialia*, 48:2187–2198, 2000.

G. Winther, X. Huang, A. Godfrey, and N. Hansen. Critical comparison of dislocation boundary alignment studied by tem and ebsd: technical issues and theoretical consequences. *Acta Materialia*, 52:4437–4446, 2004a.

G. Winther, L. Margulies, S. Schmidt, and H. F. Poulsen. Lattice rotations of individual bulk grains part ii: correlation with initial orientation and model comparison. *Acta Materialia*, 52:2863–2872, 2004b.

E. Woldt and D.J. Jensen. Recrystallization kinetics in copper - comparison between techniques. *Metallurgical and Materials Transactions A-Physical Metallurgy and Materials Science*, 26(7):1717–1724, 1995. URL `ISI:A1995RJ76800009`.

G. Wu. Personal communication. 2006.

Q. Xing, X. Huang, and N. Hansen. Recovery of heavily cold-rolled aluminum: Effect of local texture. *Metallurgical and Materials Transactions A*, 37A:1311–1322, 2006.

C. Zener and J. H. Hollomon. Contributed original research. *Journal of Applied Phsics*, 15:22–32, 1944.

Q. Zhu and C. M. Sellars. Evolution of microbands in high purity aluminium-3 magnesium during hot deformation testing in tension-compression. *Scripta Materialia*, 45:41–48, 2001.

Appendix A

Diffraction

Diffraction from fcc structures
Aluminium has a fcc structure and belongs to the Fm$\bar{3}$m space group (No. 225 in H. Arnold et al. (1992)). Due to systematic absences in this space-group, the observed reflections are the following:

$$hkl : h + k, h + l, k + l = 2n \tag{A.1a}$$

$$0kl : k, l = 2n \tag{A.1b}$$

$$hhl : h + l = 2n \tag{A.1c}$$

$$h00 : h = 2n \tag{A.1d}$$

Hence allowed reflections from the crystal are 111, 200, 220, 311...

Diffraction from bcc structures
Iron has a bcc structure and belongs to the Im$\bar{3}$m space group (No. 229 in H. Arnold et al. (1992)). In this space group, the reflections conditions are the following:

$$hkl \;:\; h + k + l = 2n \tag{A.2}$$

$$0kl \;:\; k + l = 2n \tag{A.3}$$

$$hhl \;:\; l = 2n \tag{A.4}$$

$$h00 \;:\; h = 2n \tag{A.5}$$

Which correspond to the reflections 110, 200, 211, 220, 310....

Appendix B

Orientation representation, Euler angles

The relationship between the orientation of the crystallites (the crystallographic lattice) and the sample coordinate system can be described in several ways. In this study Euler angles with the convention by Bunge (Bunge, 1982) is used i.e. φ_1 ϕ and φ_2. The Euler angles are defined as the angles of three rotations conducted around first ND then RD and finally ND again, in order to rotate the axis of the orthogonal sample coordinate system (in rolling, RD, ND and TD) into the axis of lowest the crystallographic indices in the orthogonal crystallographic reference system ([001], [010] and [100] in the cubic system). Every orientation is described uniquely when the 3 angles are defined in the range (Eulerspace) given in B.1.

$$0 \leq \varphi_1 \leq 2\pi \qquad 0 \leq \phi \leq \pi \qquad 0 \leq \varphi_2 \leq 2\phi \tag{B.1}$$

Due to symmetry of the cubic system (24 equivalent orientations) Euler space is often reduced further into 8 equivalent subspaces[1] one of them being:

$$0 \leq \varphi_1 \leq 2\pi \qquad 0 \leq \phi \leq \frac{\pi}{2} \qquad 0 \leq \varphi_2 \leq \frac{\pi}{2} \tag{B.2}$$

If the sample symmetry (orthorhombic) is introduced as well, the Euler space is further reduced as given below (corresponding to H^0's subspace 1, which still contains 3 equivalent subspaces):

$$0 \leq \varphi_1 \leq \frac{\pi}{2} \qquad 0 \leq \phi \leq \frac{\pi}{2} \qquad 0 \leq \varphi_2 \leq \frac{\pi}{2} \tag{B.3}$$

[1] consisting of 3 equivalent subspaces

Texture component	$\{hkl\}$	$< uwv >$	φ_1	ϕ	φ_2	colour
Cube	$\{001\}$	$< 100 >$	0	0	0	pink
Goss	$\{011\}$	$< 100 >$	0	45	0	dark blue
Brass	$\{011\}$	$< 2\bar{1}1 >$	35.26	45	0	yellow
S	$\{213\}$	$< \bar{3}\bar{6}4 >$	58.98	36.7	63.43	light blue
Copper	$\{112\}$	$< 1\bar{1}1 >$	90	35.26	45	green
Not indexed	-	-	-	-	-	white

Table B.1: The ideal orientations of the texture components cube, Goss, brass, S and copper and colour code used in the EBSD-maps

B.1 Ideal orientations - texture components

Preferred orientations are often found after processing of metals (texture components) and are given in the table B.1 in terms of Miller indicies and the corresponding Euler angles.

In Euler space the ideal orientations run along a path referred to as a fibre. The α-fibre is the path from Goss to brass, while the β-fibre is the orientation range from brass, over S to copper.

B.2 Displaying texture components - colouring in EBSD-maps

The colouring of the noise-reduced EBSD-maps is displayed this thesis has been constructed such that random orientations i.e. orientations not within 15° of any of the ideal orientations listed in table B.1, are coloured according to their Euler angles. This is done by using red green and blue colours, with individual intensities according to the value of each of the angles as given by:

$$Red = 255 \cdot \frac{\varphi_1}{360}, \quad Green = 255 \cdot \frac{\phi}{90}, \quad Blue = 255 \cdot \frac{\varphi_2}{90} \tag{B.4}$$

in the cubic system. The ideal oriented grains are displayed with the colour given in table B.1, where a linear colouring method has been applied. The linear colouring method displays maximum colour closest to the ideal orientation and fades to white when near 15° from the ideal orientation. To make the interpretation of the EBSD-maps easier the relevant texture components have been written on top of the maps. Points not indexed are displayed in white.

Appendix C

Overview of SEM-EBSD measurements

Temp. (°C)	$\dot{\varepsilon}$ (s^{-1})	ε_{vM}	Area (mm^2)	Step size (μm)	V (kV)	MAD	Operator
350	5	0.11	0.4	0.5 and 1	12	0.65	TK
350	5	0.36	0.2	0.5	12/15	0.5	TK
350	5	0.69	0.4	0.5 and 1	15	0.5	TK
350	5	2.3	0.1	0.5 and 0.3	15	0.6	TK
400	5	0.11	0.17	1	15	0.4	TK
400	5	0.36	0.15	0.5 and 0.3	15	0.6	TK
400	5	0.69	0.1	0.5	15	0.5	TK
400	5	2.3	0.07	0.5	15	0.6	TK
500	5	0.11	0.3	1	15	0.3	TK
500	5	0.36	0.3	1	15	0.4	TK
500	5	0.69	0.4	1	15	0.5	TK
500	5	2.3	0.4	1	15	0.5	TK
500	25	0.11	0.2	10 and 0.5	15/20	0.3	TK, HK
500	25	0.36	1.1	1	15/20	0.5	TK, HK
500	25	0.69	1.5	1	15/20	0.6	TK, HK
500	25	2.3	1.2	1	15/20	0.4	TK, HK

TK: Tine Knudsen - author
HK: Kristófer Hanneson

Appendix D

Calorimetry - experimental details

D.1 Calibration of the Differential Scanning Calorimeter

The standard experimental conditions used in the DSC measurements in the current study, were a constant heating rate of 5K/minute and an inert atmosphere of 99.998% pure Ar (Alphagaz) with a flow of 100ml/minute.

Aluminium pans were used, as they have higher thermal conductivity compared to alumina pans. The aluminium pans were heat treated at 500°C for one hour prior to the experiments, in order ensure the pans were fully recrystallized and to create a small inert Al_2O_3-layer on the surface of the pans, to inhibit alloying during measurements. The pans were afterwards cleaned in an ultrasonic bath with ethanol.

The differential scanning calorimeter was calibrated using a two-step calibration procedure, as described in (Seiko, 1995)

At first a calibration program was run with an empty specimen chamber using standard experimental conditions. The calibration program served to ensure a correspondence between the measured temperature in the specimen chamber and the temperature setting in the PC control unit.

Next the DSC was calibrated with respect to the measured signals of enthalpy and temperature. This corresponds to determining the proportionality constant of the apparatus, as described in (Seiko, 1995) and (Flammersheim

Metal	Fusion heat (J/g)	Melting temperature (°C)	purity	Supplier
Indium	28.58	156.60	Min. 99.9%*	In stock
Tin	60.42	231.93	99.999 %	From Alfa Aesar
Lead	23.00	327.47	99.9999 %	From Alfa Aesar

Table D.1: Standards used for calibration (Flammersheim et al., 2003).* *Pure within the detection limit of SEM/EDX analysis i.e. min. 99.9% pure*

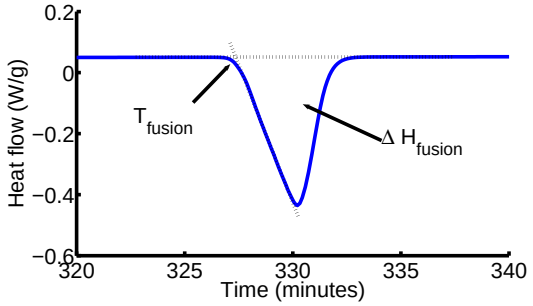

Figure D.1: Definition of melting point, and illustration of the integration of the fusion peak, used during calibration.

et al., 2003). In practice this was done by measuring the melting enthalpy and temperature of pure metals in the temperature range used, using standard experimental conditions. Table D.1 shows the standards used and their properties.

The calibration was conducted by measuring the melting enthalpy of 10mg of each standard, and an empty aluminium pan was used as a reference. In figure D.1 is the data analysis illustrated.

Each calibration was conducted by heating/cooling the standard above/below the melting/solidification temperature 3 times successively. This program was chosen in order to ensure the optimal thermal conductivity and to ensure the reproducibility of the measurements. The temperature and enthalpy were determined by the average of the last two fusion peaks in the program. This scheme was chosen, because the thermal conductivity changes from the first to the second measurement, due to an enhanced contact between the standard and the sample pan. The contact increased due to the melting of standard, when the standard changes from for instance a roll of material to a lump.

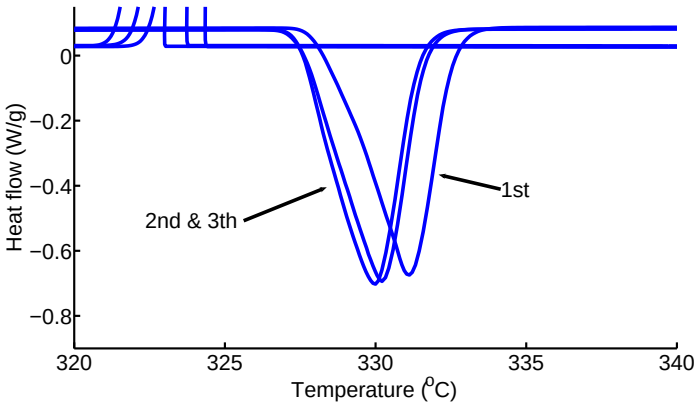

Figure D.2: 3 lead fusions peaks measured during calibration

Standard\H_{fusion}	$\Delta_{1st-Average(2nd-3th)}$ (%)	$\Delta_{2nd-3th}$(%)	Weight (%)	Peak reading (%)
In	0.6	0.1	0.5	0.1
Pb	0.15	0.05	-	0.05
Sn	0.4	0.15	0.35	0.05

Table D.2: Evaluation of the precision of the calibration of the enthalpy

The endothermic response measured during the calibration with a lead standard is illustrated in figure D.2. From the figure a clear difference between the 1st and the two following fusion peaks is seen, in that the 1st peak has a less steep slope, than the following two. Numerical DSC simulations find the same peak shape changes, when the conductivity changes (Flammersheim et al., 2003).

In the temperature range chosen In and Pb do not alloy with Al, while alloying between Al and Sn can exist (Pha, 2007). Due to the temperature pretreatment of the aluminium pan, this effect is however reduced, and comparable to other experimental factors, as will be shown in the following.

Alloying between Sn and Al during the calibration procedure, would lead to a difference in enthalpy between the first and the following two fusion peaks. This difference in enthalpy is measured and given in percent for the 3 standard metals in table D.2. In the same table other difference are given. These are difference between peaks 2 and 3, the difference due to imprecision in sample weight and finally the precision by which each peak is integrated.

From table D.2 it may be seen that there is a maximum of 0.6% difference

Standard\T_{fusion}	$\Delta_{1st-Average(2nd-3th)}$ (%)	$\Delta_{2nd-3th}$(%)
In	0.3	0
Sn	0.05	0.04
Pb	0.3	0

Table D.3: Precision of the temperature calibration

between the first and the following peaks. This difference can be due to both different thermal conductivities (surface energy) and if alloying between the sample pan and standard is seen. Since $\Delta_{1st-Average(2nd-3th)}$ for tin is similar to the values obtained for lead and indium, the potential alloying effect between tin and aluminium is not significant. The difference due to different thermal conductivities and changes in surface energy and further illustrated in figure D.3, where fusion peaks of tin measured in alumina and aluminium pans are displayed. In both measurements the first peaks are different from the next two, which are more similar in shape, as expected when the thermal conductivity increases. The 2nd and 3th peaks are however not identical, which means that a slight effect of alloying might have have occurred.

In table D.3 the difference in measured melting temperatures are given, calculated as for the enthalpy measurements. From this table it can be seen, that the temperature differences between the first peak and the following peaks are at a maximum 0.3%.

From the above it can be concluded that the differences observed between the calibration curves are less than 1% which includes eventual alloying between a standard and the sample pan.

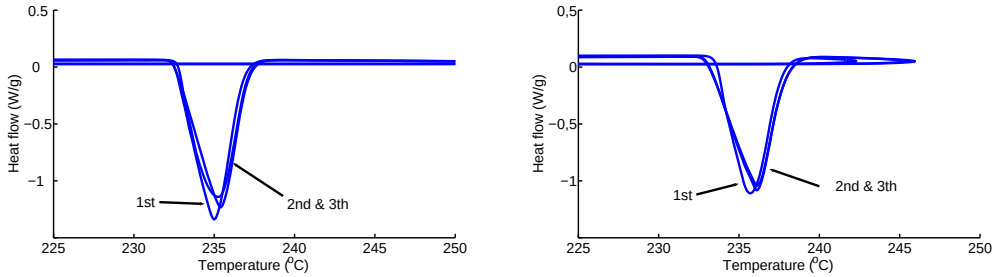

Figure D.3: Tin fusion peaks, left aluminium pans right alumina pans

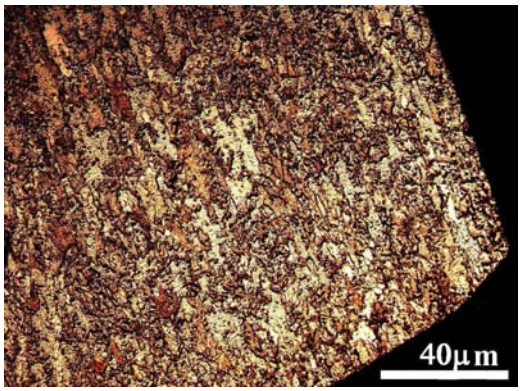

Figure D.4: Optical image of a copper sample after DSC measurements

D.2 Validation of the sample preparation method

In order to ensure, that the deformation introduced during punching, was removed by the following polishing, a microscopical examination was conducted on two specimens. An optical image of a polished and etched cross section of a copper sample after recrystallization is given in figure D.4.

In this figure no clear difference in grain structure is observed between the edge of the sample compared to the middle, hence the deformation introduced during the specimen preparation, has not introduced a large enough deformation to change the recrystallization microstructure which ensues.

Figure D.5 is an orientation image of the cross section of a recrystallized aluminium sample. In the orientation image, no clear difference is observed in the near middle region compared to the edge region, hence deformation induced by the punching is not observed under the current conditions.

In the above, no clear effect of punching of the specimens has been observed. The deformation of prepared samples, can be estimated as follows. If the deformation left in a prepared specimen due to polishing with a 4000 silicon-carbide grid paper (grain size 6μm), is the depth affected due to polishing, this is 0.1*6μm*4 = 2.4μm (Wert, 2004). If the entire specimen was polished this corresponds to 0.7% of the total specimen volume[1], i.e. the affected volume is very small, and the extra energy stored in the volume is not considered significant compared to the prior deformation of at least 70% cold rolling.

[1]Calculated for the copper specimens

In conclusion, from the microstructural analysis and the rough calculation, it is concluded, that the specimen preparation does not contribute significant in to the energy measured.

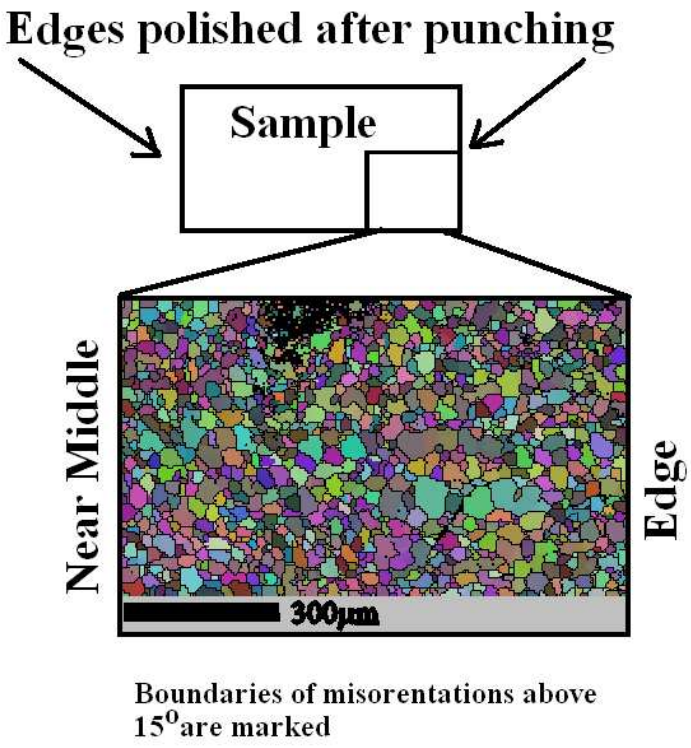

Figure D.5: Orientation image of an aluminium sample after DSC measurements

Appendix E

Paper A

MICROSTRUCTURAL EVOLUTION IN ALUMINIUM (AA1050) PLANE STRAIN COMPRESSED AT 0.7 T_M

T. Knudsen, G. Winther and N. Hansen

Center for Fundamental Research: Metal Structures in Four Dimensions, Materials Research Department, Risø National Laboratory, DK-4000 Roskilde Denmark

ABSTRACT

The microstructural evolution during plane strain compression of aluminium (AA1050) at a temperature of 350^0C (0.7 T_M), a strain rate of 5 s^{-1} and from strains of 0.11 to 0.69 is described. At a small strain (ε = 0.11) aluminium has developed a microstructure with characteristic extended planar dislocation boundaries known from cold deformed structures, whereas at a higher strain (ε = 0.69) a structure with wavy extended dislocation planar boundaries with less directionality is observed. The microstructural evolution possibly relates to the stress-strain behaviour showing strain hardening at low strain approaching saturation at larger strain.

1. INTRODUCTION

Recent analysis of hot deformed materials reveals that aluminum at high strain rates develops a microstructure with characteristics resembling that of cold deformed materials (Juul Jensen, Lyttle and Hansen 1998). Analysis of these structures may therefore further the understanding of the physical mechanisms behind the evolution of microstructures during hot deformation and thereby combine the traditionally separate areas of cold and hot deformation. Extensive studies of the structural evolution during cold deformation is therefore now followed up in a study where aluminium (AA1050) is deformed by plane strain compression at temperatures from 350°C to 500°C. Results from this study is presented in the following covering the microstrucural evolution and the stress strain behavior during deformation at 350°C with a strain rate of 5 s^{-1}

2. EXPERIMENTAL

The samples to be plane strain compressed were prepared as follows. Two plates of 99.5% pure aluminium were heat treated under conditions where impurities, mainly Si (0.16%) and Fe (0.24%) precipitate. From the plates samples measuring 60x50x10 mm were fabricated. The samples were thereafter heat-treated 6 h at 500^{0}C, thereby reaching an average grain size of 80 μm.

The samples were lubricated with a graphite lubricant and plane strain compressed in a thermomechanical compression machine at a strain rate of 5 s^{-1} to strains up to 1.3 at room temperature and 350°C. The plane strain compression was conducted at IMMPETUS at The University of Sheffield. The raw data was corrected for friction (μ = 0.1), origin displacement, specimen spread and presented in terms of equivalent stress-strain curves (based on von Mises criterion), using the standard procedure as described in the book of Loveday, Mahon, Roebuck, Sellars and van der Winden (2000).

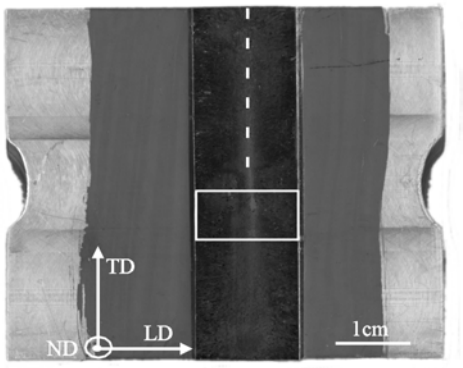

Fig. 1. Plane strain compressed sample. The thermocouple in the sample is marked with a dotted white line, whilst the part taken out for preparation of TEM foils is marked with a white box. The normal (ND), longitudinal (LD) and transverse directions (TD) are marked.

From the samples compressed to strains of 0.11 and 0.69 at 350°C TEM foils for structure investigations were prepared. The TEM foils were prepared from parts of the samples marked with a white box in Fig. 1. This part was chosen in order to avoid any effects on the microstructure from the thermocouple and non-plane strain conditions around the edges of the sample. The sample was sliced using a diamond string, polished and electropolished. From each slice three circular TEM foils were punched out. The foils were taken in the middle and in each side, but still away from the edges and faces of the sample. The foils were prepared for examination in the longitudinal plane (LD/ND).

The TEM foils were analyzed in a 200 kV Philips CM20 microscope and all micrographs taken in bright field mode. In a Philips CM20, the image rotates with magnification making it necessary to connect the macroscopic directions of the samples at each magnification using double exposure of the micrographs. The estimated precision of this is ±5 degrees. Furthermore tilt is not accounted for in the

measurement, which also gives rise to uncertainties. These uncertainties are however not important for the conclusions of this paper.

3. RESULTS

Mechanical properties. Equivalent stress-strain curves from the plane strain compression are seen in Fig. 2 together with curves of the strain hardening rates as a function of stress. The stress-strain curves are fitted to a modified Voce equation

$$\sigma = \sigma_0 + (\sigma_{ss}-\sigma_0)(1-\exp(-C\varepsilon))^n, \quad (1)$$

where σ_{ss}, σ_0 , C and n are fitting parameters. The stress-strain curve at room temperature (Fig. 2a) shows a parabolic increase in stress with increasing strain. At higher strains the stress increases almost linearly. In Fig. 2b the strain hardening rate at room temperature shows a continuous decrease as a function of stress.

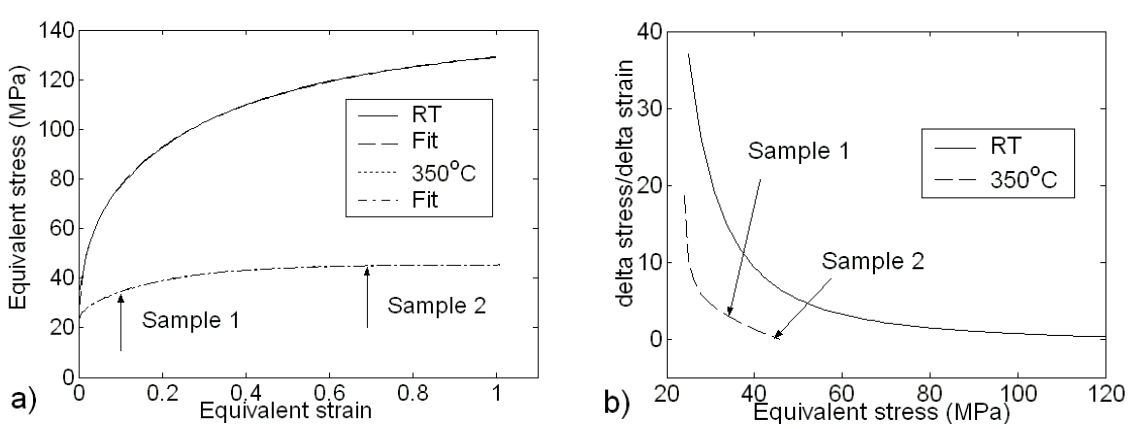

Fig. 2. a) Equivalent stress-strain curves for aluminium plane strain compressed at room temperature and 350°C. The fits are made to the modified Voce equation in Equation (1). b) Strain hardening rate ($d\sigma/d\varepsilon$) as a function of stress. Calculated from the modified Voce fit. In both figures strains chosen for structural examinations are marked.

The stress-strain curve at 350°C (Fig. 2a) shows strain hardening at low strains while at increasing strains the stress approaches saturation. The strain hardening rate at 350°C (Fig. 2b) shows a continuous decrease and is approaching zero at the highest stresses.

On the basis of the stress-strain curves two samples were chosen for the first TEM investigations. These samples are specimens deformed at 350°C to strains of 0.11 and 0.69 as marked on the Fig. 2a and 2b. The samples chosen for morphological investigations are thus representative for the strain-hardening region and the region where the stress-strain curve has almost saturated, respectively.

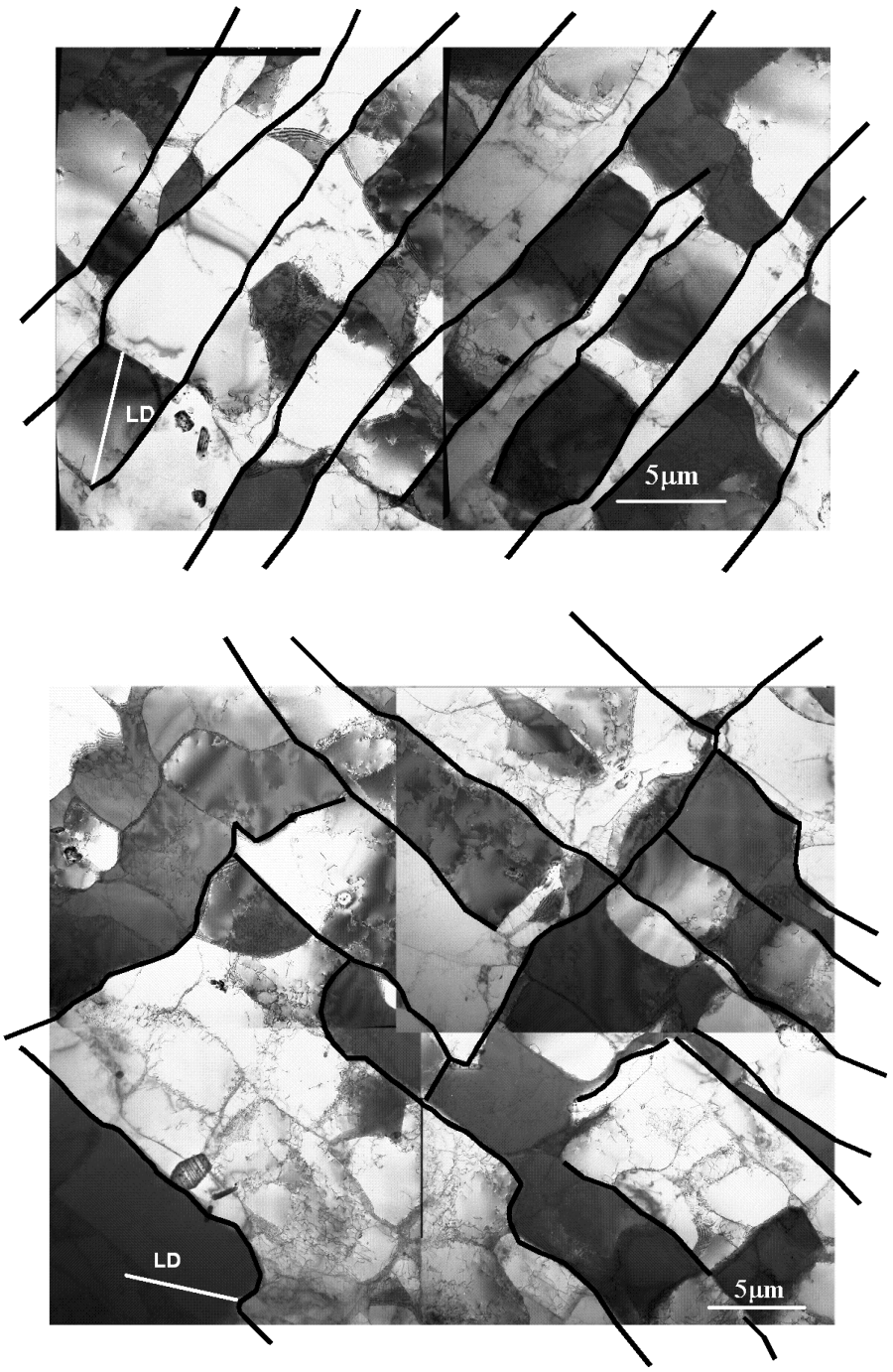

Fig. 3. TEM micrographs of typical structures of aluminium strained to 0.11. Top: Cell block structure delineated by extended dislocation boundaries inclined 25° to LD. Bottom: Cell block structure delineated by extended dislocation boundaries which are inclined 25° to LD. A set of boundaries perpendicular to the dominant set is also seen.

3.2 Morphology. At a strain of 0.11 typical structures are shown in Fig. 3. In the micrographs of Fig. 3, the specimen has developed a cell block structure, which are delineated by extended almost planar dislocation boundaries. The boundaries are inclined approximately 25° to the longitudinal direction (LD). The spacing between the boundaries varies between 0.5 µm and 15 µm.

The above described structural morphology resembles the cell block structure typical for cold deformation. The most significant difference is that the inclination of the extended boundaries delineating the cell blocks is somewhat lower to LD than the typical inclination to RD in cold rolling. This inclination is however known to correlate with the crystallographic orientation, which may explain the difference (Liu, Juul Jensen and Hansen 1998).

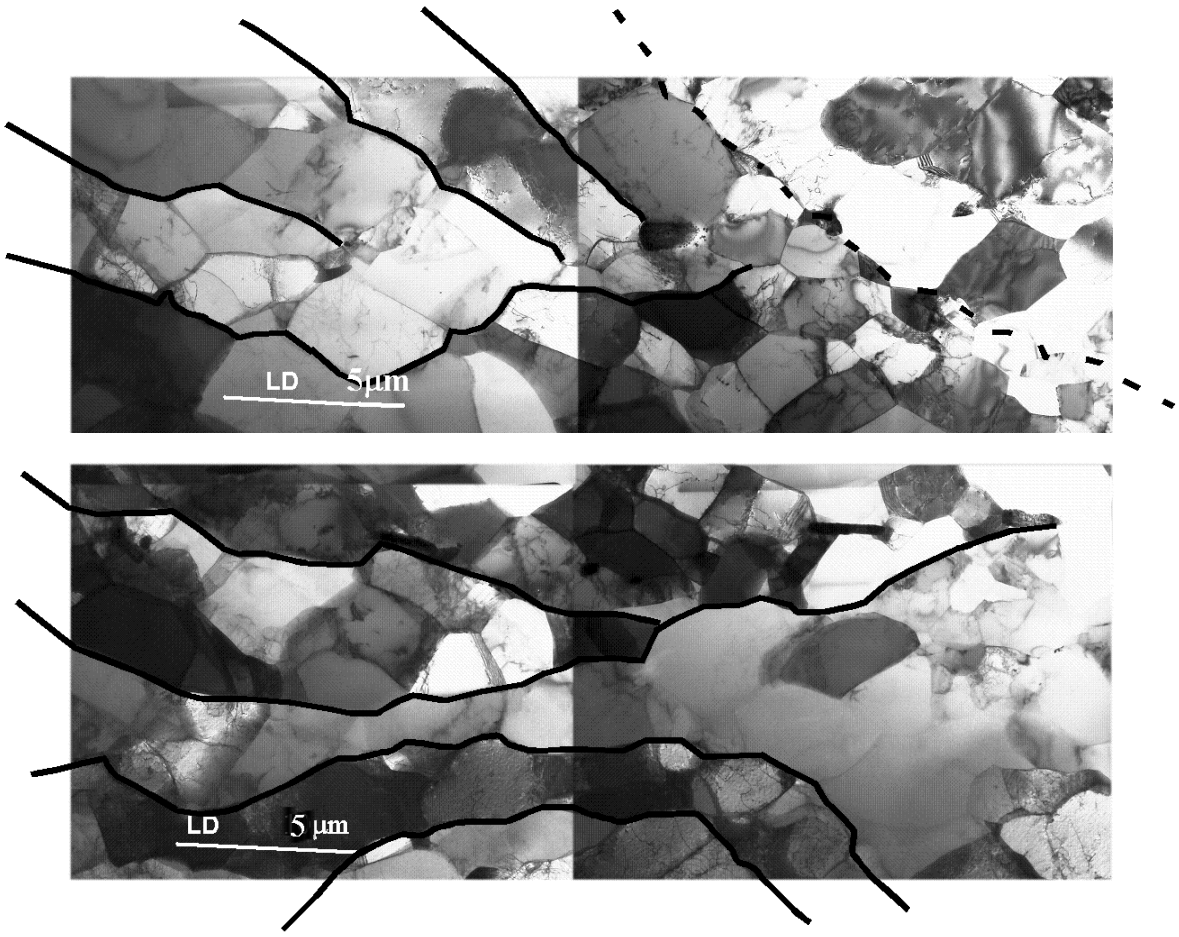

Fig. 4. TEM micrographs of aluminium strained to 0.69. Cell blocks are delineated by extended boundaries, in which cells are seen. The dotted line marks a grain boundary.

At a strain of 0.69 the microstructure contains cell blocks delineated by extended dislocation boundaries (Fig. 4). The extended dislocation boundaries have less directionality than seen at low strain and the boundaries are wavier.

4. CONCLUSION

Aluminium (AA1050) plane strain compressed at 350°C (0.7 T_M) develops a microstructure which at low strain (0.11) resembles the typical cell block structure observed after cold deformation of aluminium. At larger strain (0.69) a cell block structure is still apparent but the cell block boundaries have become wavy and their directionality is less well defined. The observed morphological changes possibly relate to the changes in stress strain behavior from strain hardening a low strain to almost saturation a larger strain. The conditions chosen therefore appear to have caught a transition between typical cold and hot deformation structures.

ACKNOWLEDGEMENTS

The authors gratefully acknowledge the Danish National Research Foundation for supporting the Center for Fundamental Research: Metal Structures in Four Dimensions, within which this work was performed. The authors are also grateful to Dr. E. Johnson for lending out the microscope at The University of Copenhagen and being helpful in general and to G. Christiansen for preparing the TEM foils. Finally, Dr. E. J. Palmiere and Mr. A. J. Lacey, The Department of Engineering Materials, at The University of Sheffield are thanked for plane strain compression of the samples.

REFERENCES

Juul Jensen, D., Lyttle, M. T., and Hansen, N. (1998). Hot and cold deformed aluminum: Deformation microstructure and recrystallization behaviour. In: Hot Deformation of Aluminium Alloys II. Eds. T.R. Bieler et al. (The Minerals, Metals & Materials Society) 9-21.

Loveday, M. S., Mahon, G. J., Roebuck, B., Sellars, C. M., and van der Winden, M. R. (2000). Measurement good practice guide: measuring flow stress in plane strain compression tests. (National Physical Laboratory, Teddington, Middlesex, United Kingdom).

Liu, Q., Jensen, D. J., and Hansen, N. (1998). Effect of grain orientation on deformation structure in cold-rolled polycrystalline aluminium. Acta Mater. 46, 5819-5838.

Appendix F

Paper B

Image analysis for X-ray studies of the dynamics of individual embedded subgrains during recovery

C. Gundlach[1], S. Schmidt[1], L. Margulies[1,2], T. Knudsen[1], W. Pantleon[1] and H. F. Poulsen*[1]

An advanced image analysis algorithm is presented for extracting growth curves for individual embedded subgrains during static recovery of deformed metals. The data are obtained by three dimensional X-ray diffraction microscopy. Based on a 5D multicomponent labelling scheme embedded in the full five dimensional experimental space, the algorithm is much faster and less biased than one previously used for the same purpose. The use of the methodology is demonstrated on a study of static recovery in an AA1200 specimen cold rolled to a true strain of 2.

Keywords: Recovery, X-ray diffraction, Synchrotron radiation, 3DXRD, Image analysis

Introduction

Traditionally static recovery has been studied in several ways.[1] One method is by use of bulk probes, and includes calorimetry, conductivity and hardness measurements. The results represent an average over all processes and over the heterogeneity of the specimen. A second method uses electron microscopy on the surface of sectioned samples, both before and after annealing.[1–3] While a wealth of detailed information is acquired, the dynamics of the microstructure can only be probed statistically in this manner. (*In situ* electron microscopy studies have been reported by several groups, but are generally not considered as being representative of bulk behaviour for geometric reasons.)

Recently, an X-ray diffraction method has been introduced, which enables direct observation of the dynamics of individual embedded subgrains during annealing.[4] The method is an extension of three dimensional X-ray diffraction (3DXRD)[5,6] conventionally used for structural characterisation of grains within millimetre to centimetre thick polycrystals. By focusing the X-ray beam from a synchrotron source to dimensions of about 5×5 μm and by using foils, diffraction spots arising from individual subgrains were monitored as function of annealing time. As a result growth curves – representing the change in volume – have been determined for nine subgrains simultaneously.[4]

As reported, this method is, however, limited by overlap of the diffraction spots. Due to the requirement for having a ratio of foil thickness to subgrain diameter of 10 or more (to ensure that the dynamics of the subgrains in the centre of the foil can be considered as bulk) many hundreds or thousands of subgrains are illuminated simultaneously. This implies that the probability of overlapping diffraction spots on the detector becomes large. As a result, grain statistics are poor and there is a danger that the method is biased, in the sense that the probed subgrains are special. This problem is accentuated by the fact that many spots, which look clearly 'distinct' to the eye, cannot be resolved by the image analysis applied.

In this paper a superior image analysis technique is presented whereby the number of 'visible' spots is much improved. The algorithm developed is based on two underlying concepts. First, to perform the image analysis in the five dimensional space spanned by all experimental dimensions including time. Second, to separate close lying neighbours in this space by a combination of an extension of the classical 'labelling of components scheme' from 2D,[7] with a multicomponent fitting to the known spatial variation of the X-ray beam.

In the following the 5D data analysis methodology is described in detail, and its use is demonstrated for characterising the recovery of a cold rolled AA1200 foil.

Experimental

The sample material used was AA1200, with an original grain size of 75 μm, which had been cold rolled to a true strain of 2 prior to the annealing experiment. The deformation induced microstructure in this material has been extensively characterised by TEM after cold rolling[8] and subsequent annealing.[9] The average size of the subgrains in the deformed state was found to be 1 μm along the rolling direction and 0·43 μm along the normal direction. A foil of the deformed material was prepared and inserted by means of a special specimen

[1]Center for Fundamental Research: Metal Structures in 4 Dimensions, Materials Research Department, Risoe National Laboratory, 4000 Roskilde, Denmark
[2]European Synchrotron Radiation Facility, BP 220, 38046 Grenoble, France

*Corresponding author, email henning.friis.poulsen@risoe.dk

Published by Maney on behalf of the Institute
Received 24 August 2005; accepted 19 September 2005
DOI 10.1179/174328405X71675

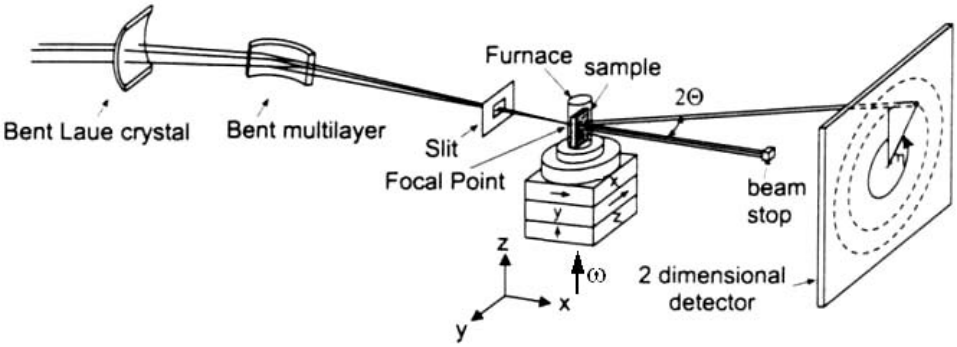

1 Sketch of experimental setup. Laboratory coordinate system (*x*,*y*,*z*) and the diffraction angle 2θ, the angle η on the detector and the rotation angle ω around the z axis are defined

holder in a small evacuated furnace for *in situ* 3DXRD investigations following the procedures described earlier.[4]

The experiment was performed using the dedicated 3DXRD microscope[5] at beam line ID-11 at the European Synchrotron Radiation Facility. A monochromatic 50 keV X-ray beam was focused to a spot with a size as small as possible with the microscope at the time of the experiment. The resulting beam profile was carefully measured and found to be approximately Gaussian with a full width at half maximum (FWHM) of 5·7 μm and 5·7 μm in horizontal and vertical directions, respectively. The foil was positioned at the focal spot and exposures were acquired with a two dimensional detector while rotating the sample around the ω axis. (This and other experimental parameters are defined in the sketch shown in Fig. 1.) The detector, a 14-bit FRELON CCD coupled to an image intensifier, was positioned at a distance of 0·32 m from the sample, such that the first five Debye–Scherrer rings were fully visible. The η-resolution was about 0·2° (η is the azimuthal angle, see Fig. 1). Based on scaling arguments,[6] a reference of known thickness and the integrated intensity in the diffraction pattern, the foil thickness was estimated to be 3 μm.

The sample was subjected to isochronal annealing. Starting at 200°C, the temperature was increased in steps of 8 K to a final temperature of 374°C. At each temperature, the following measuring scheme was applied: exposures were made at 31 equidistant ω positions, spanning 6°. During each exposure the sample was oscillated by $\pm$0·1°. This ω scanning was repeated at 16 positions in a spatial 4×4 (y,z) grid, with a distance of 4 μm between the nodes of the grid. An example of the raw data from one exposure is shown in Fig. 2. The holding time at each temperature step was 15 min. Potential positional drifts during the heat treatment were excluded by regular tests of the position of reference points.[4]

Algorithm

The aim of the data analysis is

(i) to identify which parts of the diffraction patterns (which spots) originate from a single subgrain
(ii) to find the position of the subgrain by fitting the intensity distribution in the 4×4 (y,z) grid to the known beam profile
(iii) based on the above to determine the integrated intensity of the entire reflection.

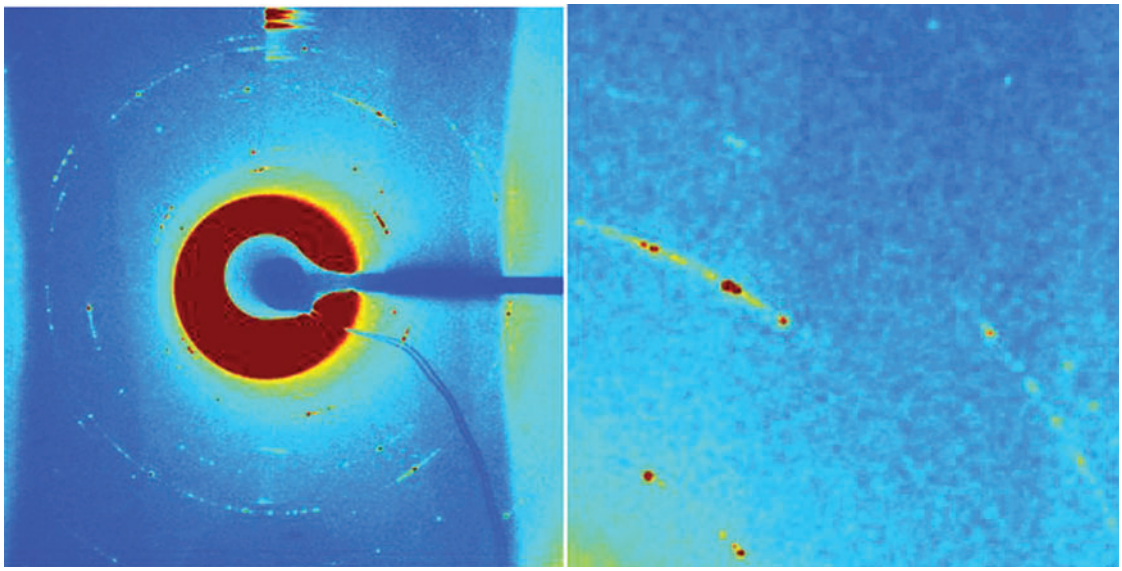

2 Example of raw data for one particular exposure acquired at 200°C. Left: full image. Enhanced intensity close to the centre of the image is an experimental artefact due to lack of screening of background. Right: Zoom of same image. Diffraction pattern comprises distinct but close lying and at times overlapping diffraction spots

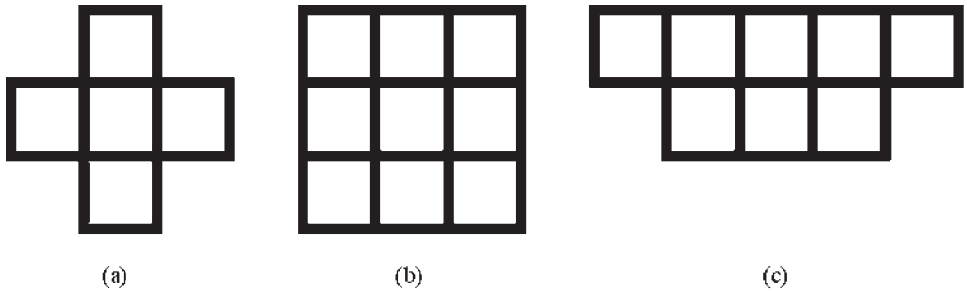

3 Illustration of connectivity rules used for blob identification: (*a*) 4-connectivity, (*b*) 8-connectivity, and (*c*) special connectivity rule designed for (ω, t) plane

After correction for structure and Lorentz factor, the intensity is directly proportional to the volume of the associated subgrain, with a constant of proportionality that is easily determined by calibration.[6]

The straightforward approach[4] published earlier is sequential. First, spots are separated based on raw images, then their (y,z) position and integrated intensity is fitted simultaneously to a single Gaussian distribution and finally their intensities are monitored as function of time. It is found that this approach gives rise to artefacts unless one puts quite conservative constraints on the proximity of spots in the raw images.

The revised algorithm is not sequential but based on image analysis in the 5D experimental space parameterised by (η, ω, y, z, t). This space is large, with $900 \times 31 \times 4 \times 4 \times 23 \approx 10^8$ volume elements (voxels). The algorithm comprises two steps.

Blob finding in 5D space

A 5D array T of intensities is generated based on the background subtracted raw data, corrected for two crystallographic factors: the structure and Lorentz factors. By defining a threshold a binary array T_{bin} is created. This global threshold value is the only adjustable parameter in the algorithm and is set by an analysis of the background. First, the background and its dependence on the position on the detector is determined as a median value from all images in a measuring cycle and subtracted from each image. The threshold is defined as five times the standard deviation of the statistical fluctuations in the remaining background signal.

Next, connected parts – in the following called 'blobs' – in T_{bin} are determined by extending the two pass labelling algorithm[7] to 5D. The nature of connectivity in the various dimensions can be adjusted to the problem at hand. Usually, 4- or 8-connectivity is used in blob finding algorithms in 2D. As illustrated in Fig. 3*a*, 4-connectivity implies that each pixel in the blob is associated with at least one neighbouring pixel, positioned to the north (N), south (S), west (W) or east (E), which are also included in the blob. In the case of 8-connectivity, there should be at least one neighbour within the blob in either N, NW, W, SW, S, SE, E, or NE direction, as shown in Fig. 3*b*. Applying this terminology to all pairs of dimensions in the list (η, ω, y, z, t), we find the following settings to be superior:

As default all 2D planes are 4-connected.

The (η, ω) plane is 8-connected, as the mosaic spread of a given spot may be anisotropic with an arbitrary direction.

The (ω, t)-plane is special. A pixel at (ω, t) is connected to any of the 5 pixels ($\omega-2\Delta\omega$, $t-\Delta t$), ($\omega-\Delta\omega$, $t-\Delta t$), (ω, $t-\Delta t$), ($\omega+\Delta\omega$, $t-\Delta t$), ($\omega+2\Delta\omega$, $t-\Delta t$) as well as ($\omega-\Delta\omega$, t) and ($\omega+\Delta\omega$, t). This rule is designed specifically for this type of experiment. Apparently, the aluminium foil bends slightly during annealing causing a shift in ω of the observed spots. This shift is compensated by the suggested relaxed connectivity rule. Note, that no forward connectivity in the time coordinate is allowed.

Blobs extending to the ω or η borders of the 5D space are excluded as the integrated intensity may not have been measured fully. (In principle the distribution is continuous in η. However, for numerical reasons, the full 5D volume for a given Debye–Scherrer ring is divided into subvolumes corresponding to η intervals of 20°, which are analysed separately.)

Multicomponent fitting

The remainder of the analysis is performed blob by blob. For each blob the intensity distribution in the corresponding part of T is projected onto the (y,z,t) subspace. Within this subspace, for each time step a multicomponent Gaussian least squares fit is made to the (y,z) distribution. All Gaussians have fixed FWHMs given by the beam size.

The number of Gaussian distributions considered in the multicomponent fitting was determined by the number of local maxima in the spatial 4×4 grid. The grid positions of the local maxima were chosen as initial values in the multicomponent fit. The fit is accepted

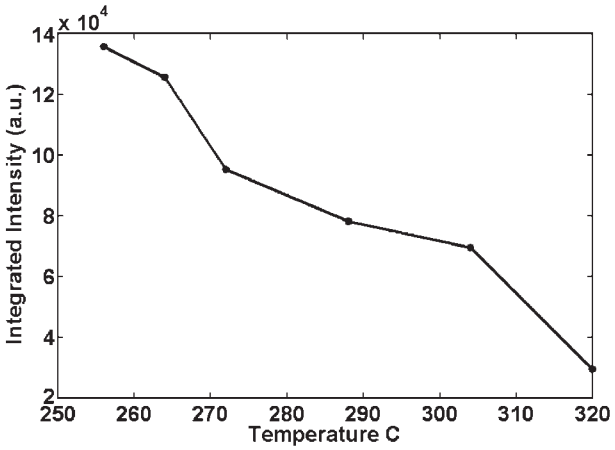

4 Evolution of single individual subgrains during isochronal annealing. Decreasing integrated intensity as a function of successively increasing annealing temperature corresponds to shrinkage of the subgrain

based on conventional criteria for convergence and the norm of the residual. Peaks with a maximum outside of an inner rim of 2 μm from the borders in y and z are excluded as it is deemed impossible to determine their position – and thereby the integrated intensity – with sufficient accuracy.

This procedure is repeated for each time step. If a valid peak is found at the 'same' (y,z) position – within an error of 2 μm – and over at least five contiguous time steps, the evolution in integrated intensity of this peak is identified as a valid growth curve. (The slight lateral motion of the blob was caused by the furnace sample system not being in thermal equilibrium during heating. The position of markers has been monitored repeatedly and thermal equilibrium was assumed when the same position was detected twice. Apparently, this was not sufficient and relaxation in the furnace sample systems has caused further lateral displacements during the measurement.)

The motivation for the multicomponent fit was to remove outliers. By trial and error it was found that (typically low intensity) tails from neighbouring spots disrupt a fit to a single Gaussian distribution. Hence, the typical final result of the fitting procedure is either none or one valid growth curve per blob, but in certain cases several growth curves are identified.

This second part of the algorithm has essentially two types of adjustable parameters, namely the convergence parameters for the fit and the allowed 'wiggle' of the position of the peak.

The algorithm as presented was implemented in MATLAB.

An example of a resulting growth curve is provided in Fig. 4 showing a shrinking subgrain. Scaling the required processing time for a subset of the data, performing a complete data analysis of all data with parameters as defined above is estimated to last about one week.

Discussion

The prospect of measuring an ensemble of growth curves of individual elements within a local bulk region of a deformed microstructure should be emphasised. Relevant research topics include.

1. Characterisation of the variation in growth behaviour as function of position or orientation.
2. Determination of kinetics and activation energies for recovery.
3. Tests of coarsening models for recovery.

It should also be noted that synchrotron beam lines are under development, with the aim of providing hard X-ray beams with a spot size of the order 100 nm. With such beams it is expected that it will be possible to characterise the stability of a diversity of nanostructures in an analogous manner to the analysis of subgrains in deformation structures on a micrometre scale, as outlined here.

It may be argued that the ultimate image analysis tool for the problem discussed in this article would be to find blobs in 5D space using a watershed algorithm. However, we estimate such methods would be prohibitively slow numerically and furthermore argue that threshold based segmentation plus multicomponent fitting is a good – and much faster – approximation to the watershed algorithm in this case.

Acknowledgments

The authors thank J. R. Bowen and N. Hansen for scientific discussions, V. Honkimäki for use of software, Q. Xing for sample preparation, and ESRF for provision of beam time. This work was supported by the Danish National Research Foundation and by the Danish Research Council SNF (via Dansync).

References

1. F. J. Humphreys and M. Hatherley: 'Recrystallization and related annealing phenomena'; 1995, Oxford, Pergamon.
2. P. Faivre and R. D. Doherty: *J. Mater. Sci.*, 1979, **14**, 897–919.
3. A. Godfrey, D. Juul Jensen and N. Hansen: *Acta Mater.*, 2001, **49**, 2429–2440.
4. C. Gundlach, W. Pantleon, E. M. Lauridsen, L. Margulies, R. D. Doherty and H. F. Poulsen: *Scr. Mater.*, 2004, **50**, 477–481.
5. H. F. Poulsen: 'Three-dimensional X-ray diffraction'; 2004, Berlin, Springer.
6. E. M. Lauridsen, D. Juul Jensen, H. F. Poulsen and U. Lienert: *Scr. Mater.*, 2000, **43**, 561–566.
7. H. Bässmann and Ph. W. Besslich: 'Bildverarbeitung ad oculos'; 1991, Berlin, Springer.
8. Q. Liu, X. Huang, D. J. Lloyd and N. Hansen: *Acta Mater.*, 2002, **50**, 3789–3802.
9. Q. Xing, X. Huang and N. Hansen: *Mater. Sci. Forum*, 2004, **467–470**, 209–214.

Appendix G

Paper C

Stored Energy in Nickel Cold Rolled to Large Strains, Measured by Calorimetry and Evaluated from the Microstructure

T. KNUDSEN, W.Q. CAO, A. GODFREY, Q. LIU, and N. HANSEN

High-purity polycrystalline nickel (99.99 pct purity) was cold rolled to equivalent von Mises strains from 1.4 to 4.5 (70 to 98 pct reduction in thickness). The stored energy of the deformed samples was measured using both microstructural parameters obtained from transmission electron microscope (TEM) investigations and differential scanning calorimetry (DSC). For the microstructure-based estimate of the stored energy, the required parameters are the misorientation angles across, and the spacings between the dislocation boundaries and high-angle boundaries present after deformation. It was found that the stored energy determined from both TEM and DSC investigations increased linearly with strain, with the latter being larger by a factor of between 1.9 and 2.7. This difference can be reduced by considering the contribution to the stored energy from other sources.

DOI: 10.1007/s11661-007-9421-1

I. INTRODUCTION

THE processing of metals by plastic deformation requires mechanical energy, of which only a small fraction is stored in the metal in the form of dislocations, point defects, high-angle boundaries, and, in some materials, twins.[1] The stored energy can be measured directly by calorimetry[1,2,3–11] or it can be estimated based on a microstructural characterization.[12–14] In recent studies, the correlation between the stored energy of the deformation and the characteristics of the deformed microstructure has been analyzed.[12,14] In these studies, it has been shown that the stored energy can be estimated by applying the Read–Shockley equation to the boundaries observed in the deformed microstructure. Note that, in this article, we use the term ''dislocation boundaries'' to refer to boundaries with a misorientation angle of less than 15 deg, and the term ''high-angle boundaries'' to denote all other boundaries in the microstructure (including the original grain boundaries and those boundaries with a misorientation angle >15 deg formed during deformation). For aluminum, it has been observed that there is a relationship between the stored energy and both the applied strain and the flow stress after deformation.[12] The topic of stored energy is of general importance in various materials science fields, including, for example, recovery, recrystallization, and crystal plasticity. The correct estimation of the stored energy in a deformed metal is, therefore, crucial when analyzing and modeling such phenomena.

The objective of the present study is to supplement the microstructure-based method by measuring the stored energy directly by differential scanning calorimetry (DSC). This permits analysis of the question of whether other sources of stored energy exist in addition to the energy stored in the form of dislocations and high-angle boundaries. Studies with a similar objective have been carried out previously by combining calorimetry, dislocation density measurements by using transmission electron microscopy, and X-ray line broadening.[15,16] These earlier studies were focused on single crystals of copper deformed in tension to low and medium strains. In contrast, the present study concentrates on polycrystalline nickel samples deformed by cold rolling to a thickness reduction of 70 to 98 pct (ε_{vM} = 1.4 to 4.5). At these large strains, linear work hardening (stage IV) dominates. The calorimetric measurements have been carried out by the annealing of high-purity (99.99 pct) nickel, which is chosen in preference to the aluminum used in the previous studies,[12,13] in order to optimize the precision of the calorimetric measurements. The reason for this is that the heat release in pure nickel is predominantly caused by recrystallization over a fairly narrow temperature range, whereas in aluminum, the heat release is caused by both recovery and recrystallization and takes place over a large temperature interval.[1] Furthermore, the stored energy in nickel is approximately 5 to 10 times larger than the stored energy in aluminum for an equivalent strain.[1]

As part of the present investigation, the stored energy of high-purity copper (99.99 pct purity) was also determined. The copper was used as an internal standard,[3] allowing the precision of the DSC measurements to be estimated by comparison with previous measurements

T. KNUDSEN, Ph.D. Student and N. HANSEN, Doctor Techn., are with the Center for Fundamental Research: Metal Structures in Four Dimensions, Risø National Laboratory, Roskilde, Denmark. Contact e-mail: tine.knudsen@risoe.dk W.Q. CAO, formerly Ph.D. Student with the Department of Materials Science and Engineering, Tsinghua University, Beijing, P.R. China, is currently Post Doctor, with the Department of Materials Engineering, Monash University, Monash, VIC 3800, Australia. A. GODFREY Professor, is with the Department of Materials Science and Engineering, Tsinghua University, Beijing, China. Q. LIU, Professor, is with the Department of Materials Science and Engineering, Chongqing University, Chongqing, P.R. China.

Manuscript submitted May 15, 2007.
Article published online January 3, 2008

conducted in house as well as at other laboratories. For copper of this purity, it has previously been shown by DSC[4] that the energy release is related to recrystallization, *i.e.*, the heat flow curve shows only one stage. This behavior makes Cu a very suitable material to be used as a standard.

II. EXPERIMENTAL

High-purity polycrystalline nickel (99.99 pct purity) with a grain size of 80 to 100 μm was cold rolled to thickness reductions of 70 pct ($\varepsilon_{vM} = 1.4$), 90 pct ($\varepsilon_{vM} = 2.7$), 95 pct ($\varepsilon_{vM} = 3.5$), and 98 pct ($\varepsilon_{vM} = 4.5$), as described in Reference 17. The microstructural parameters were obtained from a previous study in which thin foils were examined in a JEOL* 2000FX transmission electron microscope (TEM) operated at 200 keV. The misorientations were calculated from the analysis of convergent-beam Kikuchi patterns.[17] The deformed nickel was stored a long time at RT, before the DSC analysis at Risø. To examine whether this storage had any effect, some newly deformed nickel samples were also analyzed in a parallel experiment at Tsinghua University. As will be shown later, no significant difference was found between the two data sets.

*JEOL is a trademark of Japan Electron Optics Ltd., Tokyo.

High-purity polycrystalline copper (99.99 pct purity) with an average grain size of 25 μm was cold rolled 90 pct ($\varepsilon_{VM} = 2.7$), as described in Reference 3, and was used to validate the stored-energy measurements. The copper material and samples were stored in a freezer at −30 °C prior to the DSC analysis.

For the DSC measurements, samples of nickel cold rolled 95 and 98 pct and copper cold rolled 90 pct were prepared from the rolled sheets, by punching out disks with a diameter of 6 mm. The deformation introduced by the punching was removed by polishing the disks on silicon-carbide paper (grit 1000/4000), to give a maximum diameter of 4.5 mm (the maximum allowable diameter of the sample pan in the DSC equipment). Samples of material cold rolled 90 and 70 pct were prepared from the rolled sheets by cutting square-shaped samples (approximately 5×5 mm) on an ACCUTOM-5 (Struers Ballerup, Denmark), using the lowest cutting rate and water cooling. Disk-shaped samples with a diameter of 4.5 mm were then obtained by polishing on silicon-carbide paper (grit 1000/4000).

The samples were prepared in order to maximize the amount of material per sample, given the constraint on the sample diameter; hence, the sample weight varied from 35 to 400 mg. The surface of each sample was polished, in order to enhance the heat conductivity between the sample and the sample pan, and was cleaned after polishing in an ultrasonic bath of ethanol. Before use, the aluminum sample pans were heat treated at 500 °C for 1 hour.

The DSC measurements (Risø) were carried out in a heat flux calorimeter from Seiko Instruments Inc., Japan (DSC 120), with the data analysis conducted using the accompanying software. Note that the exothermic peaks are displayed positive. The experiments were conducted with a constant heating rate of 5 K/min, in an inert atmosphere of argon (100 mL/min), with a fully annealed sample as the reference.

The nickel samples were heated from room temperature (RT) to well above the recrystallization temperature: 500 °C for the lowest-strain and 475 °C for the highest-strain samples. The copper samples were heated from RT to 350 °C. Two consecutive measurements were conducted on each sample. This was done in order to ensure that the sample was fully recrystallized and to obtain a baseline for the quantitative measurements. Three samples were examined at each strain level for the nickel; two samples were examined for the copper material.

Additional nickel samples were prepared at Tsinghua University by cold rolling high-purity nickel (99.99 pct purity) to reductions of 70 pct ($\varepsilon_{vM} = 1.4$), 90 pct ($\varepsilon_{vM} = 2.7$), 93 pct ($\varepsilon_{vM} = 3.1$), 96 pct ($\varepsilon_{vM} = 3.7$), and 98 pct ($\varepsilon_{vM} = 4.5$). One sample per strain was prepared by spark cutting 3-mm square-shaped samples (10 to 30 mg) from the rolled sheets. The stored energy was measured using power-compensated DSC (Perkin-Elmer Inc., Wellesley, USA). The specimens were heated at 10 K/min from RT to 500 °C, in an inert atmosphere.

Nickel samples for yield stress measurement were also prepared at Tsinghua University. For these samples, 99.99 pct pure nickel was cold rolled to thickness reductions of 10 pct ($\varepsilon_{vM} = 0.12$), 20 pct ($\varepsilon_{vM} = 0.26$), 37 pct ($\varepsilon_{vM} = 0.53$), 50 pct ($\varepsilon_{vM} = 0.8$), 70 pct ($\varepsilon_{vM} = 1.4$), 90 pct ($\varepsilon_{vM} = 2.7$), and 98 pct ($\varepsilon_{vM} = 4.5$). From the rolled sheets, tensile specimens were machined, with the tensile direction parallel to the rolling direction. The tensile experiments were conducted in an Instron stress rig (Instron, Norwood, USA). The yield stress values were determined at 0.2 pct plastic deformation.

For comparative purposes, the stored energy of copper cold rolled 90 pct and nickel cold rolled 95 pct (both samples from Risø), have also been measured by the NETZSCH Application Laboratory (Selb, Germany). These samples are denoted as NETZSCH samples here. The stored-energy measurements were conducted in a heat flux DSC (NETZCH model STA 449 C Jupiter, Netzsch Selb, Germany), at heating rates of either 5 or 50 K/min. The temperature programs, sample pans, gas, and gas flow were as used at Risø.

III. RESULTS

A. *Stored Energy—DSC*

Figure 1 shows two weight-normalized heat flow curves obtained for a copper sample cold rolled 90 pct. The upper curve is obtained during the first heating ramp, while the lower curve is obtained during reheating of the recrystallized sample. By comparing the two curves, two features appear: (1) a single exothermic peak is observed, which is initiated at 180 °C, and (2) a slight difference is observed between the two curves in the temperature interval 50 °C to 350 °C.

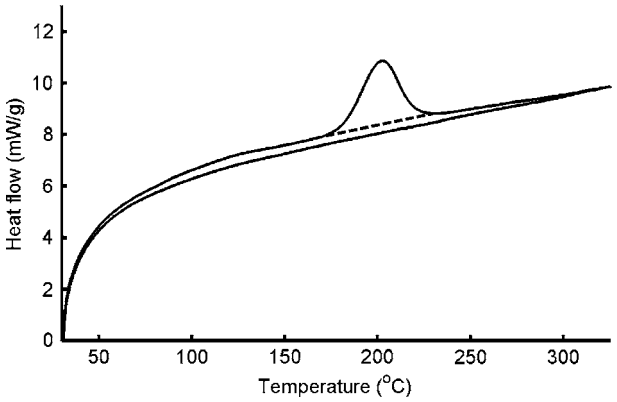

Fig. 1—Heat flow *vs* temperature of copper cold rolled 90 pct.

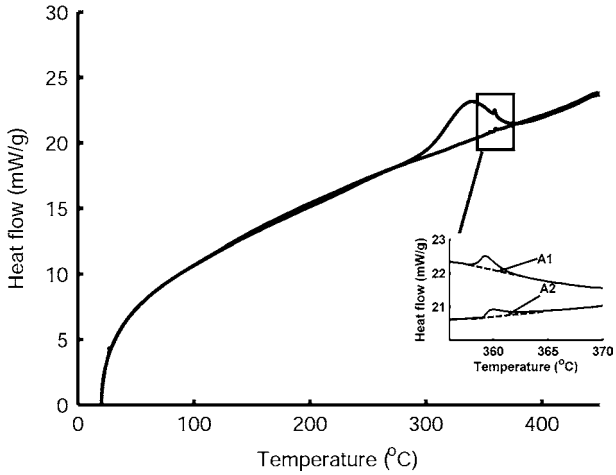

Fig. 2—Heat flow *vs* temperature of nickel cold rolled 95 pct.

The single exothermic peak is related to recrystallization of the sample; the heat released during the recrystallization is obtained by integration of this peak: (1) for the curve in Figure 1, the integration of the peak, *i.e.*, the area enclosed by the curve and the dashed line, gives a stored energy of 0.76 J/g; and (2) a slight difference is observed between the two curves in the temperature interval 50 °C to 350 °C.

Regarding the differences in the energy release curves, if recrystallization is the only process leading to heat release, the two curves should overlap everywhere except for the recrystallization peak region. If heat is released by recovery during the heating ramp, then a higher heat flux during the first heating ramp compared to the second will be seen. However, if recovery were the only reason for the difference in the temperature interval 50 °C to 350 °C, the difference between the two curves would increase with increasing temperature and would be negligible after recrystallization. Since the difference in the signal is nearly constant in this temperature interval, the difference cannot be attributed only to recovery. The observed difference, therefore, might also be of an experimental character—for example, if the heat conduction conditions change after annealing and cooling of the sample. Regardless of the origin of the small differences between the two curves, the main energy release is observed during recrystallization, and this is used to characterize the stored energy of copper.

Figure 2 shows two heat flow curves for a nickel sample cold rolled 95 pct. During the first heating ramp, two exothermic peaks, one large and one small, are observed. The large peak is observed in the temperature interval 280 °C to 385 °C, while the small peak is observed superimposed on the large peak at 358 °C. The large peak is due to the recrystallization of nickel, while the small peak is associated with the energy release during the magnetic transition of nickel. This transition is observed due to a slight difference in the heat capacity (weight) of the sample and the reference (nominally 5 mg, for the data shown in Figure 2).

In the evaluation of the energy stored in nickel due to deformation, the contribution from the magnetic transition has to be subtracted. This energy is found by integrating the small peaks on both the first and second heating curve (illustrated in the insert of Figure 2(b)). The average value of the two measurements is then taken as the energy associated with the magnetic transition. The energy stored due to deformation is found by integrating the heat flow curve from 280 °C to 385 °C and then subtracting the energy contribution from the magnetic transition. In Figure 2, the energy release from 280 °C to 385 °C is 1.54 J/g, while the energy of the magnetic transition is 0.008 J/g; hence, the energy stored due to deformation in this nickel sample cold rolled 95 pct is 1.53 J/g. All curves were corrected in a similar manner. The two heat flow curves in Figure 2 show nearly no signal difference between the first and second heating ramps in the temperature range outside the recrystallization peak. The main part of stored energy is released, therefore, during recrystallization, and the peak related to recrystallization can be used to determine the stored energy of the nickel samples.

The calorimetric measurements were validated using the copper samples. Two samples have been measured at Risø and one sample at NETZSCH.** The data are presented in Table I, in which the mean, the standard deviation (σ), and the standard error of the mean (SE ($= \sigma \times N^{-0.5}$)) are given. The Risø measurements give an average stored energy of 0.77 J/g, equivalent to 6.88 MJ/m^3 (SE = 0.13 MJ/m^3). The NETZSCH measurements give a stored energy of 6.70 MJ/m^3, *i.e.*, just 2.6 pct lower than the Risø measurements. This is considered as a very good agreement.

Stored-energy data obtained from all the nickel samples are also shown in Table II. The standard deviation of the Risø experiments is, in this case, 10 to 13 pct. This is significantly higher than for the copper samples; the origin of this is yet to be explored. The standard error of the Tsinghua data is estimated to be 10 pct, based on the upper limit of the standard error of the Risø data.

**In the NETZSCH evaluation, the recrystallization peak was also used to characterize the stored energy in copper.

Table I. Stored Energy of 90 Percent Cold-Rolled Copper

	Risø	NETZSCH
E_{DSC} (J/g)	0.77	0.75
σ	0.015	—
E_{DSC} (MJ/m^3)*	6.88	6.70
σ	0.13	—
SE	0.09	—

*Density of copper: 8933 kg/m^3.[18]

From Table II, it is possible to compare the Risø data with the NETZSCH data. In nickel cold rolled 95 pct, the stored energy measured at Risø is 14.2 MJ/m^3, while the NETZSCH determined value is 14.7 MJ/m^3. This corresponds to the NETZSCH measurement being 3.5 pct higher than the Risø measurement; hence, these data are also in very good agreement.

The effect of heating rate is demonstrated in Table III, where data obtained at heating rates of 5 and 50 K/min are listed (only one sample has, however, been examined at each rate). If energy is released due to recovery prior to recrystallization, it can expected that an increase in the heating rate will give an increase in the stored energy measured from the recrystallization peak. Given the small difference in the obtained values (Table III), it is concluded that the present experiment shows no influence from the heating rate. Consequently, the data obtained at Risø with a heating rate of 5 K/min are directly comparable to the data obtained at Tsinghua, where a heating rate of 10 K/min was used.

The nickel stored-energy data are displayed in Figure 3, together with error bars showing the standard error. From the figure, it is seen that the Risø data display a linear increase of stored energy with strain, though some deviation is seen for the measurement conducted at the highest strain. This deviation may be related to experimental error, as samples at these reductions are very thin and light (32 to 37 mg). A small sample mass could, for example, lead to a lower pressure between the sample and the sensor and, consequently, to a large experimental error.

The stored-energy data from the measurements conducted at Tsinghua are also displayed in Figure 3.

Table III. Stored Energy Measured at Different Heating Rates

Sample	ε_{vM}	Heat Rate (K/min)	E_{DSC} (MJ/m^3)	Difference
Cu	2.7	5	6.73	—
Cu	2.7	50	6.77	0.6 pct
Ni	3.5	5	14.7	—
Ni	3.5	50	14.95	1.7 pct

A similar linear dependence between stored energy and strain is found, except for a higher stored energy for the highest strain sample. Furthermore, it is noted that the Risø and Tsinghua data agree reasonably well, given the estimated experimental errors. In Figure 4, the weighted averages of all data are plotted as a function of strain, excluding, however, the 93 and 96 pct measurements, as only one measurement was conducted at each of these strains. Figure 4 shows that the weighted average of the measured stored energies (E_{DSC}) increases linearly with strain (ε_{vM}) in the entire strain interval, following a relationship given by E_{DSC} (MJ/m^3) = 2.3 ε_{vM} + 5.9. The weighted average of the measured stored energies is used in the subsequent analysis: the data are given as E_{DSC} in Table V.

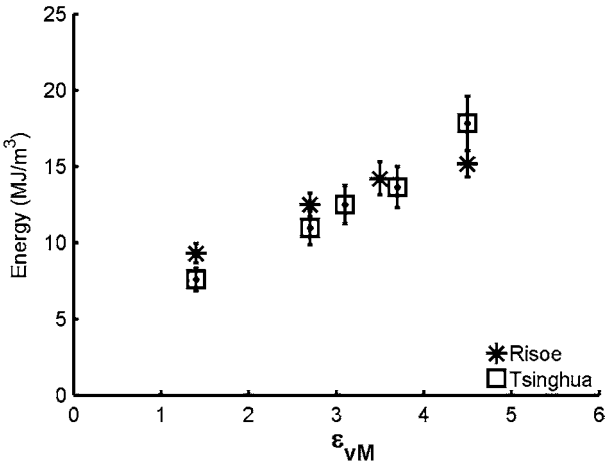

Fig. 3—Stored energy measured with DSC as a function of strain.

Table II. Stored Energy of Cold-Rolled Nickel

Laboratory	Thickness Reduction (Pct)	ε_{vM}	E_{DSC} (J/g)	σ (J/g)	SE (J/g)	E_{DSC} (MJ/m^3)*	σ (MJ/m^3)*	SE (MJ/m^3)*
Risø	70	1.4	1.04	0.12	0.07	9.3	1.1	0.64
Risø	90	2.7	1.4	0.15	0.09	12.5	1.3	0.78
Risø	95	3.5	1.59	0.21	0.12	14.2	1.89	1.09
Risø	98	4.5	1.70	0.17	0.09	15.1	1.5	0.86
NETZSCH	95	3.5	1.65	—	—	14.7	—	—
Tsinghua	70	1.4	0.85	—	0.13	7.6	—	1.1
Tsinghua	90	2.7	1.23	—	0.18	11.0	—	1.7
Tsinghua	93	3.1	1.4	—	0.21	12.5	—	1.9
Tsinghua	96	3.7	1.53	—	0.23	13.6	—	2.0
Tsinghua	98	4.5	2.0	—	0.30	17.8	—	2.7

*Density of nickel 8907 kg/m^3.[18]

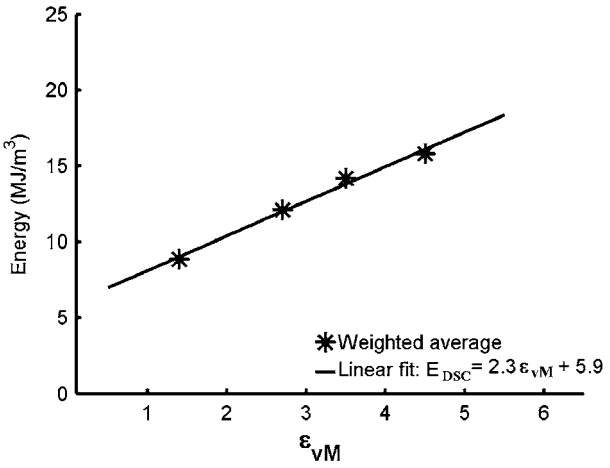

Fig. 4—Weighted average of the stored energy measured with DSC as a function of strain.

B. *Stored Energy—TEM*

The microstructural parameters used for estimation of the stored energy were obtained from an earlier TEM investigation of cold-rolled high-purity nickel (99.99 pct).[17,19] The deformed microstructure is subdivided by extended boundaries (geometrically necessary boundaries (GNBs)) and by short interconnecting boundaries (incidental dislocation boundaries (IDBs)), which together form a cell block structure. Between the GNBs and IDBs, a loose dislocation structure is present with a fairly low dislocation density. The average spacing between the boundaries (d_{av}^{IDB}, d_{av}^{GNB}), the distribution of misorientation angles, and the average misorientation angles ($\theta_{av}^{\mathrm{IDB}}$, $\theta_{av}^{\mathrm{GNB}}$) across the boundaries were determined from longitudinal sections of the cold-rolled samples (Figure 5). The average parameters from these TEM measurements are summarized in Table IV. A number of high-angle boundaries (defined as boundaries with a misorientation angle >15 deg) are present in the microstructure. For example, after a 70 pct reduction, 7 pct of the 325 analyzed boundaries are high-angle boundaries, while in the sample cold rolled 98 pct, this figure increases to 28 pct of 410 analyzed boundaries.

Table IV. Microstructural Parameters and Estimated Stored Energy for Cold-Rolled Nickel[20]

Reduction	70 Pct	90 Pct	98 Pct
Strain	1.4	2.7	4.5
$\theta_{av}^{\mathrm{IDB}}$	2.2	2.7	3.0
$\theta_{av}^{\mathrm{GNB}}$	7.9	14.8	19.7
d^{IDB} (μm)	0.42	0.39	0.31
d^{GNB} (μm)	0.28	0.21	0.13
S_V^{IDB} (μm^{-1})	3.10	3.13	3.95
S_V^{GNB} (μm^{-1})	4.36	5.82	9.19
χ ($\theta_{av}^{\mathrm{IDB}}$)	1.05	1.05	1.05
χ ($\theta_{av}^{\mathrm{GNB}}$)	1.08	1.08	1.05
$E_{\mathrm{IDB},av}$ (MJ/m^3)	1.09	1.26	1.70
$E_{\mathrm{GNB},av}$ (MJ/m^3)	3.02	4.66	7.58
$E_{\mathrm{TEM},av}$ (MJ/m^3)	4.12	5.93	9.28
$E_{\mathrm{TEM,dist}}$ (MJ/m^3)	3.29	4.88	8.16

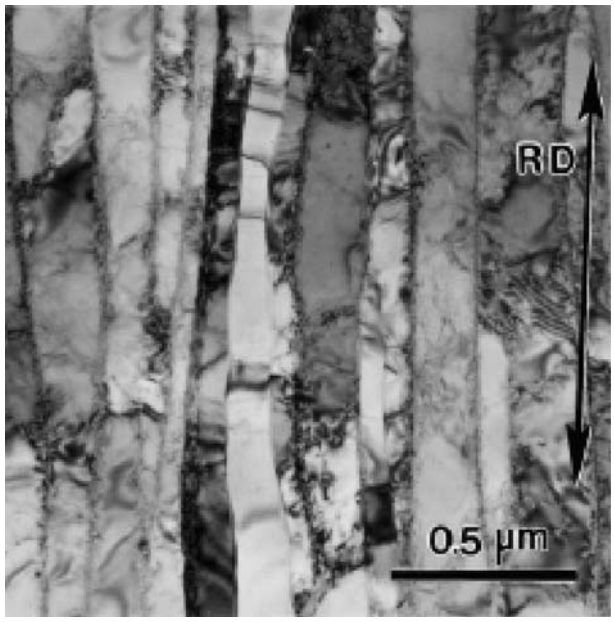

Fig. 5—Microstructure of nickel cold rolled 98 pct, longitudinal section, from Ref. 17.

If we assume that the total energy stored (E) in a deformation microstructure is due only to the dislocations left behind after deformation, then the stored energy is given by the energy of a dislocation line per unit length (E_{dis}) times the density of dislocations (ρ); *i.e.*,

$$E = \rho \cdot E_{\mathrm{dis}} \qquad [1]$$

The presence of dislocations in boundaries with misorientations from very small to large angles makes it impossible, however, to determine the dislocation density directly. Hence, an estimate of the stored energy in the deformation structures cannot be made simply by using the relationship given in Eq. [1]. If it is assumed, however, that the dislocations are arranged in low-energy dislocation structures (LEDS), the energy of a given boundary per unit area (γ) is related to the misorientation angle (θ) of the boundary through the Read–Shockley equation:[12,20]

$$\gamma = \gamma_m \left(\frac{\theta}{\theta_m}\right)\left[1 - \ln\left(\frac{\theta}{\theta_m}\right)\right] : \theta < \theta_m$$
$$\gamma = \gamma_m : \theta \geq \theta_m \qquad [2]$$

where γ_m is taken as the grain-boundary energy per unit area for nickel 0.87 Jm^{-2},[21] and θ_m is taken as 15 deg.[12]

The stored energy of a deformation microstructure (E_{TEM}) can, therefore, be evaluated as the boundary energy per unit area multiplied by the area per volume fraction (S_V) of the boundaries, *i.e.*,

$$E_{\mathrm{TEM}} = S_V \cdot \gamma \qquad [3]$$

As described previously, the nickel-deformed microstructure contains two boundary types: GNBs and

IDBs. The three-dimensional (3-D) arrangement of the GNBs and IDBs differ. The IDBs consist of cell boundaries with a nearly equiaxed configuration. The IDBs are enclosed by the GNBs, which are extended parallel planar dislocation boundaries. This stereological difference has to be taken into consideration when the area per volume fraction is evaluated from the average spacing (d) of the two boundaries. In References 22 and 23, it is shown that the area per volume fraction of infinitely long GNBs (S_v^{GNB}) and of IDBs (S_v^{IDB}) can be evaluated from the average spacings (d^{GNB}, d^{IDB}) according to

$$S_V^{\mathrm{GNB}} = \frac{1}{d^{\mathrm{GNB}}}; S_V^{\mathrm{IDB}} = \frac{\pi}{2 \cdot d^{\mathrm{IDB}}} \quad [4]$$

This is, however, an idealized description of the microstructure. In reality, the GNBs are not infinitely long, but terminate to form cell blocks. In the evaluation of S_v, an extra contribution from the cell-block ends has to be added to S_v^{GNB}, and this contribution has to be subtracted from S_v^{IDB}. Values of S_v^{IDB} and S_v^{GNB} taking this into account are reported in Reference 19, and the values given there are used in the current calculations (Table IV).

From the microstructural parameters determined in the TEM, it is, therefore, possible to calculate the energy stored in the structure by the use of Eq. [3], in which the two boundary types are considered separately; *i.e.*,

$$E_{\mathrm{TEM}} = S_V^{\mathrm{GNB}} \cdot \gamma^{\mathrm{GNB}} + S_V^{\mathrm{IDB}} \cdot \gamma^{\mathrm{IDB}} \quad [5]$$

where γ^{GNB} is the energy per unit area of the GNBs and γ^{IDB} is the energy per unit area of the IDBs, calculated from Eq. [2]. The stored-energy calculations were conducted in two slightly different ways. In the first method, the average spacings and average misorientations ($\theta_{av}^{\mathrm{GNB}}$, $\theta_{av}^{\mathrm{IDB}}$) from Reference 19 are used. Use of the average of the misorientation angles leads, however, to an overestimate of the total stored energy.[12] To account for this overestimate, the average misorientation angle is, therefore, corrected by a scaling factor χ, defined in Eq. [10] in Reference 12. The scaling factor for GNBs, $\chi(\theta_{av}^{\mathrm{GNB}})$, and IDBs, $\chi(\theta_{av}^{\mathrm{IDB}})$, are given in Table IV. The stored energy calculated using the first method ($E_{\mathrm{TEM,avg}}$) is therefore given by

$$E_{\mathrm{TEM,avg}} = S_V^{\mathrm{GNB}} \frac{\gamma(\theta_{av}^{\mathrm{GNB}})}{\chi(\theta_{av}^{\mathrm{GNB}})} + S_V^{\mathrm{IDB}} \frac{\gamma(\theta_{av}^{\mathrm{IDB}})}{\chi(\theta_{av}^{\mathrm{IDB}})} \quad [6]$$

where $\gamma(\theta_{av}^{\mathrm{GNB}})$ is the boundary energy per unit area for GNBs, calculated from the average misorientation angle of the boundaries and, likewise, $\gamma(\theta_{av}^{\mathrm{IDB}})$ is the boundary energy per unit area for IDBs. In the second method, the distributions of the misorientation angles are considered in the calculation of the boundary energy per unit area, as explained here. The misorientation angle data are given in Reference 19 as histograms. From each bin in the histograms are both the average misorientation angles calculated ($\overline{\theta}_{\mathrm{bin}}^{\mathrm{GNB}}$, $\overline{\theta}_{\mathrm{bin}}^{\mathrm{IDB}}$) by and the corresponding boundary energy per unit area found ($\gamma_{\mathrm{bin}}^{\mathrm{GNB}}(\overline{\theta}_{\mathrm{bin}}^{\mathrm{GNB}})$, $\gamma_{\mathrm{bin}}^{\mathrm{IDB}}(\overline{\theta}_{\mathrm{bin}}^{\mathrm{IDB}})$) by the use of Eq. [2]. The stored energy in one bin is calculated by multiplying $\gamma_{\mathrm{bin}}^{\mathrm{GNB}}(\overline{\theta}_{\mathrm{bin}}^{\mathrm{GNB}})$ (or $\gamma_{\mathrm{bin}}^{\mathrm{IDB}}(\overline{\theta}_{\mathrm{bin}}^{\mathrm{IDB}})$) with the boundary area per volume of the bin ($S_{V\text{–bin}}$), as given by Eq. [3], and the total stored energy associated with one boundary type is found by summing the contribution from all bins in the histogram. Finally, the total stored energy ($E_{\mathrm{TEM,dist}}$) at each strain is given by the sum of contributions from each of the boundary types (GNBs and IDBs).

For each boundary type, $S_{V\text{–bin}}$ is determined from S_V^{GNB} (or S_V^{IDB}) multiplied by $n_{\mathrm{bin}}^{\mathrm{GNB}}/N_{\mathrm{GNB}}$ (or $n_{\mathrm{bin}}^{\mathrm{IDB}}/N_{\mathrm{IDB}}$), where $n_{\mathrm{bin}}^{\mathrm{GNB}}$ (or $n_{\mathrm{bin}}^{\mathrm{IDB}}$) is the number of boundaries in the bin and N_{GNB} (or N_{IDB}) is the total number of boundaries measured. The calculation is summarized in Eq. [7]:

$$E_{\mathrm{TEM,dist}} = \left(\sum_{\mathrm{bin}} \gamma_{\mathrm{bin}}^{\mathrm{GNB}}(\overline{\theta}_{\mathrm{bin}}^{\mathrm{GNB}}) \cdot n_{\mathrm{bin}}^{\mathrm{GNB}} \right) \frac{S_V^{\mathrm{GNB}}}{N_{\mathrm{GNB}}} + \left(\sum_{\mathrm{bin}} \gamma_{\mathrm{bin}}^{\mathrm{IDB}}(\overline{\theta}_{\mathrm{bin}}^{\mathrm{IDB}}) \cdot n_{\mathrm{bin}}^{\mathrm{IDB}} \right) \frac{S_V^{\mathrm{IDB}}}{N_{\mathrm{IDB}}} \quad [7]$$

The values of S_V^{GNB} and S_V^{IDB} for each of the distributions are taken from separate TEM measurements (over a large area) of the average boundary spacings for the GNBs and IDBs. This method involves an implicit assumption that there is no correlation between each misorientation angle and the area per volume of boundaries with that misorientation angle. Both estimates are given in Table IV and are plotted as a function of strain in Figure 6, together with the weighted average of the DSC measurements.

Figure 6 shows a linear relationship between the stored energy based on the microstructure (E_{TEM}). A linear least squares fit to the data gives a proportionality constant between E_{TEM} and ε_{vM} of 1.6 or 1.7, where the lower value corresponds to the value obtained considering the complete misorientation angle distribution (method 2), rather than just the average values (method 1). In the following discussion, only data obtained using the distribution of misorientation angles are used. The DSC-measured stored energy (E_{DSC}) is also plotted in Figure 6, where it is seen to be consistently higher than the stored-energy estimate based on the microstructural data ($E_{\mathrm{TEM,dist}}$). The ratio between the $E_{\mathrm{TEM,dist}}$ and E_{DSC} at each strain level is given in Table V. From this, it is seen that the ratio $E_{\mathrm{DSC}}/E_{\mathrm{TEM,dist}}$ decreases with increasing strain.

C. *Yield Stress*

The measured yield stress is displayed as a function of strain in Figure 7. The stress-strain curve initially shows a parabolic increase up to a strain of $\varepsilon_{vM} \approx 1.0$, which is

Table V. Stored Energy Determined by DSC and TEM

	70 Pct	90 Pct	98 Pct
E_{DSC} (MJ/m^3)	8.9	12.1	15.8
$E_{\mathrm{TEM,dist}}$ (MJ/m^3)	3.3	4.9	8.2
$E_{\mathrm{DSC}}/E_{\mathrm{TEM,dist}}$	2.7	2.5	1.9

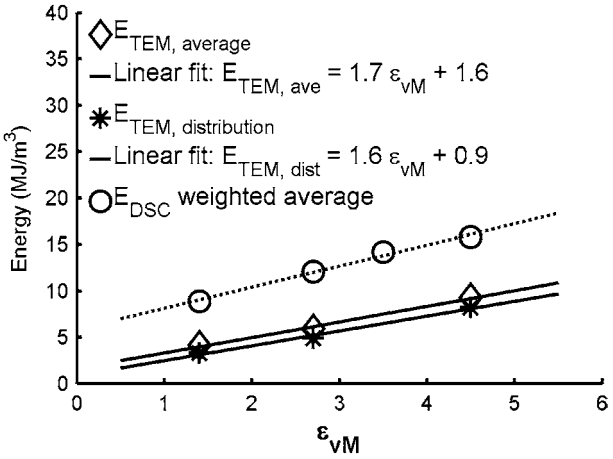

Fig. 6—Stored energy estimated from the microstructural TEM data. DSC data are also displayed.

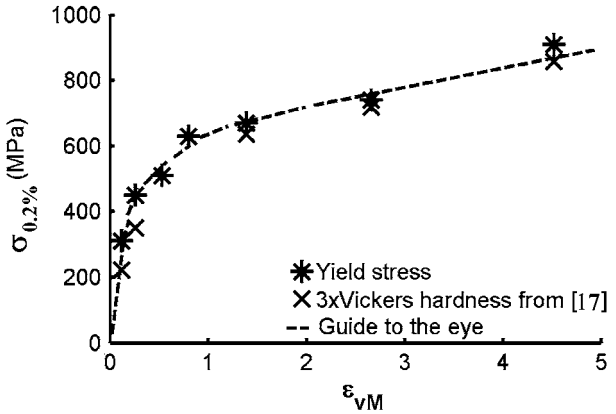

Fig. 7—Yield stress *vs* strain and 3 times Vickers hardness *vs* strain from Ref. 17.

characteristic of the stage III work-hardening regime. This is followed by a linear work hardening at larger strains, which is characteristic of the stage IV work-hardening regime. These observations are more clearly seen in Figure 8, where the work-hardening rate as a function of stress is displayed.

IV. DISCUSSION

A. *Stored Energy—DSC*

The energy stored in a deformed metal, in the most general case, can be thought of as arising from contributions from dislocations, high-angle boundaries, internal stresses, and point defects. The contribution to the stored energy of the point defects, if present, can be identified as a separate peak in a DSC measurement. In the present study, however, for both the Cu and Ni samples, the DSC measurements showed that the stored energy was released during heating in one stage (peak), which is related to the recrystallization of the samples (Figures 1 and 2). Thus, we can exclude point defects as a significant contribution to the stored energy. It is

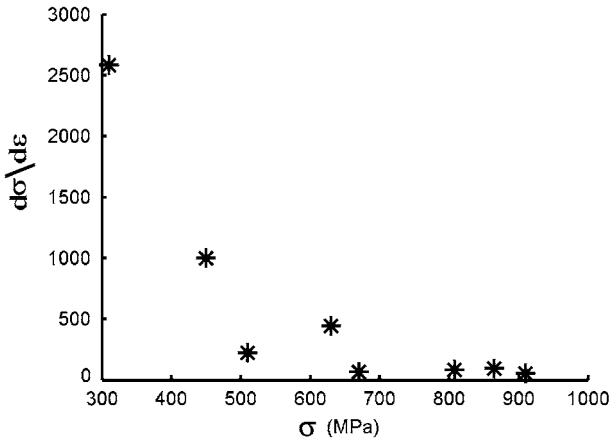

Fig. 8—Work-hardening rate as a function of stress.

suggested that the annihilation of such defects may have taken place already during deformation, due to the high purity of both copper and nickel.

The observation that, for Cu, the energy release takes place in one stage, due to recrystallization, is in agreement with findings reported elsewhere.[1,4,5,24–26] Furthermore, the assumption that the energy release due to recovery is a minor effect is also supported by the findings of Reference 24, where the energy released during recovery of tensile-deformed (39.5 pct) high-purity copper (99.999 pct purity) was just 3 pct of the total stored energy. In the present study, the stored energy of copper cold rolled 90 pct was determined to be 6.9 MJ/m^3. For commercial oxygen-free high conductivity (OFHC) copper (99.96 to 99.98 pct purity), deformed in compression at RT, the stored energy was found to be linearly related with the strain.[4] From Figure 6 of Reference 4, the relationship between stored energy and strain can be expressed as E (cal/g) = 0.0023 ε – 0.01, where ε is the percent reduction. A 90 pct reduction corresponds, therefore, to a stored energy of 7.35 MJ/m^3, which is just 4 pct higher than the value measured in the current study, *i.e.*, the two findings are very similar. Slightly lower values of 5.9 and 7.0 MJ/m^3 were determined for 99.9996 pct pure copper with initial grain sizes of 15 and 50 μm cold rolled 93 pct in Reference 5, while in Reference 25, a somewhat lower stored energy for 90 pct cold rolled 99.99 pct pure copper of 4.22 MJ/m^3 is reported.

The observation that, for deformed nickel, the energy release takes place by recrystallization in one stage has been reported in Reference 9. Other observations, however, carried out under different conditions, report up to three exothermic peaks during the heating of nickel.[1,4,6,9,27] In these reports, the three peaks were related to the annihilation of vacancies, recovery, and recrystallization. Such an energy release was, for example, observed to take place in impure nickel (99.6 pct purity) deformed in torsion to ε_{vM} = 2.56 at RT.[4] In that study, it was found that the energy release during the third stage, *i.e.*, recrystallization, was 6.7 MJ/m^3, while the total energy release was 18.4 MJ/m^3. In the current work, the total measured stored energy at

ε_{vM} = 2.6 is 11.9 MJ/m^3, a value 35 pct lower. The difference between the values may be related to the difference in the purity of the metals, as it is known that the presence of impurities can increase the energy stored during plastic deformation.

In contrast, for 99.99 pct pure nickel cold rolled 90 pct,[9] only one peak related to recrystallization was observed, with an energy release of 5.7 MJ/m^3, lower than the value observed in the present work by a factor of 2, roughly. Because the purity of the nickel is similar to the one used in the current work, the rather large difference in stored energy cannot be attributed to a difference in purity. A possible explanation of the differences might, therefore, be different conditions during cold rolling.

The finding that stored energy increases linearly with strain in certain strain ranges has, furthermore, previously been observed in 99.99 pct copper,[5,27] 99.99 pct pure nickel,[9] and 99.999 pct pure silver.[7]

Based on these data, therefore, the contributions to the stored energy are reduced to those from dislocations, high-angle boundaries, and internal stresses related to the microstructural features. Considering first the internal stresses, it has been suggested that these are minimized through a structural organization into LEDS.[28] For such LEDS, it was furthermore suggested that internal stresses cannot exceed the flow stress, as stresses higher than this will be relaxed through yielding.[28] Based on theoretical considerations, it has been shown that the energy stored due to internal stresses is significantly smaller than (approximately one-fifth of) the energy stored in the form of dislocations.[29]

In the present study, the flow stress (0.2 pct offset) has been determined to be a function of strain (Figure 7). The stored energy caused by internal stresses can be calculated as the maximum elastic energy:

$$E_{\text{elastic}} = 0.5 \cdot \sigma \cdot \varepsilon_{vM} = 0.5 \cdot \frac{\sigma^2}{E_{\text{Young}}} \qquad [8]$$

where σ is the flow stress, ε_{vM} the strain, and E_{Young} the elastic modulus of Ni (200 GPa[30]). In the strain range considered, the flow stress increases from 670 (70 pct) to 910 MPa (98 pct); hence, the contribution from the internal stresses is about 25 to 35 pct of E_{TEM} and is roughly in agreement with the theoretical prediction.[29]

B. *Stored Energy—TEM*

The parameters characterizing the deformation structures in Ni have been determined from Kikuchi line measurements in a TEM. An alternative method would be to use the electron backscattering diffraction (EBSD) technique.[12,14] The limited angular resolution of this method (up to 2 deg for heavily deformed samples) results, however, in a number of low-angle boundaries being undetected in an investigation of a deformed sample. As a result, a stored-energy analysis based on EBSD data will lead to an underprediction, with the error being larger at smaller applied strains. For large strains, the two methods may give comparable results.[12] In the present study, the TEM method was chosen for all samples, in order to facilitate the comparison of data over the entire strain range.

The stored energy has been calculated using the Read–Shockley formalism, as expressed in Eq. [2]. This equation includes the energy stored in the dislocations and the dislocation core, but excludes the contribution of internal stresses caused by the presence of the dislocations.[20] The structure of the deformed Ni, as previously described, contains dislocation boundaries and high-angle boundaries ($>$ 15 deg), where the latter includes both those present in the starting material and those introduced during cold rolling. The contribution from the high-angle boundaries is taken into account through the grain-boundary energy (Eq. [2]). For samples deformed to large strains, this contribution may account for a large fraction of the stored energy, as the fraction of high-angle boundaries may be as high as 60 to 80 pct.[31] In the present experiment, the fraction of high-angle boundaries increases from 7 to 28 pct as the rolling reductions is increased from 70 to 98 pct.

In the calculation of E_{TEM} based on the Read–Shockley equation, the contribution from dislocations stored between boundaries has not been included. The density of such dislocations has been estimated in Reference 19 to be about 10^{14} m^{-2}, or one dislocation per cell at a reduction strain of 98 pct. The energy associated with these loose dislocations (E_{Loose}) can be calculated from the relationship

$$E_{\text{Loose}} = \tfrac{1}{2} \cdot \rho \cdot G \cdot \mathbf{b}^2 \qquad [9]$$

where G is the shear modulus, **b** is the length of the Burgers vector, and ρ is the dislocation density. Taking values for nickel of G = 79 GPa[32] and b = 0.249 nm[33] gives the stored energy of loose dislocations as 0.24 MJ/m^3. This value corresponds to a mere 3 pct increase in strain, an insignificant contribution in the present sample.

C. *Comparison of E_{DSC} and E_{TEM}*

A comparison of E_{DSC} and E_{TEM} shows that the ratio $E_{\text{DSC}}/E_{\text{TEM,dist}}$ is 1.9 to 2.7 and decreases with increasing strain (Table V). If, however, stored-energy values calculated based on average misorientations angles are used, the ratio $E_{\text{DSC}}/E_{\text{TEM,av}}$ decreases to 1.7 to 2.1. Additionally, if the contribution of internal stresses is included to $E_{\text{TEM,dist}}$, the fraction $E_{\text{DSC}}/E_{\text{TEM,dist}}$ is reduced to 1.5 to 2. A comparable discrepancy between E_{DSC} and E_{TEM} has been observed in previous studies.[1,2,15] For example, in a recent study of polycrystalline copper deformed by cold rolling in the strain range 1 to 3,[16] the dislocation density derived on the basis of calorimetry data was higher by a factor of 1.5 to 2 than the dislocation density determined from the X-ray line profile analysis.

For this discussion, we assume that E_{DSC} is taken as the most correct estimate of the stored energy and discuss why the E_{TEM} value is lower. Consider first that the dislocation density is not determined directly in the TEM characterization; instead, the dislocation density is estimated based on the assumption that the dislocations

are organized in rotation boundaries with a misorientation angle θ. For such boundaries, the area density of dislocations stored in the boundary is of the order of θ/b. In most cases, θ/b gives a minimum number for the dislocation density, because some dislocations may screen each other (*i.e.*, $+b$ and $-b$) and thus not contribute to θ.[28] These redundant dislocations have an average density of $1/h - \theta/b$, where h is the average distance between all the dislocations in a boundary. Such redundant dislocations may be present in significant numbers at low strain, whereas with the increasing perfection of boundaries at larger strain, their contribution will decrease. Such a reduction will be reflected in a decrease in the ratio E_{DSC}/E_{TEM} with increasing strain, as observed (Table V). An example of a boundary with no redundant dislocations is illustrated in a high-resolution electron microscope (HREM) micrograph[34] of copper deformed to large strain (Figure 9(a)). For such boundaries, the individual dislocations can be identified and the distance between the dislocations, h, can be determined, allowing the area density of dislocations to be calculated as $1/h$. For the boundary in Figure 9(a), there is good agreement between the two area densities $1/h$ and θ/b, showing that the dislocation density in the boundary can be accounted for solely on the basis of the misorientation angle. Extra dislocations may, however, also be present in some boundaries, as illustrated in Figure 9(b) (also from Reference 34). The presence of such dislocations near or at boundaries has also been observed in conventional TEM studies,[17] and will contribute to the stored energy measured by DSC, but not to that calculated from the microstructure.

Extra dislocations may also be present in the regions near the high-angle boundaries. However, HREM observations of high-angle boundaries in the deformed metal show that such boundaries have the same characteristics as grain boundaries in undeformed metals. As a consequence, the energy of all high-angle boundaries in Eq. [2] can be taken as γ_m, and the contribution of these boundaries added to the contribution from the dislocation (< 15 deg misorientation) boundaries. It is, however, a characteristic of deformed microstructures that the dislocation boundaries and high-angle boundaries are interconnected at triple lines. Such an interconnection is illustrated in Figure 2 in Reference 35. It may, therefore, be hypothesized that these interconnections are associated with an additional amount of stored energy in the microstructure. The magnitude of such junction energies is, however, a subject for further work.

To summarize the discussion of the TEM and DSC stored energy, the measured stored energy is higher initially by a factor of 2.7, compared to the stored energy calculated from the microstructure. This difference decreases to a factor of 1.9 in the stage IV work-hardening regime. If internal stresses are considered, and if a general uncertainty of 20 pct in the experimental data is assumed, the stored-energy values measured with the two methods approach each other with increasing strain, as illustrated in Figure 10.

D. *Stored Energy and Flow Stress*

In the present study, the flow stress has been determined for samples deformed over a large strain range, from 0.12 to 4.5 (Figure 7). Hardness measurements for the nickel material characterized by TEM are also given.[17] A fairly good agreement is seen between the two sets of data. Initially, the stress-strain curve displays a predominant stage III work-hardening regime, which is followed at a strain of ≈ 1 by a stage IV work-hardening regime. The stored energy has only been measured at large strains for which a linear relationship with strain was obtained (Figure 4).

The linear relationship at large strains is used to calculate the ratio between the stored energy and the expended energy. This ratio can be calculated in different ways. In the following, it is estimated as the instantaneous increase in stored energy, from the plastic work, expressed by the equation

$$W = \int \sigma d\varepsilon \qquad [10]$$

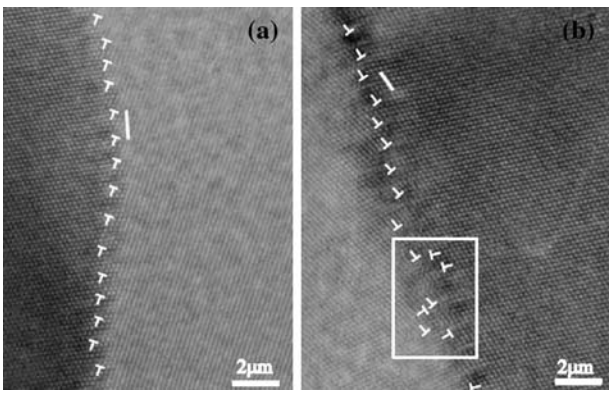

Fig. 9—High-resolution transmission electron microscopy of low-angle boundaries in Cu (99.99 pct) from Ref. 34. (*a*) 11-deg low-angle boundary, well described by edge dislocations and (*b*) 14-deg low-angle boundary described partly by edges dislocations and partly by random edges dislocations, emphasized in the white box.

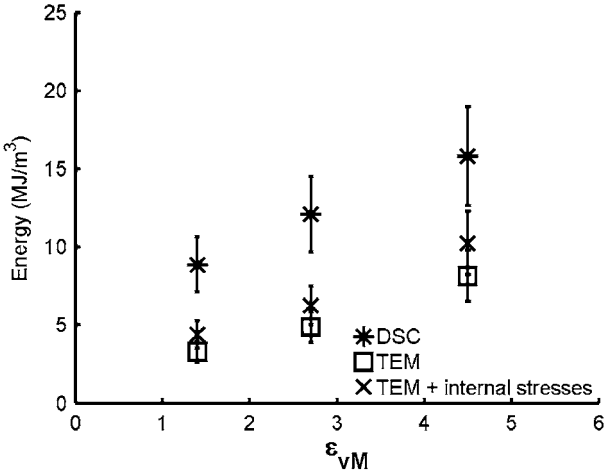

Fig. 10—Stored energy as a function of strain. Measured by DSC and evaluated by TEM.

where W is the plastic work, σ is the flow stress, and ε the strain. The stress in stage IV can be expressed by the equation

$$\sigma = \sigma_0 + \Theta\varepsilon \quad [11]$$

where Θ is the work-hardening rate and σ_0 the extrapolated flow stress at $\varepsilon = 0$. From Eqs. [10] and [11], we can write

$$W = \sigma_0\varepsilon + {}^1\!/_2\Theta\varepsilon^2 \quad [12]$$

The experiments show that a linear relationship exist between the stored energy and the strain:

$$E = E_0 + m\varepsilon \quad [13]$$

where E_0 is the extrapolated stored energy at $\varepsilon = 0$ and m is the proportionality constant between E and ε. If the instantaneous energy storage ratio is defined as

$$\beta = \frac{dE}{dW} \quad [14]$$

the value of β can be found from Eqs. [12] and [13]:

$$\beta = \frac{dE}{d\varepsilon} \Big/ \frac{dW}{d\varepsilon} = \frac{m}{\sigma} \quad [15]$$

In the current work, $m = 2.3$ and $\sigma \in [670 \text{ to } 910]$; therefore, $\beta \in [0.002 \text{ to } 0.003]$. This means that, initially, between stage III and stage IV, 0.3 pct of the expended energy is stored in the metal and, later, in stage IV, this drops to 0.2 pct.

Alternatively, the instantaneous ratio of the total stored energy to the total expended work can be calculated. By doing so, it is found that, at a reduction of 70 pct, just 1.2 pct of the plastic work is stored in the metal, whereas at 98 pct, only 0.5 pct is stored, *i.e.*, the energy stored decreases in the stage IV work-hardening regime. This decrease may be directly related to the way dislocations are stored in the two stages. In stage III, the dislocations are primarily stored in dislocations boundaries, while in stage IV, the structures contain an increasing density of deformation-induced high-angle boundaries, which may be better able to absorb and annihilate dislocations during deformation. As a result, the rate of increase in the dislocation density and in the stored energy will be smaller in stage IV than in stage III.

V. CONCLUSIONS

The stored energy in high-purity (99.99 pct) Ni, cold rolled to equivalent von Mises strains of 1.4 to 4.5 (70 to 98 pct thickness reduction), has been determined by DSC and also estimated based on a quantitative microstructural characterization from TEM data by applying the Read–Shockley equation. The conclusions are the following.

1. The stored energy measured by calorimetry is higher by a factor of 1.9 to 2.7 than the value based on an estimate of the energy stored in dislocation boundaries and high-angle boundaries. This discrepancy can be reduced by introducing contributions both from dislocations stored between the boundaries and from internal stresses.
2. The stored energy determined both by calorimetry and microscopy increases linearly with strain in the strain range examined. In this interval, the flow stress also increases linearly with strain (stage IV work hardening).
3. The ratio between the stored energy and the expended energy is small in stage IV and decreases with increasing strain.
4. The consistency between values obtained in this comparative study validates both the calorimetric- and the microstructure-based techniques. The former may be preferred for bulk analysis, whereas the latter is preferable for an analysis of local variations in the stored energy, due to heterogeneities in the deformed microstructure, which are important for the recovery and recrystallization behavior during subsequent annealing.

ACKNOWLEDGMENTS

Two of the authors (TK and NH) gratefully acknowledge the Danish National Research Foundation for supporting the Center for Fundamental Research: Metal Structures in Four Dimensions, within which this work was performed. Two other authors (AG and QL) acknowledge the National Natural Science Foundation of China for financial support under Contract Nos. 50571049 and 50571051. The authors are also grateful to Dr Wolfgang Pantleon for his help in full discussions and for proposing the use of Eq. [11].

REFERENCES

1. M.B. Bever, D.L. Holt, and A.L. Titchener: *Prog. Mater Sci.*, 1973, vol. 17, pp. 1–177.
2. D. Rönnpagel and C. Schwink: *Acta Metall.*, 1978, vol. 26, pp. 319–31.
3. E. Woldt and D. Juul Jensen: *Metall. Trans. A*, 1995, vol. 26A, pp. 1717–24.
4. L.M. Clarebrough, M.E. Hargreaves, and G.W. West: *Proc. R. Soc. London, Ser. A*, 1955, vol. 232, pp. 262–70.
5. B. Hutchinson, S. Jonsson, and L. Ryde: *Scripta Metall.*, 1989, vol. 23, pp. 671–76.
6. F. Bell: *Arch. Eisenhüttenwesen*, 1965, vol. 36, pp. 745–49.
7. A. Zahia, F. Salhi, J. Aride, D. Monya-Siesse, and G. Moya: *J. Alloys Compd.*, 1992, vol. 188, pp. 264–67.
8. R.O. Williams: *Trans. TMS-AIME*, 1962, vol. 224, pp. 719–26.
9. I. Baker, L. Liu, and D. Mandal: *Scripta Metall.*, 1995, vol. 32 (2), pp. 167–71.
10. F. Bell and O. Krisement: *Acta Metall.*, 1962, vol. 10, pp. 80–83.
11. L.M. Clarebrough, M.E. Hargreaves, and G.W. West: *Philos. Mag.*, 1953, vol. 44, pp. 913–15.
12. A. Godfrey, W.Q. Cao, N. Hansen, and Q. Liu: *Metall. Mater. Trans. A*, 2005, vol. 36A, pp. 2371–78.
13. A. Godfrey, N. Hansen, and D. Juul Jensen: *Metall. Mater. Trans. A*, 2007, vol. 38A, pp. 2329–39.
14. A. Godfrey, Q. Liu, D. Juul Jensen, and N. Hansen: *Proc. 25th Risø Int. Symp.*, C. Gundlach, K. Haldrup, N. Hansen, X. Huang, D. Juul Jensen, T. Leffers, Z.J. Li, S.F. Nielsen, W. Pantleon, J.A. Wert, and G. Winther: 2004, pp. 317–22.

15. T. Ungar, H. Mughrabi, D. Rönnpagel, and M. Wilkens: *Acta Metall.*, 1984, vol. 36, pp. 333–42.
16. T. Ungar, E. Schafler, P. Hanák, S. Bernstorff, and M. Zehetbauer: *Mater. Sci. Eng., A*, doi:10.1016/j.msea.2006.03.156.
17. D.A. Hughes and N. Hansen: *Metall. Trans. A*, 1993, vol. 24A, pp. 2021–37.
18. *The Periodic System of the Elements*, Linde Press, Aarhus, Denmark, 1993.
19. D.A. Hughes and N. Hansen: *Acta Mater.*, 2000, vol. 48, pp. 2985–3004.
20. W.T. Read and W. Shockley: *Phys. Rev.*, 1950, vol. 78, pp. 275–89.
21. L.E. Murr: *Interfacial Phenomena in Metals and Alloys*, Addison-Wesley, London, 1975, Chap. 3.
22. A. Godfrey and D.A. Hughes: *Mater. Charact.*, 2002, vol. 48, pp. 89–99.
23. A. Godfrey and D.A. Hughes: *Acta Mater.*, 2000, vol. 48, pp. 1897–1905.
24. P. Gordon: *Trans. AIME*, 1955, vol. 203, pp. 1043–52.
25. D. Mandal and I. Baker: *Scripta Metall.*, 1995, vol. 33 (5), pp. 831–36.
26. G. Gottstein, H. Steffen, and H. Wollenberger: *Scripta Metall.*, 1973, vol. 7, pp. 451–56.
27. D. Michell and E. Lovegrove: *Philos. Mag.*, 1960, vol. 5, pp. 499–518.
28. D. Kuhlmann-Wilsdorf: *Mater. Sci. Eng., A*, 1989, vol. 113, pp. 1–41.
29. N. Hansen and D. Kuhlmann-Wilsdorf: *Mater. Sci. Eng.*, 1986, vol. 81, pp. 141–61.
30. *Hütte, Des Ingenieurs Taschenbuch Theoretische Grundlagen*, 28*th* edition, Verlag von Wilhelm Ernst & Sohn, Berlin, 1955, p. 1048.
31. O.V. Mishin, D. Juul Jensen, and N. Hansen: *Mater. Sci. Eng., A*, 2003, vol. A342, pp. 320–28.
32. N. Hansen: *Scripta Mater.*, 2004, vol. 51, pp. 801–06.
33. J.S. Koehler: *Phys. Rev. B*, 1970, vol. 2 (2), pp. 547–51.
34. K. Ikeda, K. Yamada, N. Takata, F. Yoshica, H. Nakashima, and N. Tsuji: *Proc. 25th Risø Int. Symp.*, C. Gundlach, K. Haldrup, N. Hansen, X. Huang, D. Juul Jensen, T. Leffers, Z.J. Li, S.F. Nielsen, W. Pantleon, J.A. Wert, and G. Winther, eds., Risoe National Laboratory, Roskilde, Denmark, 2004, pp. 357–62.
35. A.R. Jones, B. Ralph, and N. Hansen: *Proc. R. Soc. London, Ser. A*, 1979, vol. 368, pp. 345–57.

Appendix H

Report A

GFF Basis material AA 1050

Tine Knudsen

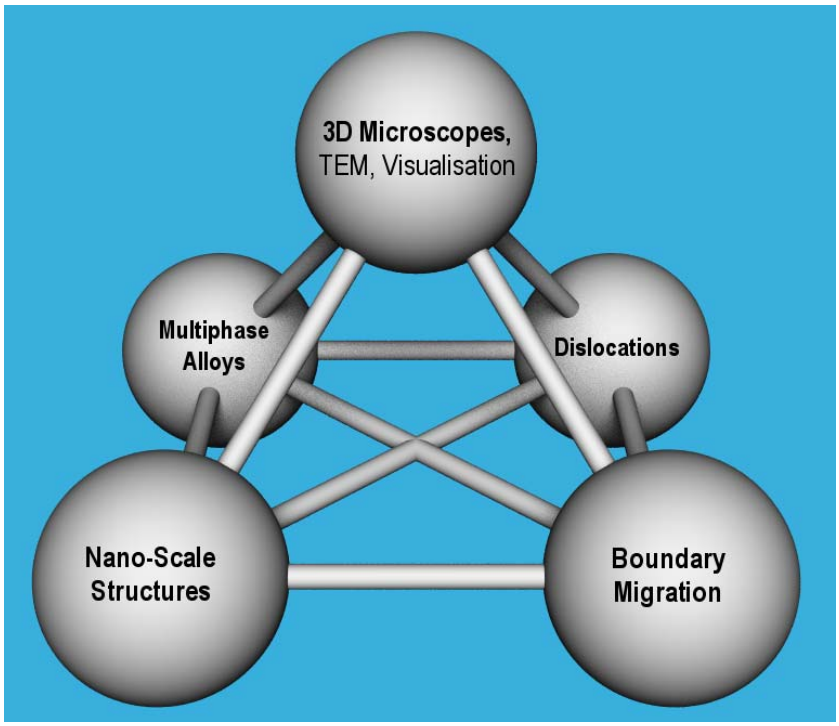

Risø National Laboratory, Roskilde, Denmark
October 2006

Abstract

In the present study a large amount of commercially pure aluminium (AA 1050), was produced to serve as a stock material for The Center for Fundamental Research: Metal Structures in Four Dimensions.
Plates of commercially pure aluminium were cut, heat treated, cold rolled and heat treated again to produce a total of 30 aluminium plates of various sizes. The materials were characterized chemically and with the electron back scattered diffraction pattern technique (EBSP). The data analyzed from the EBSP were characterized with respect to grain size, aspect ratio (RD/ND), distribution of grain sizes and the texture components Cube {100}<001>, Brass {110}<1$\bar{1}$2>, Copper {112}<11$\bar{1}$>, S {12$\bar{3}$}<634>, Goss {011}<100>, C2 {001}<110>, A {310}<1$\bar{3}$0>, B {310}<001> and C1 {122}<2$\bar{2}$1>. Besides, [200] pole figures and orientation distribution functions (ODFs) were plotted. One plate was characterized in nine different locations and since that plate did not show any systematic variation in texture, grain size or distribution of these, the same was assumed to apply to the remaining plates.

From characterization following describes the basis material:

- The material is 99.5% pure
- The major impurities are Si and Fe
- The grain size is 70μm (mean chord length)
- The grains are elongated in the RD/ND plane with an average aspect ratio of 1.3
- The distribution of the grain sizes is not log normal.
- The average texture of the material is fairly random, though with a weak Cube texture (4xrandom).
- Tendency for large grains to be of Cube orientation.

Texture component	Random theoretical vol.%	Measured vol.%	Ratio measured/random
Cube	2.2	9	4
Goss	2.2	2	0.9
Brass	4.4	2	0.5
S	8.8	5	0.6
Cu	4.4	3	0.7
C2	2.2	1	0.2
A	4.4	13	3
B	4.4	15	3
C1	8.8	4	0.4

Contents

Preface

The aim of the present study was to produce a large amount of commercially pure aluminium (AA1050), which could serve as a basic material for The Center for Fundamental Research: Metal Structures in Four Dimensions. The basic material has to have a homogeneous texture and an average grain size below 100µm.

The work was initiated by Dorte Juul Jensen. The samples were rolled and heat treated by Palle H. Nielsen. The EBSP studies were mainly carried out by Preben Olesen, while Tine Knudsen was responsible for additional EBSP characterizations, analyzing the data and writing this report.

1 Procedure

The basis material consists of 30 plates. To determine if these were homogeneous, samples were analyzed in order to investigate the variation between the plates and within one plate. From the material 9 samples were taken from plate no. one and 6 samples from the other plates. The samples were characterized with respect to the texture, the average grain size and the distribution of grain sizes. The textures were analyzed with respect to the texture components Cube {100}<001>, Brass {110}<1 $\bar{1}$ 2>, Copper {112}<11 $\bar{1}$ >, S {12 $\bar{3}$ }<634>, Goss {011}<100>, C2 {001}<110>, A {310}<1 $\bar{3}$ 0>, B {310}<001> and C1 {122}<2 $\bar{2}$ 1> together with calculation of pole figures and ODFs.

2 Experimental

2.1 Material

The material described in the current study was fabricated from a plate of commercially pure aluminium AA1050 delivered by METALCENTRET in Glostrup.

2.2 Sample preparation

8 plates of size 155x400x25mm and 2 plates of size 200x400x25mm were cut from an aluminium AA1050 plate with the dimensions 1000x2000x25mm. The remainder of the plate was put in stock. The AA1050 plate is 99.5% Al and the complete chemical analysis is given in appendix A.1. The plates were heated separately in a GCA furnace (series 2110 model 2027). The material was heat treated to minimize the amount of Si and Fe in solid solution. The temperature program is shown in figure no. 1.

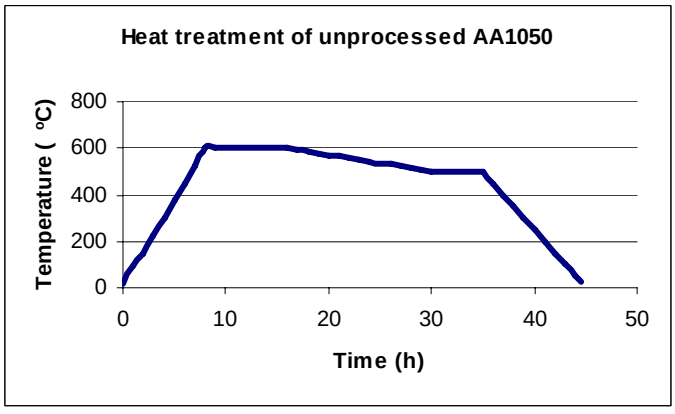

Figure 1: Sketch of the temperature program used on the unprocessed aluminium

After the heat treatment the plates were sprayed with a petroleum/oil solution (1:1 vol %) and cold rolled 60% with an L/h ratio in the range of 1 (defined in appendix A.2), so the imposed texture was as homogenous through the plate thickness as possible. After rolling the plates were cut again, thereby creating a total of 30 plates. 12 plates with dimensions 250x140x10mm, 12 plates with dimensions 300x150x10mm and finally 6 plates of the size 300x200x10mm. The plates were thereafter reheated separately in a Heraus furnace (at 400^{o}C) and then in a Scandia furnace (550^{o}C) in order to recrystallize the aluminium and obtain the desired grain size. The temperature program is shown in figure 2.

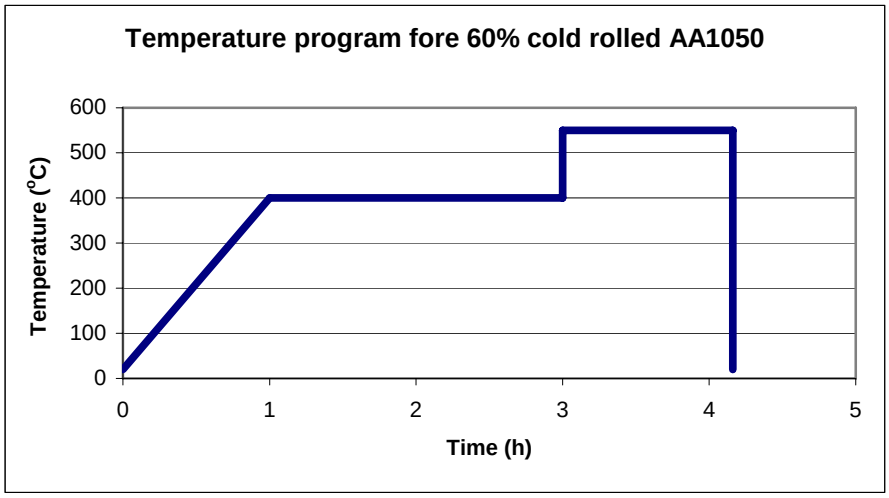

Figure 2: Sketch of the temperature program used to recrystallize the cold rolled aluminium

From the 30 plates, 11 samples were taken for analysis of texture and grain size. 9 samples were taken from plate no. 1 and one sample was taken from plate no. 5, 10, 15, 20, 25, and 30. Figure 3 shows the position in the respective plates from where the samples were taken and the plate no. is written.

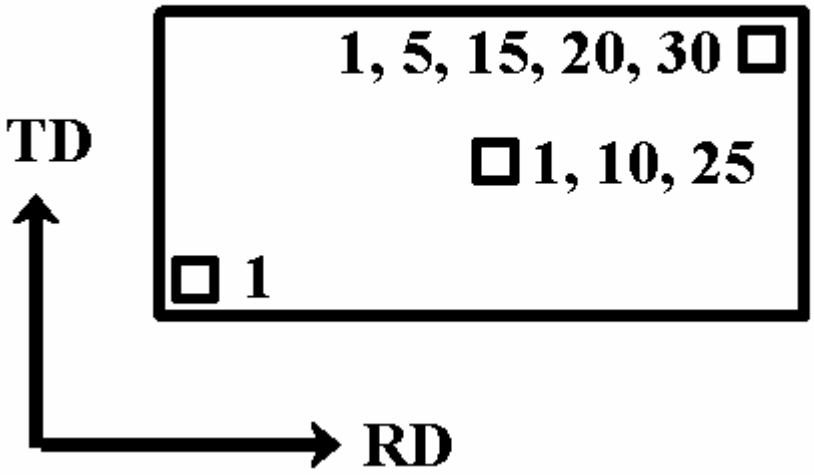

Figure 3: Illustration of the positions, from were each sample was taken in the respectively plates. The numbers refer to the plate number from where the sample was taken.

The samples from plate no. 1 are denoted 1L when taken from the left corner of the plate (see figure 3), 1M when taken from the middle of the plate and 1R when taken from the right top corner. The samples were taken near the surface, at one quarter thickness and in the middle of the RD/ND plane. The data recorded is denoted by the plate number, position in the RD/TD plane (L, M, R) and finally its position in the ND/RD plane (surface, ¼ thickness and middle). The samples from every fifth plate were taken from and analyzed in the middle of the RD/ND plane and only denoted by the plate number.

The samples were ground and polished with silicon carbide paper, diamond paste and thereafter in a suspension of silica. Finally they were electro polished in a solution consisting of 300ml ethanol, 60ml water, 50ml 2-butoxy ethanol and 40 ml perchloride acid.

2.3 Data acquisition

The samples were analyzed in a scanning electron microscope (JEOL JSM-840 equipped with a NORDIF model C1 EBSP-detector) and from the EBSP data, orientation images (OI) were obtained.

All the samples were analyzed in the RD/ND plane with a step size of 5μm in both directions covering an area of 0.7mm^2. The sample 1M1/4 was re-examined by EBSP analysis using a step size of 20μm in the RD direction and 10μm in the ND direction covering a total area of 10mm^2. This was done in order to determine if the properties determined in the small EBSP scans, were representative.

2.4 Data processing

The data from the EBSP measurements were analyzed and visualized in the Dos program CroPlot v. 1.55. For the picture processing in CroPlot the colour method 0 was chosen (defined in appendix A.3), and the grains were defined as having disorientation angles either greater than 15^0 or greater than 5^0. A disorientation angle of 15^0 is commonly used to define a grain, however during the picture processing the description of the grains did not seem satisfactory due to clustering of grains with similar orientations, therefore 5^0 was also chosen. This is illustrated in figure 4, in which the left image has boundaries marked defined by having disorientation angles greater than 5^0, while the image to the right has boundaries marked with disorientation angles greater than 15^0.

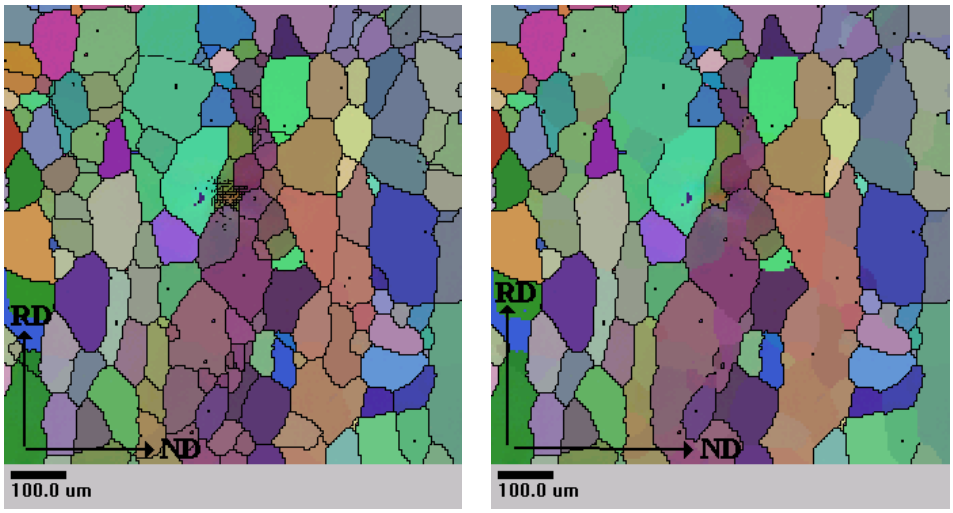

Figure 4: OI of sample 1L 1/4 thickness. In the left image boundaries with a disorientation angle greater than 5^0 is marked, while the right image has marked boundaries of disorientations greater than 15^0.

The texture of the material was analyzed in the Dos program TexStat, where the fraction of the respective texture components is defined by integrating over a 15 degrees spread about the component in Euler space. Every texture component was analyzed separately, hence overlapping is accepted. The following texture components were used Cube {100}<001>, Brass {110}<1 $\bar{1}$ 2>, Copper {112}<11 $\bar{1}$ >, S {12 $\bar{3}$ }<634>, Goss {011}<100>, C2 {001}<110>, A {310}<1 $\bar{3}$ 0>, B {310}<001> and C1 {122}<2 $\bar{2}$ 1>. Pole figures and ODFs were calculated with ODFPlot v. 1.25 and PFPlot v.1.70.

3 Results

3.1 Grain size

The average grain size was found by manual analysis of OIs from CroPlot, on which no grain boundaries have been drawn (linear intercept method). An example is shown in figure 5.

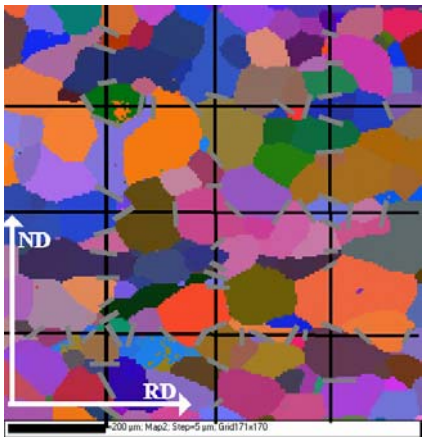

Figure 5: Illustration of the linear intercept method. The OI is from sample 15, the grey lines mark grain boundaries intercept with the black lines.

From these results the aspect ratio was also calculated. The results can be seen in table 1 together with the sample standard deviations of the measurements and the 95% confidence interval. The average grain size (an area based method which assumes round grains) is also calculated in CroPlot. The values are shown in table 2. Note: the different disorientation angles used. In the same table are medians also given. This is done in order to determine if the average grain sizes are significantly influenced by a few large grains.

Table 1: Grain size and aspect ratio of the aluminium samples

Sample	ND (μm)	RD (μm)	Average (μm)	Aspect Ratio RD/ND	File
1L surface	68.5	120.5	95	1.8	Ba302
1L ¼ thickness	55.7	80.4	68	1.4	Ba296
1L middle	61.9	66.7	64	1.1	Ba290
1M surface	71.6	84.5	81	1.3	Ba295
1M¼ thickness	67.6	95.1	81	1.4	Ba297
1M middle	59.3	73.2	66	1.2	Ba288
1R surface	45.4	62.9	54	1.4	Ba300
1R¼ thickness	56.8	93.2	75	1.6	Ba301
1R middle	56.5	82.7	70	1.5	Ba289
Average of plate no. 1	**60±6**	**84±13**	**73 ±9**	**1.4 ±0.2**	
Sample standard deviation	8	17	12	0.2	
5	59.7	75.0	67	1.5	Ba365
10	66.7	72.7	70	1.1	Ba367
15	54.8	97.8	76	1.8	Ba369
20	62.2	71.6	67	1.2	Ba381
25	66.0	81.8	74	1.2	Ba378
30	61.7	76.6	69	1.2	Ba380
Average between plates*	**62 ±5**	**79±10**	**71 ±4**	**1.3 ±0.3**	
Sample standard deviation	4	10	4	0.3	
1M¼ thickness	**81.1**	**172.3**	**126.7**	**2.1**	Ba506

*In this the average of plates no. 5 10 15 20 25 30 has been used

OIs from the respective measurements are displayed in appendix A.3.

Table 2: Grain size of aluminium samples determined in CroPlot.

Sample	Median d $>5^o$ (µm)	Mean d $>5^o$ (µm)	Median d $>15^o$ (µm)	Mean d $>15^o$ (µm)
1L surface	21.4	23.3	22.6	24.6
1L¼ thickness	51.7	59.5	74.9	84.1
1L middle	55.0	60.0	62.7	77.4
1M surface	57	65.4	69.4	84.3
1M¼ thickness	51.7	61.2	58.4	90.0
1M middle	54.1	58.9	61.4	74.7
1R surface	53.2	56.2	69.6	77.6
1R¼ thickness	43.3	50.5	59	63.9
1R middle	51.4	58.1	69.8	73.7
Average of plate no. 1 (-Lsurface)	**52±3**	**59±4**	**66 ±5**	**78±7**
Sample standard deviation	4	4	6	8
5	45.0	51.4	47.9	60.4
10	24.2	26.0	28.1	29.0
15	54	63.5	63.1	74.7
20	55.8	60.7	69.3	76.3
25	52.3	57.7	63.1	70.1
30	57.5	63.1	65.0	77.9
Average between plates *	**53±6**	**59±6**	**62±10**	**72±9**
Sample standard deviation	5	5	8	7
1M¼ thickness	**65.8**	**74.3**	**60.6**	**99.0**

*In this the average of plates no. 5 15 20 25 30 has been used

The grain size determined with the linear intercept method (LIM) varies in plate no. 1 (table 1 only small scans) between 45.4µm and 71.6µm in the ND direction with an average of 60µm. In the RD direction the grain size varies between 62.9µm and 120.5µm with an average of 84µm. The average grain size in both directions is 73µm. The aspect ration of the grains varies between 1.1 and 1.8 and the average aspect ratio is 1.4.

The variation of the grain sizes (LIM) between plates, determined in the small scans, varies between 54.8µm and 66.7µm in the ND plane and between 71.6µm and 97.8µm in the RD plane which gives a variation in aspect ration between 1.1 and 1.8. The average grain size is 62µm in ND 79µm in RD hence 71µm on average in both directions. The average aspect ratio is 1.3.

The grain sizes determined in the large scan is 81.1µm in ND and 172.3µm in RD hence the average grain size is 127µm and the aspect ratio is 2.1.

The grain size calculated in CroPlot assuming spherical grains varies in plate no. 1 (table 2) between 24.6μm and 90μm, when the grain is defined with a disorientation of greater than 15^0. The grain size determined in 1L surface is 24.6μm. This very small value, is probably due to noise during data acquisition (see appendix A.4), hence the data are not included in further analysis. The average grain size in plate number one is 78μm and the corresponding average median is 66μm.

The grain sizes determined in different plates varies between 29μm and 78μm with an average of 72μm, and the corresponding average median is 62μm. The grain size of 29μm found in sample 10 is properly due to noise during data acquisition. This sample is therefore neglected together with sample 1L surface, in the further analysis.

The grain size determined in the large scan is on average 99μm and the median is 60.6μm.

Grains defined by disorientations of 5^0 in plate no. 1 varies between 23.3μm and 65.4μm with an average of 59μm and an average median of 52μm.The grain size determined in different plates varies between 26μm and 63.5μm, with an average of 59μm and a median of 53μm.The grain size determined in the large EBSP scan is 74.3μm and the median 65.8μm.

3.2 Grain size distribution

Histograms of the normalized grain size distributions of each measurement are shown in the data sheets in appendix A.4 together with the corresponding OIs, [200] pole figures and ODFs.
The normalized grain size distribution in individual measurements, can in general be described as an asymmetric normal distribution, with a larger amount of large grains, indicating a log normal distribution. The number of grains pr. measurement are however low, therefore is several scans grouped and the distributions from this grouping displayed in the following. The distribution of all small scans measurements in plate no. one (1Lsuface is not included) is seen in figure 6, where a plot of the frequency as a function of the natural logarithm of grain sizes is displayed. The distribution is fitted with a normal function. From the fit it is seen that the grain size distribution is not distributed evenly about the center, due to a larger amount of small grains compared to large grains.

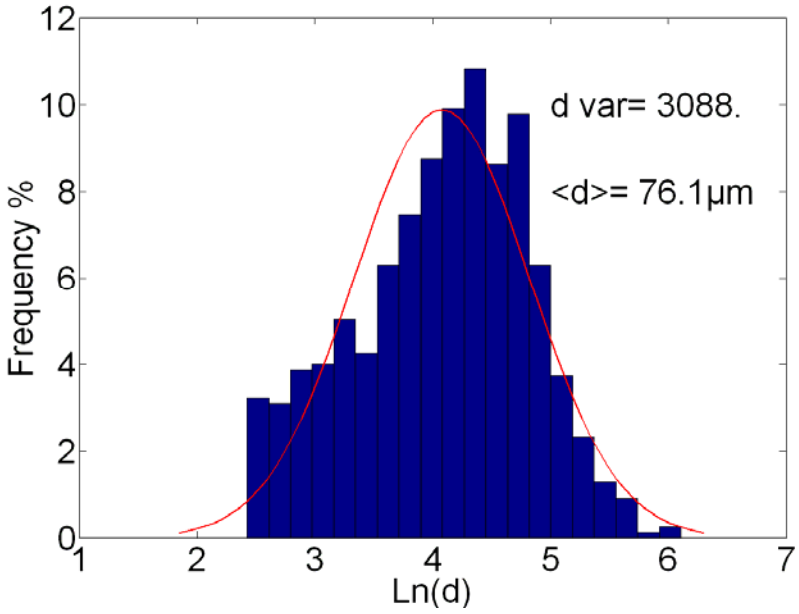

Figure 6: Semi log plot of the grain size distribution in plate no. 1 (spherical grains defined by a disorientation greater than 15^{o}).

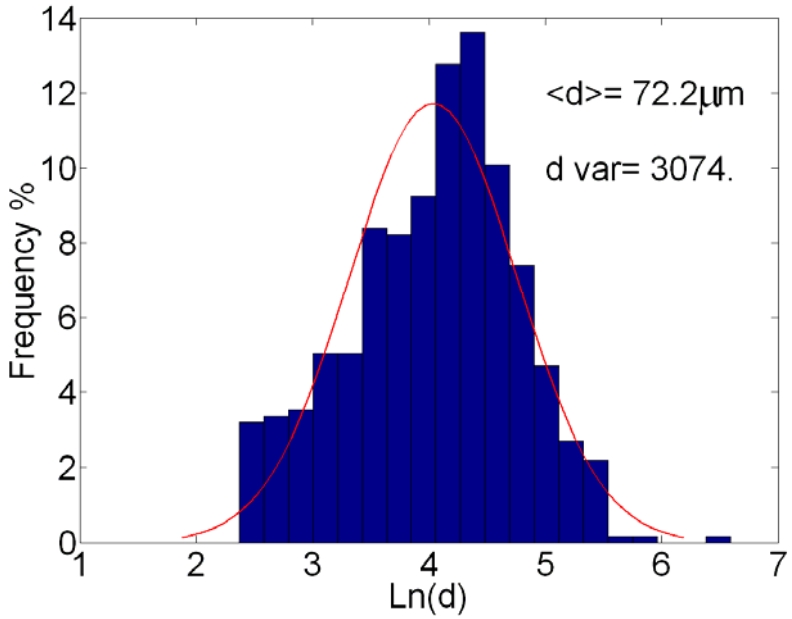

Figure 7: Semi log plot of the grain size distribution in all small scans in plate 5, 15, 20, 25 and 30 (spherical grains defined by a disorientation greater than 15°)

In figure 7 a log normal plot of all small scans in plates 5, 15, 20, 25, and 30 are presented and the distribution is fitted to a normal function. The distribution is asymmetric around the mean value, with a higher amount of small grains. Like wise the grain size distribution determined during the large scan shows a larger fraction of small grains compared to a log normal distribution (figure 8).

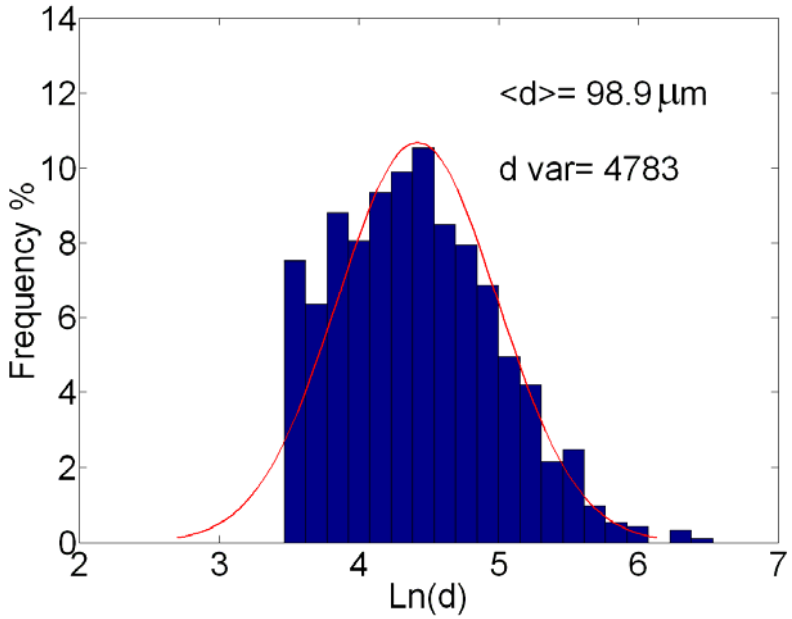

Figure 8: Semi log plot of the grain size distribution of the large scan (spherical grains defined by a disorientation greater than 15°)

In figure 9 all measurements conducted in the RD/ND plane with a small step size are displayed and the semi log plot fitted with a normal function.

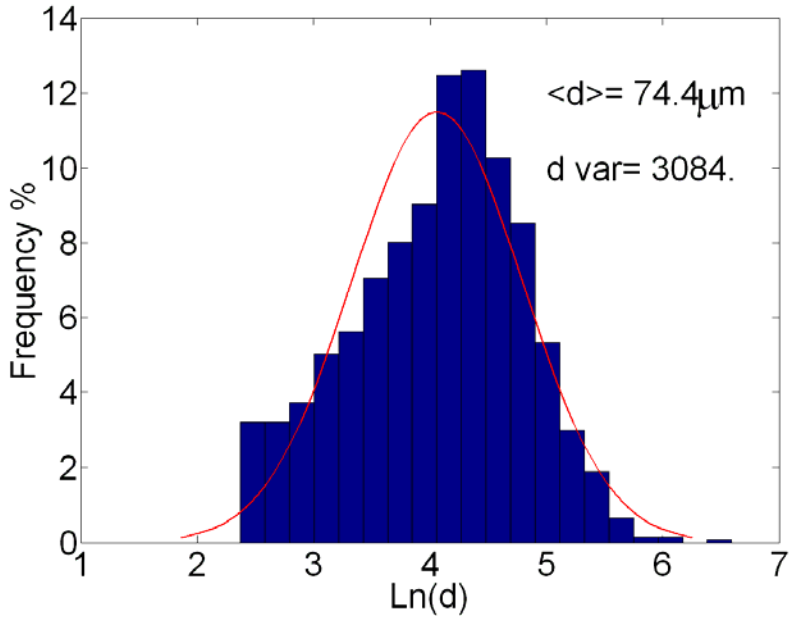

Figure 9: Semi log plot of the grain size distribution of all measurements in the RD/ND plane (only small step size and spherical grains defined by a disorientation greater than 15°)

This distribution is also not well described by the normal function.

And finally in figure 10 is the grain size distribution of all measurements conducted with the smallest step size and with grain defined with disorientations above 5^0 displayed. This grain size distribution are also asymmetric.

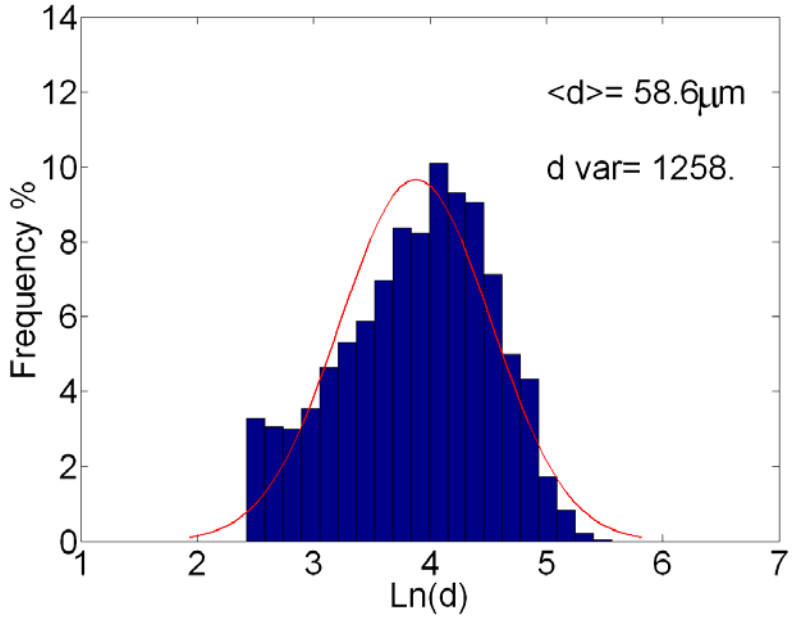

Figur 10 Semij log plot of the grain size distribution of all measurements in the RD/ND plane (only small step size and spherical grains defined by a disorientation greater than 5^0)

The mean grain sized determined in figure 9 is 74.4µm +/-3 µm (95% confidence interval) it corresponds to (disorientations above 15^0) or +/- 1.5 (disorientations above 5^0).

3.3 Texture

The textural analysis classified the EBSP data into 9 different texture components: Cube {100}<001>, Brass {110}<11$\bar{2}$>, Copper {112}<11$\bar{1}$>, S {123}<63$\bar{4}$>, Goss {011}<100>, C2 {001}<110>, A {310}<1$\bar{3}$0>, B {310}<001> and C1 {122}<2$\bar{2}$1>. Furthermore [200] pole figures and ODFs were plotted. The result of the analysis is shown in tables 3 and 4, together with the sample standard deviations of the measurements and the 95% confidence interval. Table 3 contains the Cube texture components and the rolling texture components (overlap has not been accounted for), while table 4 contains the Rotated Cube (C2), A, B and C1 texture components together with a column containing the percentages of the data not classified in one of the chosen texture components.

Table 3: Texture analysis part 1.

Sample\Volume fraction (%)	Cube	Brass	Copper	Goss	S	Brass+ Copper+ Goss+S
1L surface	8.4	1.4	1.2	0.5	2.5	5.6
1L ¼ thickness	9.0	2.1	0.0	0.0	0.0	2.2
1L middle	10.0	0.1	3.6	0.0	1.8	5.5
1M surface	18.2	1.0	1.8	0.3	4.0	4.3
1M¼ thickness	12.9	0.2	0.5	3.4	0.7	4.8
1M middle	7.2	1.3	1.4	0.1	8.9	11.6
1R surface	15	0.9	2.8	0.1	10	13.8
1R¼ thickness	4.3	2.6	5.9	2.5	7	18
1R middle	7.4	9.0	3.4	0	9.9	22.2
Average of plate no. one	**10±4**	**2±2**	**2±2**	**1±1**	**5±3**	**10±6**
Standard sample deviation	4	3	2	1	4	7
5	14.4	0.5	1.2	0.2	2.0	3.9
10	6.3	0.1	0.6	1.8	2.8	5.3
15	1.5	4.2	5.0	8.1	14.5	31.9
20	7.7	0.7	4.4	1.3	4.1	10.6
25	11.9	5.8	5.5	0.4	5.9	17.7
30	9.9	2.9	1.7	1.3	2.7	8.7
Average between plates*	**9±6**	**2±3**	**3±3**	**2±4**	**5±6**	**13±13**
Standard sample deviation	5	2	2	3	5	10
1M ¼ thickness	**16.7**	**0.8**	**0.4**	**1.3**	**1.7**	**4.3**

*Average of plate no. 5 10 15 20 25 and 30

The [200] pole figures and orientation ODFs from the respective measurements are displayed in appendix A.4.

The main texture components of plate no. one are: A, which varies from 6.4% to 25.1%, with an average of 15%. B, which varies from 5.5% to 19.7% with an average of 11%, and cube, which varies from 4.3% to 18.2% with an average of 10%. There is on average 10% of the rolling textures with S being the strongest texture component with an average of 5%. C1 is on average 2% and C2 (rotated cube) 1%.

The A texture component is also the strongest in other plates examined, here the volume percentages vary between 3.2% and 18.5% with an average of 13%. The texture component B varies between 5% and 22.3% with an average of 15% and the cube varies between 1.5% and 14.4% with an average of 9%. 13% is the average volume percentages of the rolling textures, where S is the strongest texture component with an average of 5%. C1 texture is 4% on average while the C2 component is 0.4%.

In the large scan, the strongest texture component is cube with 17 vol% then B (16%) and A(14%) only 4% are rolling textures, with S being the strongest texture component (2%).

Table 4: Texture analysis part 2.

Sample\Volume fraction (%)	C2	A	B	C1	Not classified
1L surface	0.2	6.6	6.6	3.1	69.7
1L ¼ thickness	0.3	20.9	14.1	0.6	53.0
1L middle	0	11.2	19.7	0.3	53.3
1M surface	0.0	21.8	18.7	0.3	36.7
1M¼ thickness	0.6	14.6	10.3	0.8	56.1
1M middle	1.1	6.4	9.2	1.2	63.3
1R surface	0.8	14.5	7.5	5.0	43.3
1R¼ thickness	2.3	11.6	8.4	2.6	52.9
1R middle	4.0	25.1	5.5	6.0	30.0
Average of plate no. one.	**1± 1**	**15± 6**	**11± 4**	**2±2**	**51±10**
Standard sample deviation	1	7	5	2	13
5	0	15.3	22.3	3.0	41.1
10	0	18.5	12.5	0.9	56.6
15	1.3	3.2	5	11.0	46.2
20	0	15.9	16	6.0	43.8
25	0.9	12.3	20.2	1.1	35.9
30	0.3	13.3	15	1.3	51.5
Average between plates*	**0.4 ±1**	**13± 7**	**15± 8**	**4±5**	**46±9**
Standard sample deviation	1	5	6	4	7
1M ¼ thickness	**0.7**	**13.7**	**15.5**	**2.5**	**46.6**

Average of plates no. 5 10 15 20 25 and 30

4 Discussion

4.1 Grain size

The average grain size of plate no, 1 was 73μm measured with the linear intercept method and the average aspect ration was 1.4, hence the grains are elongated.

At first sight there appears to be no clear tendency in the grain size variation within plate no. one. In order to investigate this further the data was grouped first according to the position in the RD/ND plane and afterwards according to the position in the TD/RD plane. In table 5 the grouping of the data is displayed together with the 95% confidence interval of the measurements. In table 5 it is seen that in the RD/ND plane there is a tendency of larger grains in both ND and RD directions at the surface and at ¼ thickness compared to the middle. This is also reflected in the decrease in aspect ration from 1.5 at the surface to 1.3 in the middle.

Table 5: Average grain sizes found in plate no 1 with linear intercept method.

Position	Average grain size (μm) (ND)	Average grain size (μm) (RD)	Average grain size (μm)	Average aspect ratio
1.surface(RD/ND)	62 ±34	89±72	77±52	1.5±0.7
1. 1/4 thickness(RD/ND)	60±16	90±20	75±16	1.5±0.3
1. middle (RD/ND)	59±7	74±20	67±8	1.3±0.5
1.L (RD/TD)	62±16	89±69	76±42	1.4±0.9
1.M (RD/TD)	66±16	84±27	76±22	1.3±0.3
1.R (RD/TD)	53±16	80±38	66±27	1.5±0.3

A similar variation is seen in the RD/TD plane, where the average grain size is larger, at the L and M positions. The aspect ratio varies from 1.5 in the right corner to 1.3 in the middle.

Table 6: Average grain sizes found in plate no 1 by assuming spherical grains and a disorientation greater than 15^0.

Position	Median of the grain size(μm)	Average Grain size(μm)
1.surface(RD/ND)	70±1	81±43
1.1/4 thickness(RD/ND)	64±23	79±34
1. middle (RD/ND)	65±11	75±5
1.L.(RD/TD)	69±78	81±43
1.M.(RD/TD)	63±6	83±8
1.R.(RD/TD)	66±15	72±18

When grains were characterized by spheres with a disorientation greater than 15^0, the average grain size in plate no. one was 78μm, and when the data was grouped as described above, the tendency for larger grains sizes at the surface and ¼ thickness compared to the middle of the RD/ND plane is the same (table 6). Since the average median is larger at the surface, it means that more grains are larger at the surface compared to those at ¼ thickness and in the middle. (Note that the surface position only contains 2 measurements). In the TD/RD plane the largest average grain size are found in the middle, since however the average medians are lower compared to the other positions, this indicates a few large grains in the middle part.

From above it can be concluded, that the grain sizes in plate no. one varies both in the TD/RD plane and in the ND/RD plane with a tendency for small grains in the middle of the RD/ND plane and in the right corner of the TD/RD plane. The tendencies are only found by grouping the data, and the variations between each data group are within the 95% confidence interval of each of the individual data group, apart from the average grain size of the middle of the RD/ND plane and the median of 1. surface. Hence there seems to be no clear overall systematic trend in the spatial variation of the grain size. Furthermore the variations or tendencies in the RD/ND plane are comparable to the variations in the TD/RD plane. Note however that the statistics are poor, which is also reflected in the larges 95% confidence intervals.

The average grain size found within the small scans between plates 5 to 30 was 71μm (LIM), which corresponds well to the average grain size in plate no

one of 73μm (LIM). The average aspect ratio was 1.3 and 1.4 (see table 1 and 2). The average grain size, determined by assuming spherical grains with a disorientation greater than 15^0, between plates were 72μm and the corresponding grain size in plate no. one was 78μm. The differences are within the 95% confidence intervals of the measurements. Furthermore the average grain size, when grains were defined with a disorientation greater than 5^o, was 59μm in both plate no. one and the average between plates.

The data for samples 5, 10, 15, 20, 25 and 30 were collected in the middle of the RD/ND plane, therefore the average value of these plates, is compared with the average values given in tables 5 and 6. By doing so, it is seen that the average grain size (LIM) of plate no. 1 middle (RD/ND) is 67μm, which is lower than the average grain size between plates, which is 71μm. The reverse applies to the value determined with disorientations greater than 15^0 where the average grain sizes are 75μm and 72μm respectively. The differences described are with one exception, within the 95% confidence intervals of the data, so even though the statistic are poor, the difference between the average values of the data determined from plates no. 5 10 15 20 25 and 30 and data from plate no. one are no larger than the spread within the respectively data groups. In conclusion there is no significant difference between plate no. one and the remaining plates examined.

The average grain sizes were determined by the linear intercept method and by the area based method, in which the diameter of the corresponding circle is found. The relationship between the linear intercept and the diameter determined by the area base method depend on the shape and distribution of the grains. If the grains are described as space filling tetrakaidecahedra of equal size then $d_{ECD}/d_{LIM}= 1.224$ [1,2]. In the current study the proportionality constant between the average grain sizes determined is 1.0 in the between plates data and 1.1 in plate no one, and thereby smaller than the expected 1.2. This might reflect that the grains are elongated, and the shape approximation is not valid. Since however, that the aspect ratio between the average grain size determined by assuming a disorientation of 5^0 and the linear intercept is 1.2, This indicates, that the grain size determined by linear intercept, also includes grains, with disorientations lower than 15^0.

The grain sizes determined in the large scan are larger than in the small scans. The average the grain size found was 99μm (spherical grains) and 127μm (LIM) with an aspect ratio of 2.1. The average grain size of 99μm is larger that found in the small scans, but not so different compared to the LIM parameter. The high aspect ratio of 2.1 reflects the high LIM value. The average grain size found in the small scans is not reconfirmed in the large scans, and can be an artefact attributed to the larger step size in the large scan.

In conclusion the grain size of the material varies within plate no one and between plates. There is no clear tendency in the variation of the grain size in the RD/ND or TD/RD directions, and the variations are not specific to any direction. The average grain size measured in between plates is 71 (LIM) or 72μm (spherical grains), while the grain size determined in plate no. one was 73μm (LIM) and 78 (spherical grains) respectively.

4.2 Grain size distributions

The grain size distributions of the individual measurements were displayed as normalized histograms. The histograms were asymmetrically distributed around

the maximum value. In order to increase the statistics, and make the data analysis easier, the data were grouped into the following 5 groups

1. All small scans form plate no. one (figure no. 6)
2. All small scans within plates (figure no. 7)
3. The large scan in the RD/ND plane (figure no.8)
4. All measurements of the RD/ND plane conducted with a small step size (figure no.9).
5. All measurements of the RD/ND plane conducted with a small step size, with grains defined with a disorientation above 5^0 (figure no. 10).

From each of the groups semi log plots were displayed of the grain sizes and fitted with a normal function. All the distributions contained a larger amount of small grains, compared to a perfect log normal distribution. A log normal distribution of the grain size is often observed, therefore it is of relevance to investigate, if there is artefacts in the measurements. The grain size used during EBSD measurements defines the minimum grains size detected, hence the larger amount of small grains is not a step size effect. Another explanation can be introduction of artefacts in the measurements, when noise is present during the data acquisition. This was clearly seen in sample 10 and sample 1L surface, was the average grain size (spherical grains) where unrealistically low, and inspection of the orientation images showed large amounts of noise (black lines in the pictures). An artificial large amount of small grains is however also reported to occur, when grain sizes are determined by an area based method using EBSP and another software to calculate the grain size [2]. Visual inspection of the grain size distribution all shows a larger amount of small grains compared to the log normal distribution. In Croplot a requirement of minimum of 4 data points to define a grain are given, hence the artificial amount of small grains observed in another software, does not seem to apply here. Furthermore the grain size distributions all shows the same "shoulder" of small grains, hence the amount of small grains are not an artefact. It is furthermore noted that the distribution obtained from plate no. one are similar to the distribution from the between plates data ($<d>$ and σ^2 are similar). The spread in terms of sample standard deviation of the total grain size distribution are 56 (small step size and disorientations above 15^0) ie. 95% of the grains have a diameter below 187μm. The standard deviation for grains defined by disorientations above 5^0 (and small step size) are 36 hence 95% of the grains have a diameter below 131μm. The grain size distributions display same "shoulder" regardless of the disorientation used. In conclusion the grain size distribution is not perfectly log normal and the distributions are similar in plate no. one and in other plates.

The average grain sizes determined by stacking the data (displayed in figures 6 -9) were lower than the average determined by averaging of the individual files. This is due to the difference in the weighting of the individual data points during the averaging in the two methods. The mean grain size determine in all small scans given with the 95% confidence interval was 74.4μm ±3μm, when grains were defined by disorientations above 15^0 and 58.6μm ±1.5μm when grains were defined by disorientations above 5^0.

4.3 Texture

The texture analysis displayed in tables 3 and 4, found that all small scans of plate no. one, had the major texture components A, B and Cube, while the remaining texture components only showed locally large values. The sum of all rolling textures (Brass, Copper, S and Goss) was on average as strong as the

average cube texture. It is however worth noting that, there might be overlap between Brass and S and/or S and Copper.

The texture variation in plate no. 1 showed no overall clear tendency, therefore the data is grouped with respect to the position in the ND direction (surface, middle and ¼ thickness), and the data displayed in tables 7 and 8 together with 95% confidence interval.. By doing so, the cube texture is seen to be 40% larger at the surface positions compared to that averaged over positions. The rolling textures are 30% stronger in the middle positions compared to the average.

When texture components are grouped according to the TD/RD positions (Left, Right, Middle) also displayed in tables 7 and 8 the following can be seen. The middle position, contains 30% more cube texture compared to the average, the right corner of plate no. 1 has 80% more rolling texture components compared to the average while the remaining texture components varied less. Hence the texture varies in the RD/ND and TD/RD plane of plate no. 1 especially the rolling and cube texture components. In general the texture data is connected with a large amount of scatter, reflected in the large 95% confidence interval.

In general the standard deviations of the data groups are large compared to the average values, therefore more data are needed in order to determine whether or not the texture variations seen within plate no. one is due to random scatter or process induced variations. The large amount of rolling texture in the 1R data group however, indicates that the texture variations seen are due to random scatter, since the texture induced during rolling more likely would produce large texture differences in the ND plane.

The texture found in the map of sample no. 1M conducted on a larger scale, found a dominant cube texture (17%) 14% A texture and 16% B texture, while the amount of rolling texture was only 4%. Compared to the texture composition in the sample 1M 1/4 thickness, (13% cube, 15% A 10% B and 5% rolling textures) the amount of cube is larger and the B texture smaller in the large scan.

Table 7: Average texture components found in plate no 1.

Sample\Volume fraction (%)	Cube	Brass	Copper	Goss	S	Brass+ Copper+ Goss+S
1M (RD/TD)	13±14	0.8±1.4	1±4	1±5	5±10	7±10
1L (RD/TD)	9±2	1±2.5	2±5	0.2±0.8	1±3.2	4±5
1R (RD/TD)	9±14	4±11	4±4	0.9±3.5	9±4	18±10
1surface (RD/ND)	14±12	1±0.7	2±2	0.3±0.5	6±10	8±13
1 ¼ (RD/ND)	9±11	2±3	2±8	2±4	3±10	8±21
1 middle (RD/ND)	8±4	3±12	3±3	0.0±0.1	7±11	13±21

The textural analysis of the small scans in other plates (sample no. 5, 10, 15, 25, 30) shows the same variation in texture, which is a more or less dominant cube texture component together with A and B texture components, and a more or less strong rolling texture component depending on the amount of cube texture That is, a strong cube texture is generally observed to a weak rolling texture. Furthermore the average texture determined between the plates is similar to the average of the texture components in plate no. one.

Table 8: Average texture components found in plate no 1.

Sample\Volume fraction (%)	C2	A	B	C1	Not classified
1M (RD/TD)	0.6±1.4	14±19	13±13	0.8±1.1	52±34
1L (RD/TD)	0.2±0.4	13±18	14±16	1±4	59±24
1R (RD/TD)	2±4	17±18	7±4	5±4	42±29
1surface (RD/ND)	0.3±1	14±19	11±17	3±6	50±43
1 ¼ (RD/ND)	1±3	16±12	11±7	1±3	54±5
1 middle (RD/ND)	2±5	14±24	11±18	3±8	49±42

The average texture found in the large scan (last row in tables 3 and 4) are comparable to the average textures found in the small scan (1M1/4 in tables 3 and 4).

In the pole figures in appendix A.4 all the [200] pole plots besides that from sample no. 15 have a more or less dominant cube texture. The same applies to the ODFs.

In conclusion, the observed variations in texture are not significant considering the large experimental scattering. However there is clearly a local variation but it is not possible to conclude anything about the variations in or between plates.

4.4 General discussion

Generally there was no clear tendency in the variation of grain size and texture in plate no. one. If however the data were grouped with respect to positions in the RD/ND plane and then in the RD/TD plane the following appeared. In the RD/ND plane the grains were on average larger at the surface position and in this position the amount of cube texture was higher than average. The same tendency was seen in middle of the TD/RD plane in plate no. one. The smallest average grains size was found in the right corner of the plate. In this part the rolling texture components were stronger than the average rolling texture components of the plate. Hence grains with a cube texture are larger than grains with rolling texture, which has been described previously [3]. This might also partly be the reason for the larger grains size determined in the large scan, since the texture of the measurement contained a stronger cube texture compared to the average texture (17 vol. % versus 9 vol.%). The spatial variations are of a similar size in the RD/ND and TD/RD directions, and they are mainly within the 95% confidence interval of the measurements. The average values determined in plate no. one (average grain size, texture and aspect ratio), were similar to the average values determined in other plates, hence the variations between plates were similar to the variations within plate no one.

A truly random material will theoretically have the vol. % of the individual texture components as given in table 9 [4] In the table the ratio between the measured texture[1] and the theoretical random texture are also given. From this ratio it can be seen, that the most dominant texture component, compared to a random texture, is the cube texture (4 x random) and the A and B texture (3 x

[1] Calculated as a weighted average between all plates. This also applies to the average texture composition given in the following.

random), while the expected C1 texture is 5 times lower than the random texture.

Texture component	Random theoretical vol.%	Measured vol.%	Ratio measured/random
Cube	2.2	9	4
Goss	2.2	2	0.9
Brass	4.4	2	0.5
S	8.8	5	0.6
Cu	4.4	3	0.7
C2	2.2	1	0.2
A	4.4	13	3
B	4.4	15	3
C1	8.8	4	0.4

Table 9: Theoretical vol. % of the texture components used in current analysis. The texture analysis is calculated by integrating over 15^0 in Euler space of the individual texture components.

The average grain sizes varied depending on the step size used during the measurements and of naturally on the definition of the grain (disorientation above 5^0 or 15^0). If a small step size was used the average grain size is 72μm (LIM) or 76μm (spherical grains). Regardless of the disorientation used (5^0 or 15^0) the grain distributions were not perfectly log normal distributed. The asymmetric distributions are definitely not due to poor statistics and are believed to be real. Based on this, the average grain size of the material is regarded as best described, by the grain size determined by linear intercept measured from EBSP maps recorded with the smallest step size. Therefore the grain size of the material is described by an average of all the LIM values determined from this, which is 72μm. This average grain size is not refund in the EBSP measurements conducted with larger step sizes over larger area. This can be an effect of the different step size as discussed above or just local variations. The aspect ratio is 1.3.

To sum up. The average grain size of the material is 70μm and the aspect ratio is 1.3. The average texture of the material in volume % is Cube 9% (4 x random) Brass 2% (0.5 x random) Copper 3% (0.7 x random), Goss 2%(0.9 x random), S 5%(0.6 x random) C2 1%(0.2 x random), A 13%(3 x random), B 15% (3 x random) and C1 4% (3 x random). The texture composition in one small scan was confirmed by EBSP measurements conducted over large area. The grain size and texture varied locally and it is not possible to conclude anything about the global variations.

5 Conclusions

30 plates (12 250x140x10mm, 12 300x150x10mm and 6 300x200x10mm) of commercially pure aluminium (AA 1050) were fabricated in order to serve as basic material. The plates were characterized chemically and with EBSP. The variations within a plate and between plates were investigated and did not exhibit clear systematic trends.

From above following describes the basis material:

- The material is 99.5% pure
- The major impurities are Si and Fe
- The grain size is 70μm (mean chord length)
- The grains are elongated in the RD/ND plane with an average aspect ratio of 1.3
- The distribution of the grain sizes is not log normal.
- The average texture of the material is fairly random, though with a weak Cube texture (4xrandom).
- Tendency for large grains to be of Cube orientation.

Texture component	Random theoretical vol.%	Measured vol.%	Ratio measured/random
Cube	2.2	9	4
Goss	2.2	2	0.9
Brass	4.4	2	0.5
S	8.8	5	0.6
Cu	4.4	3	0.7
C2	2.2	1	0.2
A	4.4	13	3
B	4.4	15	3
C1	8.8	4	0.4

References

1. Underwood, E. E. Quantitative stereology. (1970) Addison-Wesley, Reading MA.
2. Cao, W. Q., Godfrey, A. and Liu, Q. Determining dislocation cell sizes for high-strain deformation microstructures using the EBSP technique. Journal of Microscopy vol. 211, (2003) p. 219
3. Juul Jensen, D. Growth rates and misorientation relationships between growing nuclei/grains and the surrounding deformed matrix during re-crystallization. Acta metal. mater. vol. 43, (1995) no. 11 pp. 4117
4. Personal communications with Torben Leffers.

Appendix

A1. Analysis report

Chemical analysis of the AA 1050 basis material in weight %.

Lyreco

Date/Time : 16.11.95 09:17:48 Mark : Program : AL-11
Status : 1 Type : 1 Instrument: L Weight :
Sample-No : S 4170
Quality :
Sample-ID : OES5RISØ.4
Part :

Si %	Fe %	Cu %	Mn %	Mg %	Cr %
0.162	0.238	0.0041	0.0046	0.0027	0.0007

Zn %	Ti %	B %	Be %	Na %	Li %
0.0127	0.0227	0.0038	<0.0001	0.0003	0.0001

Ca %	Ni %	Pb %	Sn %	Zr %	Bi %
0.0006	0.0029	0.0017	<0.0001	0.0008	0.0011

Sr %	Cd %	Sb %	Co %	V %	P %
<0.0001	0.0011	0.0005	0.0003	0.0069	<0.0004

Al %
99.53

Underskrift

A.2 Rolling Geometry

The L/h ratio is defined as:

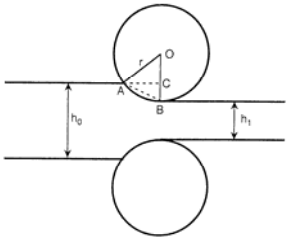

Figure 10: Definitions of parameters in rolling geometry

$$BC = (h_0 - h_1)/2$$
$$\overline{AC}^2 = r^2 - \overline{OC^2}$$
$$\overline{AB}^2 = \overline{AC}^2 + \overline{BC}^2 = r(h_0 - h_1)$$

Contact Length L:

$$\frac{L}{h} = \frac{\sqrt{\sqrt{r(h_0 - h_1)}}}{(h_0 + h_1)/2}, h = (h_0 + h_1)/2$$

A.3 Colouring of orientations images

In Croplot an orientation in 3D is represented by an unit vector **v** and an angle ω. From which the vector **h** is defined as **h**=**v**ω. In doing so, the disorientation between orientation $\mathbf{h}_1$and $\mathbf{h}_2$ is approximated by $|\mathbf{h}_1-\mathbf{h}_2|$.
In Croplot the 3D orientations are mapped in RGB-values (each ranging from 0 to 255) with different methods depending on which of the equivalent orientations in the given crystal symmetry that are mapped and the mapping method. In current report method 0 has been chosen, and the description of the method from the manual are therefore given below.

Method 0: Among the equivalents to each orientation, pick the one with the smallest rotation angle ω, i.e. the one closest to the cube. For a cubic crystal $\omega \leq \omega_{max}=62.8^0$. Therefore, $max(h_x)=max(h_y)=max(h_z)=\omega_{max}$ and $min(h_x)=min(h_y)=min(h_z)= -\omega_{max}$. The formula for mapping $\mathbf{h} = (h_x\ h_y\ h_z)^T$ to RGB space are:

$$R = (h_x + \omega_{max})/(2\omega_{max})$$
$$G = (h_y + \omega_{max})/(2\omega_{max})$$
$$B = (h_z + \omega_{max})/(2\omega_{max})$$

With R, G, B $\subset$ [0,1]

A.4 Data sheets

The histograms of the normalized grain size distributions were constructed by grouping data in intervals of 0.25 (for data with disorientations greater than 15^0 an average of 100 grains were found) or in intervals of 0.2 (for data with disorientations greater than 5^0 an average of 175 grains were found). The OI are coloured as described in appendix A.3 and the ODF's are sectioned in the phi2 intervals of 5^0.

Sample no. 1L middle

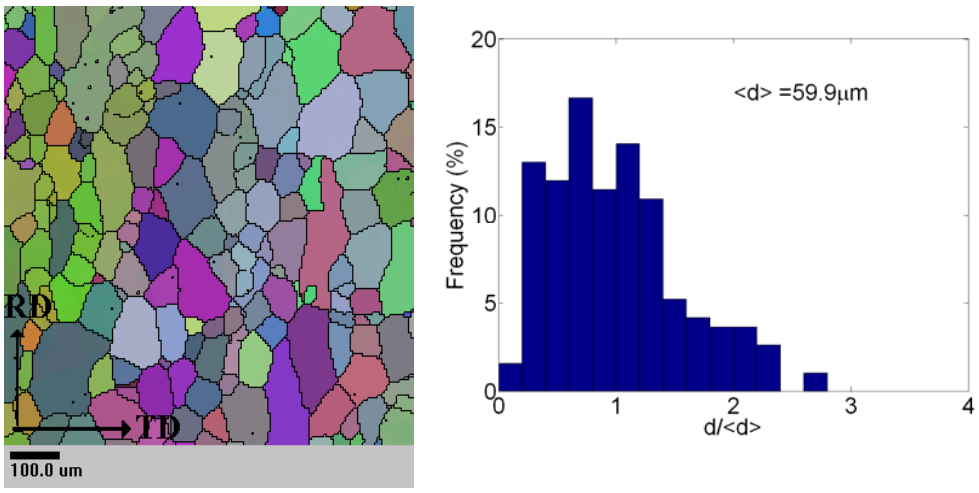

Figure 11: OI and grain size distribution of sample 1L middle. Calculated with a dis-orientation angle greater than 5^0.

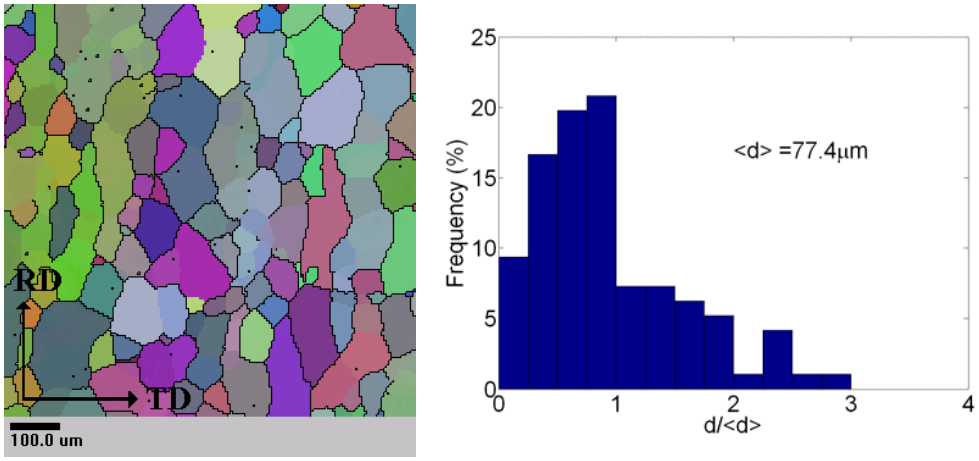

Figure 12: OI and grain size distribution of sample 1L middle. Calculated with a dis-orientation angle greater than 15^0.

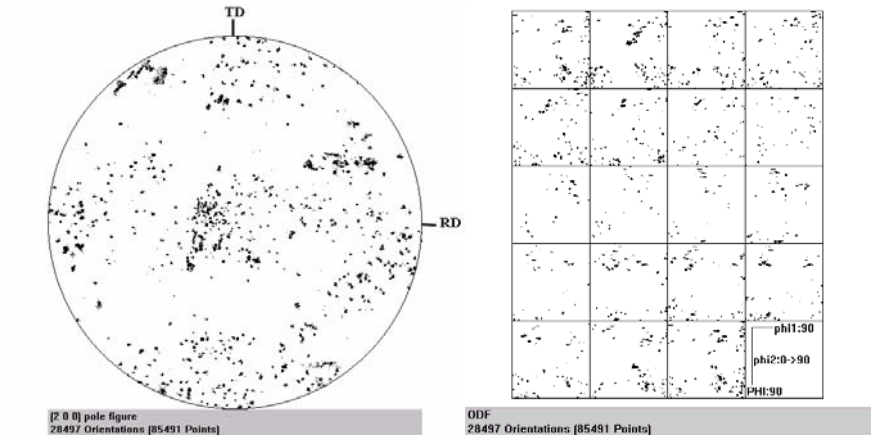

Figure 13: [200] Pole figure and ODF from sample 1L middle.

Sample no. 1L surface

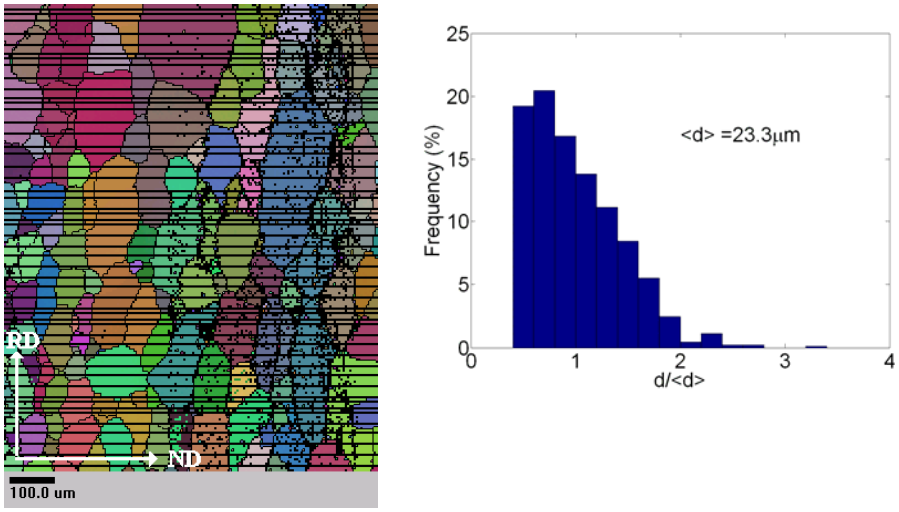

Figure 14: OI and grain size distribution of sample 1L surface. Calculated with a disorientation angle greater than 5^0.

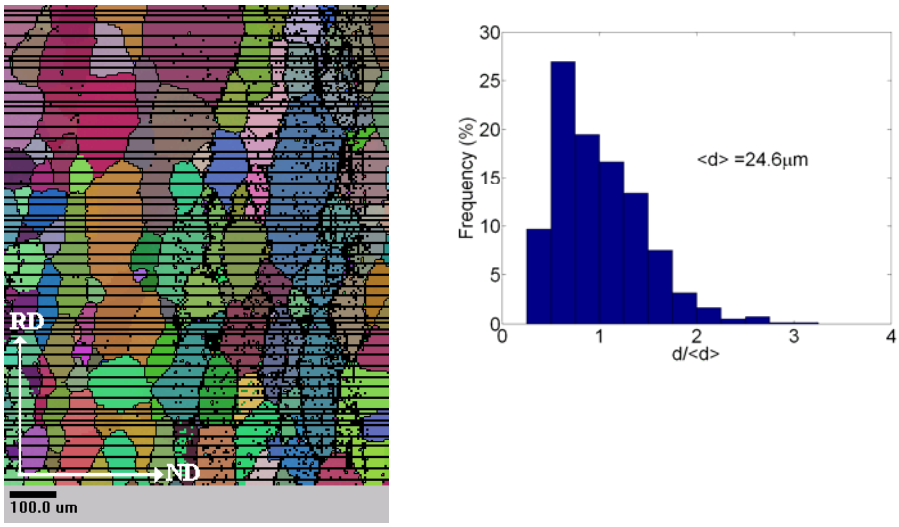

Figure 15: OI and grain size distribution of sample 1L surface. Calculated with a disorientation angle greater than 15^0.

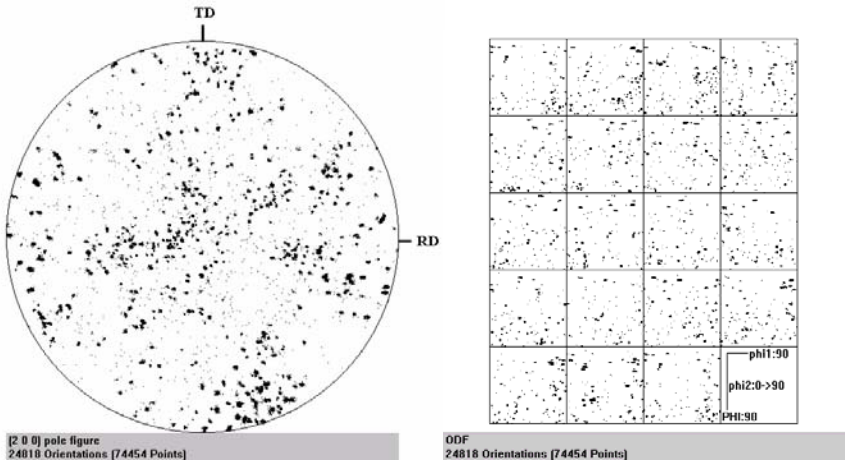

Figure 16: [200] Pole figure and ODF of sample 1L surface. The ODF is sectioned in phi2 intervals of 5^o.

Sample no. 1L ¼ thickness

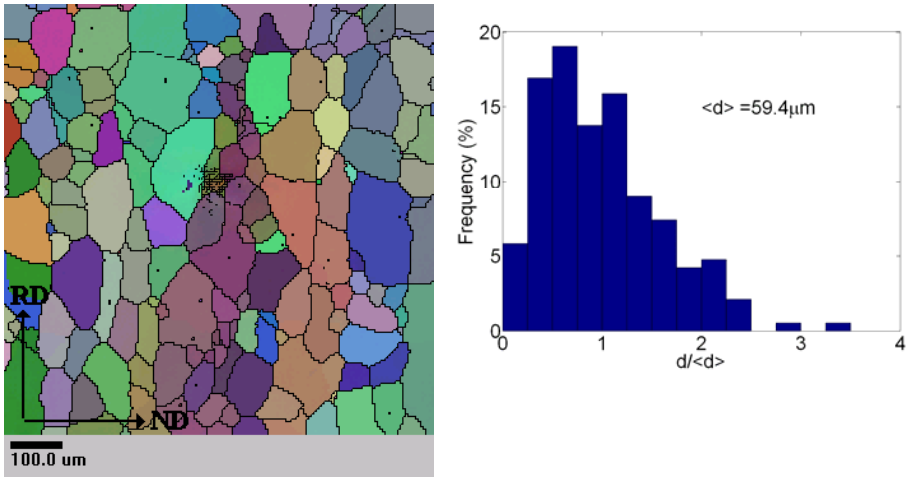

Figure 17: OI and grain size distribution of sample 1L ¼ thickness Calculated with a disorientation angle greater than 5^0.

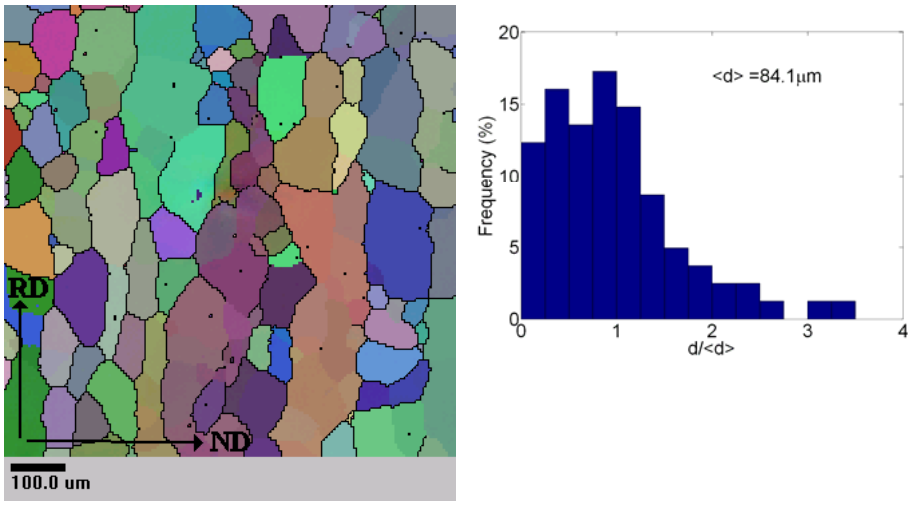

Figure 18: OI and grain size distribution of sample 1L ¼ thickness. Calculated with a disorientation angle greater than 15^0.

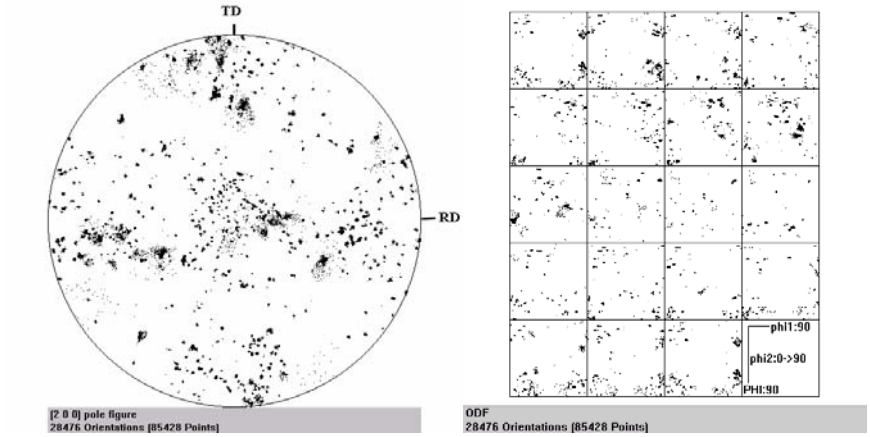

Figure 19: [200] Pole figure and ODF of sample 1 L 1/4. The ODF is sectioned in phi2 intervals of 5^o.

Sample no. 1M middle

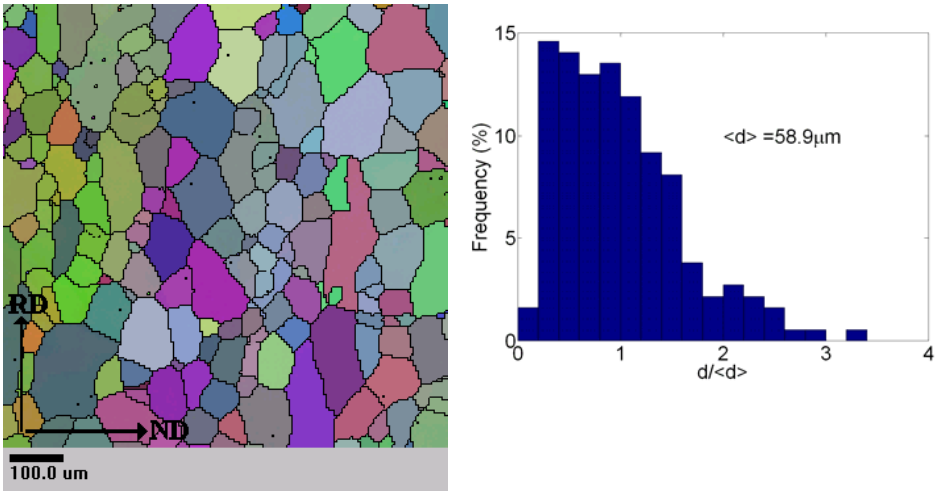

Figure 20 OI and grain size distribution of sample 1M middle. Calculated with a disorientation angle greater than 5^0.

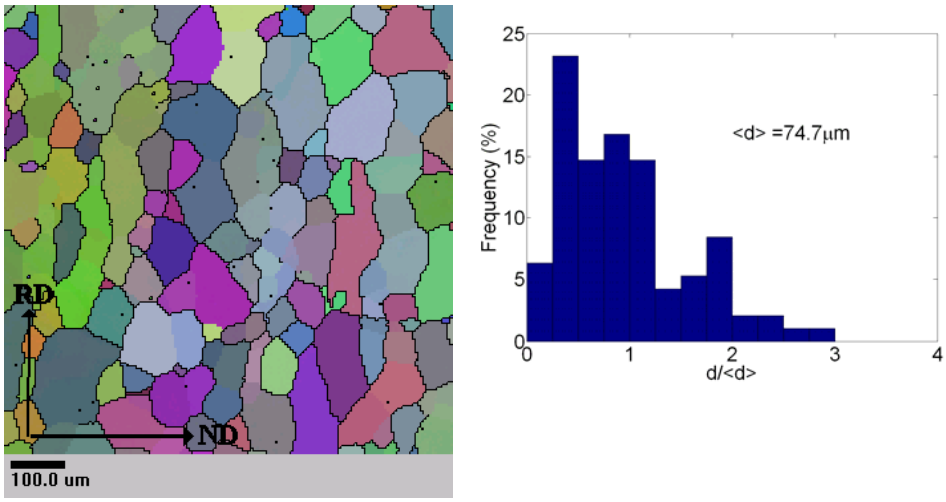

Figure 21: OI and grain size distribution of sample 1M middle. Calculated with a disorientation angle greater than 15^0.

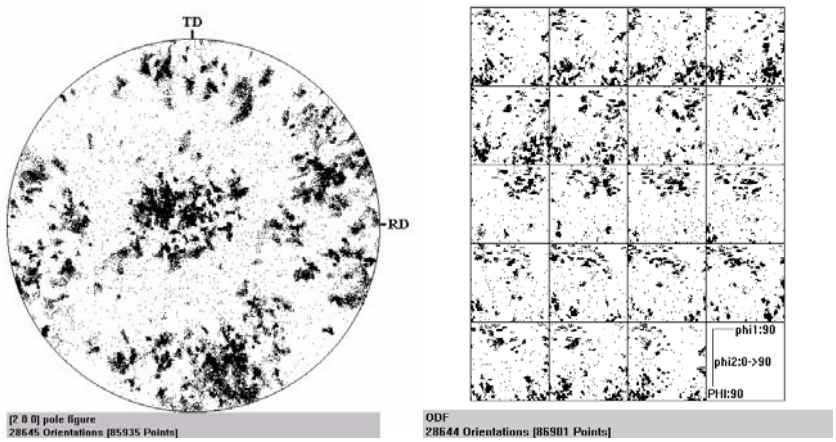

Figure 22: [200] Pole figure and ODF of sample 1M middle. The ODF is sectioned in phi2 intervals of 5^o.

Sample no. 1M surface

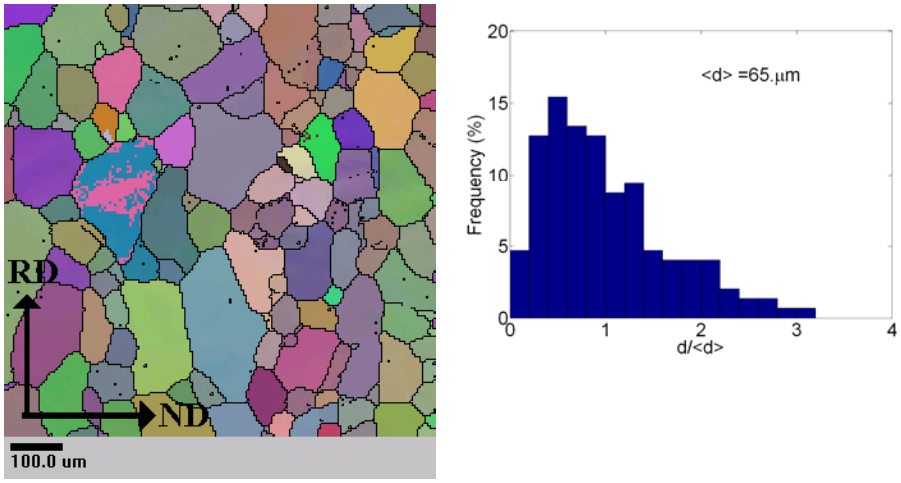

Figure 23: OI and grain size distribution of sample 1M surface. Calculated with a disorientation angle greater than 5^0.

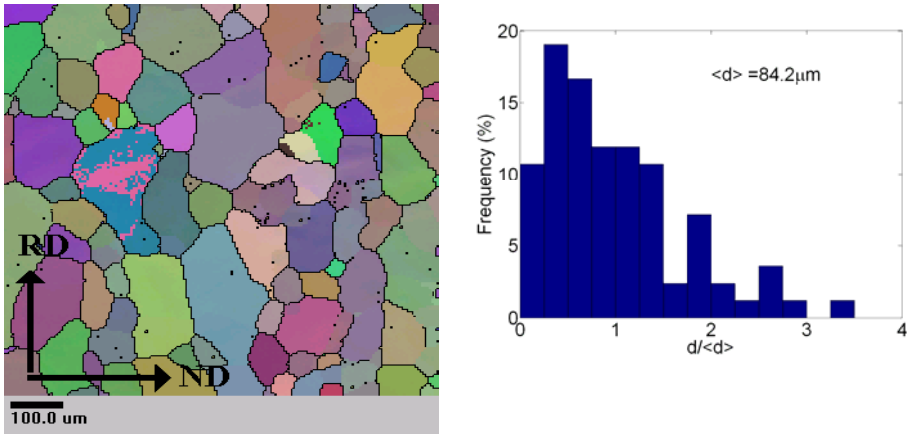

Figure 24: OI and grain size distribution of sample 1M surface. Calculated with a disorientation angle greater than 15^0.

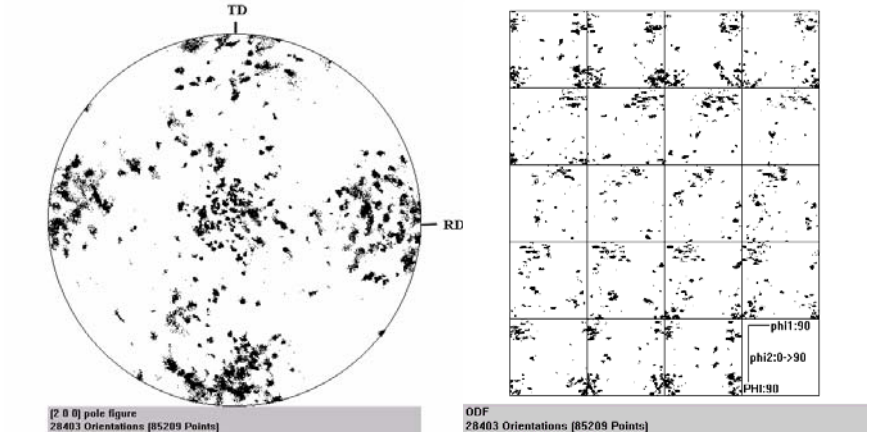

Figure 25: [200] Pole figure and ODF of sample 1M surface. The ODF is sectioned in phi2 intervals of 5^o.

Sample no. 1M ¼ thickness

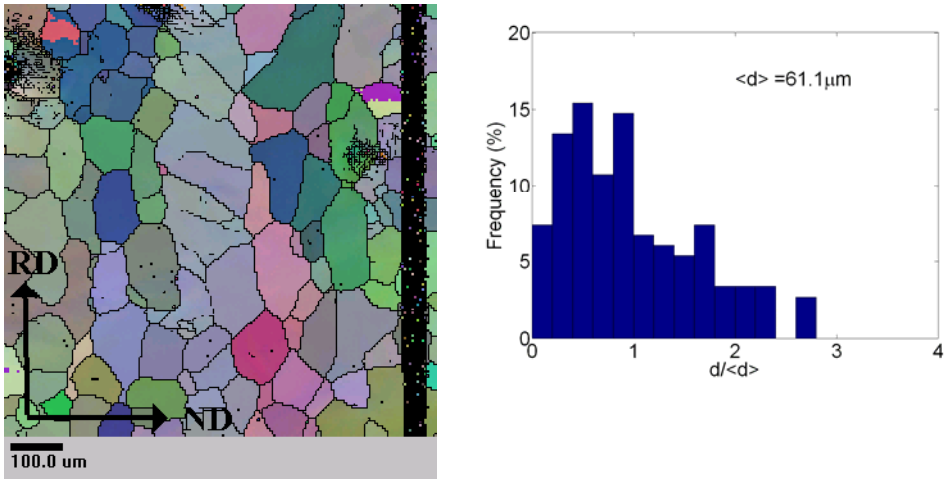

Figure 26: OI and grain size distribution of sample 1M ¼ thickness. Calculated with a disorientation angle greater than 5^0.

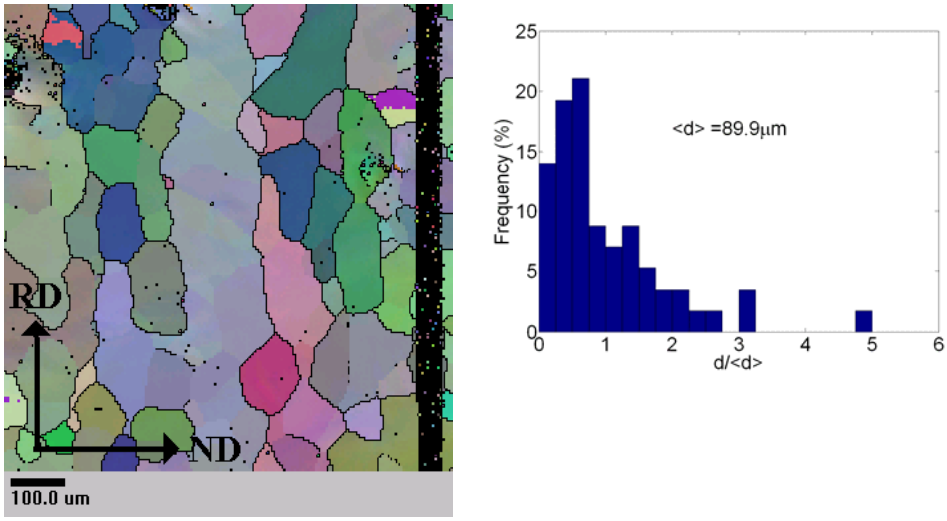

Figure 27: OI and grain size distribution of sample 1M ¼ thickness. Calculated with a disorientation angle greater than 15^0.

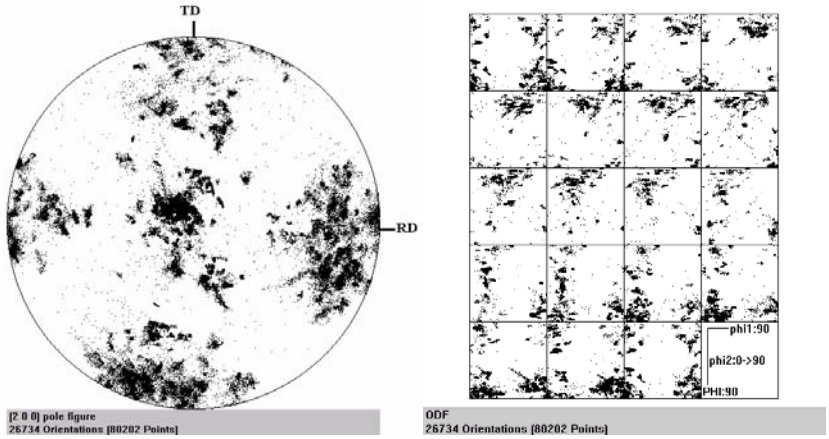

Figure 28: [200] Pole figure and ODF of sample 1M ¼ thickness. The ODF is sectioned in phi2 intervals of 5^o.

Sample no. 1R middle

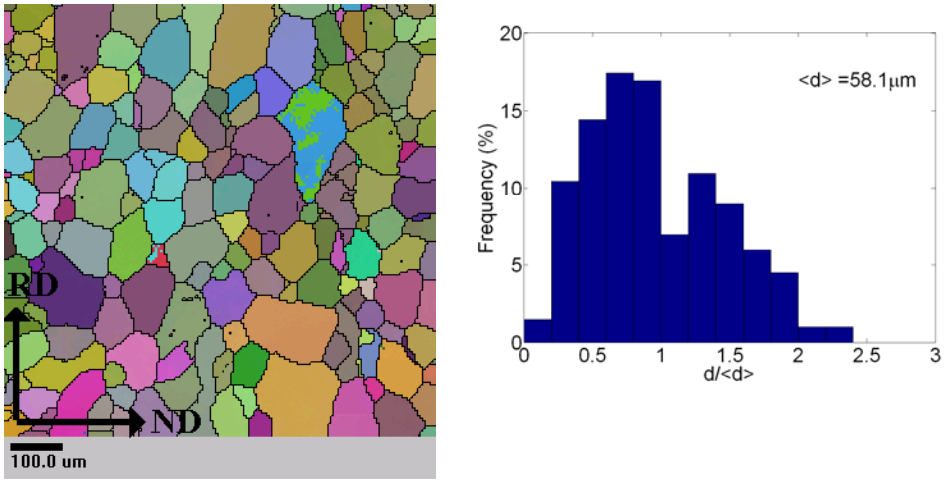

Figure 29: OI and grain size distribution of sample 1R middle. Calculated with a disorientation angle greater than 5^0.

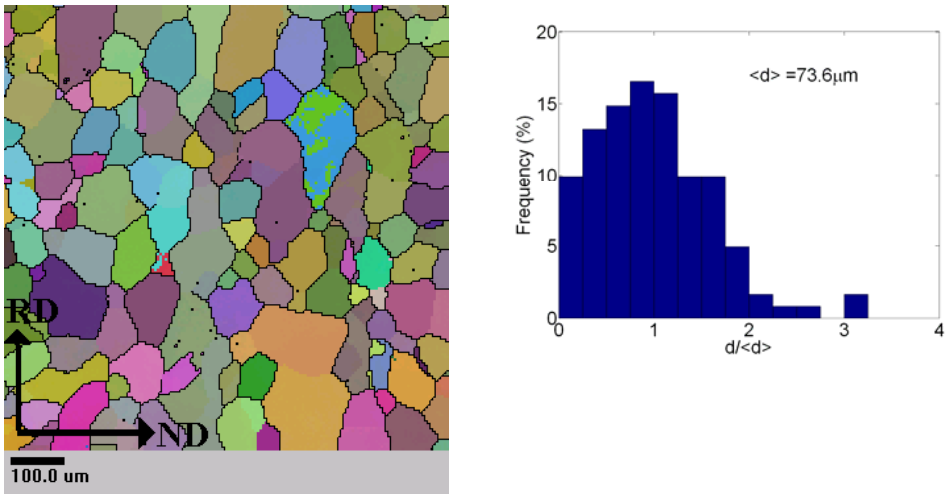

Figure 30: OI and grain size distribution of sample 1R middle. Calculated with a disorientation angle greater than 15^0.

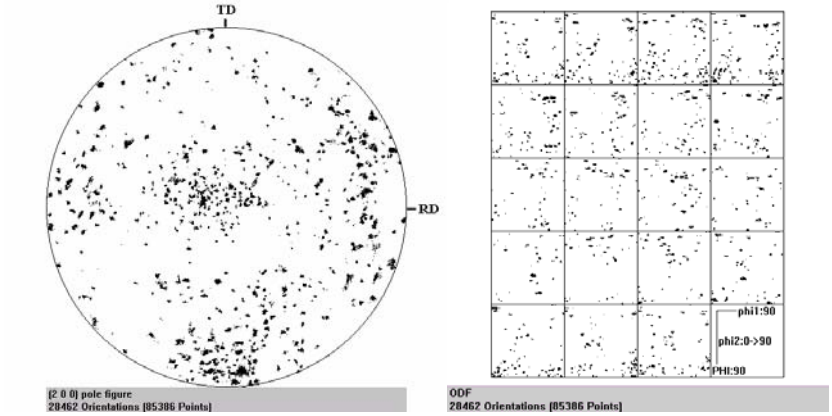

Figure 31: [200] Pole figure and ODF of sample 1R middle. The ODF is sectioned in phi2 intervals of 5^o.

Sample no. 1R surface

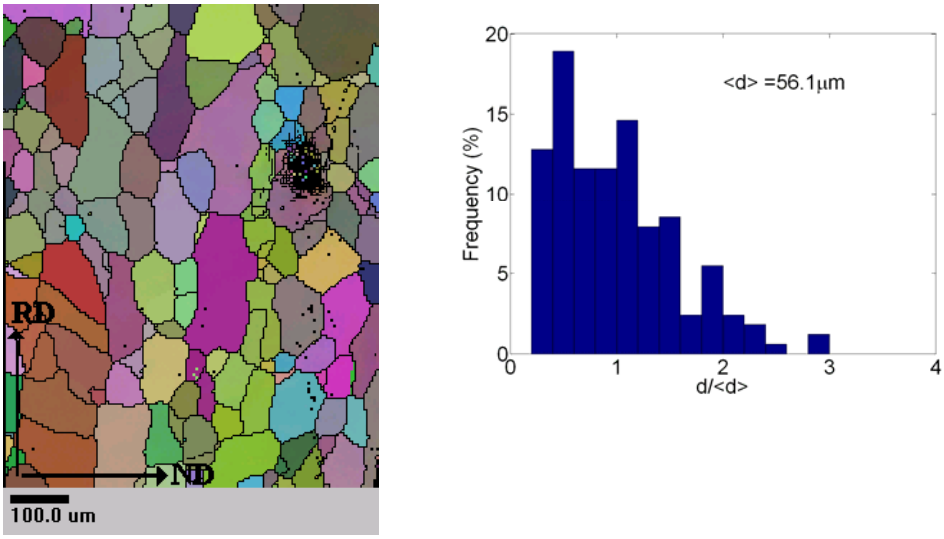

Figure 32: OI and grain size distribution of sample 1R surface. Calculated with a disorientation angle greater than 5^0.

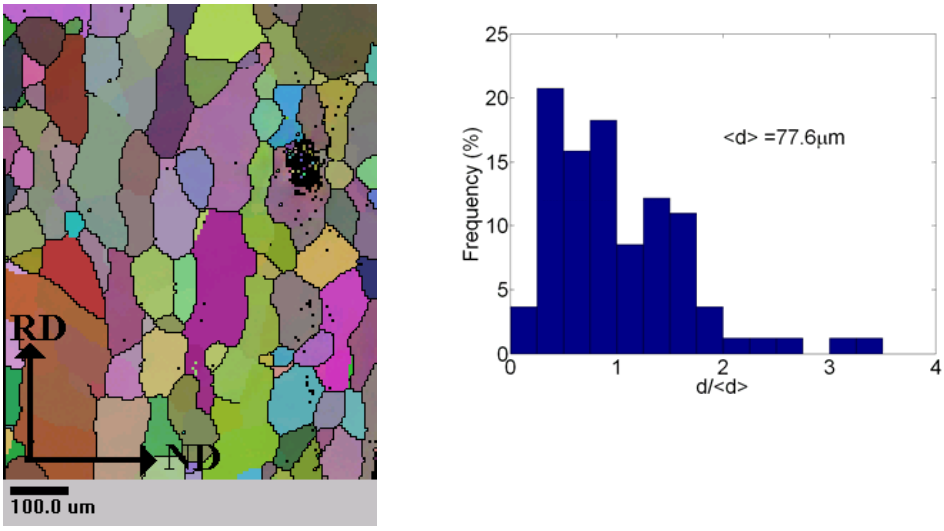

Figure 33 OI and grain size distribution of sample 1R surface. Calculated with a disorientation angle greater than 15^0.

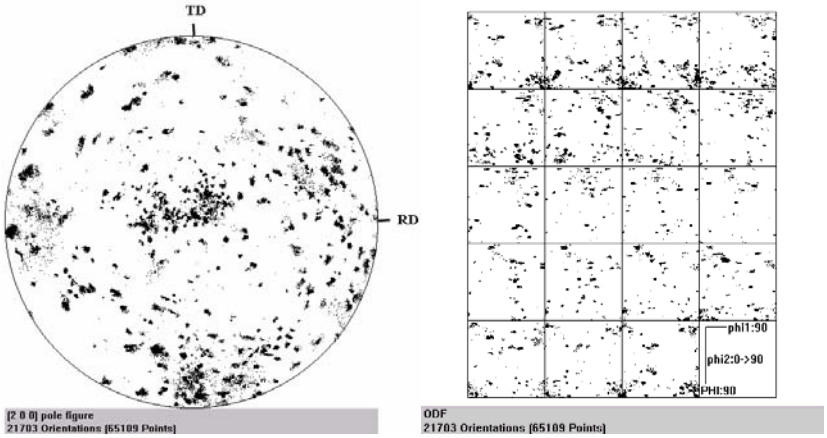

Figure 34 : [200] Pole figure and ODF of sample 1R surface. The ODF is sectioned in phi2 intervals of 5^o.

Sample no. 1R ¼ thickness

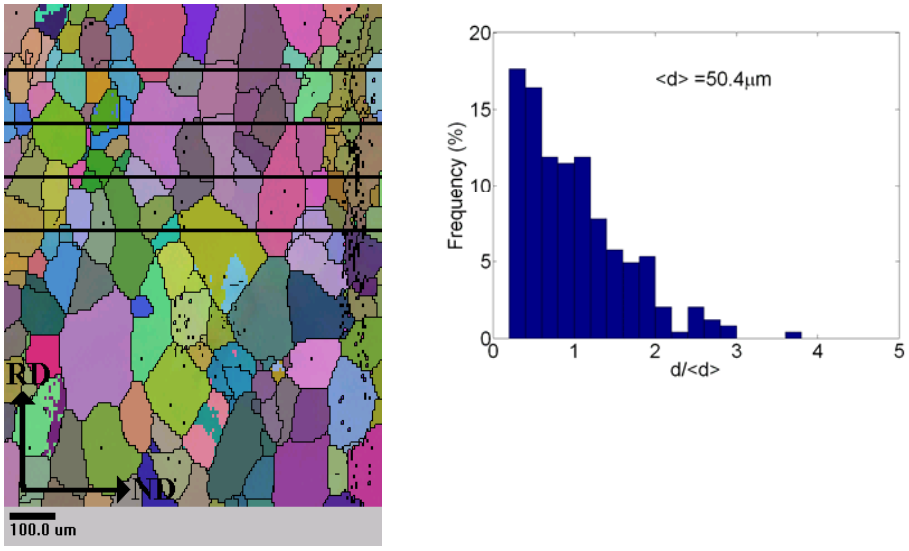

Figure 35: OI and grain size distribution of sample 1R ¼ thickness. Calculated with a disorientation angle greater than 5^0.

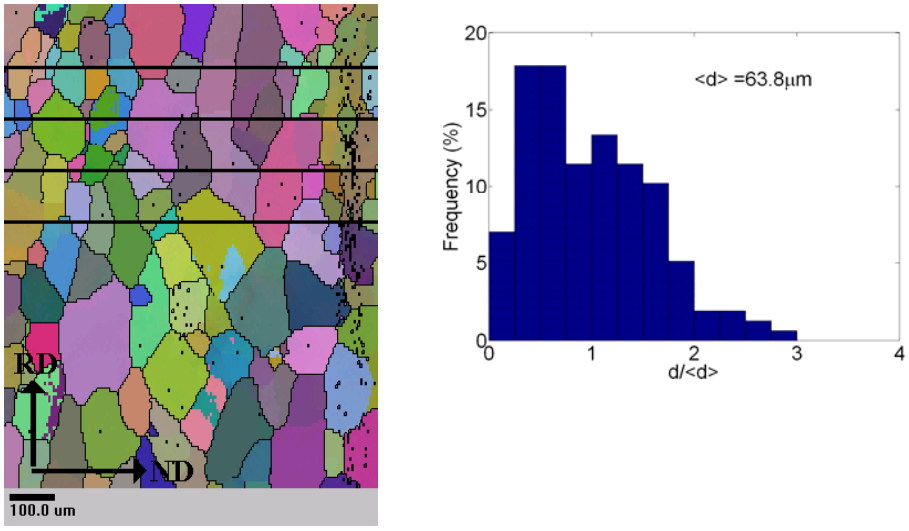

Figure 36: OI and grain size distribution of sample 1R ¼ thickness. Calculated with a disorientation angle greater than 15^0.

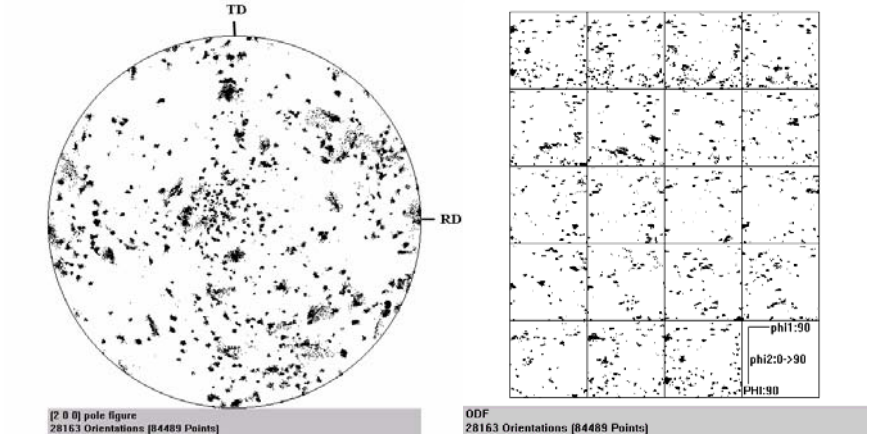

Figure 37: [200] Pole figure and ODF from sample no. 1R ¼ thickness. The ODF is sectioned in phi2 intervals of 5^o.

Sample no. 5

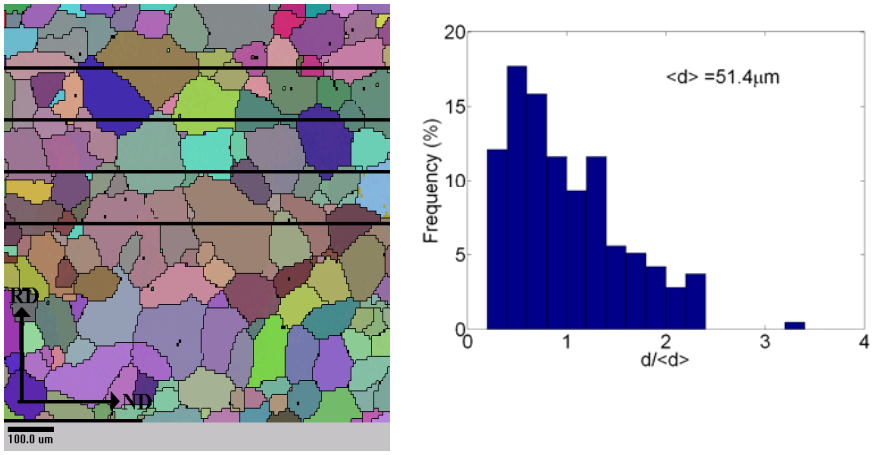

Figure 38: OI and grain size distribution of sample 5. Calculated with a disorientation angle greater than 5^0.

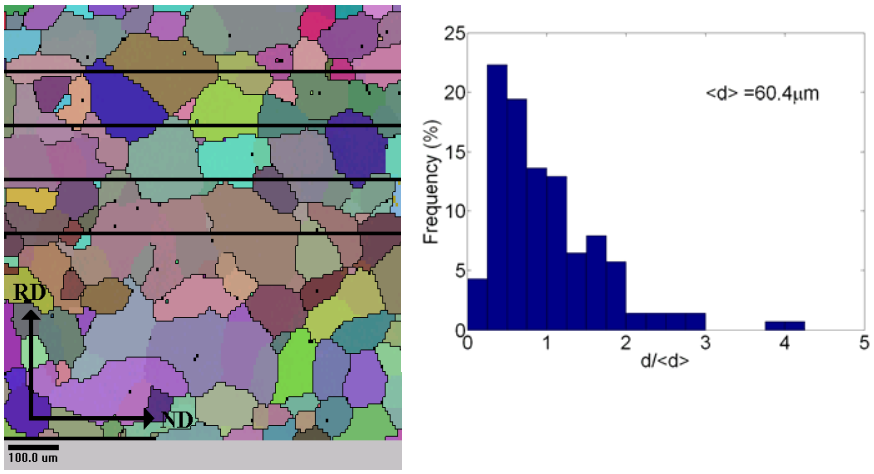

Figure 39 OI and grain size distribution of sample 5. . Calculated with a disorientation angle greater than 15^0.

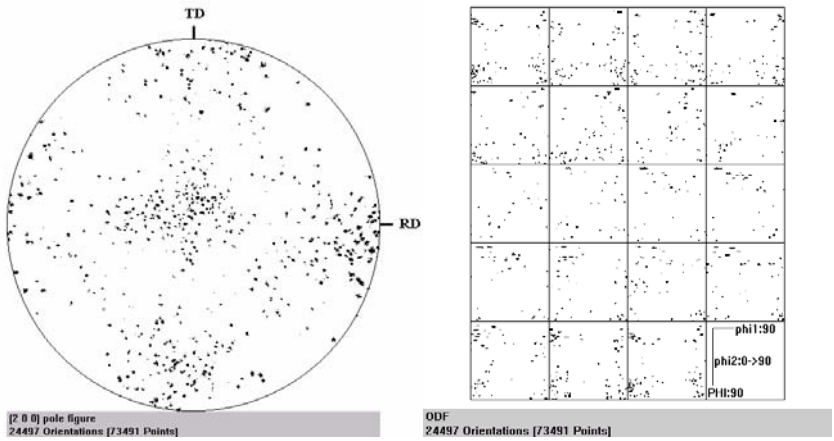

Figure 40: [200] Pole figure and ODF from sample no. 5. The ODF is sectioned in phi2 intervals of 5^o.

Sample no. 10

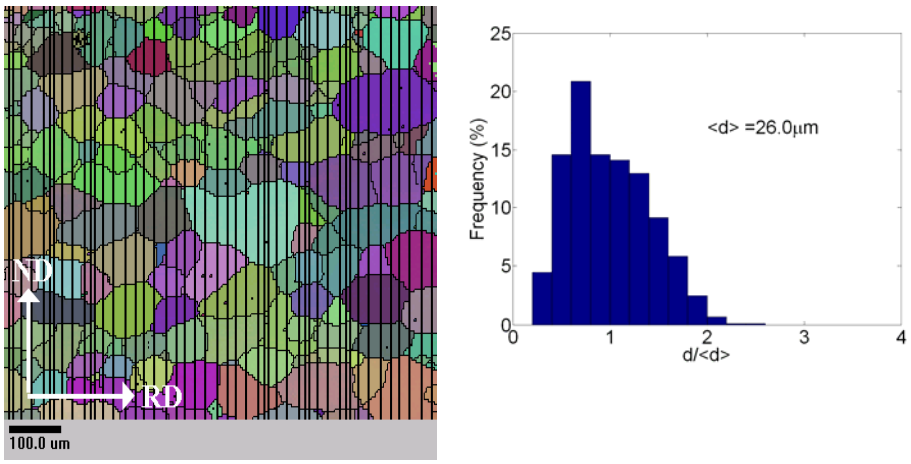

Figure 41: OI and grain size distribution of sample no. 10. Calculated with a disorientation angle greater than 5^0.

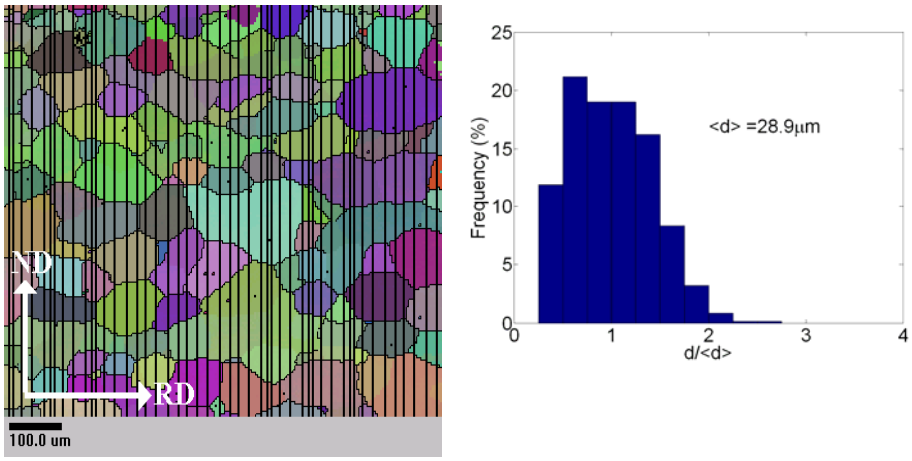

Figure 42 OI and grain size distribution from sample no. 10. Calculated with a disorientation angle greater than 15^0.

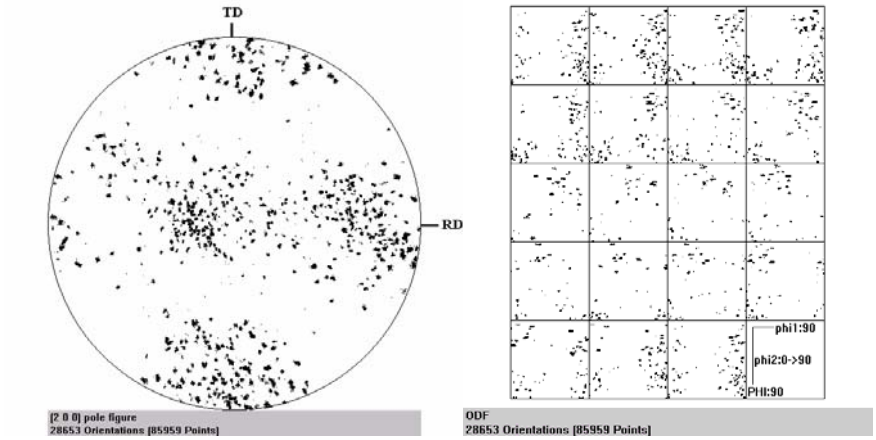

Figure 43: [200] Pole figure and ODF from sample no. 10. The ODF is sectioned in phi2 intervals of 5^o.

Sample no. 15

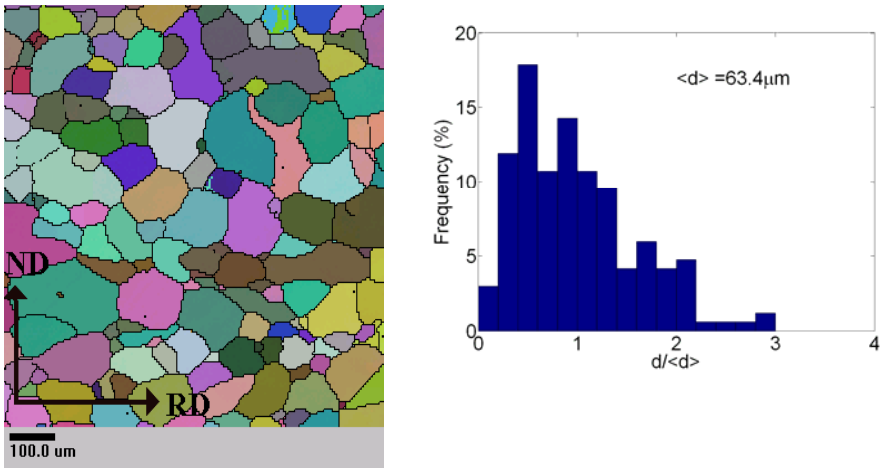

Figure 44: OI and grain size distribution of sample no. 15. Calculated with a disorientation angle greater than 5^0.

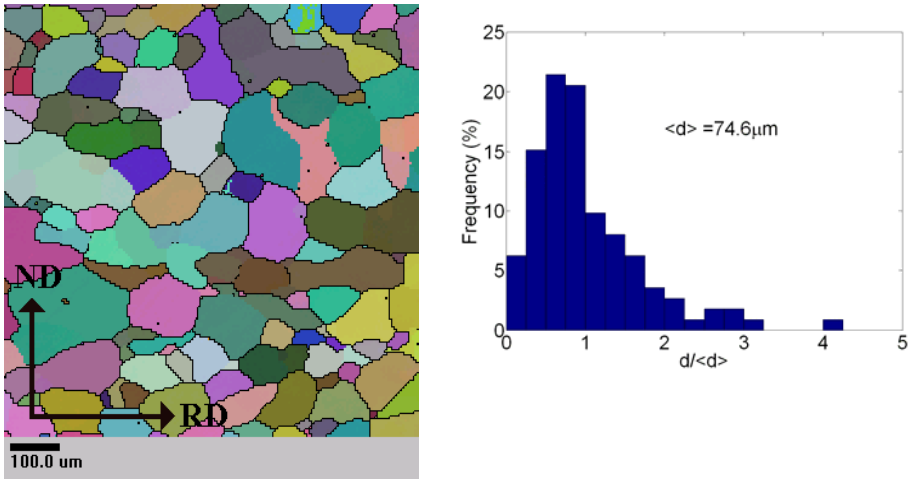

Figure 45: OI and grain size distribution of sample no. 15. Calculated with a disorientation angle greater than 15^0.

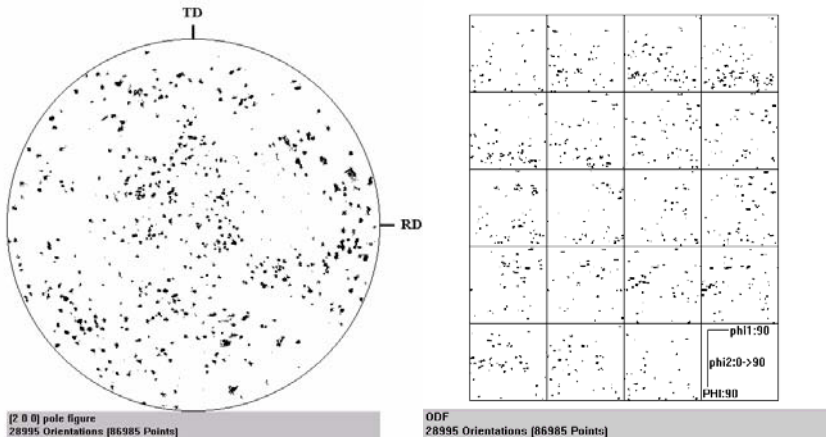

Figure 46: [200] Pole figure and ODF from sample no. 15. The ODF is sectioned in phi2 intervals of 5^o.

Sample no. 20

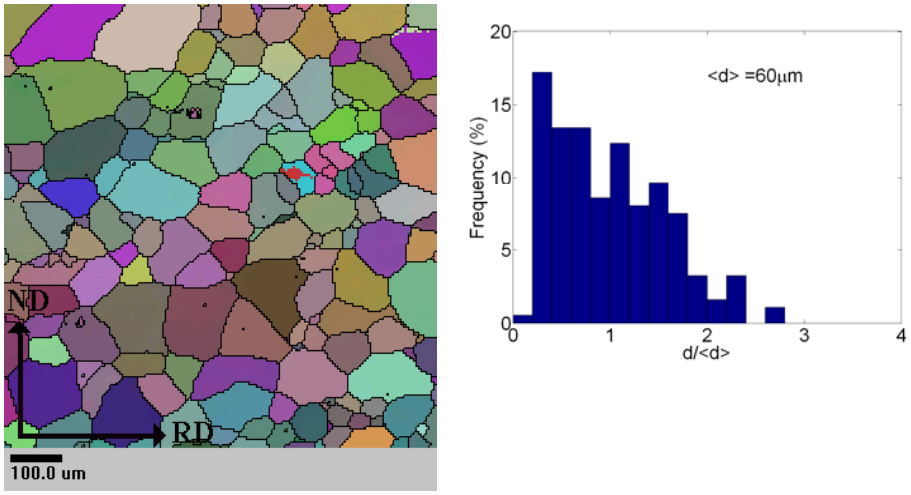

Figure 47: OI and grain size distribution of sample no. 20. Calculated with a disorientation angle greater than 5^0.

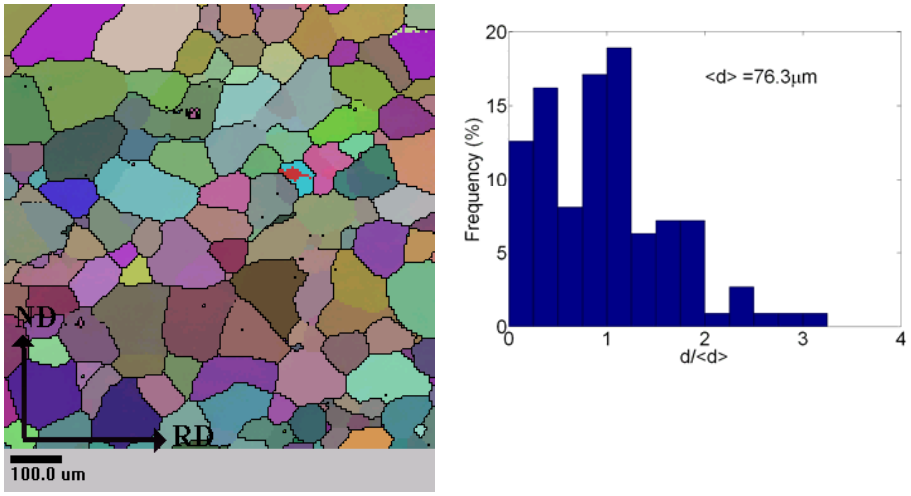

Figure 48: OI and grain size distribution of sample no. 20. Calculated with a disorientation angle greater than 15^0.

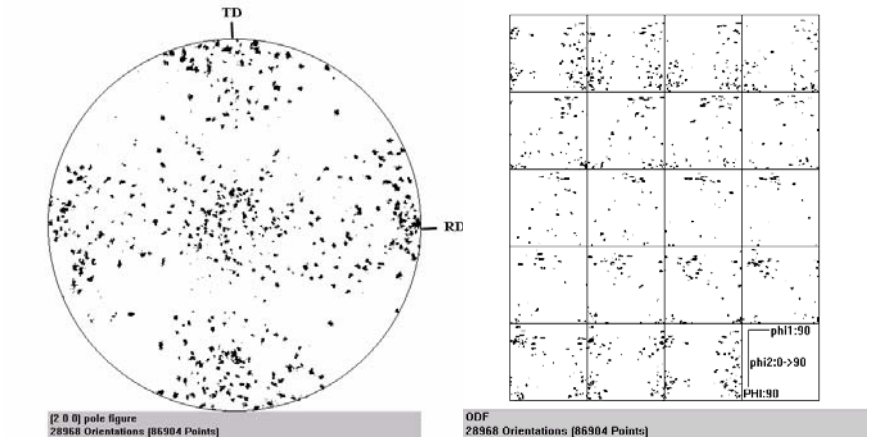

Figure 49: [200] Pole figure and ODF from sample no. 20. The ODF is sectioned in phi2 intervals of 5^o.

Sample no. 25

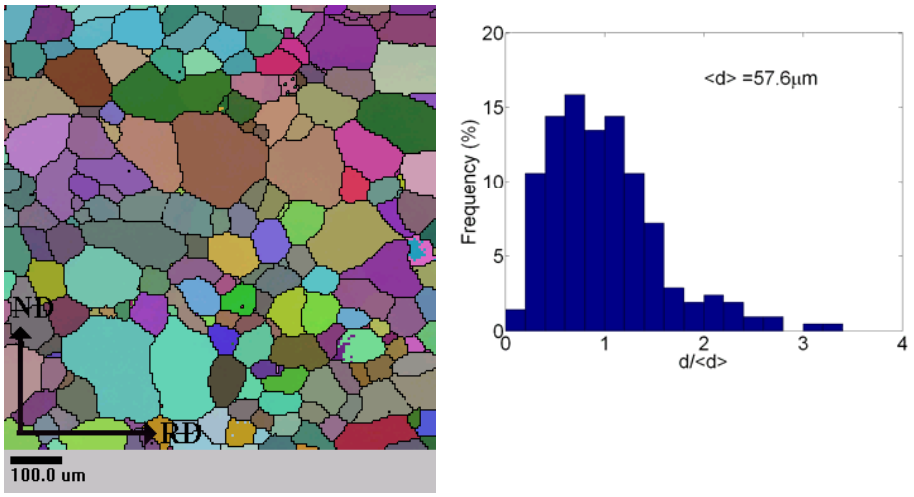

Figure 50: OI and grain size distribution from sample no. 25. Calculated with a disorientation angle greater than 5^0.

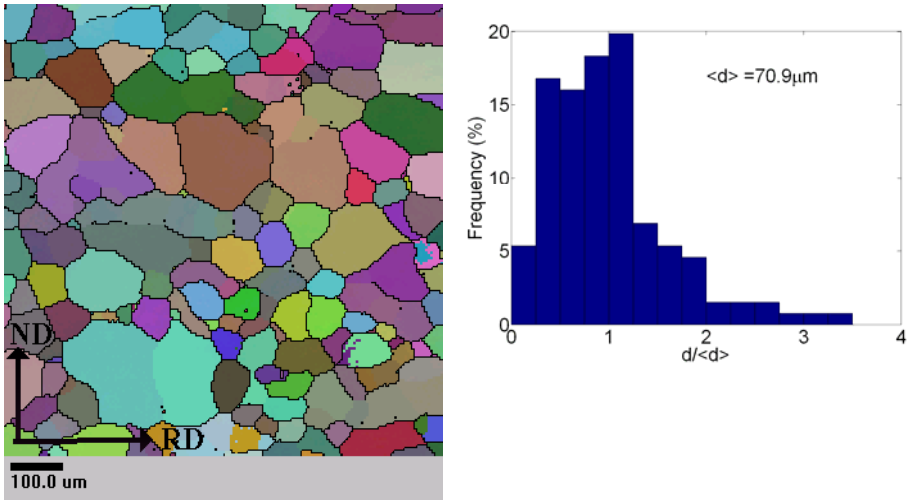

Figure 51: OI and grain size distribution of sample no. 25. Calculated with a disorientation angle greater than 15^0.

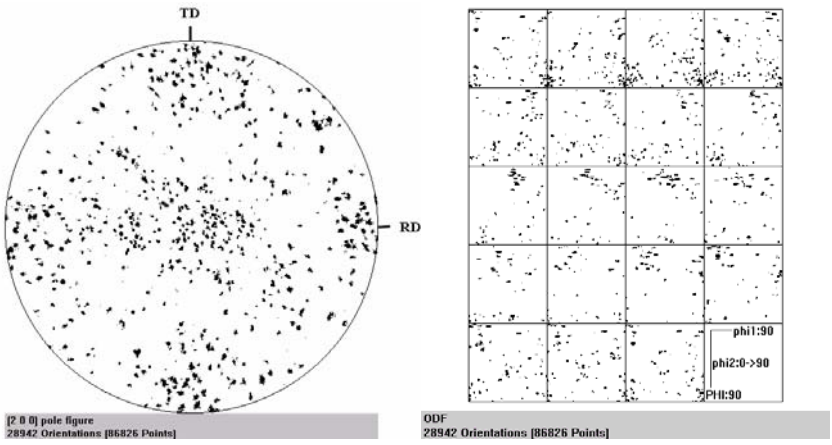

Figure 52: [200] Pole figure and ODF from sample 25. The ODF is sectioned in phi2 intervals of 5^o.

Sample no. 30

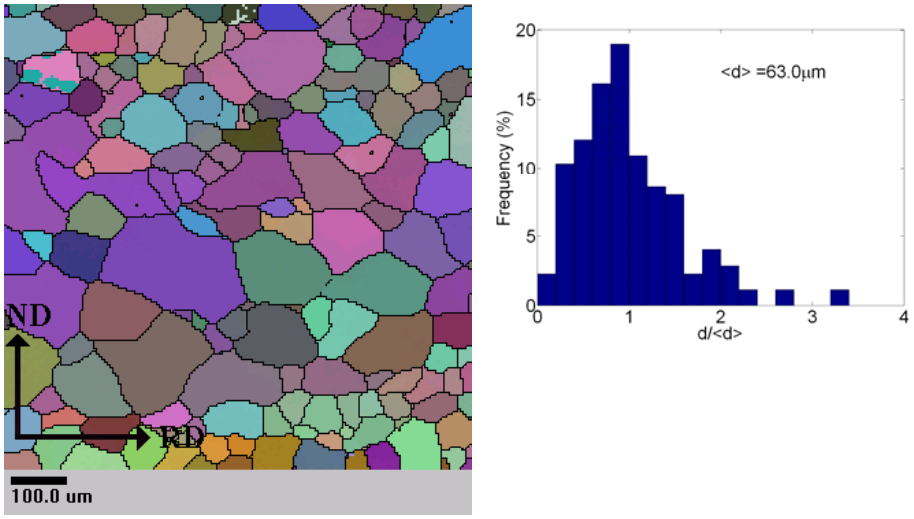

Figure 53: OI and grain size distribution of sample 30. Calculated with a disorientation angle greater than 5^0.

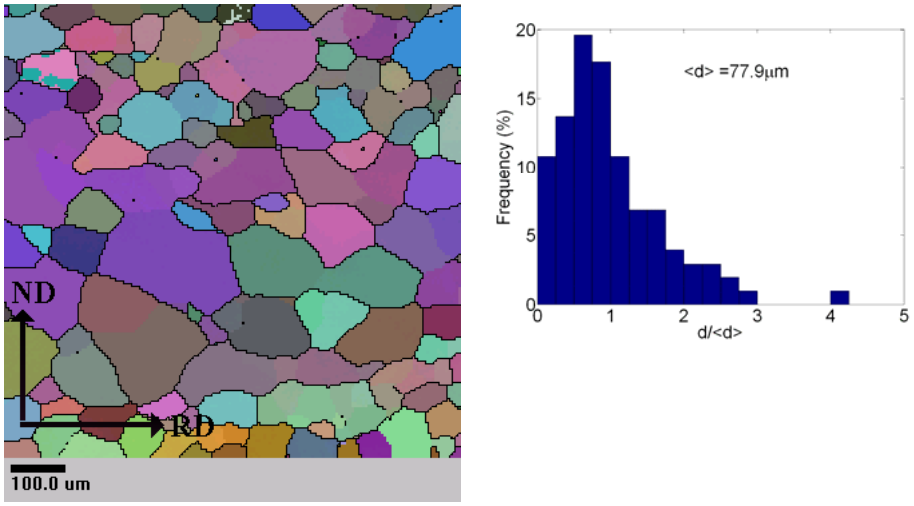

Figure 54: OI and grain size distribution of sample no. 30. Calculated with a disorientation angle greater than 15^0.

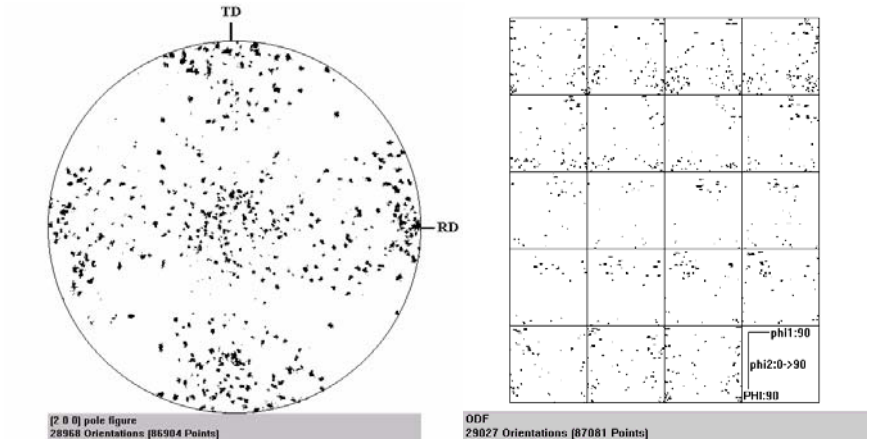

Figure 55: [200] Pole figure and ODF from sample no. 30. The ODF is sectioned in phi2 intervals of 5^o.

Sample no. 1M

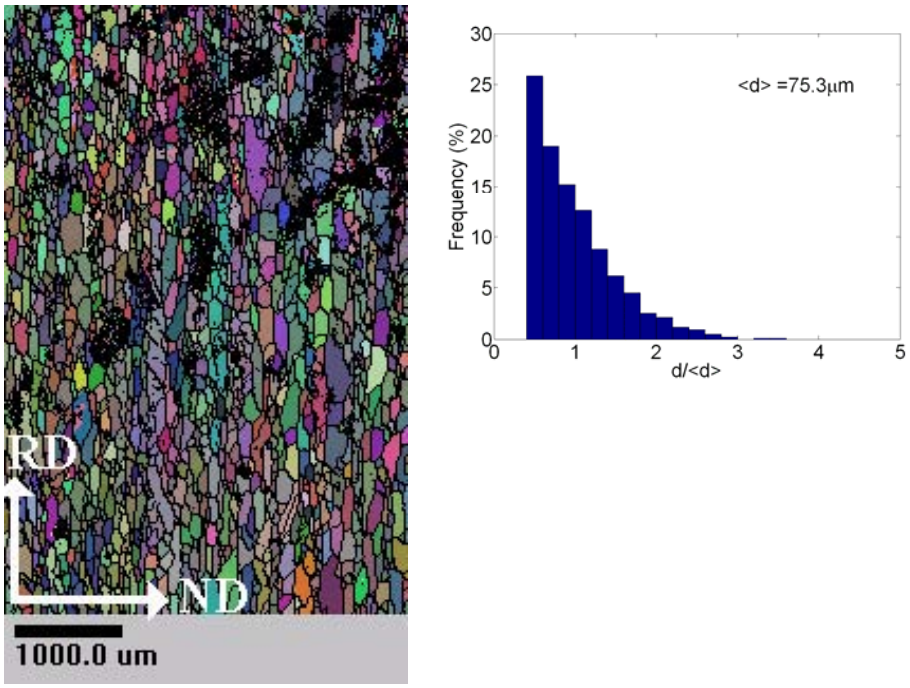

Figure 56: OI and grain size distribution of sample no. 1M. Calculated with a disorientation angle greater than 5^0.

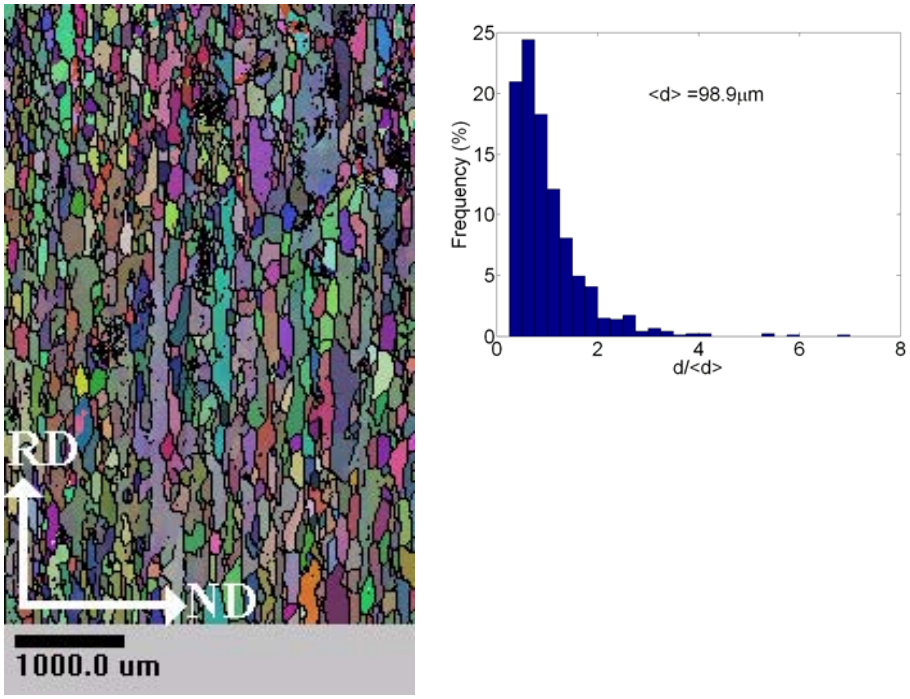

Figure 57: OI and grain size distribution of sample no. 1M. Calculated with a disorientation angle greater than 15^0.

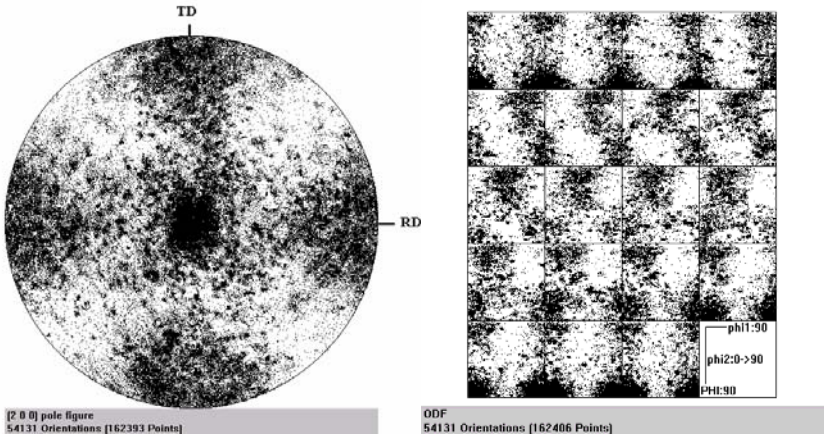

Figure 58: [200] Pole figure and ODF from sample 1M. The ODF is sectioned in phi2 intervals of 5°.

Bibliographic Data Sheet *Risø-I-2143 (EN)*

Title and authors

GFF Basis material AA 1050

Tine Knudsen

Department or group

Center for Fundamental Research:
Metal Structures in Four Dimensions
AFM

Date

October 2006

Sponsorship

Danish Research Foundation

Pages 53 Tables 9 Illustrations 58 References 4

Abstract (max. 2000 characters)

This internal report describes the production and characterization of a large amount of commercially pure aluminium (AA 1050), produced to serve as a stock material for The Center for Fundamental Research: Metal Structures in Four Dimensions.

Plates of commercially pure aluminium were cut, heat treated, cold rolled and heat treated again to produce a total of 30 aluminium plates of various sizes. The materials were characterized chemically and with the electron back scattered diffraction pattern technique (EBSP). The data analyzed from the EBSP were characterized with respect to grain size, aspect ratio (RD/ND), distribution of grain sizes and the texture components Cube {100}<001>, Brass {110}<1 $\bar{1}$ 2>, Copper {112}<11 $\bar{1}$ >, S {12 $\bar{3}$ }<634>, Goss {011}<100>, C2 {001}<110>, A {310}<1 $\bar{3}$ 0>, B {310}<001> and C1 {122}<2 $\bar{2}$ 1>. Besides, [200] pole figures and orientation distribution functions (ODFs) were plotted. One plate was characterized in nine different locations and since that plate did not show any systematic variation in texture, grain size or distribution of these, the same was assumed to apply to the remaining plates.

The characteristics of the material are following:

- The material is 99.5% pure
- The major impurities are Si and Fe
- The grain size is 70μm (mean chord length)
- The grains are elongated in the RD/ND plane with an average aspect ratio of 1.3
- The distribution of the grain sizes are not log normal.
- The average texture of the material in volume % is Cube 9% (4 x random) Brass 2% (0.5 x random) Copper 3% (0.7 x random), Goss 2%(0.9 x random), S 5%(0.6 x random) C2 1%(0.2 x random), A 13%(3 x random), B 15% (3 x random) and C1 4% (3 x random)

Information Service Department: 2 copies